Zonal Flow and Spectra in Two-Dimensional Rayleigh–Bénard Convection

Philip Winchester
Keble College
University of Oxford

A thesis submitted for the degree of
Doctor of Philosophy

Trinity 2023

Preface

The research described in this thesis was performed in the Oxford Centre of Industrial and Applied Mathematics at the Mathematical Institute, University of Oxford between October 2019 and July 2023, and was supervised by Professor Peter D. Howell and Dr Vassilios Dallas.

This thesis describes my own original work and no part of this thesis has been submitted previously for a degree of the University or elsewhere.

At the time of writing, two papers based on the work presented in this thesis have been published, co-authored with P. D. Howell and V. Dallas. A paper based on the onset of zonal modes in 2D Rayleigh-Bénard convection, presented in §3, has been published in the *Journal of Fluid Mechanics* [185] and the zonal flow reversals, presented in §4, has been published in *Physical Review Fluids* [184]. In both publications, I performed the theoretical analysis, while P. D. Howell and V. Dallas supervised the research.

Philip Winchester
Oxford, July 2023

Acknowledgements

First and foremost, I owe a big thanks to my supervisors, Peter D. Howell and Vassilios Dallas. Without their patience and wisdom, completing this thesis would not have been possible. I have learnt so much from them both and am so grateful for their unwavering support over the last four years.

I am also grateful to Andrew Fowler, Andrew Wells, and Peter Read for insightful discussions and guidance in my transfer and confirmation of status examinations. Thanks also to Ian Hewitt and John Wettlaufer for an excellent viva and for providing many insightful comments that have greatly improved the quality of this thesis.

More broadly, I would like to thank my fellow graduate students in OCIAM and Oxford Mathematics, with special thanks to Amy Kent, Arkady Wey, Edwina Yeo, Helen Saville, Isabelle Scott, Michael McPhail, Michael Negus, Thomas Chandler, and Yidan Xue, for their friendship and mathematical advice.

On a more personal note, I would like to thank Daniele Dorigoni, Marianne Peetz, and Owen Dennis for being great role models and for inspiring my interest in mathematics before my time in Oxford. Without their encouragement, I would not have had the confidence to pursue this subject I have learnt to love.

Thanks to my housemates George Robinson, James Fox, Jess Cowell, Lewis Anderson, and Liam Elbourne. My time in Oxford would not have been nearly as rewarding without them. I know they will all go on to do great things.

Thanks to my friends Adam Örjebrink, Beth Cohen, Emil Ljung, Fanny Berg, Hector McKimm, James Gunn, Oliver Winchester, Tavi Chetty, and Victor Larsson who have all travelled great distances to share some of the good times with me in Oxford. Adam, Beth, and Tavi, thank you for being the best friends and girlfriend I could ever hope for, and for your unwavering support and guidance on personal matters.

Thanks to my brother, Oliver, and parents, David and Jasmina Winchester for their unconditional love and support throughout.

Finally, financial support from EPSRC, the Mathematical Institute, Keble College, SIS, and Helsingborgs Handelsförening are gratefully acknowledged.

Abstract

In this thesis, we study two-dimensional Rayleigh-Bénard convection at a wide range of Prandtl numbers.

Following two introductory chapters, the subsequent three chapters focus on a horizontally periodic domain with free-slip top and bottom boundaries. This configuration encourages mean horizontal flows of zero horizontal wavenumber, which can be considered as an idealisation of zonal flows in planetary atmospheres, tokamaks, and annular cylindrical convection experiments. In chapter 3, we study the onset of zonal modes from a steady state that emerges at the onset of convection. In our fourth chapter, we study the dynamics when zonal modes are present. Our study unveils the presence of several bifurcations within the turbulent regime, in particular, a sequence of bifurcations leading to reversals of a very strong zonal flow. Chapter 5 generalises our analysis from a previously studied two-dimensional flow to a quasi-two-dimensional flow. We introduce a third spatial direction, and explore how narrow the domain must be in this direction to render the flow truly two-dimensional.

In chapter 6, we study two-dimensional Rayleigh-Bénard convection with periodic boundary conditions to emulate the dynamics far from walls. This chapter aims to understand how spectra, fluxes, and global variables vary with both the Rayleigh and Prandtl number.

Finally, the thesis concludes with a summary of the main findings together with an outlook on possible further research directions for each project.

Contents

List of Figures

Chapter 1

Prologue

1.1 Overview

Convection refers herein to fluid motion driven by variations in the fluid's density in the presence of a gravitational field. The Hadley cell serves as a key example of such convective flow, which is a large-scale tropical atmospheric circulation characterised by the ascending warm air near the equator, its poleward flow at altitudes of 12-15 km, and subsequent descent at roughly 30 degrees latitude, ultimately returning equatorward near the surface. The circulatory pattern in the Hadley cells contributes to the development of the prevailing easterly trade winds, a significant feature in atmospheric dynamics.

Early explanations of the consistent trade winds, like that proposed by Edmond Halley in 1687, attributed the phenomenon to the Earth's rotation and the daily cycle of solar heating [76]. However, Halley's model could not account for the observed continuous easterly wind direction and wind speeds of 5-10 m/s [129]. A more accurate model was subsequently proposed by George Hadley in 1735, who integrated the Coriolis force into the model, explaining the westward deflection of the wind produced by Hadley cells [75].

While this example illustrates the rich history of the studies of convection, today convection is a key area in various fields, including meteorology, geophysics, astrophysics, and industrial processes. It plays a critical role in planetary and stellar interiors [25, 148], in the Earth's mantle [41, 54, 91, 138], and has profound effects on our planet at a global scale. Convection-driven phenomena, such as cloud formation and large-scale ocean circulations, significantly affect our climate by regulating temperature [49], recycling nutrient-rich water [113], ice formation [181, 183], and acting as a major sink for anthropogenic carbon dioxide [43]. Volcanic eruptions serve as prime examples of thermal convection at play, revealing intricate structures and turbulent eddies [158].

There are also numerous practical applications, not least in batch melting processes in the metal and glass industry [17, 68]. The endeavour to understand these captivating phenomena hinges on three fundamental laws: the conservation of mass, momentum, and energy.

1.2 Thesis Outline

In this thesis, we focus on thermal convection, specifically, two-dimensional (2D) Rayleigh-Bénard (RB) convection. The governing equations are derived in chapter 2, we discuss some of the solutions' qualitative features and review the literature on zonal flow in convective systems. Zonal flow in 2D RB convection with horizontal periodicity and free-slip top and bottom boundaries will be the central theme of chapters 3–5. This configuration encourages mean horizontal flows of zero horizontal wavenumber, and can be considered as an idealisation of zonal flows in planetary atmospheres, tokamaks, and annular cylindrical convection experiments, as discussed in §2.5. When present, zonal flows are typically very strong and can suppress [63] or in some cases enhance [188] convective heat transfer depending on the studied domain and boundary conditions. They have therefore been a central theme in both experimental [57], and numerical and theoretical studies [63, 77, 131, 136, 174, 175, 188].

In chapter 3, we study the stability of a steady state consisting of a pair of counter-rotation convection rolls that emerge at the onset of convection. We show that the steady state contains no zonal flow, and that zonal flow can only emerge once it has become unstable. In our 2D domain, it is computationally feasible to consider a large parameter space and we perform the stability analysis across twelve orders of magnitude in the Prandtl number and six orders of magnitude in the Rayleigh number, observing diverse qualitative behaviors. We are able to capture some of these qualitative behaviours with a model derived from a weakly non-linear analysis.

In chapter 4, we study the dynamics when zonal flow is present. Building on the findings of Goluskin et al. [63], we explore a wide range of Prandtl numbers and observe bifurcations within the turbulent regime that lead to previously unobserved zonal flow reversals, the qualitative characteristics of which are found to depend on the Prandtl number and aspect ratio.

Chapter 5 generalises our analysis from a previously studied two-dimensional flow to a quasi-two-dimensional flow. We take the 2D flows studied in the preceding chapters, introduce a third spatial direction, and add three-dimensional (3D) disturbances. The primary objective is to determine how narrow the domain must be in the direction perpendicular to the 2D flow to render the flow truly two-dimensional.

Chapter 6 is different from the rest in that it does not study zonal flow. Instead, here we study 2D RB convection with periodic boundary conditions to emulate the dynamics far from walls at much larger Rayleigh numbers. The purpose of this chapter is to understand how energy spectra, fluxes, and global variables vary with both the Rayleigh and Prandtl number. Our study expands on previous research, which mainly focused on the scenario when the Prandtl number is 1 [10, 14, 28, 29, 38, 106, 154, 162].

Finally, in chapter 7, the thesis concludes with a summary of the main findings together with an outlook on possible further research directions for each project.

Chapter 2

Two-Dimensional Rayleigh-Bénard Convection

Rayleigh-Bénard convection is the most studied thermal convection scenario, having become a favoured model for investigating instabilities, bifurcations, pattern formation, and turbulence [11, 62, 145]. RB convection occurs when a horizontally planar layer of fluid, which may be two- or three-dimensional and of finite or infinite horizontal extent, is heated from below and cooled from the top. This results in an unstably stratified layer of fluid with warmer, thus lighter, fluid at the bottom, and cooler, hence denser, fluid at the top.[1] Fluid motion is driven by this temperature gradient. However, it is essential to understand that temperature disparities on their own do not trigger convection. The instability created by this temperature difference needs to surpass the restraining effects of viscosity and diffusivity on fluid motion. Once convection kicks in, movement and thermal diffusion will strive to balance the temperature across the field, so to maintain convection, we need to consistently disrupt this equilibrium. This can be achieved by continually heating and cooling from the bottom and top, respectively.[2] This process can be observed in everyday situations like heating water in a pot or in the Earth's mantle and atmosphere.

There are many other convective systems that are governed by similar dynamics. For instance, in seawater, it is the salinity that serves the function of temperature, and in electroconvection, electric charge and electric potential act as analogues for temperature and gravitational potential, respectively.

[1] Note that the densities of certain fluids do not increase monotonically with temperature; for example, in the interesting case of penetrative convection in water which is most dense at 4 °C [165].

[2] Convection can be achieved through different methods as well, for example, by heating the fluid internally [64], or by heating and cooling the sidewalls [140].

2.1 Governing Equations

The equations governing RB convection are the mass conservation equation, the momentum equation, coupled with the heat transport equation, and an equation of state in which the density depends linearly on the temperature [36], i.e.

$$\rho_t + \nabla \cdot (\rho \boldsymbol{u}) = 0, \tag{2.1a}$$

$$\rho[\boldsymbol{u}_t + (\boldsymbol{u} \cdot \nabla)\boldsymbol{u}] = -\nabla p - \rho g \mathbf{e}_y + \mu \nabla^2 \boldsymbol{u}, \tag{2.1b}$$

$$\rho c_p [T_t + \boldsymbol{u} \cdot \nabla T] = k \nabla^2 T, \tag{2.1c}$$

$$\rho = \rho_0 [1 - \alpha(T - T_0)], \tag{2.1d}$$

where $\rho(\boldsymbol{x}, t)$ is the density, $\boldsymbol{u}(\boldsymbol{x}, t)$ is the velocity, $p(\boldsymbol{x}, t)$ is the pressure, $\mathbf{e}_y$ is the unit upward vector and T is the temperature. The constants g, μ, c_p, k, ρ_0 and α are the gravitational acceleration, dynamic viscosity, specific heat, thermal conductivity, density at the reference temperature T_0 of the top plate, and the thermal expansion coefficient, respectively. In this thesis, we will study 2D RB convection where the spatial domain extends horizontally by $x \in [0, L_x]$ and vertically by $y \in [0, L_y]$.

We define our boundary conditions in the following two sections before non-dimensionalising the governing equations (2.1).

2.1.1 Kinematic Boundary Conditions

The kinematic boundary conditions in chapters 3–5 will be periodic in x and free-slip in y, i.e.

$$\mathbf{n} \cdot \boldsymbol{u} = \mathbf{n} \cdot \nabla (\boldsymbol{u} \cdot \mathbf{t}) = 0 \quad \text{at } y = 0, L_y, \tag{2.2a}$$

$$\boldsymbol{u}(x + L_x, y, t) = \boldsymbol{u}(x, y, t), \tag{2.2b}$$

where $\mathbf{n}$ and $\mathbf{t}$ and normal and tangent to boundary, respectively. At free-slip boundaries, the fluid flows parallel to the boundary, and the boundary exerts no shear stress on the fluid. Boundaries in some astrophysical, geophysical and fusion-related applications are modelled well as free-slip.

In chapter 6, the kinematic boundary conditions will be fully periodic, which is an idealised approach to study RB convection far from walls, thereby avoiding the complexities of boundary layers.

We restrict our analysis to these boundary conditions because they are convenient both numerically and analytically.

2.1.2 Thermal Boundary Conditions

As for the kinematics boundary conditions, the thermal boundary condition will be horizontally periodic in chapters 3–5. On the horizontal boundaries, we will be imposing fixed-temperature (Dirichlet) boundary conditions. This approach involves applying a vertical temperature gradient across the layer such that $T = T_0 + \Delta T$ at $y = 0$ and $T = T_0$ at $y = L_y$. This remains constant over time, effectively simulating boundaries with infinite thermal conductivity.

In chapter 6, we impose a constant average vertical temperature gradient by writing the temperature field as $T(x, y, t) = \Delta T\,(1 - y/L) + \theta(x, y, t)$. The temperature perturbation, θ, satisfies periodic boundary conditions.

2.1.3 Dimensionless Equations

We non-dimensionalise (2.1) as follows:

$$\begin{gathered} \boldsymbol{u} \sim \frac{\kappa}{L_y}, \quad \kappa = \frac{k}{\rho_0 c_p}, \quad t \sim \frac{L_y^2}{\kappa}, \quad \boldsymbol{x} \sim L_y, \\ p - [p_0 + \rho_0 g (L_y - y)] \sim \frac{\mu\kappa}{L_y^2}, \quad T - T_0 \sim \Delta T, \end{gathered} \tag{2.3}$$

where p_0 is the pressure at the top of the fluid layer, which we take as constant. The non-dimensionalised equations take the form,

$$-\mathrm{B}T_t + \nabla \cdot [(1 - \mathrm{B}T)\boldsymbol{u}] = 0, \tag{2.4a}$$

$$\frac{1}{\mathrm{Pr}}[1 - \mathrm{B}T][\boldsymbol{u}_t + (\boldsymbol{u} \cdot \nabla)\boldsymbol{u}] = -\nabla p + \mathrm{Ra}T\mathbf{e}_y + \nabla^2 \boldsymbol{u}, \tag{2.4b}$$

$$(1 - \mathrm{B}T)(T_t + \boldsymbol{u} \cdot \nabla T) = \nabla^2 T, \tag{2.4c}$$

where the density has been algebraically removed, and the non-dimensional parameters Ra, Pr, and B are the Rayleigh, Prandtl and Boussinesq numbers, which are defined as

$$\mathrm{Ra} = \frac{\alpha \Delta T g L_y^3}{\nu\kappa}, \quad \mathrm{Pr} = \frac{\nu}{\kappa}, \quad \mathrm{B} = \alpha \Delta T, \tag{2.5}$$

where $\nu = \mu/\rho_0$ is the kinematic viscosity. The Rayleigh number is a measure of the strength of the heating and may be thought of as the ratio of inertial forces to viscous forces. The Prandtl number is the rate at which the fluid dissipates momentum, divided by the rate at which it dissipates heat. Unlike the Rayleigh number, the Prandtl number depends only on the molecular properties of the fluid and does not depend on the geometry. If a fluid has a high Prandtl number, it means that the fluid strongly resists motion but is not very good at conducting heat. An example of this is the Earth's mantle, where the Prandtl number is of order 10^{23}. Conversely, if a fluid has a low Prandtl number, it indicates that the fluid offers less resistance to motion and is efficient at conducting heat. Examples of fluids with low Prandtl numbers include liquid metals and stellar plasmas.

Our fourth non-dimensional parameter is Γ, the width-to-height aspect ratio

$$\Gamma = \frac{L_x}{L_y}. \tag{2.6}$$

We now make the Boussinesq approximation, which says that $\mathrm{B} \ll 1$, and we ignore terms including B in (2.4). The Boussinesq approximation is applicable when (a) the vertical dimension of the fluid is much less than any scale height, and (b) when the motion-induced fluctuations in density and pressure do not exceed, in order of magnitude, the total static variations of these quantities [149]. In RB convection, it has been shown that the Boussinesq approximation can be applied up to Rayleigh numbers of nearly 10^{17} [69], five decades above the largest Rayleigh number considered in this thesis. However, there are many generalisations of simple RB convection where non-Boussinesq effects need to be considered. For example, in rotating RB convection, the length scale $(L_y g)^{1/2}/\Omega$, where Ω is the angular velocity of the rotation, can be much smaller than L_y. Consequently, assumption (a) above does not hold. While we make comparisons between simple RB convection and more complex systems or natural phenomena, it is important to remember that the Boussinesq approximation may not always be applicable.

Introducing the streamfunction, ψ, for a two-dimensional incompressible velocity field $\boldsymbol{u} = \mathbf{e}_z \times \nabla\psi$, where $\mathbf{e}_z$ is the unit vector along the z direction, we arrive at the 2D Boussinesq equations of thermal convection:

$$\nabla^2\psi_t + \{\psi, \nabla^2\psi\} = \mathrm{RaPr}T_x + \mathrm{Pr}\nabla^4\psi, \tag{2.7a}$$

$$T_t + \{\psi, T\} = \nabla^2 T, \tag{2.7b}$$

where $\{f, g\} = f_x g_y - g_x f_y$ is the standard Poisson bracket.

In the absence of motion, $\psi = 0$, the steady state temperature profile is linear,

$$T = 1 - y. \tag{2.8}$$

We define the temperature perturbation θ by

$$T = 1 - y + \theta, \tag{2.9}$$

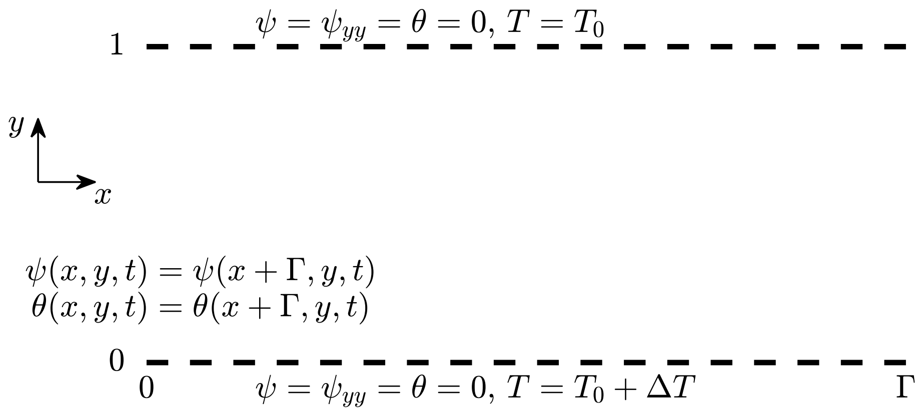

Figure 2.1: Sketch of the domain under study.

which yields

$$\nabla^2\psi_t + \{\psi, \nabla^2\psi\} = \mathrm{RaPr}\theta_x + \mathrm{Pr}\nabla^4\psi, \tag{2.10a}$$

$$\theta_t + \{\psi, \theta\} = \psi_x + \nabla^2\theta. \tag{2.10b}$$

The boundary conditions imposed on ψ and θ and the domain under study are depicted in Figure 2.1. The free-slip and fixed-temperature boundary conditions translate to

$$\psi = \psi_{yy} = \theta = 0 \text{ at } y = 0, 1, \tag{2.11}$$

and the periodic boundary condition is

$$\psi(x, y, t) = \psi(x + \Gamma, y, t), \tag{2.12}$$

and similarly for θ.

Given these boundary conditions, it is convenient to decompose the streamfunction into basis functions with Fourier modes in the x-direction and sine modes in the y-direction, viz.

$$\begin{aligned}\psi(x, y, t) &= \sum_{k_x\in\mathbb{Z}} \sum_{k_y\in\mathbb{Z}_{>0}} \widehat{\psi}_{k_x,k_y}(t)\mathrm{e}^{i2\pi k_x x/\Gamma} \sin(\pi k_y y) \\ &= \sum_{k_x,k_y} \widehat{\psi}_{k_x,k_y}(t)\phi_{k_x,k_y}(x, y),\end{aligned} \tag{2.13}$$

where $\widehat{\psi}_{k_x,k_y}$ is the amplitude of the (k_x, k_y) mode of ψ, and we have the constraint $\widehat{\psi}_{k_x,k_y} = \widehat{\psi}^*_{-k_x,k_y}$ ($*$ denoting complex conjugate). We decompose θ in the same way. This kind of decomposition will serve as the basis for all analytical and numerical methods in this thesis.

The set-up for the problem with periodic boundary conditions will be discussed separately in chapter 6.

2.1.4 Notation

We will be examining various quantities, averaged over space, time, or both. Accordingly, we define these averages as follows:

$$\langle f\rangle_{\boldsymbol{x}}(t) = \frac{1}{\Gamma}\int_0^1\int_0^\Gamma f(x,y,t)\,dxdy, \tag{2.14a}$$

$$\langle f\rangle_t(x,y) = \lim_{\tau\to\infty}\frac{1}{\tau}\int_0^\tau f(x,y,t)\,dt, \tag{2.14b}$$

$$\langle f\rangle_{\boldsymbol{x},t} = \langle\langle f\rangle_{\boldsymbol{x}}(t)\rangle_t. \tag{2.14c}$$

And with these, the energies

$$E_x^u(t) = \frac{1}{2}\langle\psi_y^2\rangle_{\boldsymbol{x}} = \text{horizontal kinetic energy}, \tag{2.15a}$$

$$E_y^u(t) = \frac{1}{2}\langle\psi_x^2\rangle_{\boldsymbol{x}} = \text{vertical kinetic energy}, \tag{2.15b}$$

$$E^u(t) = E_x^u(t) + E_y^u(t) = \text{(total) kinetic energy}, \tag{2.15c}$$

$$\widehat{E}^u(k,t) = \frac{1}{4}\sum_{k'\in C(k)} k'^2|\widehat{\psi}_{k_x,k_y}|^2 = \text{kinetic energy spectra}, \tag{2.15d}$$

$$E^\theta(t) = \frac{\mathrm{Ra}\,\mathrm{Pr}}{2}\langle\theta^2\rangle_{\boldsymbol{x}} = \text{potential energy}, \tag{2.15e}$$

$$\widehat{E}^\theta(k,t) = \frac{\mathrm{Ra}\,\mathrm{Pr}}{4}\sum_{k'\in C(k)}|\widehat{\theta}_{k_x,k_y}|^2 = \text{potential energy spectra}, \tag{2.15f}$$

where

$$k = \sqrt{\left(\frac{2\pi k_x}{\Gamma}\right)^2 + (\pi k_y)^2}, \tag{2.16a}$$

$$C(k) = [k-\pi/2, k+\pi/2). \tag{2.16b}$$

2.2 The Nusselt Number

In the study of turbulent flows, much effort has been devoted to understanding how integral quantities change based on varying control parameters. This importance is twofold: these quantities have direct physical significance, and there are few other methods to study such intricate flows. Of the various quantities studied, the Nusselt number garners a lot of attention. This is a dimensionless number that encapsulates the comparative effectiveness of convective and conductive heat transfer. Studying the Nusselt number is particularly important as it helps us understand the influence of fluid movement on heat transport.

To compute the Nusselt number, one needs to decide on a surface or volume to measure the heat flux, or the rate of heat flow. In the specific case of RB convection, most researchers focus on the vertical heat flux. This can be assessed across a chosen horizontal plane within the fluid or averaged over the whole layer of the fluid. In this thesis, we will adopt the most commonly used definition, where the Nusselt number is defined as the ratio of the total vertical heat flux (convection + conduction) to that by conduction alone, averaged over the entire layer, or mathematically:

$$\mathrm{Nu} = \frac{H_{\mathrm{cond}} + H_{\mathrm{conv}}}{H_{\mathrm{cond}}}. \tag{2.17}$$

The Nusselt number can therefore be thought of as an amplification factor, capturing how much more effectively heat traverses the fluid due to fluid motion.

From the dimensionless temperature equation, written in the standard form of a conservation law, $\partial_t T + \nabla \cdot (\boldsymbol{u}T - \nabla T) = 0$, one sees that the heat flux at a point comprises a conductive part, $-\nabla T$, and a convective part, $\boldsymbol{u}T$. We are interested in the average vertical heat flux across the entire layer, so we defined

$$H_{\mathrm{cond}} = \langle -\nabla T \cdot \mathbf{e}_y \rangle_{\boldsymbol{x}} = \frac{1}{\Gamma}\int_0^{\Gamma} \left[T|_{y=0} - T|_{y=1} \right] dx = 1, \tag{2.18a}$$

$$H_{\mathrm{conv}} = \langle \boldsymbol{u}T \cdot \mathbf{e}_y \rangle_{\boldsymbol{x}} = \langle \psi_x (1 - y + \theta) \rangle_{\boldsymbol{x}} = \langle \psi_x \theta \rangle_{\boldsymbol{x}}. \tag{2.18b}$$

We now define the instantaneous, $\mathrm{Nu}(t)$, and time averaged Nusselt number, Nu:

$$\mathrm{Nu}(t) = 1 + \langle \psi_x \theta \rangle_{\boldsymbol{x}}, \quad \mathrm{Nu} = 1 + \langle \psi_x \theta \rangle_{\boldsymbol{x},t}. \tag{2.19}$$

2.2.1 Classical Versus Ultimate Scaling

At present, there exist two prominent theories regarding the scaling of the Nusselt number with the Rayleigh and Prandtl numbers as the Rayleigh number approaches infinity, known as "classical" and "ultimate" scaling. These two theories present a significant unsolved problem in this field of study [46].

The classical scaling asserts that $\mathrm{Nu} \sim \mathrm{Ra}^{1/3}$. It was simultaneously and independently proposed by Priestly [132] and Malkus [111] in 1954. Priestley argued that the dimensional heat flux should become independent of the depth of the cell for turbulent convection, at least for sufficiently large aspect ratio domains, in other words, that

$$\mathrm{Nu}\frac{\kappa \Delta T}{L_y} \sim \text{independent of } L_y. \tag{2.20}$$

Since $\mathrm{Ra} \sim L_y^3$, the above condition only holds if $\mathrm{Nu} \sim \mathrm{Ra}^{1/3}$. Malkus formulated an elaborate maximal dissipation theory which additonally predicted a uniform scaling in Pr. The central concept of the classical scaling theory is that the heat flux is restricted by the transport across the thermal boundary layers.

In contrast, the ultimate scaling asserts $\mathrm{Nu} \sim \mathrm{Pr}^{1/2}\mathrm{Ra}^{1/2}$, at least for $\mathrm{Pr} \lesssim 1$ [38]. It was proposed by Spiegel [150] in the early 1960s based on different physics. Spiegel postulated that for large enough Rayleigh numbers, plumes are able to transport heat without regard for the boundary layers. The scaling is derived in the limit of large Péclet number $\mathrm{Pe} = \sqrt{2\langle E^u \rangle_t}$ and large Reynolds number $\mathrm{Re} = \sqrt{2\langle E^u \rangle_t}/\mathrm{Pr}$. At large Péclet number, the convective term, $\{\psi, \theta\}$, is much larger than the thermal diffusion term. Hence, the convective term balances the buoyancy term, ψ_x, in the heat transport equation (2.10b), i.e.

$$\{\psi, \theta\} \approx \psi_x \implies \sqrt{\langle \theta^2 \rangle_{\boldsymbol{x},t}} \sim 1. \tag{2.21}$$

Similarly, at large Reynolds number, the convective term, $\{\psi, \nabla^2\psi\}$, is much larger than the viscous dissipation term, so the convective term balances the buoyancy term, $\mathrm{RaPr}\theta_x$, in the momentum equation (2.10a), i.e.

$$\{\psi, \nabla^2\psi\} \approx \mathrm{RaPr}\theta_x \implies 2\langle E^u \rangle_t \sim \mathrm{RaPr}. \tag{2.22}$$

For the Nusselt number, we therefore have

$$\mathrm{Nu} = 1 + \langle \psi_x \theta \rangle_{\boldsymbol{x},t} \approx \langle \psi_x \theta \rangle_{\boldsymbol{x},t} \approx \sqrt{2\langle E^u \rangle_t}\sqrt{\langle \theta^2 \rangle_{\boldsymbol{x},t}} \sim \mathrm{Pr}^{1/2}\mathrm{Ra}^{1/2}. \tag{2.23}$$

Soon after Spiegel's work, logarithmic corrections in Ra were included in the scaling by Kraichnan [97].[3]

Theoretical studies have proposed a transition from the classical to ultimate scaling at $\mathrm{Ra} \gtrsim 10^{14}$ [72], but sophisticated laboratory experiments have reported on both ultimate [37, 135] and classical [120, 167] scaling in the ultra-high Rayleigh number regime.

Direct numerical simulations of the equations of motion are an alternative approach to study the problem. Unfortunately, ultra-high Rayleigh number simulations require very fine spatial resolution, small time steps and long runs to generate reliable statistics which leaves simulations in three dimensions extremely expensive [141, 152]. However, Iyer et al. [87] have simulated Rayleigh numbers up to 10^{15} in slender domains, obtaining results consistent with the classical scaling.

[3] While Kraichnan's paper in 1962 [97] was published before Spiegel's [150] in 1963, Spiegel's work actually predates this as testified by Batchelor [5] in 1960.

To date, the only numerical evidence of the ultimate scaling is from works that have modified the structure of the boundary layers. Either by considering a fully periodic domain which effectively removes the boundary layers [14, 29, 106], or by considering rough boundaries that enhance the interaction between the boundary layers and the core flow, driving the generation of a larger number of thermal plumes which in turn increases convective heat transfer [66, 163, 190, 191]. However, in the latter case, it has been suggested that the scaling may revert back to the one with smooth boundaries for large enough Rayleigh numbers, but that the Rayleigh number range at which the ultimate scaling manifests might be extended for roughness with more length scales [190, 191]. Toppaladoddi et al. [164] studied 2D RB convection with a fractal boundary and computed the exponent β using power-law fits of $\mathrm{Nu} \sim \mathrm{Ra}^{\beta}$ for Rayleigh numbers between 10^8 and 10^{10} and observed $\beta = 0.288 \pm 0.005$, $\beta = 0.329 \pm 0.0065$, and 0.352 ± 0.011 for different degrees of roughness.

The recent study by Zhu et al. [189] suggests a transition to the ultimate regime in 2D RB convection with no-slip top and bottom boundaries. However, since the time of its publication, the validity of these findings has been met with scepticism, as pointed out in subsequent works by Doering et al. [45] and Lindborg [105].

For completeness, we mention that a third scaling, namely $\mathrm{Nu} \sim \mathrm{Ra}^{2/7}\mathrm{Pr}^{-1/7}$, has been proposed by Casting et al. [32], Shraiman and Siggia [143, 145], which agrees well with experimental results [32, 120] at small Prandtl numbers. For a derivation of this scaling, the reader is referred to the papers [32, 143, 145] or the more recent book by Verma [170].

2.3 Qualitative Features of RB Convection

Modern research in Rayleigh-Bénard convection is rooted in the experiments of Henry Bénard in 1900 [7][4] and the theoretical work of Lord Rayleigh in 1916 [134]. Rayleigh showed that for our set-up displayed in Figure 2.1 with free-slip horizontal boundaries, only the conductive state with $\psi = \theta = 0$ (illustrated in Figure 2.2 (a)) is stable until the Rayleigh number reaches some critical value Ra_c. Intriguingly, this critical value depends only on the aspect ratio (Γ), not on the Prandtl number, as discussed further in chapter 3.

Upon reaching Ra_c, a new steady state consisting of pairs of laminar counter-rotating convection rolls (illustrated in Figure 2.2 (b)), referred to as the *Steady*

[4] Bénard [7] studied convection in a liquid layer with a free upper surface in contact with air, where effects of surface tension come into play (Bénard-Marangoni convection). So while not strictly equivalent, it laid the ground for Rayleigh's subsequent analysis [134].

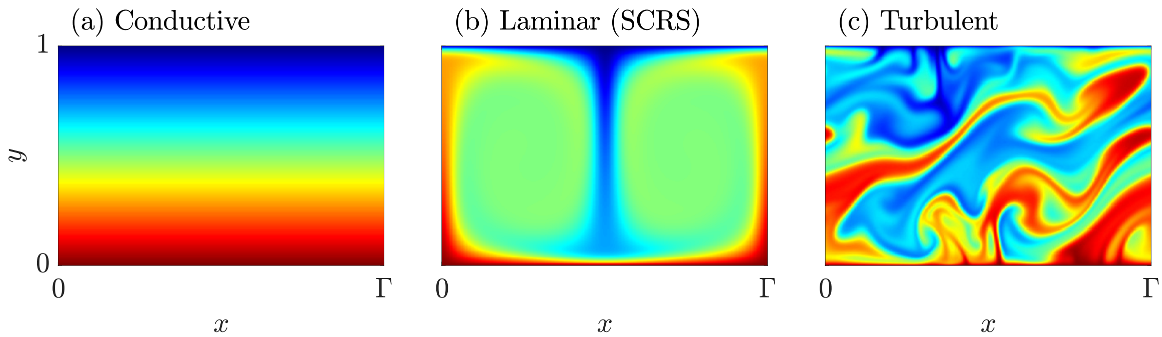

Figure 2.2: Temperature fields at different Rayleigh numbers showing the conducive state, an instance of the SCRS, and turbulent flow.

Convection Roll State (SCRS) in this thesis, bifurcates from the conductive state. This phenomenon is prevalent in RB convection across a range of geometries and boundary conditions. However, the value of Ra_c and the number of convection rolls can vary.

As the Rayleigh number increases further, multiple other solution branches emerge. The details of the bifurcation structure depend strongly on the geometry, boundary conditions, and Prandtl number, but the number of solutions reliably increases with Ra [15]. However, the vast majority of these are unstable in much of the parameter space. For large enough Ra, all solutions are unstable, after which only spatiotemporal chaos is physically realisable. When these chaotic flows become sufficiently robust and complex, they are often termed turbulent (illustrated in Figure 2.2 (c)), though there is no universally precise definition for the onset of turbulence [4].

2.3.1 Shearing Versus Non-Shearing Convection

In the set-up illustrated in Figure 2.1, with $\mathrm{Pr} > 1$ and large Rayleigh numbers, the flow will typically orient itself in one of two flow states, these are the so-called *Shearing* and *Non-Shearing* convection states [63, 175]. In Figure 2.3 we illustrate the difference between these with parameters fixed at $(\mathrm{Ra}, \mathrm{Pr}, \Gamma) = (10^7, 10, 2)$. Firstly, in column (a), we see that the majority of the kinetic energy is held in the horizontal direction when in the shearing state: the fraction E^u_x/E^u rarely drops below 95%. On the other hand, the kinetic energy oscillates around an equipartitioned mean in the non-shearing state. In (b) we observe that the Nusselt number is significantly smaller in the shearing state in comparison with its non-shearing counterpart. The temperature field images in column (c) provide insight into this difference. The non-shearing state presents the familiar convection roll pattern, where thin, heat-transferring plumes cross the entire layer. However, in the shearing state, even though these plumes

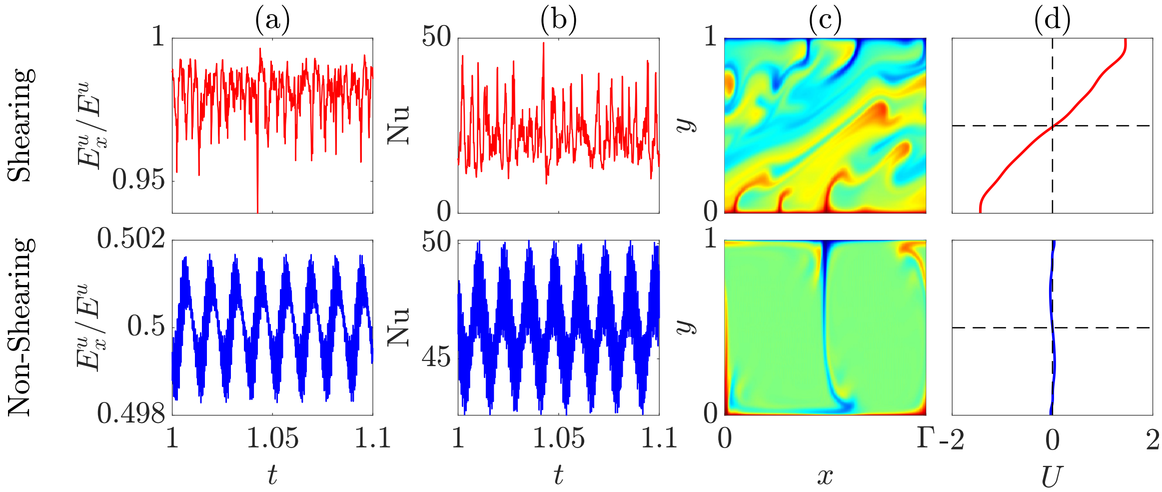

Figure 2.3: Shearing (top row) and non-shearing (bottom row) convection. In both instances, we have $(\mathrm{Ra}, \mathrm{Pr}, \Gamma) = (10^7, 10, 2)$. (a) and (b) show time series of the normalised kinetic energy held in the horizontal direction and the Nusselt number, respectively. Time is shown on the thermal time scale L_y^2/κ. (c) shows instantaneous realisations of the temperature fields. The hottest fluid (red) is one dimensionless unit warmer than the coldest fluid (blue). (d) Shows the associated instantaneous zonal flows, $U(y,t)$, normalised with the rms velocity, $u_{rms} = \sqrt{\langle \psi_x^2 + \psi_y^2 \rangle_{\boldsymbol{x},t}}$.

appear more frequently, they can not cross the entire layer due to the presence of zonal flow, which limits the overall convective heat transfer.

Finally, in (d), we see the defining feature that distinguishes the two, which is that the shearing state has prominent zonal flow which is horizontally sheared. In this instance, the zonal flow, defined by

$$U(y,t) = -\frac{1}{\Gamma}\int_0^\Gamma \psi_y(x,y,t)\,dx, \tag{2.24}$$

is such that $U > 0$ in the upper part of the domain, but the centre line symmetry about $y = 1/2$ could equally have broken in the opposite way, in which case the sign of U would be reversed. There is no net zonal flow in the non-shearing state. A final observation is that the time series displayed in Figure 2.3 are chaotic in the shearing state, resulting in a turbulent flow, but quasi-periodic in the non-shearing state. However, as we shall see, this is typically not the case as many non-shearing states are also turbulent.

2.4 Zonal Flow

As evident in §2.3.1, the key characteristic differentiating shearing from non-shearing convection is the presence of zonal flow in the former, while it is absent in the latter. At first glance, it might seem counterintuitive that zonal flow can emerge in RB convection since buoyancy only drives fluid motion in the vertical direction. However, the fluid must also move horizontally since the confining geometry forces it to recirculate.

One of the first accounts of zonal flow in buoyancy-driven systems came from Rory Thompson [159] who in 1970 observed that convection cells in the atmosphere of Venus are vertically sheared. Large-scale zonal flow in buoyancy-driven systems has since been found frequently in nature. How Jupiter's cloud-level zonal winds are generated and maintained has been a major scientific puzzle for decades. There are two main contenders to explain the origin of the winds: (i) They are maintained and generated by deep thermal convection and extend deep into Jupiter's interior [47, 86, 142, 160, 179] and (ii) they are associated with horizontal temperature differences between belts and zones and confined to a very thin stably stratified weather layer below which there exists an unknown convective circulation [23, 61, 79, 88]. Kong et al. [96] recently showed that the Juno gravitational measurements alone cannot discriminate between these two different scenarios, so the origin of the winds is still a mystery. In Fujisawas review article [57], it is stated that zonal flows could be one of the great discoveries in the research on magnetically confined plasma aimed at controlled nuclear fusion, since the concept could provide a new framework for the fundamental understanding of plasma turbulence and transport. In experiments of rapidly rotating slender cylindrical cells, Zhang et al. [188] reported zonal flow along the boundaries which enhanced heat transport there. The shearing instability which generates this net zonal flow has been studied both in the full Boussinesq equations [127, 136] and in several modal truncations [3, 9, 80, 82, 84, 136].

Each chapter of this thesis holds its own literature review that contextualises the key points relevant to that particular chapter. However, since zonal flow will be a central theme throughout the entirety of this thesis, we will review its pertinent literature in the sections to follow.

2.4.1 Shearing Mechanism

In RB convection, zonal flow is driven by an energy transfer from horizontal scales, which are driven by buoyancy [65]. This mechanism has been called the shearing or tilting mechanism. However, it is important to note that the mere presence of the shearing mechanism does not ensure sustained zonal flow. The mechanism must be strong enough to transfer energy to the zonal flow as quickly as the zonal flow loses energy through viscous dissipation. Previous studies have shown that larger Rayleigh numbers, smaller Prandtl numbers, and narrower horizontal domains favour zonal flows [63, 84, 136, 175].

The energy fluxes needed to sustain zonal flows are depicted in Figure 2.4, alongside the relevant terms in the momentum equation (2.10). Energy is injected to horizontal scales (modes with horizontal wavenumber not equal to zero), and leaves at an equal rate either via viscous dissipation, or by feeding the zonal flow (modes with horizontal wavenumber equal to zero).

The physics behind the shearing mechanism is well understood [24, 65, 84, 159] and can be best explained by considering the shearing flow in Figure 2.3 (c) which displays an instantaneous realisation of a temperature field with a strong left and right moving zonal flow in the lower and upper half of the domain, respectively. As hot plumes rise due to buoyancy forces, they experience a tilting effect from the sheared mean flow, causing them to ultimately divert completely towards the right as they approach the upper boundary. This diversion contributes to the zonal flow in the upper part of the domain. Similarly, cold plumes, while accelerating downward, undergo a leftward tilting motion, feeding the zonal flow in the lower part of the domain.

The shearing mechanism is a fundamental hydrodynamical principle that can sustain zonal flow whenever roughly two-dimensional flows are being driven on horizontal scales, regardless of whether the driving force is buoyancy or not. Finn et

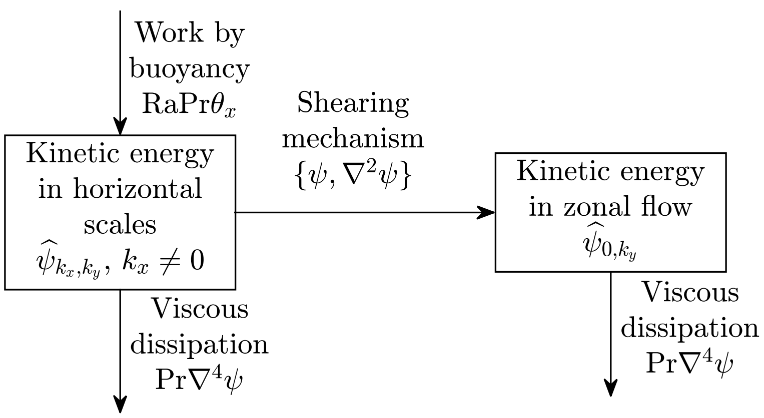

Figure 2.4: Energy fluxes in the shearing mechanism alongside relevant terms in the momentum equation (2.10a). The $\widehat{\psi}_{k_x,k_y}$ modes are from the Fourier-sine expansion of the streamfuncton (2.13).

al. [52] demonstrated this concept by explicitly forcing a horizontal mode, which in turn contributed to the development of a zonal flow through the shearing mechanism. However, such explicit forcing overlooks key aspects of the buoyancy-driven scenario, in particular, that the zonal flow itself partially suppresses the convective heat transfer that fuels it. This effect has been highlighted by Goluskin et al. [63], and we will explore another example of this phenomenon in §4.4.

2.4.2 Zonal Flow in 2D RB Convection

Goluskin et al. [63] studied rectangular 2D RB convection with free-slip boundaries and horizontal periodicity using DNS and found a bistable regime with shearing and non-shearing states. At large enough Rayleigh numbers, only shearing states are stable, but they noted that determining the critical Rayleigh number at which the non-shearing branch loses stability is challenging due to long transients. Nonetheless, it is clear that the transition to a regime where only shearing states are stable requires a higher Rayleigh number as the Prandtl number increases. They also noticed that the Nusselt number is significantly smaller in the shearing state. This reduction is attributed to the zonal flow's ability to prevent thermal plumes from crossing the layer.

Wang et al. [175] studied the effect of varying the width-to-height aspect ratio in the range $1 \leq \Gamma \leq 128$. They found that shearing states only exist when Γ is smaller than some critical value which depends on Ra and Pr. With large aspect ratios, the flow breaks into convection rolls whose number N and mean aspect ratio $\Gamma_r = \Gamma/N$ can vary depending on the initial conditions. When $\Gamma_r \geq 8$, the convection rolls exhibit a behaviour akin to localised zonal flow, and show similar properties to a global zonal flow. Most notably, the convective heat transport decreases considerably with increasing Γ_r. For example, with $\Gamma = 16$, the heat transport for the $\Gamma_r = 16/10$ state is almost twice as high as that for $\Gamma_r = 8$. In line with this result, it has also been observed that a smaller number N of convection cells is associated with reduced convective heat transfer in 2D RB convection with no-slip plates [130, 176], in RB convection in an annulus [187], and also in Taylor-Couette flow [85].

Van der Poel et al. [131] explored the effects of varying the boundary conditions. With no-slip boundary conditions at the horizontal plates, shearing states are only seen for Γ smaller than some $\Gamma_{\min}$, which depends on Ra and Pr. Typically, $\Gamma_{\min}$ is much smaller than in the free-slip case, and the resulting zonal flow may be considered a numerical artefact. For mixed no-slip and free-slip boundary conditions, zonal flow was seen at larger Γ than in the pure no-slip case, but for significantly larger Ra than in the pure free-slip case.

2.4.3 Relaxation Oscillations and Bursts

The nature of the zonal flow depends on the Prandtl number. This dependence was highlighted by Goluskin et al. [63], who reported on two distinct regimes of shearing states with $\Gamma = 2$. For Prandtl number $\mathrm{Pr} > 2$, the zonal flow is sustained in the sense that it varies chaotically but is at no instance weak, nor strong enough to completely suppress convective heat transfer. For Prandtl number $\mathrm{Pr} < 1.5$, the zonal flow is bursting: integral quantities such as E_x^u, the horizontal component of the kinetic energy, which measures the strength of the zonal flow, undergo large non-linear relaxation oscillations on a long timescale. Meanwhile, the Nusselt number undergoes bursts synchronised with the relaxation oscillations. In Figure 2.5 we have reproduced some of the results of Goluskin et al. [63] using the DNS described in §C.1. We show time series of E_x^u, Nu and instantaneous realisations of the temperature field for RB convection with $(\mathrm{Ra}, \mathrm{Pr}, \Gamma) = (2 \times 10^7, 1, 2)$ to illustrate the qualitative differences in the flow during its quiescent phase and during a burst.

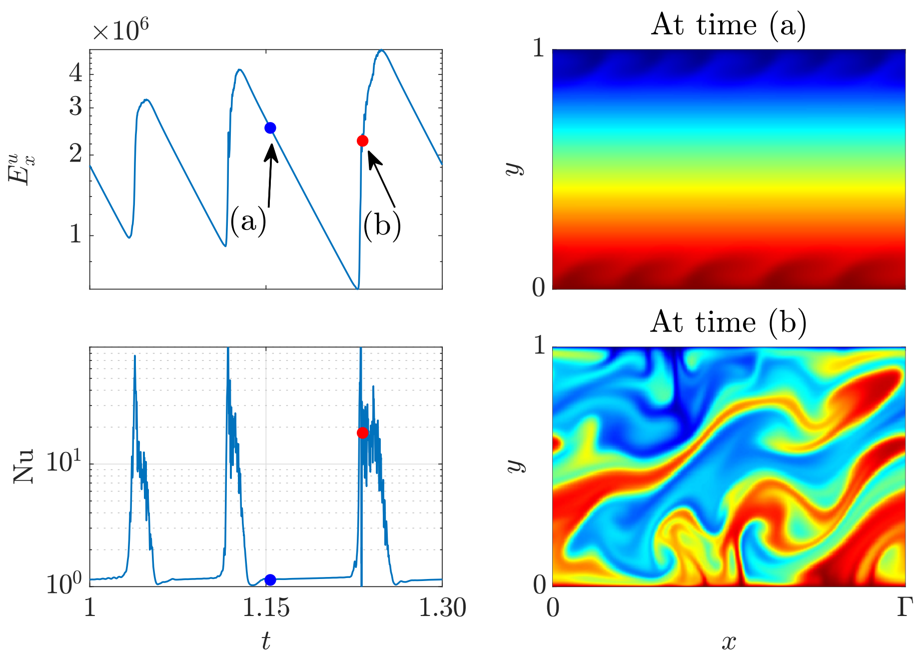

Figure 2.5: The left column shows time series of the horizontal kinetic energy and Nusselt number for $\mathrm{Ra} = 2 \times 10^7$, $\mathrm{Pr} = 1$ and $\Gamma = 2$. The right column has instantaneous realisations of the temperature fields at times (a) and (b) shown in the time series. Measurements are non-dimensionalised according to (2.3).

Leboeuf et al. [102] have discussed the underlying physics behind these oscillations. In short, when the zonal flow is very strong, it prevents thermal plumes from traversing the layer, meaning that buoyancy does very little work on the fluid and its kinetic energy decays exponentially. Bursts begin once the zonal flow is no longer strong enough to suppress the usual mechanism of convective instability. At this point, Nu grows quickly and the flow is once again energised by the buoyancy force. However, this energy is quickly transferred into zonal flow via the shearing mechanism. The zonal flow cuts out its source of momentum and the cycle continues.

The resemblance of these oscillations to the behaviour of simple predator-prey population models and the Lotka–Volterra equations is often noted [42, 59, 102, 110]. In this analogy, the place of the predator population is taken by a quantity undergoing relaxation oscillations, and the place of the prey population is taken by a bursting quantity. However, these low-order models have all made closure assumptions. The first ODE system derived from the Boussinesq equations that displays these strongly non-linear relaxation oscillations will be presented in §3.5.3.

Bursting zonal flow has been found in many other setups, most notably in rotating thermal convection [20], in annuli [156], in 2D spherical shells modelling stars [18], in gas giants [78] and in turbulent plasmas [60].

2.5 Zonal Flow in 3D Domains and Analogy to 2D RB Convection

Strong zonal flows are rare in horizontally isotropic 3D domains. If such flow does develop, it will partially suppress the motions that sustain it but not the transverse motions that can destroy it [136]. However, zonal flows are commonly seen in planetary atmospheres [90, 96], tokamaks [44, 157], and annular cylindrical convection experiments [98]. In this section, we briefly discuss some of the literature where zonal flows have been found in 3D domains and draw analogies to 2D RB Convection.

2.5.1 Planetary Atmospheres

In planetary atmospheres, the Taylor-Proudman effect suppresses variations parallel to the axis of rotation, imposing horizontal anisotropy and rendering the flow approximately two-dimensional [172]. Considering the flow at a region where gravity is parallel to the planet's axes of rotation and under the assumptions that the flow is longitudinally periodic and driven by a constant temperature gradient, gives a set-up which is analogous to 2D RB convection with horizontal periodicity and at least one free-slip horizontal boundary.

Indeed, zonal flow has been observed in 3D RB convection when the convection cell rotates about a distant horizontal axis [77, 121, 175]. However, as in the 2D case, it disappears for sufficiently large Γ, and zonal flows have not been observed for $\Gamma \geq 16$ [175].[5] Likewise, in truncated modal expansions of 3D RB convection, large-scale zonal flow only persists when the imposed convective pattern is sufficiently anisotropic [77, 114].

Novi et al. [121] studied 3D RB convection whilst varying the angle of the rotation axis with respect to the horizontal plane. Their results suggest a possible bistability of zonal jets and tilted-vortex solutions.

2.5.2 Tokamaks

The analogy with zonal flow in planetary atmospheres and in tokamaks has been discussed in the plasma physics literature [44, 173]. In a tokamak, the plasma equilibrates very quickly along magnetic field lines, which wind primarily in the toroidal direction, leaving the flow approximately two-dimensional in the radial-poloidal plane. The analogy to 2D RB convection has been discussed by Garcia et al. [60] and Goluskin [65].

2.5.3 Annular Cylinders

In the experimental work by Krishnamurti et al. [98], they studied the flow in an annular cylinder heated from bellow and reported zonal flow moving in one direction at the top of the layer and in the opposite direction at the bottom of the layers, analogous to the flow depicted in Figure 2.3. To obtain our system from theirs, we must approximate the boundaries as free-slip, assume the flow is radially uniform and azimuthally periodic, and ignore the curvature over a single azimuthal period [65].

As shown by Van der Poel et al. [131], one can obtain zonal flow with no-slip boundaries, but the horizontal period and Rayleigh number typically need to be much smaller and larger, respectively, compared to free-slip boundaries. The assumptions of radial uniformity and ignoring the curvature over a single azimuthal period are most accurate for annular cylinders with a large inner radius, r, and aspect ratio r/R close to 1, where R is the outer radius. The large inner radius minimises the curvature of each horizontal period, while the large aspect ratio suppresses radial variations.

[5] In the 3D study by Wang et. al. [175], they only have one width-to-height aspect ratio, Γ, as the domain is equally wide in the two horizontal directions.

Chapter 3

Onset of Zonal Modes

3.1 Synopsis

As the Rayleigh number is increased from 0 in 2D RB convection with free-slip boundaries and horizontal periodicity, Lord Rayleigh [134] showed that the conducive state loses stability to the SCRS. Notably, the SCRS contains no zonal modes (modes with horizontal wavenumber equal to zero), and zonal modes can only emerge once the SCRS itself has become unstable. Zonal modes can generate a net zonal flow across the convection layer and have inspired significant research in recent years. In particular, zonal flow has been found to significantly suppresses convective heat transfer [63] and can reverse in time, as we shall see in chapter 4.

In this chapter, we study the onset of zonal modes by analysing the stability of the SCRS over twelve orders of magnitude in the Prandtl number ($10^{-6} \leq \mathrm{Pr} \leq 10^{6}$) and six orders of magnitude in the Rayleigh number ($8\pi^4 < \mathrm{Ra} \leq 10^8$). Our study primarily focuses on the width-to-height aspect ratio $\Gamma = 2$, for which the SCRS emerges from the conducive state at a critical Rayleigh number of $8\pi^4$. We also consider the effects of varying Γ, particularly in the limiting cases where the Prandtl number is either very small or very large.

A literature review of previous relevant studies in §3.2, lays the foundation for the work presented in this chapter. In §3.3, we describe the problem that is under consideration and formulate it in terms of a partition into so-called even and odd modes. In §3.4, we conduct a linear stability analysis to determine the stability boundary of the SCRS in the $(\mathrm{Pr}, \mathrm{Ra})$-plane. We observe remarkably intricate features corresponding to qualitative changes in the solution, as well as three regions where the steady convection rolls lose and subsequently regain stability as the Rayleigh number is increased. Such behaviour defies our intuition that increasing the importance of buoyancy relative to viscous and thermal dissipation should always make the system less stable.

In §3.5, we study the asymptotic limit $\mathrm{Pr} \to 0$ and find that the steady convection rolls become unstable very close to the onset of convection, eventually leading to non-linear relaxation oscillations and bursts, which we explain with a weakly non-linear analysis. The bifurcation structure changes abruptly as we approach a critical aspect ratio $\Gamma \approx 2.37$, where the SCRS is stable for a couple of Rayleigh number decades, even for very small Prandtl numbers. We conduct the same weakly non-linear analysis when formally setting $\mathrm{Pr} = 0$ and observe relaxation oscillations and bursts with period and amplitude that grow without bound. In the complementary large-Pr limit, studied in §3.6, we observe that the zonal modes at the instability switch off abruptly at a large, but finite, Prandtl number. Finally, we study how the critical Rayleigh number at which this switch occurs depends on the aspect ratio, Γ.

3.2 Literature Review

3.2.1 SCRS Bifurcation Pattern

The onset of RB convection typically shows a steady cellular pattern (for example, rolls, squares or hexagons), and the stability of these cellular patterns has been studied for decades [13, 21, 22, 24, 112, 127, 136]. In a 2D periodic box, the cellular pattern (referred to as the SCRS in this chapter) takes the form of convection rolls which are invariant under reflections both in the vertical plane that separates them and in the horizontal mid-plane. Rucklidge et al. [136] showed that the vertical mirror symmetry can be broken with a pitchfork bifurcation, generating a new steady state with a net zonal flow in which any unidirectional motion at the top will be balanced by an equal and opposite motion at the bottom. The physical mechanism behind this instability is well understood and is explained via the shearing mechanism, see §2.4.1.

The vertical mirror symmetry may also be broken with a Hopf bifurcation [101, 133], which leads to oscillations in which the direction of the zonal flow alternates. These oscillations have a spatio-temporal symmetry: they are invariant under the advance of half a period in time followed by a reflection in a vertical plane, so the zonal flow is instantaneous with vanishing time average [136]. Paul et al. [127] noted that the spatio-temporal symmetry is itself broken as the Rayleigh number increases in the transition to chaotic solutions. Within the chaotic regime, stable steady states emerge as a result of an inverse subcritical Hopf bifurcation and coexistence with the chaotic attractor [127]. Upon increasing the Rayleigh number further, only stable steady states survive as the chaotic attractor disappears through a "boundary crisis". This self-organisation of the flow with increasing Rayleigh number defies our intuition that increasing the importance of buoyancy relative to viscous and thermal dissipation should make the system less stable. Self-organisation has also been observed experimentally by Fauve et al. [51] in convective flow of mercury at small Prandtl number.

3.2.2 Zero Prandtl Number Convection

The Prandtl number of a fluid can approach zero in two ways — either because the viscosity is very small or because the thermal conductivity is very large. Both cases are of interest in astrophysics and geophysics. In the zero Prandtl number limit in RB convection, the time derivative and advective term in the heat transport equation can be ignored. Since the non-linear term in the momentum equation vanishes identically for the convection roll pattern typically seen in finite Prandtl number convection, the rolls can grow without bound instead of saturating. This behaviour was first investigated by Herring [81], who in 1970 demonstrated blow-up behaviour for a large class of initial conditions in 2D. Bounded solutions close to the onset of convection are yet to be observed.

In 3D, however, finite amplitude periodic solutions between orthogonal set of rolls [161], time-independent perpendicular rolls [92], time dependant wavy rolls [99], and even chaotic solutions [124, 128] have been observed close to the onset. The three-dimensionality of the flow is apparently necessary, and in the example of wavy rolls, Kumar et al. [99] demonstrated the energy transfer from 2D rolls to a perpendicular vertical vorticity mode. This has a stabilising effect since, without the vertical vorticity, the amplitude of the rolls would grow to infinity as in the 2D case.

Experimentally, one can study zero Prandtl number convection with helium-4, which becomes a superfluid at 2.14 Kelvin with zero kinematic viscosity and infinite thermal conductivity [115].

3.3 Problem Formulation

The equations under consideration are the 2D Boussinesq equations of thermal convection (2.10). The system is non-dimensionalised using L_y, the height of the domain, ΔT, the temperature difference between the top and bottom plates, and L_y^2/κ as the time scale. where κ is the thermal diffusivity of the fluid. The domain is spanned by

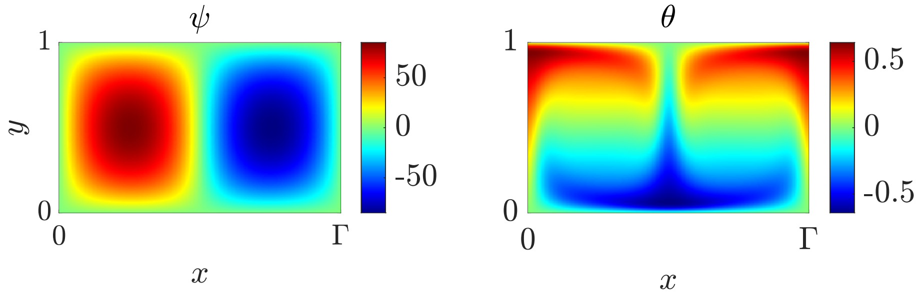

Figure 3.1: The SCRS calculated with the parameters $(\mathrm{Pr}, \mathrm{Ra}) = (1, 10^5)$ using the numerical scheme outlined in Appendix A.1.

$x \in [0, \Gamma]$ and $y \in [0, 1]$ and the boundary conditions are periodic in x and free-slip in y. We decompose both ψ and θ in the Fourier-sine basis:

$$\begin{aligned} \psi(x, y, t) &= \sum_{k_x \in \mathbb{Z}} \sum_{k_y \in \mathbb{Z}_{>0}} \widehat{\psi}_{k_x,k_y}(t) \mathrm{e}^{i2\pi k_x x/\Gamma} \sin(\pi k_y y) \\ &= \sum_{k_x,k_y} \widehat{\psi}_{k_x,k_y}(t) \phi_{k_x,k_y}(x, y). \end{aligned} \tag{3.1}$$

Rayleigh [134] showed that the static conduction state ($\psi = \theta = 0$) bifurcates supercritically to a steady pattern of counter-rotating convection rolls vertically spanning the layer ($k_y = 1$) when $\mathrm{Ra} > \mathrm{Ra}_c$ with

$$\mathrm{Ra}_c = \min_{k_x} \left(\frac{\pi^4}{4\Gamma^4} \frac{(4k_x^2 + \Gamma^2)^3}{k_x^2} \right). \tag{3.2}$$

The minimum is taken over integer wavenumbers k_x, and occurs at $k_x = 1$ provided that $\Gamma < 2^{4/3}\sqrt{1 + 2^{2/3}} \approx 4.05$. Consequently, for our set-up with $\Gamma = 2$, the modes $\widehat{\psi}_{1,1}$ and $\widehat{\theta}_{1,1}$ from Eq. (3.1) become excited through a supercritical pitchfork bifurcation at $\mathrm{Ra}_c = 8\pi^4$. The resulting steady state consists of two counter-rotating convection rolls, which will be referred to as the SCRS in the remainder of the chapter. An instance of the SCRS with the parameters $(\mathrm{Pr}, \mathrm{Ra}, \Gamma) = (1, 10^5, 2)$ is shown in Figure 3.1.

As in previous studies [34, 168], we further partition the modes into *odd modes* indicated by the letter O, with $k_x + k_y \in 2\mathbb{Z} + 1$, and *even modes* indicated by the letter E, with $k_x + k_y \in 2\mathbb{Z}$. Consistently with this notion of odd and even modes, we decompose ψ as

$$\psi^O(x, y, t) = \frac{1}{2}[\psi(x, y, t) + \psi(x + \Gamma/2, 1 - y, t)], \tag{3.3a}$$

$$\psi^E(x, y, t) = \frac{1}{2}[\psi(x, y, t) - \psi(x + \Gamma/2, 1 - y, t)], \tag{3.3b}$$

and similarly for θ^O and θ^E. Thus, ψ^O and θ^O consist only of odd modes as defined above, while ψ^E and θ^E consist only of even modes. Applying the decomposition (3.3) to equations (2.10), we find that

$$\nabla^2\psi_t^O + \{\psi^E, \nabla^2\psi^O\} + \{\psi^O, \nabla^2\psi^E\} = \mathrm{Ra}\mathrm{Pr}\theta_x^O + \mathrm{Pr}\nabla^4\psi^O, \tag{3.4a}$$

$$\theta_t^O + \{\psi^E, \theta^O\} + \{\psi^O, \theta^E\} = \psi_x^O + \nabla^2\theta^O, \tag{3.4b}$$

and

$$\nabla^2\psi_t^E + \{\psi^E, \nabla^2\psi^E\} - \mathrm{Ra}\mathrm{Pr}\theta_x^E - \mathrm{Pr}\nabla^4\psi^E = -\{\psi^O, \nabla^2\psi^O\}, \tag{3.5a}$$

$$\theta_t^E + \{\psi^E, \theta^E\} - \psi_x^E - \nabla^2\theta^E = -\{\psi^O, \theta^O\}. \tag{3.5b}$$

We observe that (ψ^O, θ^O) satisfy the linear PDEs (3.4), with coefficients that depend on (ψ^E, θ^E), while (ψ^E, θ^E) satisfy the autonomous non-linear PDEs (3.5), with forcing terms that depend on (ψ^O, θ^O).

At the onset of steady convection, the excited modes $\widehat{\psi}_{1,1}$ and $\widehat{\theta}_{1,1}$ are even modes, and indeed the SCRS has the property that $\psi^O \equiv \theta^O \equiv 0$, which remains true as we increase Ra. In this case, the system of equations (3.4)–(3.5) reduces to

$$\nabla^2\psi_t^E + \{\psi^E, \nabla^2\psi^E\} = \mathrm{Ra}\mathrm{Pr}\theta_x^E + \mathrm{Pr}\nabla^4\psi^E, \tag{3.6a}$$

$$\theta_t^E + \{\psi^E, \theta^E\} = \psi_x^E + \nabla^2\theta^E, \tag{3.6b}$$

where the even modes are decoupled from the odd modes. The SCRS has a reflection symmetry about a vertical line, which separates the counter-rotating convection rolls. Without loss of generality, we choose this vertical line to be at $x = 0$. Thus, the steady state solution (ψ^E, θ^E) of the system (3.6) is invariant under the symmetry

$$\psi^E(x, y) \mapsto -\psi^E(-x, y), \qquad \theta^E(x, y) \mapsto \theta^E(-x, y). \tag{3.7}$$

Since the zonal modes $\widehat{\psi}_{0,k_y}$ are x-independent, equation (3.7) implies that $\widehat{\psi}_{0,k_y}^E \equiv 0$. In other words, the SCRS has no zonal flow, and zonal modes can emerge only once the SCRS has become unstable.

3.4 Linear Stability Analysis

In this section, we present the linear stability analysis of the SCRS. For given values of Pr and Ra, we first numerically solve the steady state problem of Eq. (3.6), following the procedure described in Appendix A.1. We then exploit the partial decoupling of

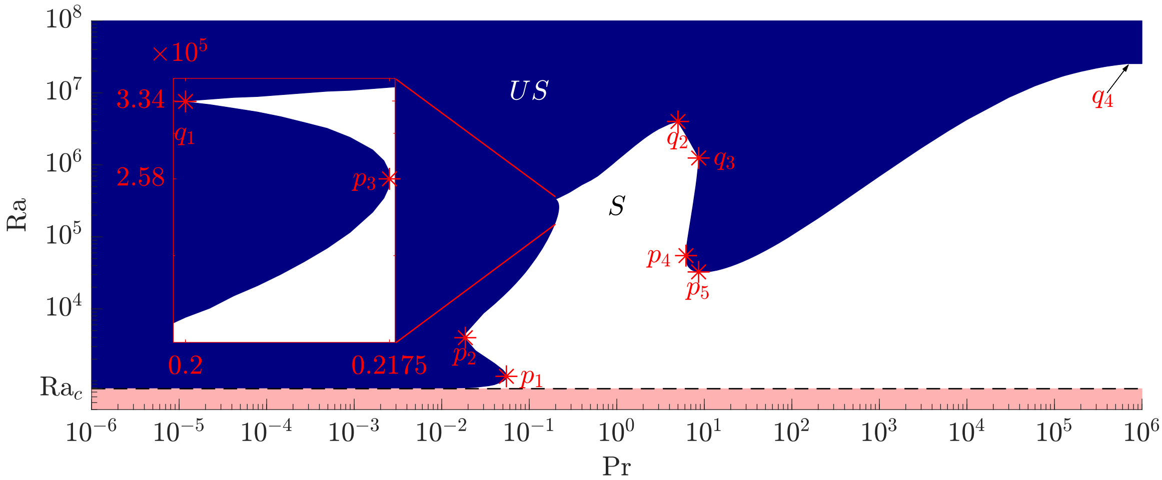

Figure 3.2: The $(\mathrm{Pr}, \mathrm{Ra})$-plane with $\Gamma = 2$, highlighting when the SCRS is linearly stable (white, S) and unstable (blue, US). Only the static conduction state is stable in the pink-shaded region below $\mathrm{Ra} = \mathrm{Ra}_c$ (dashed line). When $\mathrm{Pr} \ll 1$, the SCRS becomes unstable at $0 < \mathrm{Ra} - \mathrm{Ra}_c \ll 1$. The points p_i indicate turning points in the stability boundary, and at q_i the stability boundary is not smooth, and there is a qualitative change in the eigenfunction to which the SCRS becomes unstable. Their $(\mathrm{Pr}, \mathrm{Ra})$ values are indicated in Table 3.1.

odd and even modes to consider odd and even perturbations separately. We analyse odd perturbations by setting

$$\begin{aligned}\psi(x, y, t) &= \psi^E(x, y) + \delta \mathrm{e}^{\sigma^o t} \psi^o(x, y) \\ &= \psi^E(x, y) + \delta \mathrm{e}^{\sigma^o t} \sum_{k_x + k_y \in 2\mathbb{Z}+1} \widehat{\psi}^o_{k_x, k_y} \phi_{k_x, k_y}(x, y), \end{aligned} \tag{3.8}$$

$$\begin{aligned}\theta(x, y, t) &= \theta^E(x, y) + \delta \mathrm{e}^{\sigma^o t} \theta^o(x, y) \\ &= \theta^E(x, y) + \delta \mathrm{e}^{\sigma^o t} \sum_{k_x + k_y \in 2\mathbb{Z}+1} \widehat{\theta}^o_{k_x, k_y} \phi_{k_x, k_y}(x, y), \end{aligned} \tag{3.9}$$

where (ψ^E, θ^E) is the SCRS, $\delta \ll 1$ and ψ^o, θ^o consist only of odd modes. By substituting (3.8) into equations (2.10) and linearising with respect to δ, we obtain an eigenvalue problem for the odd growth rates σ^o (see Appendix A for details). We solve this eigenvalue problem numerically and determine that the SCRS is unstable with respect to odd perturbations if $\max[\mathcal{R}(\sigma^o)] > 0$. An analogous approach is used to determine the corresponding even growth rates σ^e and thus the stability of the SCRS with respect to even perturbations.

Figure 3.2 displays the stability of the SCRS in the $(\mathrm{Pr}, \mathrm{Ra})$-plane when $\Gamma = 2$, highlighting the stable (S) regime in white and the unstable (US) regime in blue. The pink region denotes $\mathrm{Ra} < \mathrm{Ra}_c$ where only the static conduction state is stable.

Point	$(\mathrm{Pr}, \mathrm{Ra})$
p_1	$(5.48 \times 10^{-2}, 1.16 \times 10^3)$
p_2	$(1.81 \times 10^{-2}, 4.12 \times 10^3)$
p_3	$(0.2175, 2.59 \times 10^5)$
p_4	$(6.16, 5.43 \times 10^4)$
p_5	$(9.53, 3.24 \times 10^4)$
q_1	$(0.2, 3.32 \times 10^5)$
q_2	$(4.97, 3.949 \times 10^6)$
q_3	$(8.58, 1.27 \times 10^6)$
q_4	$(7 \times 10^5, 2.54 \times 10^7)$

Table 3.1: The points p_i and q_i and their $(\mathrm{Pr}, \mathrm{Ra})$ value as they appear in Figure 3.2.

Although the SCRS does become unstable to even perturbations within the region US, we always observe that $\max[\mathcal{R}(\sigma^o)] > \max[\mathcal{R}(\sigma^e)]$ and the dominant unstable perturbation, therefore, consists of odd modes. Moreover, for $\mathrm{Pr} \lesssim 7 \times 10^5$ the most unstable eigenfunction at onset has the property that $\widehat{\psi}^o_{k_x,k_y}$ and $i\widehat{\theta}^o_{k_x,k_y}$ are purely real, so that ψ^o and θ^o break the reflection symmetry (3.7). Zonal modes $\widehat{\psi}_{0,k_y}$ with $k_y \in 2\mathbb{Z}+1$ are present in the most unstable perturbation until we reach very large Prandtl numbers (see §3.6). In particular, looking at Figure 3.3 which shows the amplitude of the three largest scale modes in the most unstable eigenfunction, we observe $\widehat{\psi}_{0,1}$ is present for $\mathrm{Pr} < \mathrm{Pr}(q_4) = 7 \times 10^5$, and is the dominant one for $\mathrm{Pr} < \mathrm{Pr}(q_2) = 4.97$ and $\mathrm{Pr}(q_3) = 8.58 < \mathrm{Pr} \lesssim 40$. As we increase the Prandtl number beyond p_4, the amplitude of $\widehat{\psi}_{0,1}$ decreases monotonically and $\widehat{\psi}_{2,1}$ becomes the dominant mode for $\mathrm{Pr} \gtrsim 40$ (see Figure 3.3 (b)). In the region $\mathrm{Pr}(q_2) = 4.97 < \mathrm{Pr} < \mathrm{Pr}(q_3) = 8.58$, $\widehat{\psi}_{1,2}$ and $\widehat{\psi}_{0,1}$ have comparable amplitudes (see Figure 3.3 (a)).

The points p_i annotated in Figure 3.2 highlight turning points in the stability boundary. The behaviour of σ^o near each such point is plotted in Figure 3.4. Fig-

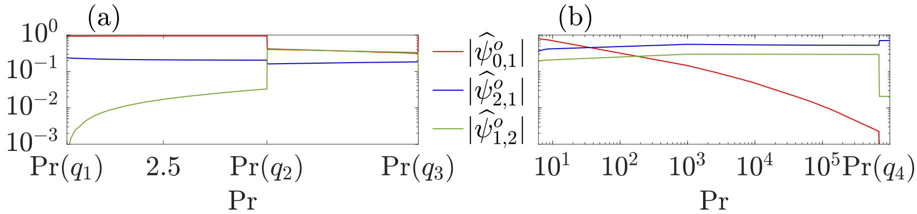

Figure 3.3: The three largest scale modes in the most unstable eigenfunction as we traverse the stability boundary (a) from $\mathrm{Pr}(q_1) = 0.2$, to $\mathrm{Pr}(q_2) = 4.97$, to $\mathrm{Pr}(q_3) = 8.58$ and (b) from $\mathrm{Pr}(p_4) = 6.16$ to $\mathrm{Pr} = 10^6$. The eigenfunction is normalised such that its l^2-norm of the modes is unity.

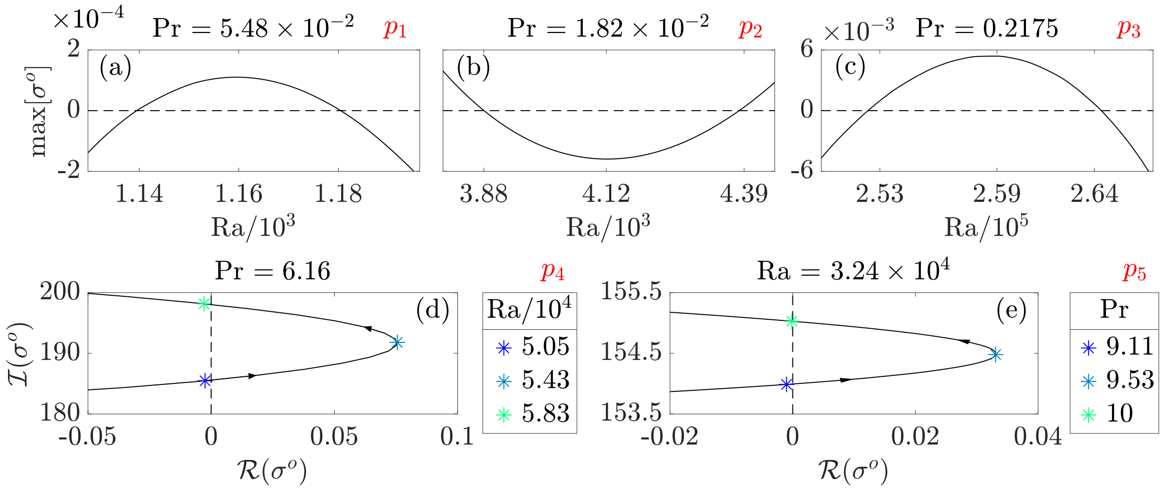

Figure 3.4: The largest odd growth rate σ^o, plotted with one dimensionless parameter varied and the other fixed. The plots show the behaviour close to each point p_i highlighted in figure 3.2. In (a)–(c), σ^o is real, while in (d) and (e), the motion of σ^o in the complex plane is tracked, with the arrows indicating the direction of increasing Ra or Pr.

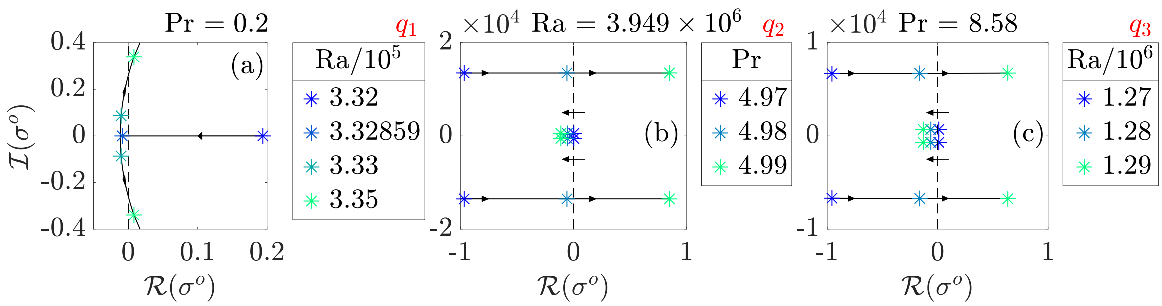

Figure 3.5: The largest odd growth rate(s) σ^o, plotted with one dimensionless parameter varied and the other fixed. The plots show the behaviour close to each of the points q_i highlighted in figure 3.2. The motion of σ^o in the complex plane is tracked, with the arrows indicating the direction of increasing Ra or Pr.

ure 3.4 (a) shows that, close to $\mathrm{Pr} = \mathrm{Pr}(p_1) = 5.48 \times 10^{-2}$ and with increasing Rayleigh number, a real eigenvalue crosses the origin twice, and the SCRS first loses and then regains stability. The same behaviour is found at $\mathrm{Pr} = \mathrm{Pr}(p_3) = 0.2175$ (Figure 3.4 (c)). Similar behaviour has been observed by [127], with Pr = 6.8 and $\Gamma = 2\sqrt{2}$. At point p_2, the opposite occurs with the SRCS first regaining and then losing stability as Ra increases (Figure 3.4 (b)). At points p_4 and p_5, we instead find complex eigenvalues crossing the imaginary axis twice as Ra increases with fixed Pr or *vice versa*; see Figures 3.4 (d) and (e).

At each point labelled q_i, the stability boundary is not smooth, and there is a qualitative change in the eigenfunction to which the SCRS becomes unstable. Fig-

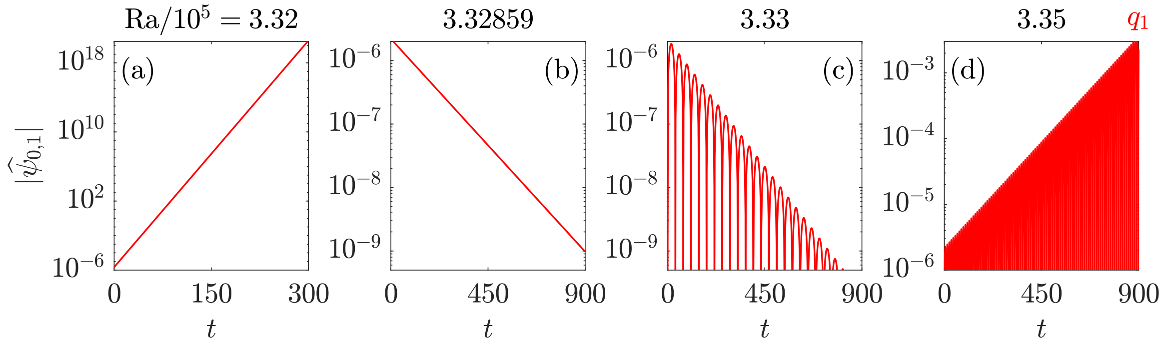

Figure 3.6: Time series of the $\widehat{\psi}_{0,1}$ mode from the linearised DNS with the right-hand side of (3.5) set to zero. Here we fix $\mathrm{Pr} = 0.2$ (q_1) and have $\mathrm{Ra} = 3.32 \times 10^5$ (a), $\mathrm{Ra} = 3.32859 \times 10^5$ (b), $\mathrm{Ra} = 3.33 \times 10^5$ (c) and $\mathrm{Ra} = 3.35 \times 10^5$ (d). The initial conditions are the SCRS with a small perturbation.

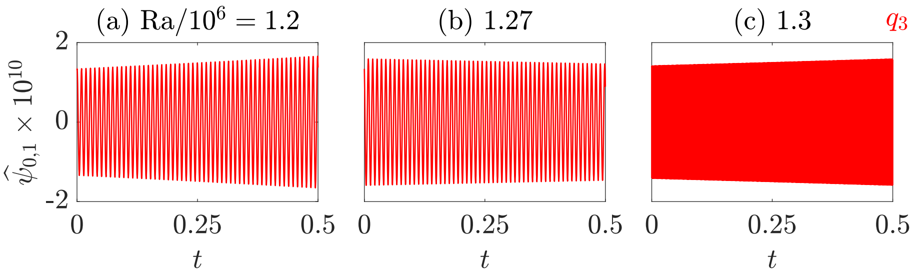

Figure 3.7: Time series of the $\widehat{\psi}_{0,1}$ mode close to q_3 from the linearised DNS with the right-hand side of (3.5) set to zero. We fix $\mathrm{Pr} = 8.57$, and the initial conditions are the SCRS with a small perturbation. Longer time series clearly showing the exponential growth and decay are in Figure A.4 of Appendix A

ure 3.5 (a) shows how, with $\mathrm{Pr} = \mathrm{Pr}(q_1) = 0.2$, the SCRS regains stability with a real eigenvalue crossing zero at $\mathrm{Ra} \approx 3.32859 \times 10^5$. With further increase in Ra, the eigenvalue splits into a complex conjugate pair, which re-cross the imaginary axis as the SCRS loses stability in a Hopf bifurcation. The cusp at q_1 occurs when these three events (i.e. the two crossings of the imaginary axis and complex conjugate pair split) happen simultaneously. These observations have been confirmed with direct numerical simulation (DNS) of the system (3.4)–(3.5), using the pseudospectral scheme described in §C.1. Figure 3.6 shows numerical results for the largest scale odd mode $\widehat{\psi}_{0,1}$ obtained with the right-hand side of (3.5) set to 0, so that we have persistent exponential growth or decay in the odd modes. With increasing Ra, we observe that the odd perturbations regain stability, become oscillatory, and finally become unstable again.

Figure 3.5 (c) shows that, with $\mathrm{Pr} = 8.58$, the SCRS regains stability through a Hopf bifurcation at $\mathrm{Ra} = 1.28 \times 10^6$ but loses stability shortly after at $\mathrm{Ra} = 1.29 \times 10^6$

with much larger oscillation frequency. The corner q_3 occurs when these two pairs of eigenvalues cross the imaginary axis simultaneously. Again, this observation has been verified with DNS close to q_3. In Figure 3.7 we fix $\mathrm{Pr} = 8.57$ and see that the odd mode $\widehat{\psi}_{0,1}$ grows at $\mathrm{Ra} = 1.2 \times 10^6$, decays at $\mathrm{Ra} = 1.27 \times 10^6$, and grows again at $\mathrm{Ra} = 1.3 \times 10^6$, but now with a much greater oscillation frequency. As shown in Figure 3.5 (b), similar behaviour occurs at corner q_2. The final corner point q_4, which lies in the large-Pr region, will be considered in more detail in §3.6. Movies showing how the dominant eigenfunction changes at each point q_i are included in the Supplementary Material of [185]. The following section studies in more detail the stability at small Prandtl number.

3.5 Stability at Small Prandtl Number

3.5.1 Observations from DNS

Figure 3.2 hints that the Rayleigh number at which the SCRS loses stability approaches Ra_c as $\mathrm{Pr} \to 0$. In Figure 3.8 we plot

$$\delta\mathrm{Ra} := \mathrm{Ra} - \mathrm{Ra}_c \tag{3.10}$$

versus Pr and indeed see that the stability boundary follows a clear power-law with $\delta\mathrm{Ra} \propto \mathrm{Pr}^2$. Moreover, this power-law persists up to $\mathcal{O}(1)$ values of $\delta\mathrm{Ra}$. When the stability boundary is crossed, at small Pr, the linear stability analysis suggests that the SCRS becomes unstable through a pitchfork bifurcation as a new steady state containing both even and odd modes emerges.

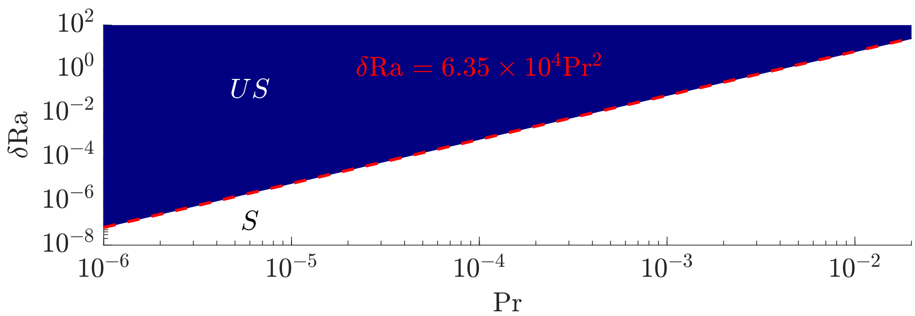

Figure 3.8: The $(\mathrm{Pr}, \delta\mathrm{Ra})$-plane for small Pr highlighting when the SCRS is linearly stable (white, S) and unstable (blue, US). On the vertical axis we plot $\delta\mathrm{Ra} = \mathrm{Ra} - \mathrm{Ra}_c$, where $\mathrm{Ra}_c = 8\pi^4$. The red dashed line indicates the power-law $\delta\mathrm{Ra} \propto \mathrm{Pr}^2$, where the prefactor has been calculated by fitting.

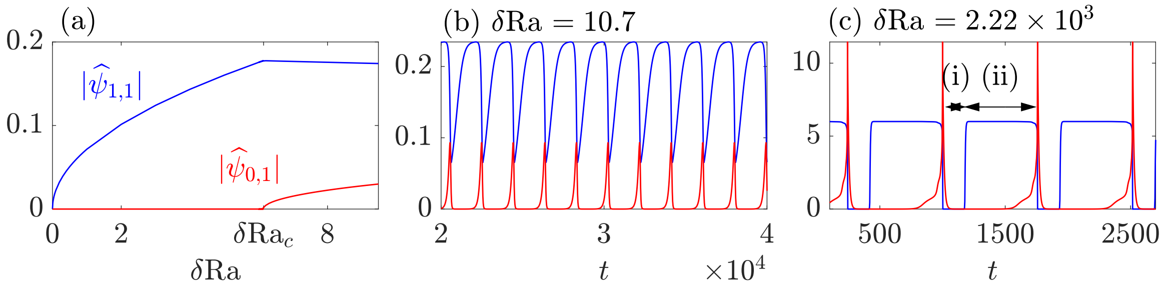

Figure 3.9: Solutions obtained from DNS with $\mathrm{Pr} = 10^{-2}$. (a) Bifurcation diagram plotting $|\widehat{\psi}_{1,1}|$ (blue) and $|\widehat{\psi}_{0,1}|$ (red) against $\delta\mathrm{Ra}$. Time series of $|\widehat{\psi}_{1,1}|$ and $|\widehat{\psi}_{0,1}|$ when (b) $\delta\mathrm{Ra} = 10.7$ and (c) $\delta\mathrm{Ra} = 2.2 \times 10^3$

This prediction has been verified with fully non-linear DNS. In Figure 3.9 (a), we plot a bifurcation diagram showing the amplitudes of the even mode $\widehat{\psi}_{1,1}$ and the odd mode $\widehat{\psi}_{0,1}$ versus $\delta\mathrm{Ra}$ with $\mathrm{Pr} = 0.01$. The SCRS emerges at $\delta\mathrm{Ra} = 0$ and becomes unstable at $\delta\mathrm{Ra} = \delta\mathrm{Ra}_c \approx 6.135$ as the new mixed steady state emerges. As $\delta\mathrm{Ra}$ increases beyond $\delta\mathrm{Ra}_c$, we observe that the amplitude of the even mode stays approximately constant while the amplitude of the odd mode increases. As $\delta\mathrm{Ra}$ increases further, the mixed steady state itself loses stability through a Hopf bifurcation, and the flow becomes oscillatory. In Figure 3.9 (b) we plot the time series of $|\widehat{\psi}_{1,1}|$ and $|\widehat{\psi}_{0,1}|$ at $\mathrm{Pr} = 0.01$ and $\delta\mathrm{Ra} = 10.7$. At this point, the mixed steady state has become unstable, and the mode $|\widehat{\psi}_{1,1}|$ undergoes non-linear relaxation oscillations whilst $|\widehat{\psi}_{0,1}|$ exhibits bursts that quickly decay away. At $\delta\mathrm{Ra} = 2.22 \times 10^3$, the relaxation oscillations and the bursts persist, but are separated by a much slower buildup phase, as shown in Figure 3.9 (c).

As indicated by the annotations in Figure 3.9 (c), the dynamics at low Prandtl number with $\delta\mathrm{Ra} > \delta\mathrm{Ra}_c$ can be partitioned into three phases, as follows.

(i) In the first phase, we are close to the static conduction state with both $|\widehat{\psi}_{1,1}|$ and $|\widehat{\psi}_{0,1}|$ approximately 0. However, because $\delta\mathrm{Ra} > 0$, the static conduction state is unstable, so that $\widehat{\psi}_{1,1}$ and other even modes grow exponentially.

(ii) The even modes grow until we are in the SCRS. Since $\delta\mathrm{Ra} > \delta\mathrm{Ra}_c$, the SCRS is unstable to odd perturbations, so that $\widehat{\psi}_{0,1}$ and other odd modes grow exponentially.

(iii) Once $\widehat{\psi}_{1,1}$ and $\widehat{\psi}_{0,1}$ are of comparable amplitude, the system quickly collapses back to the static conduction state, and the cycle continues.

These dynamics differ markedly from the chaotic behaviour found close to Ra_c in small-Pr and zero-Pr convection in 3D [124, 161]. In §3.5.2, we study a low-order model to derive an analytical expression for the power-law observed in Figure 3.8. In §3.5.3 we carry out a weakly non-linear analysis to capture the dynamics of the non-linear relaxation oscillations and bursts seen in Figure 3.9.

3.5.2 Six-Mode Model

To explain the observed power-law $\delta\mathrm{Ra} \propto \mathrm{Pr}^2$, we consider a low dimensional model which takes the simplest possible mode truncation allowing for closed triad interactions as well as both even and odd modes. We write the even and odd fields as linear combinations containing a total of six modes, as follows:

$$\psi^E = \widehat{\psi}_{1,1}\phi_{1,1} + c.c., \tag{3.11a}$$
$$\psi^O = \widehat{\psi}_{1,2}\phi_{1,1} + \widehat{\psi}_{0,1}\phi_{0,1} + c.c., \tag{3.11b}$$
$$\theta^E = \widehat{\theta}_{1,1}\phi_{1,1} + \widehat{\theta}_{0,2}\phi_{0,2} + c.c., \tag{3.11c}$$
$$\theta^O = \widehat{\theta}_{1,2}\phi_{1,2} + c.c. \tag{3.11d}$$

We now examine the system when both Pr and $\delta\mathrm{Ra}$ are small to see if we can replicate the power-law in Figure 3.8. The following analysis is done for general Γ, provided $\Gamma \lesssim 4.05$, and we fix $\Gamma = 2$ at the end.

In the $\delta\mathrm{Ra} \to 0$ limit, using standard results from the weakly non-linear analysis of the static conduction state [53], the SCRS can be written as,

$$\psi = \widetilde{\psi}_{1,1}\phi_{1,1}\delta\mathrm{Ra}^{1/2} + c.c. + \mathcal{O}(\delta\mathrm{Ra}^{3/2}), \tag{3.12a}$$
$$\theta = \widetilde{\theta}_{1,1}\phi_{1,1}\delta\mathrm{Ra}^{1/2} + \widetilde{\theta}_{0,2}\phi_{0,2}\delta\mathrm{Ra} + c.c. + \mathcal{O}(\delta\mathrm{Ra}^{3/2}), \tag{3.12b}$$

where $\widetilde{\psi}_{1,1}, \widetilde{\theta}_{1,1}, \widetilde{\theta}_{0,2}$ are all $\mathcal{O}(1)$. In particular, $\widetilde{\psi}_{1,1} = -i\sqrt{(4+\Gamma^2)/2\mathrm{Ra}_c}$ if we fix the mode phases as in Figure 3.1. We now examine the stability of the steady state (3.12), so we consider perturbations in the odd modes in (3.11), which yields the following linear system

$$\partial_t\widehat{\psi}_{0,1} = \left(\widehat{\psi}_{-1,2} + \widehat{\psi}_{1,2}\right)\frac{3\pi^2|\widetilde{\psi}_{1,1}|}{\Gamma}\sqrt{\delta\mathrm{Ra}} - \pi^2\mathrm{Pr}\widehat{\psi}_{0,1}, \tag{3.13a}$$
$$\partial_t\widehat{\psi}_{2,1} = \frac{\pi^2|\widetilde{\psi}_{1,1}|}{\Gamma(1+\Gamma^2)}\sqrt{\delta\mathrm{Ra}}\widehat{\psi}_{0,1} - i\frac{\Gamma}{2\pi(1+\Gamma^2)}\mathrm{Pr}\mathrm{Ra}\widehat{\theta}_{2,1} - \frac{4(1+\Gamma^2)\pi^2}{\Gamma^2}\mathrm{Pr}\widehat{\psi}_{2,1}, \tag{3.13b}$$
$$\partial_t\widehat{\psi}_{-2,1} = (\partial_t\widehat{\psi}_{2,1})^* \tag{3.13c}$$
$$\partial_t\widehat{\theta}_{2,1} = i\frac{\pi^2|\widetilde{\theta}_{1,1}|}{\Gamma}\sqrt{\delta\mathrm{Ra}}\widehat{\psi}_{0,1} + i\frac{2\pi}{\Gamma}\widehat{\psi}_{2,1} - \frac{4(1+\Gamma^2)\pi^2}{\Gamma^2}\widehat{\theta}_{2,1}, \tag{3.13d}$$
$$\partial_t\widehat{\theta}_{-2,1} = (\partial_t\widehat{\theta}_{2,1})^*. \tag{3.13e}$$

This system is equivalent to (A.9) in Appendix A, and may be written in the form $\partial_t \boldsymbol{v} = M\boldsymbol{v}$, where $\boldsymbol{v}$ is a vector of odd modes and

$$\det(M) \sim \mathrm{Pr}\delta\mathrm{Ra}\frac{24\pi^6|\widehat{\psi}_{1,1}|^2}{\Gamma^4}\left(\frac{16\pi^4(1+\Gamma^2)^3 - \mathrm{Ra}\Gamma^4}{\Gamma^4(1+\Gamma^2)}\right) + \dots$$
$$\dots \mathrm{Pr}^3\left(\frac{32(1+\Gamma^2)\pi^6}{\Gamma^4}\mathrm{Ra} - \frac{256(1+\Gamma^2)\pi^{10}}{\Gamma^8} - \frac{\pi^2}{(1+\Gamma^2)^2}\mathrm{Ra}^2\right) + \mathcal{O}(\mathrm{Pr}^5), \tag{3.14}$$

as $\mathrm{Pr}, \delta\mathrm{Ra} \to 0$.

We are interested in the point where M becomes singular, corresponding to an eigenvalue of M passing through zero and heralding the onset of the odd modes. Following some algebra, and discarding $\mathcal{O}(\mathrm{Pr}^5)$ corrections, we deduce $\det(M) = 0$ when,

$$\delta\mathrm{Ra} = \delta\mathrm{Ra}_c \sim \mathrm{Ra}_c\frac{3\Gamma^2(7\Gamma^4 + 20\Gamma^2 + 16)}{128(1+\Gamma^2)}\mathrm{Pr}^2. \tag{3.15}$$

In particular, with $\Gamma = 2$ we have $\delta\mathrm{Ra}_c = \frac{39}{10}\mathrm{Ra}_c\mathrm{Pr}^2$. We have thus successfully recovered the power-law observed in Figure 3.8. However, we note that $\frac{39}{10}\mathrm{Ra}_c \approx 3.04 \times 10^3$, meaning that the prefactor calculated here is approximately a factor of 20 smaller than the true prefactor calculated from the linear stability analysis of the full system in Figure 3.8. Clearly, more than 6 modes are needed to accurately calculate the prefactor.

3.5.3 Derivation of The Weakly Non-Linear Model

Having determined the asymptotic behaviour of the boundary where the SCRS loses stability, we next derive a weakly non-linear model that more accurately captures the stability boundary and describes the subsequent relaxation oscillations. We focus on the behaviour in the small-Prandtl-number limit when we are close to the stability boundary, so the parameters Pr and δRa are both small. Guided by the analysis above, we seek a distinguished limit in which $\mathrm{Pr} = \epsilon \ll 1$ and $\delta\mathrm{Ra} = O(\epsilon^2)$. The analysis is carried out for arbitrary aspect ratio $\Gamma < 2^{4/3}\sqrt{1 + 2^{2/3}}$, and the other parameters and variables are scaled as follows:

$$
\begin{aligned}
\delta\mathrm{Ra} &= \mathrm{Ra} - \mathrm{Ra}_c = r\epsilon^2, && (3.16a)\\
t &= \frac{\tau_O}{\epsilon} = \frac{\tau_E}{\epsilon^3}, && (3.16b)\\
\psi^E &= \epsilon\psi_1^E(\tau_E, x, y) + \epsilon^2\psi_2^E(\tau_E, x, y) + \mathcal{O}(\epsilon^3), && (3.16c)\\
\theta^E &= \epsilon\theta_1^E(\tau_E, x, y) + \epsilon^2\theta^E(\tau_E, x, y) + \mathcal{O}(\epsilon^3), && (3.16d)\\
\psi^O &= \epsilon^2\psi_1^O(\tau_O, x, y) + \epsilon^3\psi_2^O(\tau_O, x, y) + \mathcal{O}(\epsilon^4), && (3.16e)\\
\theta^O &= \epsilon^2\theta_1^O(\tau_O, x, y) + \epsilon^3\theta_2^O(\tau_O, x, y) + \mathcal{O}(\epsilon^4). && (3.16f)
\end{aligned}
$$

We have introduced two time-scales, τ_O and τ_E, due to the distinct time-scale separation between the odd and even modes observed, for example, in Figure 3.9 (c). The scalings of the dependent variables are constructed such that weak nonlinearity and coupling between even and odd modes enter at the same order, as we will see below. We substitute the ansatz (3.16) into the governing equations (2.10) and boundary conditions (2.11) and (2.12), and collect terms of equal order in ϵ.

First, we examine the evolution of the even modes. At $\mathcal{O}(\epsilon)$ we find

$$
\begin{aligned}
\psi_1^E &= \frac{4+\Gamma^2}{\Gamma}\pi A \sin(2\pi x/\Gamma)\sin(\pi y), && (3.17a)\\
\theta_1^E &= 2A\cos(2\pi x/\Gamma)\sin(\pi y), && (3.17b)
\end{aligned}
$$

in which the amplitude A is arbitrary, and assumed to be a function of the "slow" time variable τ_E. At $\mathcal{O}(\epsilon^2)$ we find

$$
\begin{aligned}
\psi_2^E &= 0, && (3.18a)\\
\theta_2^E &= -\pi A^2\frac{4+\Gamma^2}{2\Gamma^2}\sin(2\pi y), && (3.18b)
\end{aligned}
$$

which describes the asymptotic behaviour of the SCRS as $\delta\mathrm{Ra} \to 0$.

At $\mathcal{O}(\epsilon^3)$, we have

$$
\begin{aligned}
\nabla^2\psi^E_{1\tau_E} + \{\psi_1^O, \nabla^2\psi_1^O\} &= \mathrm{Ra}_c\theta^E_{3x} + \nabla^4\psi_3^E + r\theta^E_{1x}, && (3.19a)\\
\{\psi_1^E, \theta_2^E\} &= \psi^E_{3x} + \nabla^2\theta_3^E. && (3.19b)
\end{aligned}
$$

We note that,

$$
\begin{aligned}
\nabla^2\psi^E_{1\tau_E} &= \frac{(4+\Gamma^2)^2\pi^3}{2\Gamma^3} i\frac{dA}{d\tau_E}\phi_{1,1} + c.c., && (3.20a)\\
\{\psi_1^O, \nabla^2\psi_1^O\} &= \frac{2}{\Gamma}\langle\{\psi_1^O, \nabla^2\psi_1^O\}, \phi_{1,1}\rangle\phi_{1,1} + c.c. + \text{higher harmonics}, && (3.20b)\\
r\theta^E_{1x} &= r\frac{2\pi}{\Gamma}iA\phi_{1,1} + c.c., && (3.20c)\\
\{\psi_1^E, \theta_2^E\} &= \frac{(4+\Gamma^2)^2\pi^4}{2\Gamma^4}A^3\phi_{1,1} + c.c. + \text{higher harmonics}, && (3.20d)
\end{aligned}
$$

whence,

$$
L\begin{pmatrix}\psi_3^E\\ \theta_3^E\end{pmatrix} = \begin{pmatrix}\frac{(4+\Gamma^2)^2\pi^3}{2\Gamma^3} i\frac{dA}{d\tau_E} - r\frac{2\pi}{\Gamma} iA + \frac{2}{\Gamma}\langle\{\psi_1^O, \nabla^2\psi_1^O\}, \phi_{1,1}\rangle \\ \frac{(4+\Gamma^2)^2\pi^4}{2\Gamma^4} A^3\phi_{1,1}\end{pmatrix}\phi_{1,1} \tag{3.21}
$$
$$
+ \, c.c. + \text{higher harmonics},
$$

where

$$
L = \begin{pmatrix}\nabla^4 & \mathrm{Ra}_c\partial_x \\ \partial_x & \nabla^2\end{pmatrix}. \tag{3.22}
$$

We express the operator L in terms of the basis functions ϕ_{k_x,k_y} as followes. If

$$
v = \begin{pmatrix}a\\ b\end{pmatrix}\phi_{k_x,k_y}, \tag{3.23}
$$

then

$$
Lv = \begin{pmatrix}\left[\left(\frac{2\pi k_x}{\Gamma}\right)^2 + (k_y\pi)^2\right]^2 & i\mathrm{Ra}_c\frac{2\pi k_x}{\Gamma} \\ i\frac{2\pi k_x}{\Gamma} & -\left(\frac{2\pi k_x}{\Gamma}\right)^2 - (k_y\pi)^2\end{pmatrix} v := L_{k_x,k_y}, \tag{3.24}
$$

where we recall that $\mathrm{Ra}_c = \pi^4(4+\Gamma^2)^3/4\Gamma^4$. We note that L_{k_x,k_y} is invertible unless $|k_x| = k_y = 1$. So, it is only the $\phi_{1,1}$ term in (3.21) that causes a solvability problem.

To find a bounded solution to (3.21) of the form $(a,b)^T\phi_{1,1}+c.c.+$higher harmonic, we require

$$
L_{1,1}\begin{pmatrix}a\\ b\end{pmatrix} = \begin{pmatrix}\frac{(4+\Gamma^2)^2\pi^3}{2\Gamma^3} i\frac{dA}{d\tau_E} - r\frac{2\pi}{\Gamma} iA + \frac{2}{\Gamma}\langle\{\psi_1^O, \nabla^2\psi_1^O\}, \phi_{1,1}\rangle \\ \frac{(4+\Gamma^2)^2\pi^4}{2\Gamma^4} A^3\phi_{1,1}\end{pmatrix}. \tag{3.25}
$$

Because $L_{1,1}$ is singular, this equation has a solution if and only if the right-hand side is orthogonal to the null vector of the adjoint of $L_{1,1}$, namely

$$
L_{1,1}^* = \begin{pmatrix}\frac{(4+\Gamma^2)^2\pi^4}{\Gamma^4} & -i\frac{2\pi}{\Gamma} \\ -i\frac{\pi^5(4+\Gamma^2)^3}{2\Gamma^5} & -\frac{(4+\Gamma^2)\pi^2}{\Gamma^2}\end{pmatrix}; \tag{3.26}
$$

the relevant eigenvector is given by

$$
\eta = \begin{pmatrix} i \\ \frac{(4+\Gamma^2)^2\pi^3}{2\Gamma^3}\end{pmatrix}. \tag{3.27}
$$

Therefore the solvability condition for (3.21) is

$$\left(i, \frac{(4+\Gamma^2)^2\pi^3}{2\Gamma^3}\right)^* \begin{pmatrix} \frac{(4+\Gamma^2)^2\pi^3}{2\Gamma^3} i \frac{dA}{d\tau_E} - r\frac{2\pi}{\Gamma} iA + \frac{2}{\Gamma}\langle\{\psi_1^O, \nabla^2\psi_1^O\}, \phi_{1,1}\rangle \\ \frac{(4+\Gamma^2)^2\pi^4}{2\Gamma^4} A^3\phi_{1,1} \end{pmatrix} = 0, \tag{3.28}$$

which yields the following evolution equation for the amplitude of A:

$$\frac{(4+\Gamma^2)^2}{2\Gamma^3}\pi^3 \frac{dA}{d\tau_E} - r\frac{2\pi}{\Gamma}A + \frac{(4+\Gamma^2)^4}{4\Gamma^7}\pi^7 A^3 = \frac{2i}{\Gamma}\left\langle\{\psi_1^O, \nabla^2\psi_1^O\}, \phi_{1,1}\right\rangle. \tag{3.29}$$

The right-hand side of equation (3.29) is the inner product of the non-linear forcing term in (3.19a) with the $(1,1)$ basis function, and captures the net effect of the odd modes on the amplitude of the dominant even mode. If this term is set to zero, then equation (3.29) reduces to the standard Landau equation governing the amplitude A of weakly non-linear perturbations to the static conduction state [53].

We now turn to the odd modes to evaluate the right-hand side of equation (3.29). At lowest order, we obtain the problem

$$\nabla^2\psi^O_{1\tau_O} + \{\psi_1^O, \nabla^2\psi_1^E\} + \{\psi_1^E, \nabla^2\psi_1^O\} = \mathrm{Ra}_c\theta^O_{1x} + \nabla^4\psi_1^O, \tag{3.30a}$$

$$0 = \psi^O_{1x} + \nabla^2\theta_1^O, \tag{3.30b}$$

which can be reduced to

$$\nabla^2\psi^O_{1\tau_O} + \frac{\pi(4+\Gamma^2)}{\Gamma}A\left\{\sin\left(\frac{2\pi x}{\Gamma}\right)\sin(\pi y), \nabla^2\psi_1^O + \frac{\pi^2(4+\Gamma^2)}{\Gamma^2}\psi_1^O\right\} = \nabla^4\psi_1^O - \mathrm{Ra}_c\nabla^{-2}\psi^O_{1xx}. \tag{3.31}$$

We note that the odd modes are assumed to evolve with the "fast" time variable τ_O. Using the Fourier decomposition (2.13), i.e.

$$\psi_1^O = \sum_{k_x+k_y\in 2\mathbb{Z}+1} \widehat{\psi}_{k_x,k_y}\phi_{k_x,k_y}, \tag{3.32}$$

we can express equation (3.31) as a linear dynamical system of the form

$$\frac{d\boldsymbol{\psi}_1^O}{d\tau_O} = (AM + D)\boldsymbol{\psi}_1^O. \tag{3.33}$$

Here M and D are known constant matrices, calculated as described in §B.1 of Appendix B, and $\boldsymbol{\psi}_1^O = (\widehat{\psi}_{k_x,k_y})_{k_x+k_y\in 2\mathbb{Z}+1}$ is the vector of odd modes. Note that $AM+D$ is equivalent to matrix M in §3.5.2, but now without the crude mode truncation. In general, M and and D are infinite-dimensional matrices. However, following the two-thirds dealiasing rule [16][1], we truncate at maximum wavenumber of 21 and 43 in x and y, respectively, yielding 362 odd modes and their complex conjugates in our expansion of $\boldsymbol{\psi}_1^O$ and highly resolved numerics since $\mathrm{Ra} - \mathrm{Ra}_c = r\epsilon^2$.

We recall that A evolves on the much slower time-scale $\tau_E = \epsilon^2 \tau_O$. As justified in §B.1 of Appendix B, to leading order in ϵ, it follows that $\boldsymbol{\psi}_1^O$ is proportional to the most unstable eigenvector of the problem (3.33). We can therefore write

$$\boldsymbol{\psi}_1^O(\tau_O; A) \sim B(\tau_O)\boldsymbol{v}(A), \tag{3.34}$$

where

$$(AM + D)\boldsymbol{v}(A) = \sigma(A)\boldsymbol{v}(A), \tag{3.35}$$

with $\sigma(A)$ the eigenvalue of (3.35) with the largest real part, and $\boldsymbol{v}$ normalised such that $||\boldsymbol{v}|| = 1$. At leading order in ϵ, the net amplitude B of the odd modes thus evolves according to

$$\frac{dB}{d\tau_O} = \sigma(A)B. \tag{3.36}$$

With ψ_1^O decomposed as in (3.34), we can express the right-hand side of equation (3.29) in the form

$$\frac{2i}{\Gamma}\left\langle \{\psi_1^O, \nabla^2\psi_1^O\}, \phi_{1,1}\right\rangle = -B^2\lambda(A), \tag{3.37}$$

where

$$\lambda(A) = -\frac{2i}{\Gamma}\left\langle \{\boldsymbol{v}(A), \nabla^2\boldsymbol{v}(A)\}, \phi_{1,1}\right\rangle. \tag{3.38}$$

For a given value of Γ, the functions $\sigma(A)$ and $\lambda(A)$ can both be computed once-and-for-all from equations (3.35) and (3.38). Equations (3.29) and (3.36) then provide a closed two-dimensional autonomous system for the amplitudes A and B of the even and odd modes, respectively.

By using the scalings

$$\begin{aligned} A &= \left(\frac{4\Gamma^7}{(4+\Gamma^2)^4\pi^7}\right)^{1/3}\widehat{A} = a\widehat{A}, \qquad B = a\frac{(4+\Gamma^2)^2}{2\Gamma^3}\pi^3\widehat{B} = b\widehat{B}, \\ r &= \frac{\Gamma}{2\pi a}\widehat{r}, \qquad \tau_E = b\widehat{\tau_E}, \qquad \lambda = \frac{\widehat{\lambda}}{b^2}, \qquad \sigma = \frac{\widehat{\sigma}}{b}, \end{aligned} \tag{3.39}$$

[1] Note that the aliasing errors do not occur in this eigenvalue problem. Nonetheless, we employ the two-thirds dealiasing rule for consistency with the modal truncation in the DNS described in Appendix C.

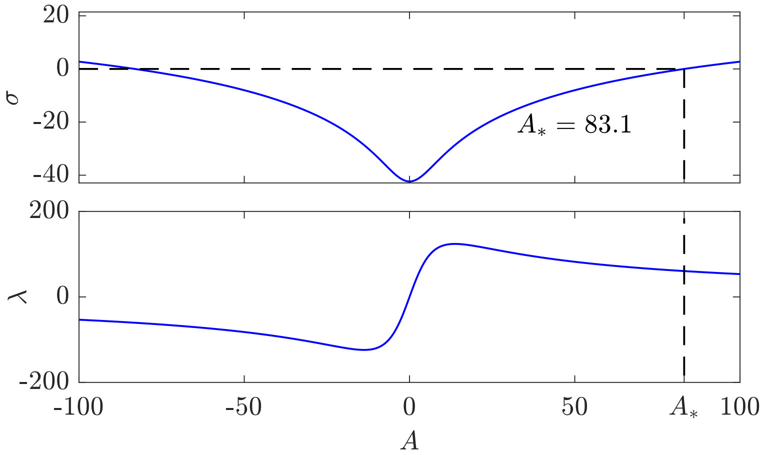

Figure 3.10: The functions $\sigma(A)$ and $\lambda(A)$ as they appear in (3.40) with $\Gamma = 2$. Highlighted is the point A_* at which $\sigma(A_*) = 0$.

we normalise the system (3.29) and (3.36) and are left with the two ODEs (after dropping hats)

$$\dot{A} = rA - A^3 - B^2\lambda(A), \tag{3.40a}$$

$$\epsilon^2\dot{B} = \sigma(A)B, \tag{3.40b}$$

where the time derivative is taken with respect to the slow time-scale τ_E. In Figure 3.10 we show the functions $\sigma(A)$ and $\lambda(A)$ (normalised according to (3.39)) in the instance when $\Gamma = 2$. The highlighted point A_* where $\sigma(A_*) = 0$ takes the value $A_* \approx 83.1$.

3.5.4 Solution of the Weakly Non-Linear Model

Since $\sigma(A)$ is an even function and $\lambda(A)$ is an odd function, we need only consider solutions of the phase plane problem (3.40) in the quadrant $A, B \geq 0$. The critical points are:

1. $(A, B) = (0, 0)$, corresponding to the pure conduction state, which loses stability through a pitchfork bifurcation as r increases through zero. This primary bifurcation excites the even modes in the system.

2. $(\sqrt{r}, 0)$ exists for $r > 0$ and represents the SCRS, with no odd modes. This state loses stability through a secondary pitchfork bifurcation at $r = r_c$ where

$$r_c = A_*^2 \approx 6.91 \times 10^3 \tag{3.41}$$

when $\Gamma = 2$, at which point the SCRS becomes unstable to odd perturbations.

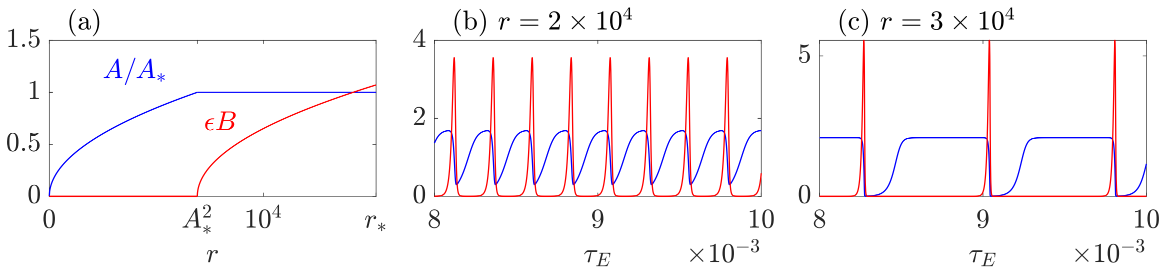

Figure 3.11: (a) Bifurcation diagram plotting A/A_* (blue) and ϵB (red) against r with $\Gamma = 2$ and $\epsilon = 10^{-2}$. Annotated are $r = r_c = A_*^2$, the point of the secondary pitchfork bifurcation and $r = r_*$, where the Hopf bifurcation occurs. (b) and (c) display time series of A/A_* and ϵB when $r = 2\times10^4$ and $r = 3\times10^4$, respectively.

3. $(A_*, \sqrt{(rA_* - A_*^3)/\lambda(A_*)})$ exists for $r > r_c$, when a mixed steady state including odd and even modes emerges. Finally, this steady state loses stability in a Hopf bifurcation at $r = r_*$ where

$$r_* = A_*^2 + \frac{2A_*^2\lambda(A_*)}{\lambda(A_*) - A_*\lambda'(A_*)}. \tag{3.42}$$

When $\Gamma = 2$, we calculate $r_* \approx 1.53\times10^4$.

We can use the value of r_c from (2) to infer the prefactor in the power-law found in §3.5.3 for the stability boundary at small Pr. Rescaling back to our original variables using (3.39), we find that $r_c = \delta \mathrm{Ra}_c/\mathrm{Pr}^2 \approx 6.35\times10^4$ which indeed gives excellent agreement with the fit obtained in Figure 3.8.

To see the bifurcations itemised above in practice, we solve equations (3.40) numerically. Figure 3.11 (a) is a bifurcation diagram showing how the nontrivial steady states identified in (2) and (3) above emerge at $r = 0$ and $r = r_c = A_*^2$, respectively. The Hopf bifurcation occurs at $r = r_*$, beyond which point the system undergoes the non-linear relaxation oscillations and bursts displayed in Figures 3.11 (b) and (c) for $r = 2\times10^4$ and $r = 3\times10^4$, respectively.

The bifurcation diagram in Figure 3.11 (a) aligns remarkably well with the corresponding diagram produced from DNS in Figure 3.9 (a). To illustrate this agreement, in Figure 3.12 we show the discrepancy between A and B values calculated in either case. Subscript WNL indicates values from the weakly non-linear model, and

$$A_{DNS} = \frac{2\Gamma\left|\widehat{\psi}_{1,1}\right|}{a\pi(4+\Gamma^2)\epsilon}, \quad B_{DNS} = \frac{\sqrt{\sum_{k_x+k_y\in 2\mathcal{Z}+1}\left|\widehat{\psi}_{k_x,k_y}\right|^2}}{b\epsilon^2}, \tag{3.43}$$

are the values calculated from the DNS solutions. As revealed in Figure 3.12, our model demonstrates remarkable accuracy in calculating both the SCRS and the mixed

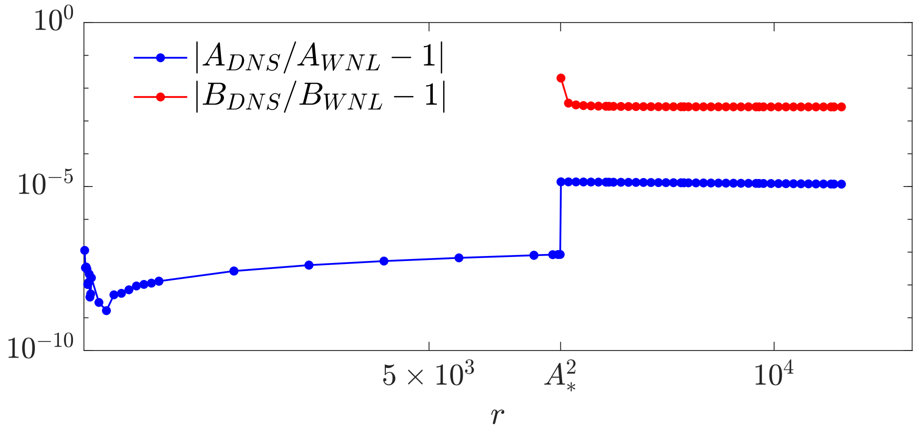

Figure 3.12: Comparison of the A and B values in the steady states calculated by the weakly non-linear analysis and DNS, subscripted by WNL and DNS, respectively.

steady state. The relative error is less than 1% throughout. Moreover, as we transition into a regime characterised by relaxation oscillations, there remains a strong qualitative agreement between the solutions generated from our model with those from the DNS. Clearly, our vastly simplified two-dimensional system is able to capture the essential dynamics of the full system.

While the system (3.40) was formally derived in the asymptotic limit as $\mathrm{Pr} \to 0$, similar relaxation oscillations are found in many parts of the $(\mathrm{Pr}, \mathrm{Ra})$-plane [63]. To our knowledge, our ODE system (3.40) is the first model that has been derived systematically from the Boussinesq equations without the need for any *ad hoc* closure assumptions that display relaxation oscillations.

Between bursts, the value of B is very small ($B_{\min} \sim 10^{-22}$ when $r = 3 \times 10^4$ and $\epsilon = 10^{-2}$), which presents significant numerical challanges. To aid our numerics, we evolved $\phi = \epsilon^2 \log B$ instead before converting back to $B = e^{\phi/\epsilon^2}$ when producing the plots in Figure 3.11. In §3.5.5, we develop a mathematical framework to study these extreme relaxation oscillations.

3.5.5 Relaxation Oscillations

We consider the system (3.40) with the substitution $\phi = \epsilon^2 \log B$, which yields

$$\dot{A} = rA - A^3 - e^{2\phi/\epsilon^2}\lambda(A). \tag{3.44a}$$

$$\dot{\phi} = \sigma(A). \tag{3.44b}$$

For notational convenience, we denote the time variable by t (not the slow time-scale τ_E as in (3.40)). We consider the parameter regime where $r > r_* > A_*^2$ and the system is expected to perform relaxation oscillations.

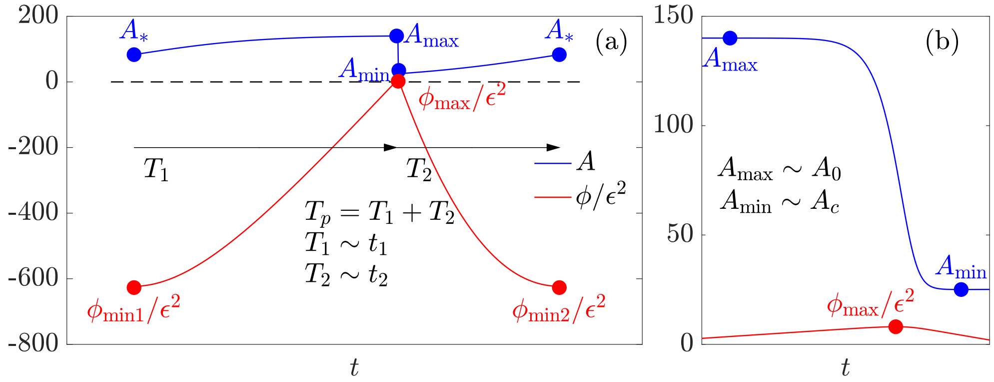

Figure 3.13: (a) One complete relaxation oscillation governed by the system (3.44) with parameter values $\epsilon = 10^{-3}$, $\Gamma = 2$, $r = 2 \times 10^4$. $\phi_{\min 1}$ and $\phi_{\min 2}$ are adjacent minima of ϕ, $A_{\max}$ and $A_{\min}$ are maxima and minima of A , respectively, and $\sigma(A_*) = 0$. T_1 is the time from the first minimum of ϕ to the its maximum, and T_2 is the subsequent time to the next minimum. The total period of oscillation is $T_p = T_1 + T_2$. (b) Blow-up of the fast time-scale region where $\phi > 0$ and A decreases rapidly. Leading-order expressions for T_1, T_2, $A_{\max}$, and $A_{\min}$ are also given in the figure.

Figure 3.13 (a) depicts one complete relaxation oscillation with parameters $\epsilon = 10^{-3}$, $\Gamma = 2$, $r = 2 \times 10^4$. At $t = 0$, we start at $A = A_*$ and $\phi = \phi_{\min 1}$. As A increases through A_*, $\sigma(A)$ changes sign, so $\phi_{\min 1}$ is a local minimum of ϕ. After time T_1, A reaches its maximum value, which we denote by $A_{\max}$, and then decreases rapidly over the short time-scale $t - T_1 = \mathcal{O}(\epsilon^2)$. The maximum value of ϕ occurs as A recrosses the critical value A_*, following which ϕ also decreases rapidly. Once A has reached its minimum value, it starts to increase again on the slow time-scale. After an additional time T_2, A returns to the value A_* for the third time. We have completed a full oscillation, and ϕ is at its subsequent local minimum, $\phi_{\min 2}$.

In the following analysis, we find leading-order expressions for the minimum and maximum values of A ($A_{\min}$ and $A_{\max}$), adjacent minimum values of ϕ ($\phi_{\min 1}$ and $\phi_{\min 2}$), the intermediate maximum ($\phi_{\max}$), and the period of oscillation $T_p = T_1 + T_2$.

We start at $A = A_*$ and $\phi = \phi_{\min 1} < 0$, so

$$\dot{A} = rA - A^3 + \text{Exp Small}, \tag{3.45a}$$

$$\dot{\phi} = \sigma(A), \tag{3.45b}$$

which yields the leading order solution

$$A(t) = \sqrt{\frac{rA_*^2}{A_*^2 + (r - A_*^2)e^{-2rt}}}, \tag{3.46a}$$

$$\frac{d\phi}{dA} = \frac{\sigma(A)}{A(r - A^2)}, \tag{3.46b}$$

$$\phi - \phi_{\min 1} = \int_{A_*}^{A} \frac{\sigma(\widetilde{A})d\widetilde{A}}{\widetilde{A}(r - \widetilde{A}^2)}. \tag{3.46c}$$

Recall that we take $r > A_*^2$, which means that $A(t) \to r$, and $\phi(t) \to \infty$ as $t \to \infty$. It follows that ϕ reaches 0 after a finite time t_1 at which point $A = A_0$, say. From (3.46a) and (3.46c) we conclude

$$\phi_{\min 1} = \int_{A_0}^{A_*} \frac{\sigma(A)dA}{A(r - A^2)}, \tag{3.47a}$$

$$t_1 = \frac{1}{2r} \log\left(\frac{A_0^2(r - A_*^2)}{A_*^2(r - A_0^2)}\right). \tag{3.47b}$$

For $t > t_1$, we have $\phi > 0$, so the term involving ϕ in (3.44a) is no longer exponentially small, and we need to introduce a fast time variable, T, to resolve the dynamics. We set

$$t = t_1 + \epsilon^2 T, \tag{3.48a}$$

$$\phi(t) = \epsilon^2 \Phi(T), \tag{3.48b}$$

so

$$\frac{d\Phi}{dT} = \sigma(A), \tag{3.49a}$$

$$\frac{dA}{dT} = \epsilon^2(rA - A^3 - \lambda(A)e^{2\Phi}). \tag{3.49b}$$

Now we expand the dependent variables as $\Phi \sim \Phi_0 + \epsilon^2\Phi_1 + \dots$ and $A \sim A_0 + \epsilon^2 A_1 + \dots$. At lowest order we have

$$\frac{d\Phi_0}{dT} = \sigma(A_0), \tag{3.50a}$$

$$\frac{dA_1}{dT} = rA_0 - A_0^3 - \lambda(A_0)e^{2\Phi_0}. \tag{3.50b}$$

By matching with the previous solution (3.46) we obtain the matching conditions

$$\Phi_0(T) \sim \sigma(A_0)T, \quad A_1(T) \sim A_0(r - A_0^2)T \quad \text{as} \quad T \to -\infty, \tag{3.51}$$

in which the constant terms are identically zero. We thus find the solutions

$$\Phi_0 = \sigma(A_0)T, \tag{3.52a}$$

$$A_1 = \left(rA_0 - A_0^3\right)T - \frac{\lambda(A_0)}{2\sigma(A_0)}e^{2\sigma(A_0)T}. \tag{3.52b}$$

We note that A_1 takes its maximum value when

$$T = \frac{1}{2\sigma(A_0)}\log\left(\frac{rA_0 - A_0^3}{\lambda(A_0)}\right) \tag{3.53}$$

and hence the maximum value of A is given asymptotically by

$$A_{\max} \sim A_0 + \frac{\epsilon^2\left(rA_0 - A_0^3\right)}{2\sigma(A_0)}\left[\log\left(\frac{rA_0 - A_0^3}{\lambda(A_0)}\right) - 1\right] + \mathcal{O}(\epsilon^4). \tag{3.54}$$

For larger values of T, A starts to decrease but Φ continues to increase. However, the above expansion becomes non-uniform when $\Phi \sim \log(1/\epsilon)$ and the final term in (3.49b) appears at leading order. So we make the new substitution

$$T = \frac{\log 1/\epsilon}{\sigma(A_0)} + \widetilde{T}, \tag{3.55a}$$

$$\Phi = \log\left(1/\epsilon\right) + \widetilde{\Phi} \tag{3.55b}$$

into (3.49) to obtain

$$\frac{dA}{d\widetilde{T}} = \epsilon^2(rA - A^3) - e^{2\widetilde{\Phi}}\lambda(A), \tag{3.56a}$$

$$\frac{d\widetilde{\Phi}}{d\widetilde{T}} = \sigma(A). \tag{3.56b}$$

To leading order, we therefore have

$$\frac{dA}{d\widetilde{\Phi}} = -\frac{\lambda(A)e^{2\widetilde{\Phi}}}{\sigma(A)}, \tag{3.57}$$

while matching with (3.52b) gives

$$A \sim A_0 - \frac{\lambda(A_0)}{2\sigma(A_0)}e^{2\sigma(A_0)\tilde{T}} \tag{3.58}$$

as $\tilde{T}, \tilde{\Phi} \to -\infty$. Integration of (3.57) therefore leads to

$$\int_A^{A_0} \frac{\sigma(\widetilde{A})d\widetilde{A}}{\lambda(\widetilde{A})} = \frac{1}{2}e^{2\widetilde{\Phi}}. \tag{3.59}$$

The maximum value of ϕ is reached when $A = A_*$ again, and is thus given by

$$\phi_{\max} \sim \epsilon^2 \left(\log 1/\epsilon + \widetilde{\Phi}_{\max} \right), \tag{3.60}$$

where

$$\widetilde{\Phi}_{\max} = \frac{1}{2} \log \left(2 \int_{A_*}^{A_0} \frac{\sigma(A) dA}{\lambda(A)} \right), \tag{3.61}$$

from (3.59).

Now combining (3.59) with (3.56a) gives

$$\frac{dA}{d\widetilde{T}} = 2\lambda(A) \int_{A_0}^{A} \frac{\sigma(\widetilde{A}) d\widetilde{A}}{\lambda(\widetilde{A})}, \tag{3.62}$$

which in principle determines the time evolution of A over this part of the dynamics. The integral on the right-hand side of equation (3.62) reaches zero as A approaches a new critical value $A_c < A_*$, which satisfies

$$\int_{A_0}^{A_c} \frac{\sigma(\widetilde{A}) d\widetilde{A}}{\lambda(\widetilde{A})} = 0. \tag{3.63}$$

We thus find that the solutions of the system (3.59) and (3.62) satisfy

$$A \sim A_c + \text{const.} e^{2\sigma(A_c)\tilde{T}}, \quad \tilde{\Phi} \sim \sigma(A_c)\tilde{T} \quad \text{as } \tilde{T} \to \infty, \tag{3.64}$$

in which we note that $\sigma(A_c) < 0$. We deduce that there is yet another inner layer, in which

$$\tilde{T} = -\frac{\log(1/\epsilon)}{\sigma(A_c)} + \hat{T} \tag{3.65}$$

and Φ is again $\mathcal{O}(1)$. In this region, we end up with exactly the same system (3.49) as above, with asymptotic solution given by

$$\Phi \sim C_1 + \sigma(A_c)\hat{T}, \tag{3.66a}$$

$$A \sim A_c + \epsilon^2 \left(C_2 + \left(rA_c - A_c^3 \right) \hat{T} - \frac{\lambda(A_c) e^{2C_1 + 2\sigma(A_c)\hat{T}}}{2\sigma(A_c)} \right). \tag{3.66b}$$

With considerable further effort, in principle one could calculate the integration constants C_1 and C_2 via higher-order matching, but for our purposes it is unnecessary. We simply note that, during this stage, Φ continues to decrease, eventually becoming negative again, while A reaches its minimum value

$$A_{\min} \sim A_c + \mathcal{O}(\epsilon^2), \tag{3.67}$$

before starting to increase again.

Finally we return to the long time-scale with

$$\hat{T} = \tilde{t}/\epsilon^2, \quad \text{i.e.} \quad t = T_1 + \epsilon^2 \log(1/\epsilon)\left(\frac{1}{\sigma(A_0)} - \frac{1}{\sigma(A_c)}\right) + \tilde{t}. \tag{3.68}$$

Now A and ϕ are both $\mathcal{O}(1)$ and $\phi < 0$ so, up to exponentially small corrections, we have the dynamical system

$$\frac{dA}{d\widetilde{t}} = rA - A^3, \tag{3.69a}$$

$$\frac{dA}{d\widetilde{t}} = \sigma(A). \tag{3.69b}$$

The matching conditions $A \to A_c$ and $\phi \to 0$ as $\tilde{t} \to 0$ are valid up to $\mathcal{O}(\epsilon^2)$, and the leading-order solutions are given by

$$A = \sqrt{\frac{rA_c^2}{A_c^2 + (r - A_c^2)e^{-2r\tilde{t}}}}, \tag{3.70a}$$

$$\phi = \int_{A_c}^{A} \frac{\sigma(\widetilde{A})d\widetilde{A}}{\widetilde{A}(r - \widetilde{A}^2)}. \tag{3.70b}$$

We have gone through a complete relaxation oscillation when ϕ is at its subsequent local minimum, $\phi_{\min 2}$, and A is back at A_*. From (3.70) we find that this occurs at $\widetilde{t} = t_2$, where

$$t_2 = \frac{1}{2r}\log\left(\frac{A_*^2(r - A_c^2)}{A_c^2(r - A_*^2)}\right), \tag{3.71a}$$

and

$$\phi_{\min 2} = \int_{A_c}^{A_*} \frac{\sigma(A)dA}{A(r - A^2)}. \tag{3.72a}$$

The total period of the oscillations is thus approximated by

$$T_p = T_1 + T_2 \sim t_1 + t_2 = \frac{1}{2r}\log\left(\frac{A_0^2(r - A_c^2)}{A_c^2(r - A_0^2)}\right). \tag{3.73}$$

In summary, we have constructed an algorithm to find successive minima and maxima of A and ϕ as follows:

$$(1) \text{ solve } \phi_{\min 1} = \int_{A_0}^{A_*} \frac{\sigma(A)dA}{A(r - A^2)} \text{ for } A_0; \tag{3.74a}$$

$$(2) \text{ solve } \int_{A_0}^{A_c} \frac{\sigma(A)dA}{\lambda(A)} = 0 \text{ for } A_c; \tag{3.74b}$$

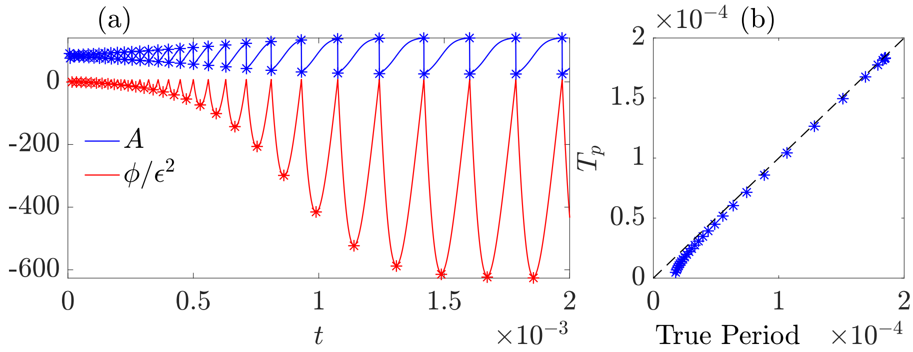

Figure 3.14: (a) Relaxation oscillations governed by the system (3.44) with parameter values $\epsilon = 10^{-3}$, $\Gamma = 2$, $r = 2 \times 10^4$. The initial conditions are $A = A_*$ and $\phi = 0$. The red stars show successive minima of ϕ, and blue stars are A_0 and A_c as calculated by the algorithm in (3.74) and (3.75). The timing of the stars is in line with the time series from the ODE solver. (b) For each relaxation oscillation in (a), we calculate the True Period between adjacent minima in ϕ, while T_p is the leading-order period given by (3.73).

and then

$$\phi_{\max} \sim \epsilon^2 \left(\log 1/\epsilon + \frac{1}{2} \log \left(2 \int_{A_*}^{A_0} \frac{\sigma(A)dA}{\lambda(A)} \right) \right), \tag{3.75a}$$

$$\phi_{\min 2} \sim \int_{A_c}^{A_*} \frac{\sigma(A)dA}{A(r - A^2)}. \tag{3.75b}$$

By starting again with $\phi_{\min 2}$, we go on to find the subsequent A_0, A_c, $\phi_{\max}$, and $\phi_{\min}$, et cetera. The system ultimately reaches a periodic orbit when $\phi_{\min 1} = \phi_{\min 2}$.

In Figure 3.14 (a) we show relaxation oscillations governed by the system (3.44) with parameter values $\epsilon = 10^{-3}$, $\Gamma = 2$, $r = 2 \times 10^4$. The initial conditions are $A = A_*$ and $\phi = 0$. The red stars show successive minima of ϕ, and blue stars are A_0 and A_c as calculated by the algorithm in (3.74) and (3.75). We see a transient where the oscillation amplitude gradually increases before reaching a periodic solution where $\phi_{\min}/\epsilon^2 \approx -623$, $A_0 \approx 140$, $A_c \approx 25.1$, and $T_p \approx 1.85 \times 10^{-4}$. Using (3.73), (3.74) and (3.75) yields excellent agreement with numerical solutions of the system (3.44). Note that the results shown in Figure 3.14 are obtained not strictly by following the algorithm presented above. Given $\phi_{\min 1}$, we calculate A_0, A_c, $\phi_{\min 2}$ and T_p as described in (3.74) and (3.75). Then, instead of using $\phi_{\min 2}$ to initialise the system, we start again with a new value of $\phi_{\min 1}$ obtained from the ODE solver. With this approach, we demonstrate that the asymptotic analysis provides a good approximation for the evolution of each single cycle of the relaxation oscillation, but without accumulating the errors incurred over multiple cycles.

In Figure 3.14 (b), we plot T_p, calculated using the estimated values of A_0 and A_c from (3.74), versus the "True Period" calculated between adjacent minima in ϕ. The two agree well, especially when the oscillation amplitude is large after the initial transient.

3.5.6 Sequence of Bifurcations

The amplitude equations (3.40) offer a way to analytically determine when the bifurcations occur, and we now compare these predictions with results from the full system. In other words, we compare $r = r_c$ and $r = r_*$ with the corresponding values of r (denoted with tildes) at which the SCRS loses stability to odd modes and where the resulting mixed steady loses stability via the Hopf bifurcation in the full system. The mixed steady state is calculated in the same way as the SCRS using the scheme outlined in §A.1 of Appendix A, but allowing for odd modes.

In Figure 3.15 (a) we plot r_c and r_* from the model (3.40), together with $\widetilde{r}_c$ and $\widetilde{r}_*$, from the full system (2.10) (with $\mathrm{Pr} = 10^{-3}$), versus aspect ratio Γ, and in Figure 3.15 (b) we plot the errors $\left|\frac{\widetilde{r}_c}{r_c} - 1\right|$ and $\left|\frac{\widetilde{r}_*}{r_*} - 1\right|$. We see that r_c and $\widetilde{r}_c$ agree very well for all Γ. In fact, this is why we can derive the power-law prefactor in Figure 3.8 using the reduced model. However, there is a discrepancy between r_* and $\widetilde{r}_*$, particularly at small values of Γ. In fact, $r_* \to \infty$ as $\Gamma \searrow 0.37$, implying that the mixed steady state emerging at $r = r_c$ is stable for all $r > r_c$ when $\Gamma < 0.37$. This is clearly not what happens in the full system: our model fails to capture the dynamics at these very small aspect ratios. This issue is resolved in §B.2, where we include $\mathcal{O}(\epsilon^2)$ corrections in the evolution of B. While these do not affect the leading order

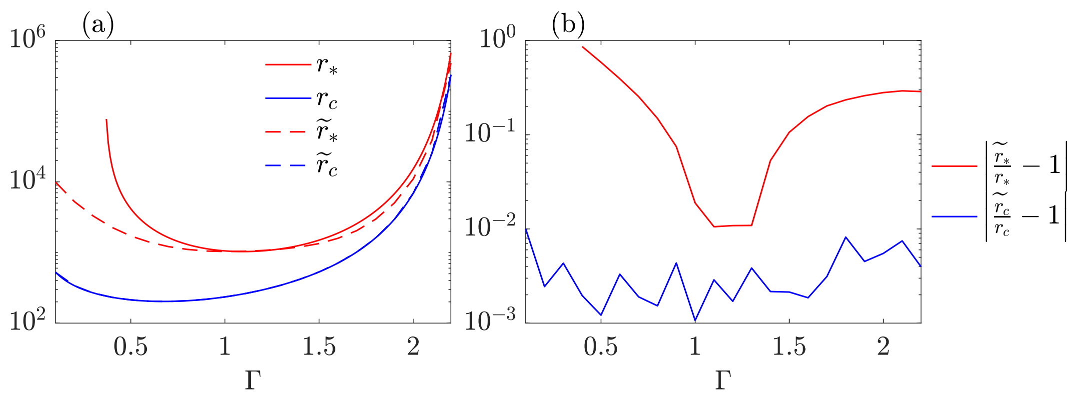

Figure 3.15: (a) r_c and r_*, from the model (3.40), and $\widetilde{r}_c$ and $\widetilde{r}_*$, from the full system (2.10) with $\mathrm{Pr} = 10^{-3}$, versus aspect ratio Γ. Note that r_* does not exist for $\Gamma < 0.37$. (b) error plot of quantities in (a).

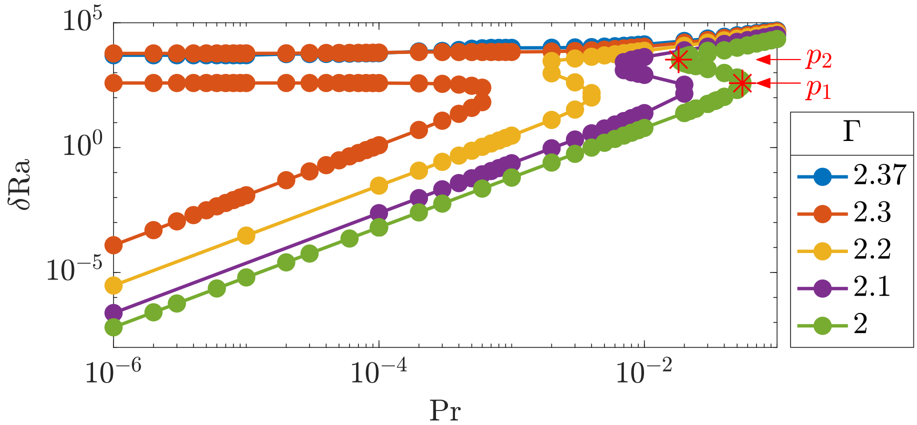

Figure 3.16: Stability boundaries in the $(\mathrm{Pr}, \delta\mathrm{Ra})$-plane for different Γ. The SCRS is stable as $\delta\mathrm{Ra} \to 0$ and either loses or regains stability as the stability boundary is crossed. Dots indicate points that have been calculated on each stability boundary. The red stars show points p_1 and p_2 when $\Gamma = 2$.

dynamics, they do affect the value of r at which the Hopf bifurcation occurs.

For larger Γ, we find that both r_c and r_* blow up as $\Gamma \to 2.37$. We examine this behaviour more closely in §3.5.7.

3.5.7 Aspect Ratio Dependence at Small Prandtl Number

Figure 3.16 shows the stability boundaries, for the full system, similar to those displayed in Figures 3.8, and 3.18, but now with varying Γ. For $\Gamma = 2$ to $\Gamma = 2.2$, the $\delta\mathrm{Ra} \propto \mathrm{Pr}^2$ power-law is clear, and the points p_1 and p_2 where the stability boundary turns back on itself are also visible. At $\Gamma = 2.3$, the point p_2 has disappeared off the left-hand side of the diagram; the system can regain and lose stability with increasing $\delta\mathrm{Ra}$ all the way down to $\mathrm{Pr} = 0$. Finally, at $\Gamma = 2.37$ the point p_1 has disappeared as well. For aspect ratios exceeding this critical value (but still less than 4.05), it is no longer the case that $\delta\mathrm{Ra}_c$ scales with Pr^2 as $\mathrm{Pr} \to 0$. The SCRS first becomes unstable at a relatively large Rayleigh number with $\delta\mathrm{Ra} \approx 5 \times 10^4$. This qualitative change in behaviour is captured in the reduced model by the blow-up of r_c as $\Gamma \to 2.37$.

3.5.8 Zero Prandtl Number

In the limit of zero Prandtl number, the 2D Boussinesq equations of thermal convection (2.7) reduce to a single equation for the streamfunction, namely

$$\nabla^2 \psi_t + \{\psi, \nabla^2 \psi\} = -\mathrm{Ra} \nabla^{-2} \psi_{xx} + \nabla^4 \psi. \tag{3.76}$$

As in the finite Prandtl number case, the $\widehat{\psi}_{1,1}$ mode becomes unstable at the critical Rayleigh number Ra_c. However, the resulting exponential solution,

$$\psi(x, y, t) = e^{\sigma t}\phi_{1,1}(x, y), \quad \text{with} \quad \sigma = \frac{4\Gamma^2}{\pi^2(4+\Gamma^2)^2}(\mathrm{Ra} - \mathrm{Ra}_c), \tag{3.77}$$

is now an *exact* solution to (3.76), because the non-linear term in (3.76) vanishes identically. The mode therefore grows without bound when $\mathrm{Ra} > \mathrm{Ra}_c$, and we do not converge to the SCRS as in the finite Prandtl number case. So the question is, what happens for a general initial condition when we are beyond the stability threshold?

In this analysis, we consider $\mathrm{Pr} = 0$ and $\mathrm{Ra} = \mathrm{Ra}_c + \epsilon^2$ with $\epsilon \ll 1$, where Γ is small enough so that $\widehat{\psi}_{1,1}$ is the only unstable mode from the static conduction state ($\psi = 0$). We then add some odd modes to see if the system reaches a bounded solution, i.e., we set $\psi = \psi^E + \psi^O$, where

$$\psi^E = \epsilon\psi_1^E(\tau_E, x, y) + \epsilon^2\psi_2^E(\tau_E, x, y) + \mathcal{O}(\epsilon^3), \tag{3.78a}$$

$$\psi^O = \epsilon^2\psi_1^O(\tau_O, x, y) + \epsilon^3\psi_2^O(\tau_O, x, y) + \mathcal{O}(\epsilon^4), \tag{3.78b}$$

$$\psi_1^E(\tau_E, x, y) = A\sin(2\pi x/\Gamma)\sin(\pi y), \tag{3.78c}$$

and ψ_1^O is determined by the same recipe (3.32)-(3.35) as in §3.5.3. Again, we have introduced two time-scales $\tau_E = \epsilon^2\tau_O$ due to the distinct time-scale separation between the odd and even modes. We conduct an almost identical weakly non-linear analysis to that in §3.5.3 and now obtain

$$\dot{A} = A - B^2\lambda(A), \tag{3.79a}$$

$$\epsilon^2\dot{B} = \sigma(A)B, \tag{3.79b}$$

where the time derivative is taken with respect to the slow time-scale τ_E. To arrive at (3.79), we have used the normalisation

$$\begin{gathered} A = \frac{4+\Gamma^2}{4}\widehat{A} = a\widehat{A}, \qquad B = a\frac{(4+\Gamma^2)\pi^2}{\Gamma^2}\widehat{B} = b\widehat{B}, \\ \tau_E = b\widehat{\tau_E}, \qquad \lambda = \frac{\widehat{\lambda}}{b^2}, \qquad \sigma = \frac{\widehat{\sigma}}{b}, \end{gathered} \tag{3.80}$$

and dropped hats.

The system (3.79) has the following steady state

$$A = A_*, \quad B = \sqrt{\frac{A_*}{\lambda(A_*)}}, \quad \sigma(A_*) = 0, \tag{3.81}$$

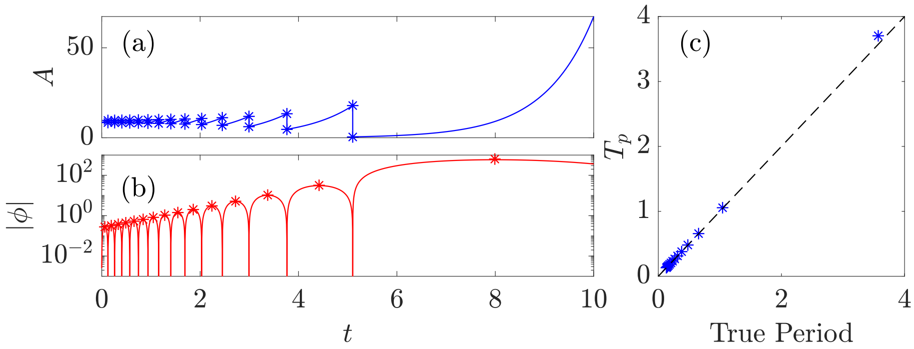

Figure 3.17: (a-b) Relaxation oscillations governed by the system (3.79) with parameter values $\epsilon = 10^{-2}$ and $\Gamma = 2$. The initial conditions are $A = A_*$ and $\phi = 0$. The red stars show successive minima of ϕ (i.e. maxima of $|\phi|$), and blue stars are A_0 and A_c as calculated by the algorithm in (3.83). (b) For each relaxation oscillation in (a-b), we calculate the True Period between adjacent minima in ϕ, while T_p is the leading-order period given by (3.84).

which is unstable if

$$1 - \frac{A_* \lambda'(A_*)}{\lambda(A_*)} > 0. \tag{3.82}$$

The inequality (3.82) is satisfied whenever $\Gamma \geq 0.4$, and we then see relaxation oscillations similar to those in §3.5.3.

As in §3.5.5, we set $\phi = \epsilon^2 \log B$ and derive the following set of equations (*cf* (3.74))

$$\phi_{\text{min1}} = \int_{A_0}^{A_*} \frac{\sigma(A)}{A}\, dA, \tag{3.83a}$$

$$\int_{A_c}^{A_0} \frac{\sigma(A)}{\lambda(A)}\, dA = 0, \tag{3.83b}$$

$$\phi_{\text{min2}} = \int_{A_c}^{A_*} \frac{\sigma(A)}{A}\, dA, \tag{3.83c}$$

to find successive leading-order minima in ϕ (ϕ_{min1} and ϕ_{min1}) and minima and maxima of A (A_c and A_0). We can also calculate the approximate period between ϕ_{min1} and ϕ_{min2}, namely

$$T_p = \log\left(\frac{A_0}{A_c}\right). \tag{3.84}$$

In Figure 3.17 (a-b) we show relaxation oscillations governed by the system (3.79) with parameter values $\epsilon = 10^{-2}$ and $\Gamma = 2$. The initial conditions are $A = A_*$ and $\phi = 0$. The red stars show successive minima of ϕ, and blue stars are A_0 and A_c as calculated by the algorithm in (3.83). In Figure 3.14 (c), we plot T_p versus the True Period calculated between adjacent minima in ϕ. Note that T_p has been calculated using the estimated values of A_0 and A_c from (3.83). In the final oscillation, A_c from (3.83) departs from its true value by about 14%, yielding a noticeable error between T_p and the True Period. Both the amplitude and period of the oscillations appear to grow without bound with the increasing amplitude generally well captured by the approximate solution. These kinds of runaway solutions are common in zero Prandtl number 2D RB convection [81, 161].

3.6 Stability at Large Prandtl Number

3.6.1 Stability Boundary

Figure 3.18 displays the (Pr, Ra)-plane for $10^5 \leq \mathrm{Pr} \leq 10^6$, highlighting where the SCRS is stable (white, S) or unstable (blue, US). At $q_4 = (7 \times 10^5, 2.54 \times 10^7)$, there is a corner in the stability boundary. This is caused by two complex conjugate pairs of eigenvalues that cross the imaginary axis simultaneously, as was discussed in §3.4.

Consequently, the stability boundaries for the two most unstable eigenfunctions cross at q_4, as indicated by the dashed curves in the inset in Figure 3.18. As noted

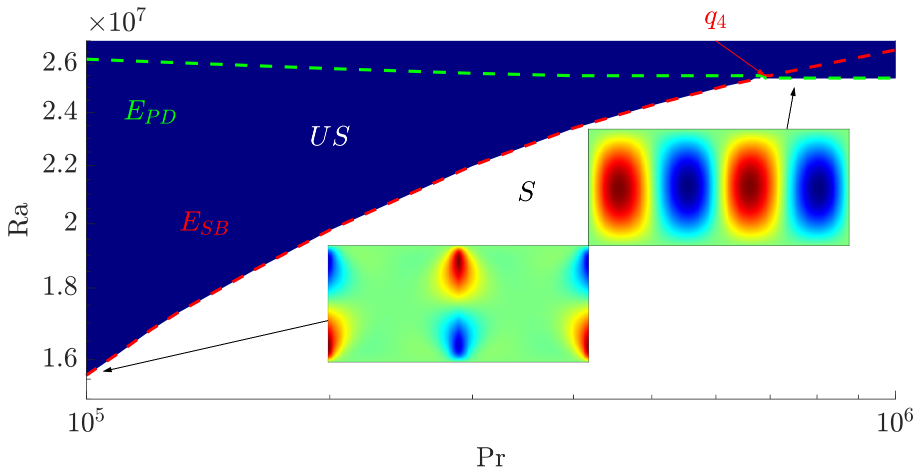

Figure 3.18: The (Pr, Ra) parameter space for large Pr highlighting when the SCRS is linearly stable (white, S) and unstable (blue, US). The point q_4 is where the stability boundaries corresponding to the symmetry breaking (red, E_{SB}) and period doubling (green, E_{PD}) eigenfunctions cross. The inserts show the odd eigenfunctions, ψ^O, associated with E_{SB} and E_{PD} where red, green and blue indicate $\psi^O > 0$, $\psi^O \approx 0$ and $\psi^O < 0$, respectively. The parameters are $(\mathrm{Ra}, \mathrm{Pr}) = (1.56 \times 10^7, 10^5)$ and $(\mathrm{Ra}, \mathrm{Pr}) = (2.54 \times 10^7, 7 \times 10^5)$.

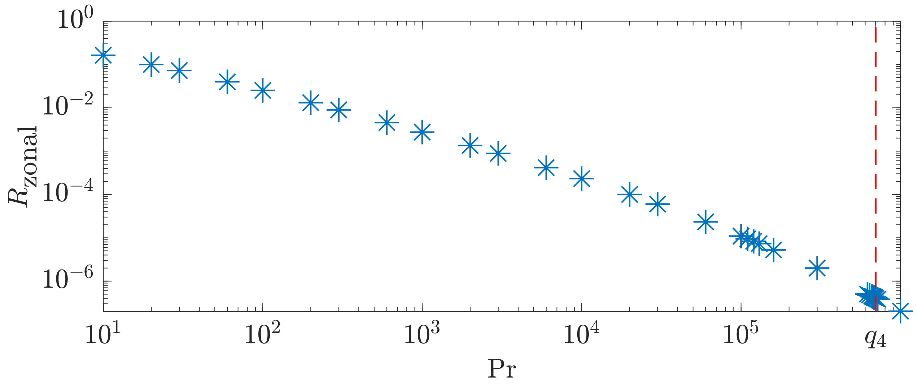

Figure 3.19: The proportion, R_{zonal}, of energy held in zonal modes in the eigenfunction E_{SB}, defined in (3.85) at the stability threshold plotted versus Pr. The red dashed line indicates the point q_4 beyond which the eigenfunction E_{PD}, with no zonal modes, becomes the most unstable.

in §3.4, the *symmetry breaking* eigenfunction (labelled E_{SB}) that is excited as we cross the red dashed curve has the property that $\widehat{\psi}^o_{k_x,k_y}$ and $i\widehat{\theta}^o_{k_x,k_y}$ are purely real and therefore breaks the reflection symmetry between counter-rotating convection rolls in the SCRS. It follows that the horizontal velocity is an even function of x, allowing instantaneous zonal flow in the solution.

The *period doubling* eigenfunction (labelled E_{PD}) corresponding to the green dashed curve has the complementary symmetry that $\widehat{\psi}^o_{k_x,k_y}$ and $i\widehat{\theta}^o_{k_x,k_y}$ are pure imaginary, and the zonal modes are therefore all zero: $\widehat{\psi}^o_{0,k_y} = 0$ for all k_y. The horizontal velocity is now an odd function of x and, although the E_{PD} eigenfunction introduces odd modes to the solution, it does not break the reflection symmetry (3.7) in the SCRS, but instead causes a period doubling in x. Consequently, zonal modes at the instability boundary switch off as we pass the point q_4. The qualitative change in the structure of the dominant eigenfunction is demonstrated by the inserts in Figure 3.18, and movies showing how these eigenfunctions evolve in time are included in the Supplementary Material of [185].

To measure the proportion of energy held in zonal modes in the eigenfunction E_{SB}, we define

$$R_{\text{zonal}} = \frac{\displaystyle\sum_{k_x} \left| k_{k_x,0} \widehat{\psi}_{k_x,0} \right|^2}{\displaystyle\sum_{k_x,k_y} \left| k_{k_x,k_y} \widehat{\psi}_{k_x,k_y} \right|^2}, \tag{3.85}$$

where $k_{k_x,k_y} = \sqrt{(2\pi k_x/\Gamma)^2 + (\pi k_y)^2}$ is the non-dimensional radial wavenumber. As shown in Figure 3.19, R_{zonal} decreases as we increase Pr along the stability boundary.

Nevertheless, E_{SB} still has a small but nonzero zonal component at the point q_4 where the eigenfunction E_{PD} takes over, and zonal modes disappear completely. The instance of E_{SB} in figure 3.18 is at the large Prandtl number $\mathrm{Pr} = 10^5$, and hence the zonal modes do not carry much energy. In the Supplementary Material of [185], there is a video of E_{SB} with $\mathrm{Pr} = 100$ (Movie 6), in which case the presence of zonal modes is clear.

As we increase the Prandtl number past q_4, the green dashed line in Figure 3.18 appears to approach a limiting value $\mathrm{Ra} = 2.54 \times 10^7$, at which the SCRS is unstable for all Pr. To examine this statement, we consider the $\mathrm{Pr} \to \infty$ limit in which the governing equations (2.10) reduce to

$$\nabla^4 \psi = -\mathrm{Ra}\theta_x, \tag{3.86a}$$

$$\theta_t + \{\psi, \theta\} = \psi_x + \nabla^2 \theta. \tag{3.86b}$$

We analyse the linear stability of the SCRS for the reduced system (3.86) as in §3.4, and we find that it becomes unstable at $\mathrm{Ra} = 2.54 \times 10^7$, consistently with the results presented in Figure 3.18. It is clear from (3.86a) that $\widehat{\psi}_{0,k_y} = 0$ in the $\mathrm{Pr} \to \infty$ limit, again in agreement with the period doubling eigenfunction identified above. We conclude that $\mathrm{Pr} > 7 \times 10^5$ is a large enough Prandtl number such that the system exhibits the asymptotic behaviour of identically zero zonal modes at the SCRS instability.

The disparity between the thermal and viscous time-scales makes it very difficult to reproduce the behaviour close to q_4 using DNS. The linear stability analysis predicts that E_{PD} oscillates with a frequency of order 10 with respect to the thermal time-scale. It is, therefore, necessary to integrate the underlying equations over at least $\mathrm{Pr}/10 \approx 7 \times 10^4$ viscous time units to observe just one complete oscillation. At the required spatial resolution, it proved unfeasible to compute enough cycles to reliably observe the exponential growth or decay associated with the Hopf bifurcation.

3.6.2 Aspect Ratio Dependence

To study how the stability boundary at asymptotically large Prandtl numbers depends on the aspect ratio, we calculate the SCRS and consider its stability under (3.86) for different Γ. In Figure 3.20, we plot the stability boundary in the (Ra, Γ)-plane. The SCRS is particularly stable when $\Gamma = 1$, in which case it only loses stability once $\mathrm{Ra} = 1.01 \times 10^8$. As we increase Γ, the SCRS becomes unstable at much smaller Rayleigh numbers. In particular, when $\Gamma = 4$, it loses stability when $\mathrm{Ra} = 4.32 \times 10^4$.

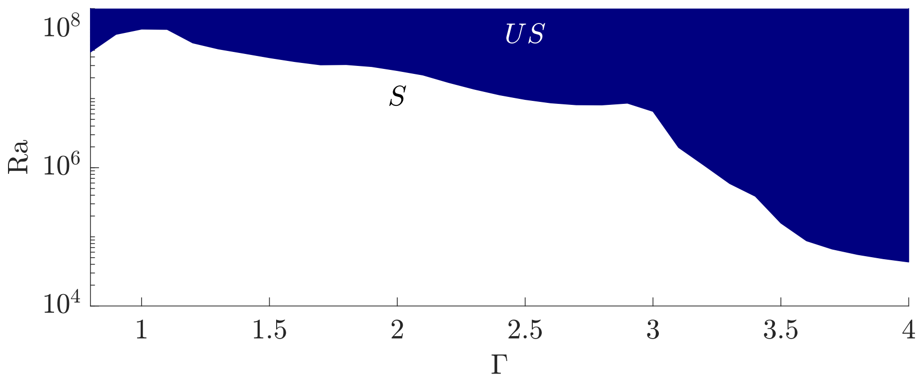

Figure 3.20: Stability boundary in the (Ra, Γ)-plane highlighting when the SCRS is stable (white, S) and unstable (blue, US), in the $\mathrm{Pr} \to \infty$ limit.

As we deal with a wide range of Rayleigh and aspect ratios in these calculations, one must be careful when deciding what resolution to use. We have set $N_x = \lfloor \sqrt{N\Gamma} \rfloor$ and $N_y = \lfloor \sqrt{N/\Gamma} \rfloor$. When Γ is small, the Rayleigh number at the stability boundary is large, meaning that we need many modes in y (large N_y) to resolve the thermal boundary layers. When Γ is small, the Rayleigh number at the stability boundary is small, but we need many modes in x (large N_x) to resolve the long and thin domain. We fix $N = 1.2 \times 10^5$ so that approximately an equal number of modes is used at each Γ.

3.7 Conclusions

This chapter concerns the onset of zonal modes in 2D RB convection. With aspect ratio $\Gamma = 2$ and increasing Rayleigh number, the first state to be excited as the pure conducting state loses stability consists of steady convection rolls, referred to in the text as the SCRS. The SCRS consists of only so-called even modes, and therefore contains no zonal modes. It becomes unstable to odd modes, which can contain zonal modes, as the Rayleigh number is increased. We determine the corresponding stability boundary in the $(\mathrm{Pr}, \mathrm{Ra})$-plane and identify corners and cusps in the boundary where qualitative changes occur to the most unstable eigenfunction. We observe three regions where the SCRS loses and subsequently regains stability as the Rayleigh number increases.

The excitation of odd modes is necessary, but not sufficient, for net zonal flow to exist. The possible qualitative behaviours in our system are delineated by the points q_1 and q_4 identified in the parameter space shown in Figure 3.2. Below and to the left of point q_1, the SCRS loses stability through a pitchfork bifurcation, and the resulting steady shear flow then itself becomes unstable and undergoes non-linear oscillations and bursts. In either case, the system produces a net zonal flow. On the other hand, to the right of point q_4, the dominant unstable odd eigenfunction preserves the reflection symmetry in the SCRS, and the zonal flow is identically zero.

Between points q_1 and q_4, the initial instability occurs through a Hopf bifurcation leading to oscillations in which the direction of the shear flow alternates [136]. Although the solution exhibits zonal flow instantaneously, the net (time-averaged) zonal flow is zero. As we shall see in Chapter 4, this range includes the case $\mathrm{Pr} = 30$ for which the initial Hopf bifurcation is the first step of a process that ultimately results in either persistent or intermittent zonal flow in the turbulent regime. We find that zonal modes become less prominent in the most unstable odd eigenfunction as the Prandtl number increases but are still present up to $\mathrm{Pr} = 7 \times 10^5$, when they abruptly switch off at point q_4.

As $\mathrm{Pr} \to 0$, the SCRS becomes unstable almost immediately as a new steady state, consisting of both even and odd modes, emerges in a pitchfork bifurcation. We observe a power-law $\delta\mathrm{Ra} \propto \mathrm{Pr}^2$ along the stability boundary. With a reduced six-model model, we can reproduce the same power-law. A more general weakly non-linear analysis yields a two-dimensional model which successfully predicts the power-law prefactor, as well as the non-linear relaxation oscillations and bursts observed in DNS at low Pr. We find that the oscillation amplitude and period grow without bound when formally setting the Prandtl number equal to zero.

We study how the sequence of bifurcations leading to the relaxation oscillations and bursts depend on Γ. There is excellent agreement between the weakly non-linear model and the full system for the critical Rayleigh number of the initial pitchfork bifurcation, but there is some disparity in the location of the subsequent Hopf bifurcation. This issue is resolved in §B.2, where we include $\mathcal{O}(\epsilon^2)$ corrections in the evolution of B. While these do not affect the leading order dynamics, they do affect the Rayleigh number at which the Hopf bifurcation occurs. The correction does provide a better fit with the full system, in particular at small Γ.

As we vary Γ, figure 3.16 shows that the $\delta\mathrm{Ra} \propto \mathrm{Pr}^2$ power-law along the stability boundary disappears abruptly as Γ increases through the value 2.37, meaning that for large aspect ratios the SCRS is stable until $\mathrm{Ra} \approx 5 \times 10^4$, even for very small Prandtl numbers. This observation poses the question of whether there exists a steady state close to $\mathrm{Ra} = \mathrm{Ra}_c$ when $\Gamma \geq 2.37$ even when the Prandtl number is formally set equal to zero.

At large Prandtl numbers, we observe a corner in the stability boundary at $q_4 = (\mathrm{Pr}, \mathrm{Ra}) = (7 \times 10^5, 2.54 \times 10^7)$, where the zonal modes in the most unstable eigenfunction switch off. As the Prandtl number increases beyond q_4, the stability boundary converges to the asymptotic value $\mathrm{Ra} = 2.54 \times 10^7$. This observation is consistent with formally taking the $\mathrm{Pr} \to \infty$ limit, which completely removes zonal modes. Our conclusion is that, with $\Gamma = 2$, no zonal modes are excited at the SCRS instability boundary for Prandtl numbers greater than 7×10^5. Instead, an unsteady state is produced consisting of both even and odd modes. It remains open to determine when this state, in turn, becomes susceptible to growing zonal perturbations. As we vary Γ, we observe that the large-Pr limiting value in the Rayleigh number along the stability boundary peaks at $\mathrm{Ra} = 1.01 \times 10^8$ when $\Gamma = 1$ and decreases monotonically as we increase or decrease Γ. When $\Gamma = 4$, the SCRS becomes unstable at the much lower Rayleigh number $\mathrm{Ra} = 4.32 \times 10^4$.

This chapter has generally focused on the aspect ratio $\Gamma = 2$. We have only varied Γ in the small and large Prandtl number limits and have observed remarkable changes in the stability of the SCRS when doing so. Likewise, for general Prandtl number, we can anticipate that the stability boundary structure and the excited solutions' properties also depend significantly on the value of Γ. In particular, if $\Gamma \geq 2^{4/3}\sqrt{1 + 2^{2/3}}$ then both odd and even modes become excited as Ra increases past Ra_c, and it is no longer clear that the odd/even mode decomposition which proves so convenient in our set-up is still able to give some insight.

In the following chapter, we use DNS to examine the dynamics at Rayleigh numbers beyond the critical Rayleigh number at which the SCRS becomes unstable.

Chapter 4

Zonal Flow Reversals

4.1 Synopsis

In chapter 3, we studied the stability of the SCRS and saw an example of how zonal flow can emerge in RB convection, despite buoyancy driving fluid motion only in the vertical direction.

In this chapter, we study the dynamics beyond the critical Rayleigh number at which the SCRS becomes unstable, using DNS. The flow is chaotic and ultimately becomes turbulent for large enough Rayleigh numbers. Our study unveils the presence of several bifurcations within the turbulent regime, some of which have previously been identified, such as in the works of Goluskin et al. [63] and Wang et. al. [175] that study a bistable regime characterised by shearing and non-shearing states. We present results over two orders of magnitude in the Prandtl number ($1 \leq \mathrm{Pr} \leq 10^2$), four orders of magnitude in the Rayleigh number ($10^4 \leq \mathrm{Ra} < 10^8$), and two width-to-height aspect ratios $\Gamma = 1$ and $\Gamma = 2$. The aim of this research is to study a hitherto unobserved phenomenon where the flow transitions between symmetric shearing states, giving rise to abrupt reversals of a very strong zonal flow.

A comprehensive literature review in §4.2 lays the foundation for the work presented in this chapter and in §4.3, we lay out the problem formulation.

In §4.4, we present results for the simulations conducted with $\Gamma = 2$. First, we give an overview indicating where in our considered parameter space zonal flow reversals occur. Subsequently, we narrow our focus to $\mathrm{Pr} = 30$, where we study the bifurcations leading to zonal flow reversals by analysing the evolution and probability density function (PDF) of the largest scale zonal mode. As we increase the Rayleigh number, the PDF first transitions from a Gaussian to a trimodal distribution, signifying the emergence of large-scale flow reversals where the flow transitions between three distinct states: two symmetric shearing states in which a zonal flow travels in opposite directions and one intermediate non-shearing state with no net zonal flow. Further increase in Ra leads to a transition from a trimodal to a unimodal PDF which demonstrates the disappearance of the zonal flow reversals.

Our analysis also reveals reversals at $\mathrm{Pr} = 1$. However, at this Prandtl number, the reversals arise without an intermediate non-shearing state and the zonal flow exhibits "bursting" behaviour, where the $\widehat{\psi}_{0,1}$ mode undergoes non-linear relaxation oscillations.

In §4.5, we consider $\Gamma = 1$ with $\mathrm{Pr} = 30$. Just like in the $\mathrm{Pr} = 1$, $\Gamma = 2$ case, the reversals here occur without an intermediate non-shearing state. They are also more frequent and occur at a smaller Rayleigh number, enabling us to use a smaller spatial resolution in our DNS and integrate further in time. We can therfore sample enough reversals to perform a comprehensive statistical analysis, which reveals that the mean waiting time between successive reversals grows exponentially with the Rayleigh number and that the waiting time itself is exponentially distributed.

Finally, we draw our conclusions in §4.6.

4.2 Literature Review

4.2.1 Bifurcations and Transitions in the Turbulent Regime

In this chapter, we study the transitions between symmetric shearing states and the bifurcations that lead to these within the turbulent regime of 2D RB convection. Bifurcation theory provides a useful tool to study the stability of stationary and temporally or spatially periodic flows, but less is known about bifurcations that occur when a control parameter is varied within the turbulent regime.

Prior research on bifurcations in turbulent flow includes the work of Stevens et al. [151]. They examined rotating 3D RB convection and discovered that the heat flux remains unaffected by the rotation rate until it reaches a critical level, beyond which the heat flux starts to rise, as if a supercritical bifurcation has occurred. Related studies have been conducted on Von Kármán swirling flows, i.e. flows generated in a cylindrical volume by the rotation of two co-axial disks, and instabilities are observed within the turbulent regime with both co-rotating [100] and counter-rotating disks [166]. In the context of the dynamo effect – the process by which a magnetic field is generated due to the flow of an electrically conducting fluid – an instability-induced symmetry break occurs in the turbulent regime. This broken symmetry, represented by the inversion of magnetic field direction ($\mathbf{B} \rightarrow -\mathbf{B}$), can statistically be reinstated if the system undergoes a secondary bifurcation. Such a bifurcation implies random transitions between turbulent states [50].

There are many other examples where bifurcations lead to transitions between distinct turbulent states. For example, Cadot et al. [27] studied the turbulent wake of a square-back body and showed that two different configurations for the mean flow can coexist and that the wake can display random switches between them. In 2D RB convection in a box geometry, random reversals of the large-scale circulation are observed in [34, 35, 153, 168]. Dallas et al. [40] saw zonal flow reversals in a Kolmogorov flow and explained these using a model based on the truncated Euler equation.

The variability in climate is often tied to transitions occurring between turbulent states. For example, the Kuroshio current is a major Northern Hemispheric western boundary current that transports an enormous amount of volume and heat/salt poleward. Transitions between the mean position of the Kuroshio current are therefore important for the global climate system [137]. Similarly, the mid-latitude atmosphere is dominated by westerly, nearly zonal flow. Occasionally, this flow is deflected poleward by blocking anticyclones that persist for 10 days or longer. Modelling the transitions between persistent and blocked zonal flow has become central to improving extended-range weather prediction [180].

4.2.2 Reversals in 2D RB Convection

There has been extensive research into reversals of the large-scale circulation (LSC) in 2D RB convection within an enclosed box geometry. These studies have examined scenarios with both no-slip [34, 35, 153] and free-slip boundary conditions [168] applied to the side walls.

Chandra et al. [34, 35] looked at 2D RB convection with no-slip sidewalls, and with $\mathrm{Pr} = \Gamma = 1$. They observed that the system undergoes a bifurcation at $\mathrm{Ra} = 2 \times 10^7$ which allows the LSC to reverse, and that the Nusselt number may be up to 6 times larger during a reversal than in the flow's quasi-stable phase. This result has been reproduced experimentally by Wang et al. [177], who measured heat flux in a quasi-2D set-up. Thermal energy is accumulated during the quasi-stable phase and released almost instantaneously during a reversal. Sugiyama et al. [153] considered a wider (Ra, Pr) parameter space with $\Gamma = 1$ and no-slip boundary conditions, both numerically and experimentally. They observed that reversals do not exist when Ra is too large, nor when Pr is too large or too small. In terms of the Prandtl number, they explained that the events leading up to a reversal are fed by plumes detaching from the plates' boundary layers. If Pr is too small, then the thermal energy carried by plumes is lost through thermal diffusion. Conversely, if Pr is too large, then the thermal boundary layer is nested in the kinematic boundary layer and thermal plumes are less likely to detach from the sidewalls.

The waiting time between successive reversals is expected to exhibit an exponential distribution [35, 125] as it does in cylindrical geometries [19]. Further to this, Ni et al. [119] have shown via experiment on a quasi-2D domain that the mean waiting time depends strongly on the width-to-height aspect ratio of the domain and has a stretched exponential Rayleigh number dependence, of the form $\exp(\mathrm{Ra}^{\alpha})$.

Verma et al. [168] examined a box geometry with $\Gamma \in \{1, 2\}$ and free-slip boundary conditions. At $\mathrm{Ra} = 10^8$, they observed reversals of the LSC for $\mathrm{Pr} \to \infty$ and for $\mathrm{Pr} = 40, 20$, but no reversals were seen for $\mathrm{Pr} < 20$.

Maity et al. [108, 109] have recently taken a novel data science approach to study the transitions of the LSC in a closed cubic cell with no-slip boundary conditions. With $\mathrm{Pr} = 0.7$ and $\mathrm{Ra} = 10^7$, their DNS has 3.84×10^6 degrees of freedom which they can reduce to only 2 collective variables that describe the transition dynamics.

4.3 Problem Formulation

Just as in chapter 3, the equations under consideration are the 2D Boussinesq equations of thermal convection (2.10). The imposed boundary conditions are periodic in x and free-slip in y. The domain is spanned by $x \in [0, L_x]$ and $y \in [0, L_y]$. We solve the dimensional governing equations using the DNS scheme described in §C.1 and non-dimensionalise our outputs using ΔT, the temperature difference between the top and bottom plates, L_y, the height of the domain and u_{rms}, the rms velocity of the flow field as the temperature, length and velocity scales, respectively. The rms velocity is defined as $u_{rms} = \sqrt{\langle \psi_x^2 + \psi_y^2 \rangle_{\boldsymbol{x},t}}$, where $\langle \cdot \rangle_{\boldsymbol{x},t}$ is the spatiotemporal average (2.14).

Using the Fourier-sine decomposition of the stream function in (2.13), it is clear that the largest scale mode, $\widehat{\psi}_{0,1}(t)$, defined as,

$$\widehat{\psi}_{0,1}(t) = \frac{2}{\Gamma} \int_0^{\Gamma} \int_0^1 \psi(x, y, t) \sin(\pi y)\, dy dx, \tag{4.1}$$

captures the main contribution to the zonal flow which is prominent in shearing states. The emergence of $\widehat{\psi}_{0,1}$ breaks the centre line symmetry $y = 1/2$, producing a net zonal flow across the layer. The symmetry can be broken either by $\widehat{\psi}_{0,1} > 0$ or $\widehat{\psi}_{0,1} < 0$, which correspond to two symmetric shearing states. In what follows,

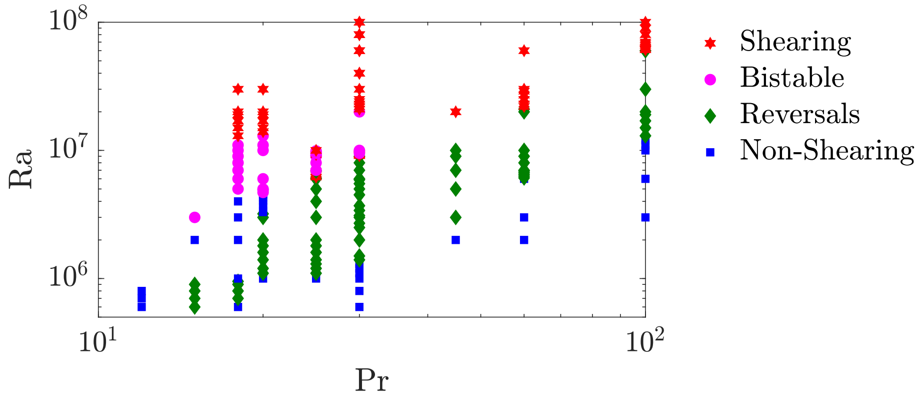

Figure 4.1: The (Pr, Ra)-plane with $\Gamma = 2$ highlighting when the flow is non-shearing (blue squares, ■), shearing (red hexagrams, ✶), reversing between these (green diamonds, ♦), or bistable (magenta circles, ●).

we report on transitions between shearing states for a selection of Prandtl numbers both with $\Gamma = 2$ and $\Gamma = 1$. A transition is recorded when the $\widehat{\psi}_{0,1}$ mode changes sign, highlighting that the zonal flow has reversed. The natures of the reversals are qualitatively different in the two aspect ratios considered.

4.4 Aspect Ratio 2

First, we focus on simulations of a domain with $\Gamma = 2$. In Figure 4.1 we plot the $(\mathrm{Pr}, \mathrm{Ra})$-plane with $\Gamma = 2$ highlighting when the flow demonstrates non-shearing, shearing, reversing, or bistable behaviour. To produce the results, we perform two DNS runs at every point. One with non-shearing initial conditions, and a second with shearing. This dual approach enabled us to identify scenarios where the flow demonstrates bistability. It is worth noting that the parameter space has been well mapped out by Goluskin et. al. [63] for $1 \leq \mathrm{Pr} \leq 10$. In Figure 4.1, we see that the bistable regime reported there shrinks with the Prandtl number as the reversing regime appears. We see reversals for $\mathrm{Pr} \geq 15$, and as the Prandtl number increases, both the upper and lower Rayleigh number bounds of the reversing regime increase, almost following a power-law relationship with Pr. Regardless, shearing convection appears to be the inevitable outcome for large enough Rayleigh numbers.

In the following section, we take a closer look at the $\mathrm{Pr} = 30$ case.

4.4.1 Reversals With $\mathrm{Pr} = 30$

Time series of $\widehat{\psi}_{0,1}$ normalised using the height, L_y, and rms velocity u_{rms}, and their corresponding probability density functions (PDFs) are displayed in Figure 4.2 for different values of Ra, but with Pr $= 30$ fixed. At Ra $= 2 \times 10^6$, the time series is turbulent with the amplitude of $\widehat{\psi}_{0,1}$ fluctuating randomly around the zero mean. This is an example of non-shearing convection as $\widehat{\psi}_{0,1}$ does not break the centreline symmetry in a statistical sense, i.e. $\langle \widehat{\psi}_{0,1} \rangle_t \approx 0$. The PDF of this time series (blue squares) is close to Gaussian.

At Ra $= 4.5 \times 10^6$, the PDF (green diamonds) has three distinct peaks. This follows the first bifurcation where the system transitions from an approximate Gaussian to a trimodal distribution with two symmetric maxima on either side of the peak around $\widehat{\psi}_{0,1} = 0$. This behaviour is related to the emergence of two symmetric shearing states, and the time series is characterised by abrupt and random transitions between these two states (i.e. $\langle \widehat{\psi}_{0,1} \rangle_t > 0$ and $\langle \widehat{\psi}_{0,1} \rangle_t < 0$) and the non-shearing state (i.e. $\langle \widehat{\psi}_{0,1} \rangle_t \approx 0$). While the system is in one of these shearing states, the centre line symmetry is broken, but over the entire time series, it is still true that $\langle \widehat{\psi}_{0,1} \rangle_t \approx 0$, meaning that the centreline symmetry is restored in a statistical sense. At this Rayleigh number, the system is mostly in the non-shearing state, and consequently, the peaks corresponding to the shearing states are smaller than the one at 0 in the PDF.

At Ra $= 6.4 \times 10^6$, we still have transitions between the three states and the PDF (green circles) is therefore trimodal. However, the system now spends longer inter-

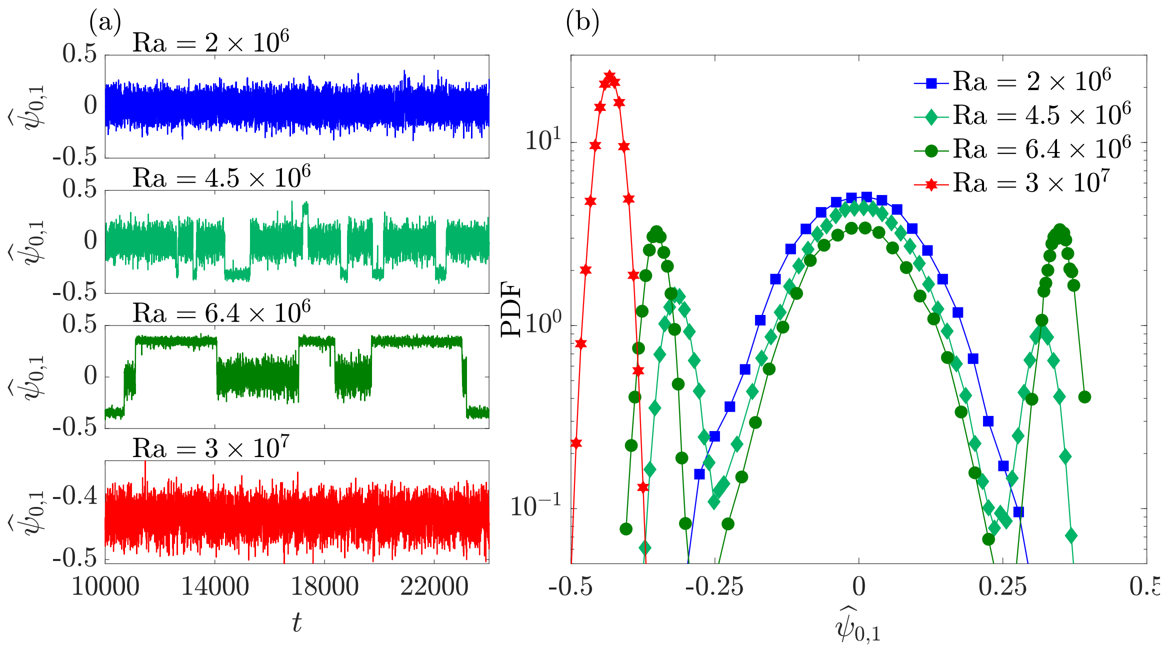

Figure 4.2: (a) Time series of the normalised large scale mode $\widehat{\psi}_{0,1}$ with $\Gamma = 2$ and (b) their corresponding PDFs for different values of Ra, and with Pr $= 30$ fixed.

vals in the symmetric shearing states, and the corresponding peaks in the PDF are therefore stronger compared with the peak at $\langle\widehat{\psi}_{0,1}\rangle_t \approx 0$. The peaks are also further apart, meaning that the zonal flow is more pronounced. As we continue increasing the Rayleigh number, the reversals become rarer until we get to a transition where no large-scale flow reversals are observed. This is seen in the case with $\mathrm{Ra} = 3 \times 10^7$ where the system was never observed to reverse, remaining stuck in one of the shearing states, and the corresponding PDF (red hexagrams) is unimodal with a non-zero mean. The PDF at $\mathrm{Ra} = 3\times10^7$ chooses either a positive or negative value of $\widehat{\psi}_{0,1}$ depending on the initial condition. This unimodal distribution indicates that ensemble averaging is not equivalent to time averaging and hence ergodicity is broken.

To understand the flow structure of the different states in Figure 4.3 we plot the normalised zonal flow profile, U, defined in (2.24) for the flow with $\mathrm{Ra} = 6.4\times10^6$. The light-coloured curves indicate instantaneous realisations of the zonal flow profile at different times. These times correspond to $\widehat{\psi}_{0,1} < 0$ for the light-blue curves, $\widehat{\psi}_{0,1} > 0$ for the light-red curves and $\widehat{\psi}_{0,1} \approx 0$ for the light-green curves. The thicker blue, red and green curves are the time averages of the corresponding light-coloured curves. The shear developed in the two shearing states is anti-symmetric about the centreline $y = 1/2$. When $\widehat{\psi}_{0,1} > 0$, we observe strong eastward and westward-moving flow in the upper half ($1/2 < y < 1$) and lower half ($0 < y < 1/2$) of the domain respectively. The opposite is true when $\widehat{\psi}_{0,1} < 0$, while there is no time-averaged zonal flow when $\widehat{\psi}_{0,1} \approx 0$ even though some instantaneous profiles can be considered having fairly

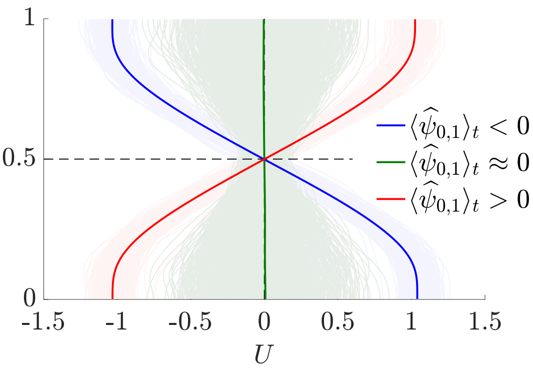

Figure 4.3: Time averaged zonal flow profiles when $\langle\widehat{\psi}_{0,1}\rangle_t < 0$ (blue), $\langle\widehat{\psi}_{0,1}\rangle_t \approx 0$ (green) and $\langle\widehat{\psi}_{0,1}\rangle_t > 0$ (red) for $\mathrm{Ra} = 6.4 \times 10^6$ and $\Gamma = 2$. The light-coloured curves represent instantaneous zonal flow profiles and the thicker curves are the averages of these.

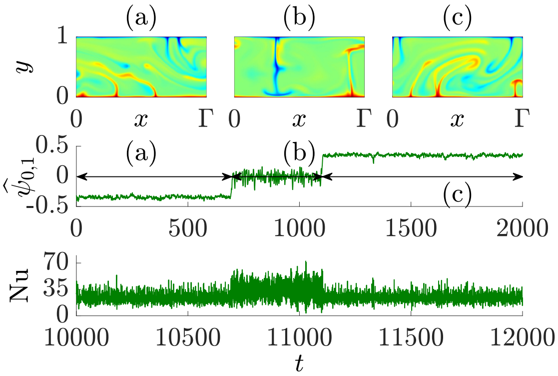

Figure 4.4: The top row of figures shows instantaneous realisations of the temperature field $T = (1 - y) + \theta$ for $\mathrm{Ra} = 6.4\times 10^6$ and $\Gamma = 2$. The middle and bottom rows have associated time series for $\widehat{\psi}_{0,1}$ and $\mathrm{Nu}(t)$ respectively, with times (a), (b) and (c) annotated.

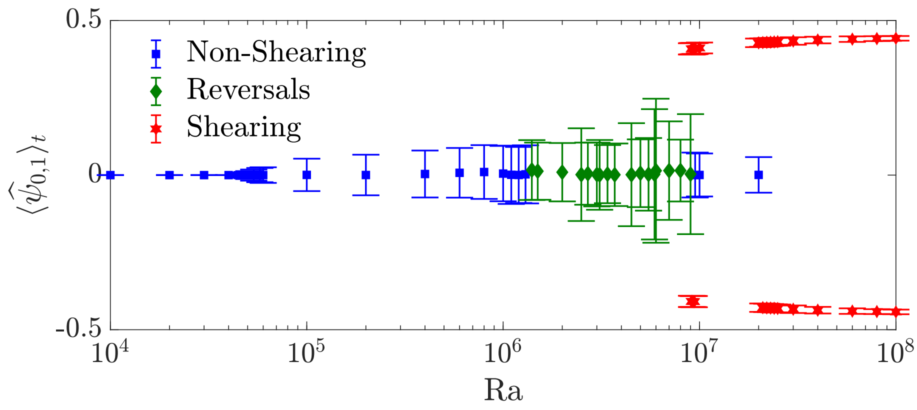

Figure 4.5: Bifurcation diagram of $\langle\widehat{\psi}_{0,1}\rangle_t$ versus Ra with the parameters $(\mathrm{Pr}, \Gamma) = (30, 2)$ fixed. Error bars show one standard deviation in the time series of $\widehat{\psi}_{0,1}$. The non-shearing, shearing and reversing regimes are highlighted by blue squares (■), red hexagrams (✸), and green diamonds (♦), respectively.

strong shear due to the fluctuations of $\widehat{\psi}_{0,1}$ around zero. The transition between the two shearing states captures the reversals of the large-scale zonal flow, which occur on a time scale much longer than the eddy turnover time, L_y/u_{rms}.

To quantify the instantaneous heat transport, we consider the time-dependent Nusselt number, $\mathrm{Nu}(t)$ defined in (2.19). Within the regime of zonal flow reversals, we observe a significant reduction in heat transport whilst the system is in a shearing state. Figure 4.4 shows instantaneous realisations of the temperature field $T = (1 - y) + \theta$ along with the time series of the normalised $\widehat{\psi}_{0,1}$ and Nu at $\mathrm{Ra} = 6.4 \times 10^6$. In shearing states such as (a) or (c), the shear prevents thermal plumes from traversing the domain, decreasing the convective heat transport. In non-shearing states such as (b), the shear is not strong enough to suppress thermal plumes and convection rolls are sustained, promoting convective heat transport. To further emphasise this observation, we observe that the time-averaged value of the Nusselt number is 34 when the flow is in a non-shearing state and only 24 in the shearing state at this Rayleigh number. Furthermore, we note that the time-averaged Nusselt number increases monotonically with the Rayleigh number, despite the system spending longer intervals in the Nusselt number suppressing shearing states within the regime of zonal flow reversals.

Figure 4.5 shows the bifurcation diagram of $\langle\widehat{\psi}_{0,1}\rangle_t$ for (Pr, Γ) = (30, 2) as we increase Ra. There are five bifurcations to note. Firstly, at $\mathrm{Ra} = 4.77 \times 10^4$, the SCRS becomes unstable, meaning that $\widehat{\psi}_{0,1}$ bifurcates from zero and starts oscillating around a zero mean. The oscillations are small and sinusoidal at first, but as we increase Ra, the amplitude increases and the oscillations become chaotic, eventually leading to a turbulent flow. Close to $\mathrm{Ra} = 1.4 \times 10^6$, there is a second bifurcation which designates the onset of zonal flow reversals. We start seeing transitions between two symmetric shearing states and a non-shearing state, which is characterised by the PDF of $\widehat{\psi}_{0,1}$ transitioning from a Gaussian to a trimodal distribution (see Figure 4.2 (b)). At $\mathrm{Ra} = 9.1 \times 10^6$ the zonal flow reversals stop, and we observe a very narrow range $\mathrm{Ra} \in [9.1 \times 10^6, 9.4 \times 10^6]$ where only the shearing state is stable. At $\mathrm{Ra} = 9.5 \times 10^6$, the non-shearing state regains stability, and the system is bistable until $\mathrm{Ra} = 2.1 \times 10^7$. For Rayleigh numbers beyond this point, only the shearing state is stable. At Rayleigh numbers within the shearing regime, we have conducted simulations with both shearing and non-shearing initial conditions to conclude that the intermediate non-shearing state between reversals is not stable and that ergodicity is truly broken.

4.4.2 Reversals With $\mathrm{Pr} = 1$

Zonal flow reversals are also observed in the $\mathrm{Pr} = 1$ case, but the preceding bifurcations and their nature are very different from the behaviour observed when $\mathrm{Pr} = 30$. Firstly, as discussed by Goluskin et. al. [63], there is a bistable regime where both shearing and non-shearing states are stable, but no transitions are seen. This regime is in $\mathrm{Ra} \in [1.5 \times 10^4, 1.33 \times 10^5]$ as seen in the bifurcation diagram in Figure 4.6 (a). The oscillations of $\widehat{\psi}_{0,1}$ in the shearing branch of the bistable regime gradually tran-

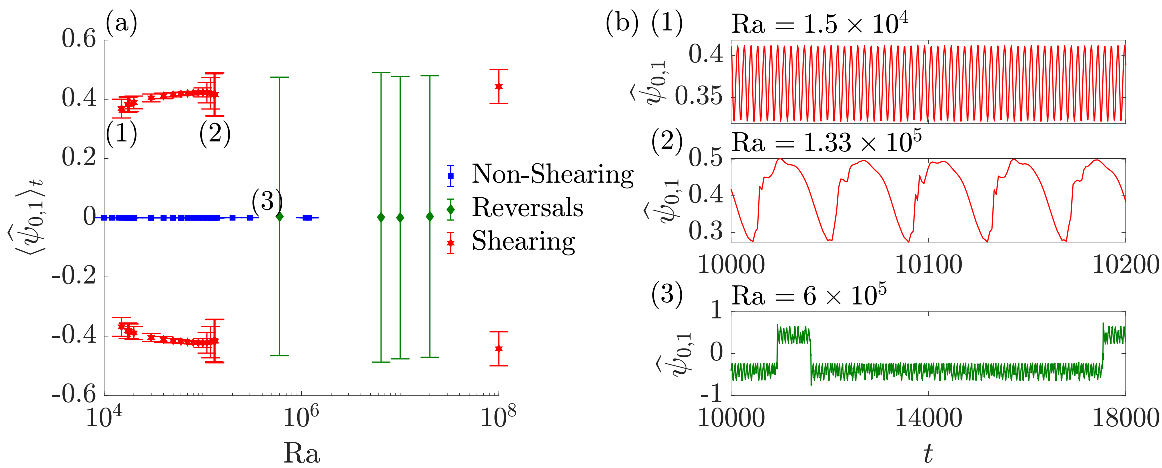

Figure 4.6: (a) Bifurcation diagram of $\langle\widehat{\psi}_{0,1}\rangle_t$ versus Ra with the parameters $(\mathrm{Pr}, \Gamma) = (1, 2)$ fixed. Error bars show one standard deviation in the time series of $\widehat{\psi}_{0,1}$. The non-shearing, shearing and reversing regimes are highlighted by blue squares (■), red hexagrams (✶), and green diamonds (♦), respectively. Three data points are highlighted and their corresponding time series are shown in (b).

sition from sinusoidal to relaxation oscillations (see Figure 4.6 (b)), where the zonal flow is “bursting”. At $\mathrm{Ra} = 1.34 \times 10^5$, the shearing state has disappeared, but the non-shearing state, which corresponds to the SCRS as studied in chapter 3 is stable until $\mathrm{Ra} = 1.15 \times 10^6$. Before this point, the shearing states have re-emerged, and at $\mathrm{Ra} = 6 \times 10^5$ we have an instance where the flow transitions between these. We observe a similar behaviour at $\mathrm{Ra} = 10^7$ and $\mathrm{Ra} = 2 \times 10^7$. In comparison with the $\mathrm{Pr} = 30$ case, we no longer have a non-shearing state meaning that the system displays abrupt zonal flow reversals as it transitions between the shearing states, as displayed in the Figure 4.6 (b) (3). The zonal flow reversals can therefore easily be missed unless $\widehat{\psi}_{1,0}$ is monitored explicitly. For example, there is no noticeable change in the kinetic energy in the system as the flow reverses. No reversals were observed at $\mathrm{Ra} = 10^8$.

4.5 Aspect Ratio 1

We have seen that the nature of the zonal flow reversals changes as we vary the Prandtl number when $\Gamma = 2$. In this section, we explore the behaviour when $\Gamma = 1$, keeping $\mathrm{Pr} = 30$ fixed. In §4.5.1 we study the qualitative features of the zonal flow reversals and note that they differ from those at $\Gamma = 2$ as they lack an intermediate non-shearing state. Moreover, they appear at a smaller Rayleigh number and occur more frequently, enabling us to use a smaller spatial resolution and integrate further in time. This allows us to sample enough reversals to perform a comprehensive statistical analysis in §4.5.2.

4.5.1 Reversals With $\mathrm{Pr} = 30$

Time series of $\widehat{\psi}_{0,1}$ normalised using the height and the rms velocity, and their corresponding probability density functions (PDFs) for different Ra are displayed in Figure 4.7 (a) and (b), respectively. At $\mathrm{Ra} = 10^5$, the time series is sinusoidal while the system is in a non-shearing state. At $\mathrm{Ra} = 6 \times 10^5$, two shearing states have emerged and the system transitions between these causing abrupt reversals of the zonal flow and a bimodal PDF (green diamonds). Note that in comparison with $\Gamma = 2$, there is no non-shearing state. At $\mathrm{Ra} = 9 \times 10^5$, zonal flow reversals persist but they have become rarer, as is clear from the time series. This is also clear from the PDFs, as they have a deeper minimum at $\widehat{\psi}_{0,1} = 0$ when $\mathrm{Ra} = 9 \times 10^5$ than when $\mathrm{Ra} = 6 \times 10^5$. At $\mathrm{Ra} = 3 \times 10^6$, no reversals were seen and the system is stuck on one of the shearing states. The PDF (red hexagrams) is unimodal with a non-zero mean.

Figure 4.8 shows the bifurcation diagram of $\langle\widehat{\psi}_{0,1}\rangle_t$ for (Pr, Γ) = (30, 1) as we increase Ra. Note that the SCRS which contains no odd or zonal modes in ψ is stable for Ra $< 10^5$. At Ra $= 10^5$, we witness the appearance of the first time-dependent non-shearing state, indicating that the SCRS has lost stability to odd and zonal modes. Consequently, $\widehat{\psi}_{0,1}$ evolves sinusoidally, as is clearly depicted in Figure 4.7 (a). This behaviour mirrors what we observe when $\Gamma = 2$ at Pr = 30, where the SCRS loses its stability at Ra $= 4.77 \times 10^4$. However, from this point, the bifurcation sequence differs markedly between the two aspect ratios. Firstly, the system is not chaotic until we enter the reversing regime at Ra $= 4.5 \times 10^5$. The two shearing states have already emerged at this point and we observe a first shearing regime at Ra $\in [2 \times 10^5, 3 \times 10^5]$[1], where the centreline symmetry and ergodicity has been broken. This regime is not bistable in the sense that no non-shearing states were observed. The centreline symmetry is restored in a statistical sense once we enter the reversing regime. The error bars in Figure 4.8 show one standard deviation in the time series of $\widehat{\psi}_{0,1}$ and within the reversing regime there is a clear trend of increasing error bars with Ra, meaning that the zonal flow is becoming increasingly pronounced. As we increase Ra further, eventually the centreline symmetry is broken again as we enter a second shearing regime at Ra $= 3 \times 10^6$.

[1] The regime bounds are only approximate.

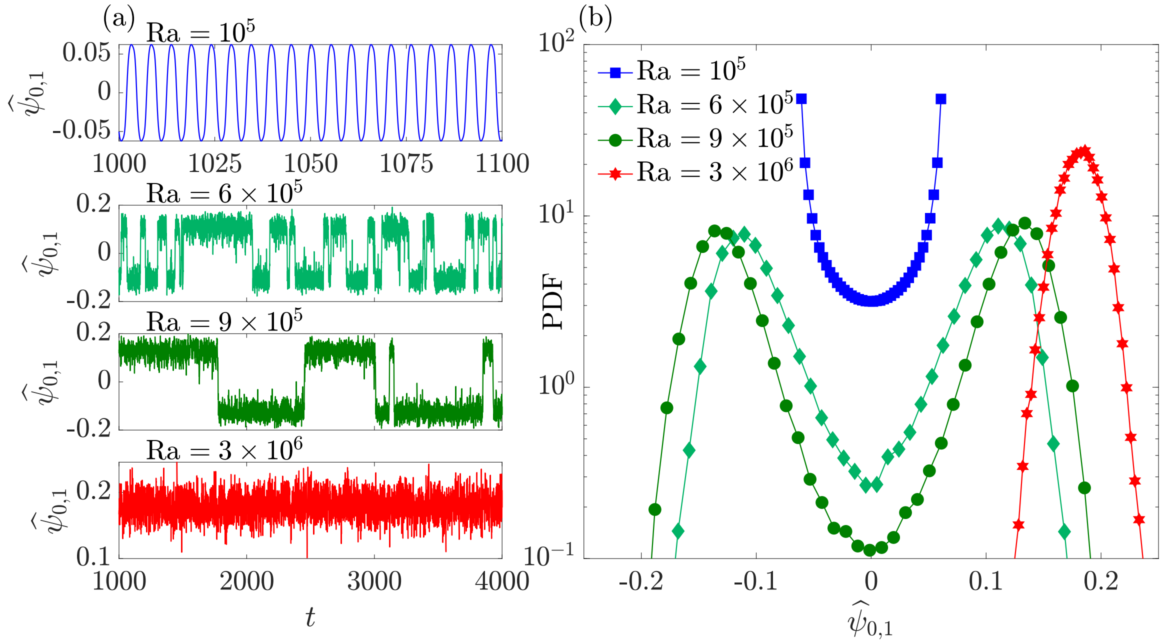

Figure 4.7: (a) Time series of the normalised large scale mode $\widehat{\psi}_{0,1}$ with $\Gamma = 1$ and (b) their corresponding PDFs for different values of Ra, and with Pr = 30 fixed.

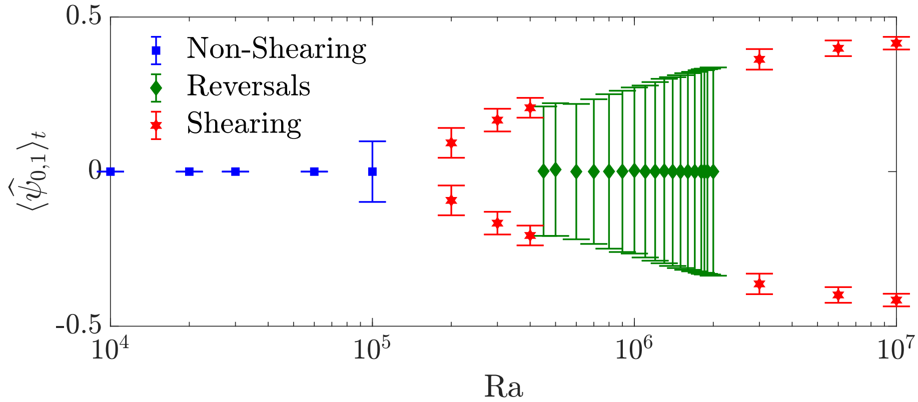

Figure 4.8: Bifurcation diagram of $\langle\widehat{\psi}_{0,1}\rangle_t$ versus Ra with the parameters $(\mathrm{Pr}, \Gamma) = (30, 1)$ fixed. Error bars show one standard deviation in the time series of $\widehat{\psi}_{0,1}$. The non-shearing, shearing and reversing regimes are highlighted by blue squares (■), red hexagrams (✱), and green diamonds (♦), respectively.

4.5.2 Statistical Analysis of Reversals

Our observations reveal that zonal flow reversals emerge at a lower Rayleigh number and with greater frequency when $\Gamma = 1$ relative to when $\Gamma = 2$. This observation enables us to solve the governing equations utilising a smaller spatial resolution. As a result, we can integrate further in time and gather sufficient reversals to execute a thorough statistical analysis. For instance, with parameters $\mathrm{Ra} = 4.5 \times 10^6$ and $\mathrm{Pr} = 30$, the system remains in a state an for average of 960 turnover times before transitioning when $\Gamma = 2$, and only 84 turnover times when $\Gamma = 1$. Further to this, every transition constitutes a reversal when $\Gamma = 1$. This is not the case when $\Gamma = 2$ due to the presence of the intermediate non-shearing state. Hence, conducting a statistical analysis is only computationally feasible when $\Gamma = 1$.

In Figure 4.9, we present a segment of the $\widehat{\psi}_{0,1}$ time series with $\Gamma = 1$, $\mathrm{Ra} = 6\times10^5$, and $\mathrm{Pr} = 30$. We define a reversal to have occurred when $\widehat{\psi}_{0,1}$ changes sign and reaches an amplitude of R, where R is the time-averaged value of $|\widehat{\psi}_{0,1}|$ across the entire time series, formulated as:

$$R = \langle|\widehat{\psi}_{0,1}|\rangle_t. \tag{4.2}$$

With this definition, we observe in Figure 4.9 that the time series starts in the positive shearing state and undergoes a reversal at $t = \tau_1$. At $t \approx \tau^*$, $\widehat{\psi}_{0,1}$ changes sign, but it does not return to the positive shearing state until $t = \tau_2$. In summary, Figure 4.9 illustrates four instances where $\widehat{\psi}_{0,1}$ changes sign, however, only two of these constitute complete reversals.

Now we have a clear definition of what a zonal flow reversal is, we define by τ_i the waiting time between successive reversals and

$$\overline{\tau} = \frac{1}{N}\sum_{i=1}^{N}\tau_i, \tag{4.3}$$

where N is the number of observed reversals for each Rayleigh number. In Figure 4.10, we plot $\overline{\tau}$ versus Ra and we observe a clear exponential behaviour, i.e.,

$$\log\left(\overline{\tau}\right) = \beta_0 + \beta_1 \mathrm{Ra}, \tag{4.4}$$

where we calculate $\beta_0 = 2.1$ and $\beta_1 = 4.1 \times 10^{-6}$ using a least square linear fit. The error bars indicate the standard error of the mean waiting times, i.e.,

$$\text{Error Bars} = \overline{\tau} \pm \frac{\sigma(\tau)}{\sqrt{N}}, \tag{4.5}$$

where $\sigma(\tau)$ is the empirical standard deviation of our observed waiting times, τ_i, for each Rayleigh number. The error bars grow with Ra predominately since the number of reversals observed, N, decreases with Ra. For example, at $\mathrm{Ra} = 2 \times 10^6$, we only observed 5 reversals over 2×10^5 turnover times, which took approximately 20 days to run on 8 3.7GHz CPUs. So while we can not rule out reversals at Rayleigh numbers greater than 2×10^6, it would take significant computational effort to observe them due to the exponential growth in the mean waiting time. Consequently,

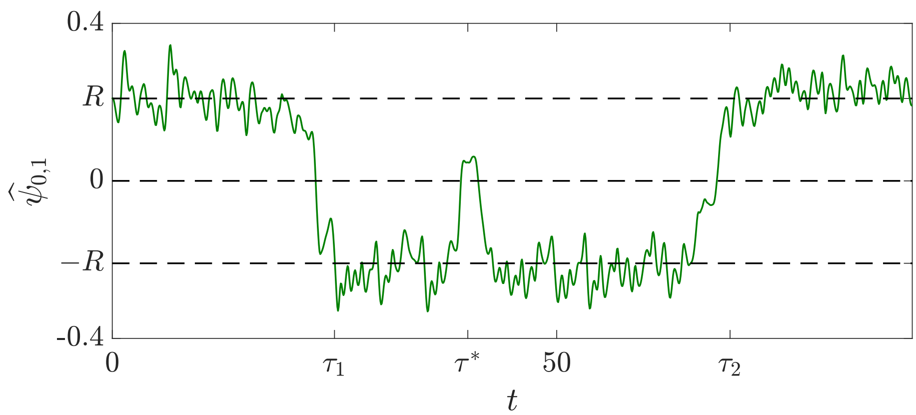

Figure 4.9: A segment of the $\widehat{\psi}_{0,1}$ time series with $\Gamma = 1$, $\mathrm{Ra} = 6 \times 10^5$, and $\mathrm{Pr} = 30$. The flow undergoes a reversal from the positive shearing state to the negative shearing state at $t = \tau_1$ and vice versa at $t = \tau_2$. At $t \approx \tau^*$, $\widehat{\psi}_{0,1}$ exhibits a transient change in sign. However, this instance is not classified as a flow reversal because $\widehat{\psi}_{0,1}$ does not reach an amplitude of R. Here, R, denotes the time-averaged value of $|\widehat{\psi}_{0,1}|$ across the entire time series, defined in (4.2).

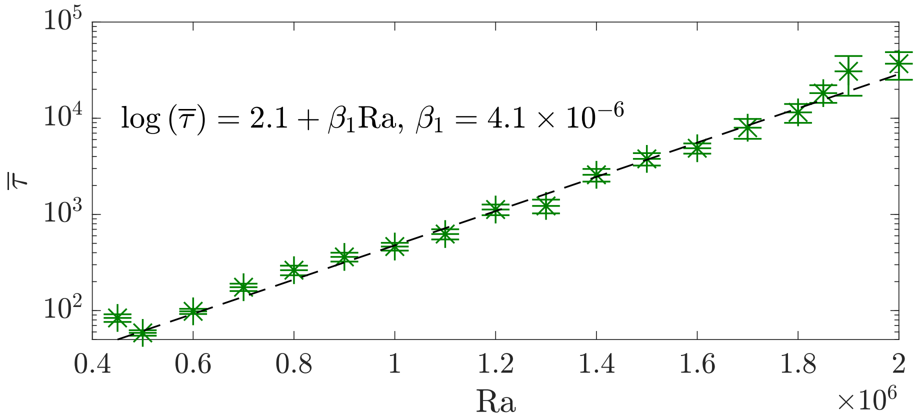

Figure 4.10: The mean reversal waiting time, $\overline{\tau}$, versus Ra. The error bars show the standard error, as defined in (4.5). The black dashed line is a fit to the data points of the form $\log(\overline{\tau}) = \beta_0 + \beta_1 \mathrm{Ra}$. We calculate $\beta_0 = 2.1$ and $\beta_1 = 4.1 \times 10^{-6}$ using a least squares linear fit.

To investigate the distribution of the waiting time, τ, we have simulated $3,316$ reversals with $\mathrm{Ra} = 6 \times 10^5$. The results are depicted in Figure 4.11. We plot the empirical cumulative distribution function, CDF_N, of $\tau - \tau_m$ where

$$\tau_m = \min_i (\tau_i), \tag{4.6}$$

estimates the minimum time required for a flow reversal to occur. Additionally, an exponential fit to the data is given by

$$\mathrm{CDF}(\tau - \tau_m) = 1 - \exp\left(-\frac{\tau - \tau_m}{\overline{\tau} - \tau_m}\right). \tag{4.7}$$

Figure 4.11 reveals a remarkable agreement between the empirical CDF and the fitted exponential function. This observation is further underscored by the figure's inset, which specifically illustrates the minor discrepancy between the two curves.

We also subjected our data to a Chi-Square goodness of fit test, with a null hypothesis that $\tau - \tau_m$ is exponentially distributed with mean $\overline{\tau} - \tau_m$. Bin widths were chosen in accordance with the Freedman–Diaconis rule [55]. Our test did not reject the null hypothesis, indicating that the difference between our data and the exponential distribution is not statistically significant. This conclusion was drawn at a 45% significance level, which is considerably higher than the conventional 5% threshold typically employed for the Chi-Square goodness of fit test. This higher percentage signifies a robust statistical agreement.

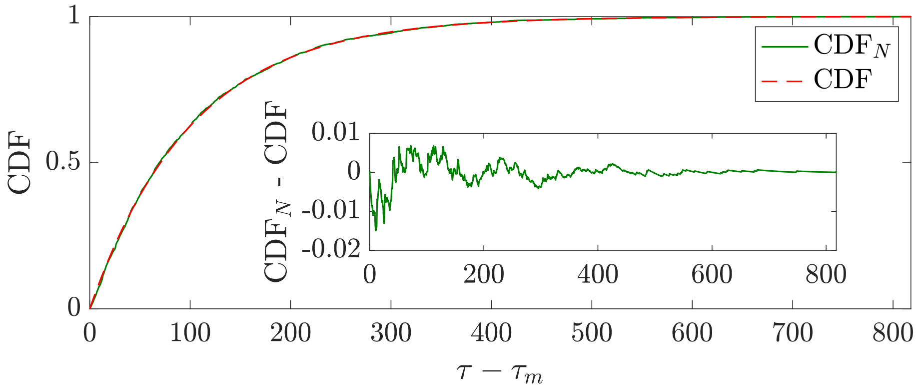

Figure 4.11: The empirical CDF of the waiting time between reversals (CDF_N, green solid line) with $\Gamma = 1$, $\mathrm{Ra} = 6 \times 10^5$, and $\mathrm{Pr} = 30$. It is fitted by an exponential distribution (CDF, red dashed line) as provided by (4.7). The inset shows the difference between the two.

4.6 Conclusions

In this chapter, we have studied the onset of zonal flow reversals within the turbulent regime of 2D RB convection. For width-to-height aspect ratio $\Gamma = 2$, we observe zonal flow reversals when $\mathrm{Pr} \geq 15$. As the Prandtl number increases, the bistable regime of non-shearing and shearing convection shrinks while the upper and lower Rayleigh number bounds of the flow reversing regime increase, almost following a power-law relationship with Pr. Regardless, shearing convection appears to be the inevitable outcome for large enough Rayleigh numbers.

We focus on the $\mathrm{Pr} = 30$ case and study the time series and PDF of the largest scale mode, $\widehat{\psi}_{0,1}$, which captures the main contribution to the zonal flow. As the Rayleigh number is increased, the PDF transitions first from a Gaussian to a trimodal distribution signifying the onset of reversals between two symmetric shearing states and a non-shearing state. The zonal flow reversals suppress the convective heat transfer as thermal plumes are not able to traverse the layer. Then, as Ra increases further, a second transition occurs from a trimodal to a one-sided unimodal distribution, where reversals cease to exist for the whole duration of the simulation.

Zonal flow reversals are also found at $\mathrm{Pr} = 1$. In this case, the system transitions abruptly between symmetric shearing states, without an intermediate non-shearing state. Here the zonal flow exhibits "bursting" behaviour, where the dominant mode undergoes non-linear relaxation oscillations.

With $\Gamma = 1$ and $\mathrm{Pr} = 30$, the zonal flow reversals also occur without an intermediate shearing state. Further to this, they are more frequent and occur at smaller Rayleigh numbers than with $\Gamma = 2$. This enables us to use a smaller spatial resolution in our DNS and integrate further in time. This way we sample enough reversals to perform a comprehensive statistical analysis, which reveals that the waiting time between successive reversals is exponentially distributed and its mean grows exponentially with the Rayleigh number, in agreement with flow reversals in other buoyancy-driven systems [18, 35, 119, 125].

While the shearing mechanism provides a high-level explanation of how zonal flow is sustained, a physical mechanism to explain zonal flow reversals is still an open question. The truncated Euler equations could be one way to theoretically understand these dynamics further like in [40, 144]. Nevertheless, it should be noted that the mechanism for zonal flow reversals must differ markedly from the one that has been used to explain reversals of the LSC in RB convection in a box geometry with no-slip walls, where the boundary layers [153] and vortex reconnection [35] play a crucial role for reversals. With free-slip walls, it has been suggested that the nonlinearity in the temperature equation plays a vital role in the reversals of the LSC [168]. However, buoyancy only does work on the vertical flow, meaning that the dynamics of $\widehat{\psi}_{0,1}$ partially decouples from the temperature equation since $\partial_x(\widehat{\theta}_{0,1}(t)\sin(\pi y)) = 0$.

Chapter 5

Quasi-Two-Dimensional Rayleigh-Bénard Convection

5.1 Synopsis

In this chapter, we will generalise our analysis from the previously studied two-dimensional flow to a quasi-two-dimensional (Q2D) flow. Here, we introduce a third spatial direction, denoted as z. The central question we seek to answer is: how narrow must the layer be in z to render the flow truly two-dimensional?

Our spatial domain is labelled Q2D since we only consider infinitesimal z dependant perturbations, thereby introducing no additional nonlinearities into the governing equations. Under these circumstances, it is sufficient to consider individual modes in z, and subsequently vary the domain size, $\Gamma_z = L_z/L_y$, to investigate how different wavenumbers, q, evolve over varying 2D background flows.

We fix the parameters $(\mathrm{Ra}, \mathrm{Pr}, \Gamma_x) = (10^7, 30, 2)$ so that the 2D background flow, governed by the now familiar system (2.10), is within the bistable regime of shearing and non-shearing convection. Our focus will be to analyse how three-dimensional (3D) perturbations grow over the SCRS, shearing, and non-shearing states.

A literature review of previous relevant studies in §5.2, lays the foundation for the work presented in this chapter. In §5.3, we derive the governing equations for the 3D perturbations. These equations are then solved using DNS, which are validated in §5.4 through a comparison with an independent eigenvalue solver.

The growth rate of 3D perturbations over different background flows is studied in 5.5. Our findings suggest that the critical wavenumber, q_c, where 3D perturbations start growing is similar in both the shearing and non-shearing states, but markedly smaller in the SCRS. We study the energy balances of the 3D perturbations and discover that the mechanisms driving the perturbations in the shearing and non-shearing states contrast significantly with those driving the perturbations in the SCRS. We further analyse the impact of kinetic energy, zonal flow, and time dependence in the background flow on the growth rate and q_c. In general, the effects are modest, even with significant changes to the background flow, but we note that a more distinct zonal flow seems to increase the growth rate, especially at smaller wavenumbers.

Finally, we draw our conclusions in §5.6.

5.2 Literature Review

Flows in Q2D layers of height significantly smaller than the lengths of the other two directions are important, due to their similarity to atmospheric flows. In such flows, the pressure scale height is hundreds or thousands of times smaller than the turbulent horizontal large-scale motions [83]. For this reason, such layers have garnered substantial interest from both experimental [48, 104, 139, 146, 147, 155] and theoretical [8, 26, 33, 58, 118, 126, 174] research groups.

One of the pivotal findings in this field is the observation of a bidirectional cascade of kinetic energy, reported, for instance, by Celani et al. [33]. Celani et al. examined the Navier-Stokes equations forced at a length scale l_f and identified a significant bidirectional cascade when the ratio $L_z/l_f \approx 1/4$, where L_z represents the domain length in its narrowest direction. This work was later built upon by Benavides et al.[8], who studied the Navier-Stokes equations in a thin layer with only one mode in the narrow z direction. The application of such a severe Galerkin truncation in the narrow direction enabled Benavides et al. to conduct a systematic exploration of the kinetic energy cascade while adjusting the ratio L_z/l_f. They observed an abrupt transition in the cascade, moving from being forward unidirectional, to bidirectional, and finally to a unidirectional inverse cascade as the ratio L_z/l_f was reduced.

Parker et al. [126] adopted a similar Galerkin truncation when they studied infinitesimal 3D perturbations over a 2D background flow in the breaking of internal gravity waves in the abyssal ocean. They found that 3D perturbations grow significantly faster than 2D ones.

Wang et al. [174] recently reported results on RB convection with one narrow direction with the parameter values $(\mathrm{Ra}, \mathrm{Pr}, \Gamma_x) = (10^8, 10, 2)$ while varying $\Gamma_z \ll 1$. They observed a hysteresis-like behaviour between shearing and non-shearing states in the (x, y)-plane (as the coordinate system is defined in this thesis).

5.3 Problem Formulation

The governing equations are now the 3D Boussinesq equations of thermal convection

$$\nabla \cdot \boldsymbol{u} = 0, \tag{5.1a}$$
$$\boldsymbol{u}_t + (\boldsymbol{u} \cdot \nabla)\boldsymbol{u} = -\nabla p + \mathrm{RaPr}\theta \mathbf{e}_y + \mathrm{Pr}\nabla^2 \boldsymbol{u}, \tag{5.1b}$$
$$\theta_t + (\boldsymbol{u} \cdot \nabla)\theta = v + \nabla^2 \theta, \tag{5.1c}$$

where $\boldsymbol{u} = (u, v, w)$. The equations have again been non-dimensionalised using L_y, the height of the domain, ΔT, the temperature difference between the top and bottom plates, and L_y^2/κ as the time scale, where κ is the thermal diffusivity of the fluid. The domain is spanned by $x \in [0, \Gamma_x]$, $y \in [0, 1]$, $z \in [0, \Gamma_z]$ and the boundary conditions are periodic in x and free-slip in y and z.

We start with a base state that is independent of z, with

$$\overline{\boldsymbol{u}} = \begin{pmatrix} -\psi_y(x, y, t) \\ \psi_x(x, y, t) \\ 0 \end{pmatrix}, \quad p = \overline{p}(x, y, t), \quad \theta = \overline{\theta}(x, y, t). \tag{5.2}$$

The base state satisfies the by now familiar system

$$\nabla^2 \psi_t + \{\psi, \nabla^2 \psi\} = \mathrm{RaPr}\theta_x + \mathrm{Pr}\nabla^4 \psi, \tag{5.3a}$$
$$\overline{\theta}_t + \{\psi, \overline{\theta}\} = \psi_x + \nabla^2 \overline{\theta}, \tag{5.3b}$$

with periodic boundary conditions in x and free-slip in y.

We now perturb (5.2) with an infinitesimal (now 3D) perturbation

$$\boldsymbol{u} = \overline{\boldsymbol{u}} + \begin{pmatrix} u^\perp \cos(qz) \\ v^\perp \cos(qz) \\ w^\perp \sin(qz) \end{pmatrix}, \quad p = \overline{p} + p^\perp \cos(qz), \quad \theta = \overline{\theta} + \theta^\perp \cos(qz), \tag{5.4}$$

where the "$\perp$" variables are functions of x, y, and t and

$$q = \frac{k_z \pi}{\Gamma_z}, \quad k_z \in \mathbb{Z}, \tag{5.5}$$

to satisfy the free-slip boundary conditions on z. Since the background fields are purely 2D and the perturbation is infinitesimal, there is no nonlinearity in the z direction, and therefore it is sufficient to consider an individual mode in z ($k_z = 1$) without loss of generality, and then vary the domain size, Γ_z, to investigate how different wavenumbers, q, grow over the background fields.

The components of the $\perp$ momentum equation are the following linear PDEs with time dependant coefficients that depend on the background flow $(\psi, \overline{\theta})$:

$$u_t^\perp + \{\psi, u^\perp\} - u^\perp\psi_{xy} - v^\perp\psi_{yy} = -p_x^\perp + \mathrm{Pr}\left(\nabla^2 - q^2\right)u^\perp, \tag{5.6a}$$

$$v_t^\perp + \{\psi, v^\perp\} + u^\perp\psi_{xx} + v^\perp\psi_{xy} = -p_y^\perp + \mathrm{RaPr}\theta^\perp + \mathrm{Pr}\left(\nabla^2 - q^2\right)v^\perp, \tag{5.6b}$$

$$w_t^\perp + \{\psi, w^\perp\} = qp^\perp + \mathrm{Pr}\left(\nabla^2 - q^2\right)w^\perp. \tag{5.6c}$$

We use (5.6c) to eliminate $p^\perp$, and the incompressibility condition

$$u_x^\perp + v_y^\perp = -qw^\perp \tag{5.7}$$

to eliminate $w^\perp$ and thus obtain

$$u_t^\perp + \{\psi, u^\perp\} - u^\perp\psi_{xy} - v^\perp\psi_{yy} - \left(F_t + \{\psi, F\}\right)_x = \mathrm{Pr}\left(\nabla^2 - q^2\right)\left[u^\perp - F_x\right], \tag{5.8a}$$

$$v_t^\perp + \{\psi, v^\perp\} + u^\perp\psi_{xx} + v^\perp\psi_{xy} - \left(F_t + \{\psi, F\}\right)_y = \mathrm{RaPr}\theta^\perp + \mathrm{Pr}\left(\nabla^2 - q^2\right)\left[v^\perp - F_y\right], \tag{5.8b}$$

where

$$F = \frac{1}{q^2}\left(u_x^\perp + v_y^\perp\right) = -\frac{w^\perp}{q}. \tag{5.9}$$

We now define

$$U = u^\perp - F_x, \quad V = v^\perp - F_y, \tag{5.10}$$

which are proportional to the x- and y-components of the vorticity in the $\perp$ field. Writing (5.8) in terms of U and W yields

$$U_t + \{\psi, U\} - \mathrm{Pr}(\nabla^2 - q^2)U = \psi_{xy}U + \psi_{yy}V + \nabla^2\psi F_y \tag{5.11a}$$

$$V_t + \{\psi, V\} - \mathrm{Pr}(\nabla^2 - q^2)V = \mathrm{PrRa}\theta^\perp - \psi_{xx}U - \psi_{xy}V - \nabla^2\psi F_x, \tag{5.11b}$$

where

$$U_x + V_y = -(\nabla^2 - q^2)F. \tag{5.12}$$

The 3D temperature perturbation $\theta^\perp$ satisfies

$$\begin{aligned}\theta_t^\perp + \{\psi, \theta^\perp\} - (\nabla^2 - q^2)\theta^\perp &= -\overline{\theta}_x u^\perp - \left(\overline{\theta}_y - 1\right)v^\perp \\ &= -\overline{\theta}_x\left(U + F_x\right) - \left(\overline{\theta}_y - 1\right)\left(V + F_y\right).\end{aligned} \tag{5.13}$$

To ensure that the periodic boundary conditions in x and free-slip boundary conditions in y are satisfied, we use a Fourier-sine basis for the expansion of V and $\theta^{\perp}$, while U is expanded using a Fourier-cosine basis, viz.

$$U(x,y,t) = \sum_{k_y=0}^{N_y} \sum_{k_x=-N_x/2}^{N_x/2} \widehat{U}_{k_x,k_z}(t) e^{i2\pi k_x x/\Gamma_x} \cos(\pi k_y y), \quad \widehat{U}_{k_x,k_y} = \widehat{U}^*_{-k_x,k_y}, \tag{5.14a}$$

$$V(x,y,t) = \sum_{k_y=1}^{N_y} \sum_{k_x=-N_x/2}^{N_x/2} \widehat{V}_{k_x,k_z}(t) e^{i2\pi k_x x/\Gamma_x} \sin(\pi k_y y), \quad \widehat{V}_{k_x,k_y} = \widehat{V}^*_{-k_x,k_y}. \tag{5.14b}$$

The expansions in (5.14) restrict our fields to real values, which is necessary to satisfy the assumed free-slip boundary conditions in z.

5.4 DNS Validation

To validate the DNS that solves equations (5.11) and (5.13), we construct an eigenvalue problem for the growth rate, σ, of U, V, and $\theta^{\perp}$ over a steady background flow. We pick solutions of (5.3) in which ψ and $\overline{\theta}$ are constant in time, set

$$U(x,y,t) = e^{\sigma t}\widetilde{U}(x,y), \quad V(x,y,t) = e^{\sigma t}\widetilde{V}(x,y), \quad \theta^{\perp}(x,y,t) = e^{\sigma t}\widetilde{\theta}^{\perp}(x,y). \tag{5.15}$$

and solve for the linear growth rate σ. Details of the construction of the eigenvalue problem are found in Appendix D. It is solved independently from the DNS, and the results derived from both approaches are juxtaposed for comparison.

Figure 5.1 shows the real part, $\mathcal{R}(\sigma)$, and imaginary part, $\mathcal{I}(\sigma)$, of the eigenvalue σ with largest real part. The background flow, $(\psi, \overline{\theta})$, is the SCRS with parameter values $(\mathrm{Ra}, \mathrm{Pr}, \Gamma_x) = (10^3, 1, 2)$. We know from the stability analysis in chapter 3

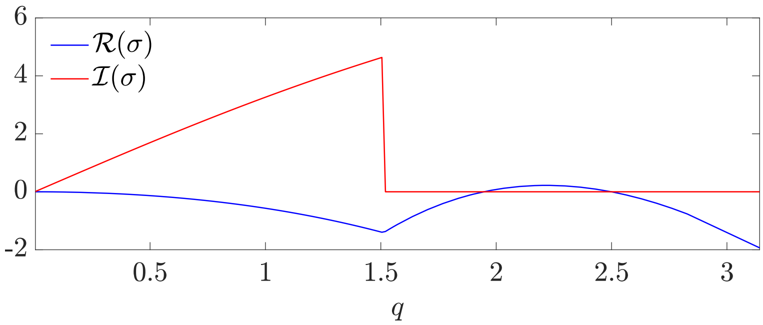

Figure 5.1: The real part, $\mathcal{R}(\sigma)$, and imaginary part, $\mathcal{I}(\sigma)$, of the eigenvalue σ with largest real part. The background flow, $(\psi, \overline{\theta})$, is the SCRS with parameter values $(\mathrm{Ra}, \mathrm{Pr}, \Gamma_x) = (10^3, 1, 2)$.

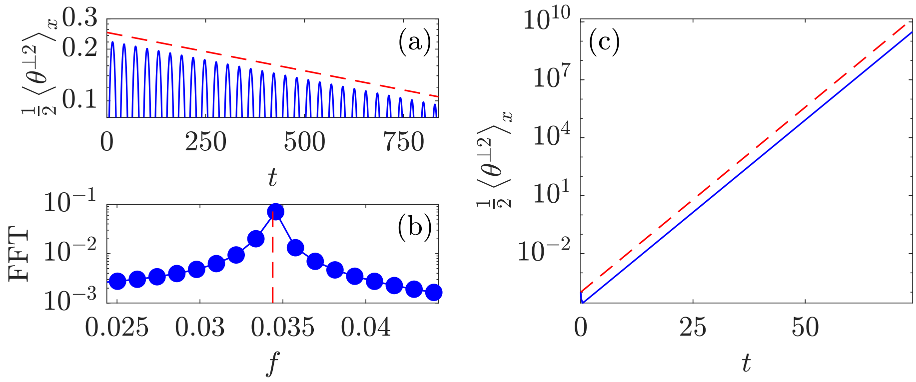

Figure 5.2: (a) Time series of $\langle \theta^{\perp 2} \rangle_{\boldsymbol{x}}/2$ from the DNS in blue with parameter values $(\mathrm{Ra}, \mathrm{Pr}, \Gamma_x, q) = (10^3, 1, 2, \pi/100)$. The red dashed line shows the decay rate predicted by the eigenvalue solver. (b) The Fourier transform of the time series in (a). The red dashed line is the oscillation frequency predicted by the eigenvalue solver. (c) Time series of $\langle \theta^{\perp 2} \rangle_{\boldsymbol{x}}/2$ from the DNS in blue with parameter values $(\mathrm{Ra}, \mathrm{Pr}, \Gamma_x, q) = (10^3, 1, 2, 2.12)$. The red dashed line is the growth rate predicted by the eigenvalue solver.

that the SCRS is stable to purely 2D ($q = 0$) perturbations at these parameter values; see Figure 3.2. However, Figure 5.1 demonstrates that the SCRS is unstable to 3D perturbations when $q \in [1.97, 2.50]$. We also note that σ is purely real for $q \geq 1.52$ and complex-valued otherwise. The abrupt transition at $q \approx 1.52$ occurs as a complex conjugate pair of eigenvalues, whose real parts increase with q, cross a purely real eigenvalue.

Figure 5.2 compares the DNS results with the solution of the eigenvalue problem for two values of q: one where σ is complex-valued and another where σ is real. In Figure 5.2 (a), the full blue line represents the time series of $\langle \theta^{\perp 2} \rangle_{\boldsymbol{x}}/2$ obtained from the DNS, with parameter values $(\mathrm{Ra}, \mathrm{Pr}, \Gamma_x, q) = (10^3, 1, 2, \pi/100)$. The red dashed line corresponds to the decay rate predicted by the solution of the eigenvalue problem, specifically $2\mathcal{R}(\sigma)$. Since σ is complex-valued for this q value, in Figure 5.2 (b) we display the Fourier transform of the time series in blue, while the red dashed line represents the oscillation frequency predicted by the eigenvalue solver, denoted as $\mathcal{I}(\sigma)/\pi$. Figure 5.2 (c) shows $\langle \theta^{\perp 2} \rangle_{\boldsymbol{x}}/2$ from DNS in blue, with parameter values $(\mathrm{Ra}, \mathrm{Pr}, \Gamma_x, q) = (10^3, 1, 2, 2.12)$, while the red line represents the growth rate predicted by the eigenvalue solver. For this q value, σ is real, indicating the absence of oscillations. In all cases, there is excellent agreement between our DNS and the eigenvalue solver, instilling confidence in the correctness of our DNS setup.

5.5 Perturbations Over Different Fields

5.5.1 Growth Rate and Critical Wavenumber

In this section, we fix the parameter values $(\mathrm{Ra}, \mathrm{Pr}, \Gamma_x) = (10^7, 30, 2)$ so that the background flow is within the bistable regime of shearing and non-shearing convection, and we analyse how 3D perturbations grow over four different background flows, namely: The shearing state (S), non-shearing state (NS), SCRS and the static conductive state (CS). Even though the SCRS and CS are highly unstable at these parameters, they are nonetheless steady solutions to (5.3).

For each background flow, we are interested in the smallest $q = q_c$ at which 3D perturbations decay, i.e. where the real part of the eigenvalue with the largest growth rate, $\mathcal{R}(\sigma)$, transitions from negative to positive. By (5.5), this gives us the largest Γ_z at which the flow remains purely two-dimensional. We now argue that we expect such a q to exist for the background flows considered.

First note that, as $q \to \infty$, the system (5.11) and (5.13) reduces to an eigenvalue problem represented by a matrix with $-\mathrm{Pr}q^2$ and $-q^2$ along the diagonal. So, to leading order as $q \to \infty$, $\sigma \sim -\min(\mathrm{Pr}, 1)q^2 = -q^2 < 0$. A more detailed derivation of this fact is provided in §D.2 of Appendix D. We also expect that $\mathcal{R}(\sigma) > 0$ when $q = 0$. This is evident for the CS which is unstable to 2D perturbations by Rayleigh [134], and so is the SCRS as shown in chapter 3. The shearing and non-shearing states are turbulent, so we expect them to have positive Lyapunov exponents when subject to 2D disturbances. So, if this holds, there exists at least one q_c where $\mathcal{R}(\sigma) = 0$.

In practice, we find that there is only one such q_c, that $\mathcal{R}(\sigma)$ is monotonic in q close to q_c, and that $\mathcal{R}(\sigma) > 0$ when $q < q_c$ and $\mathcal{R}(\sigma) \leq 0$ otherwise. This observation renders our problem of finding q_c to a binary search. We start with $q = q_1$ and find $\mathcal{R}(\sigma)$. If $\mathcal{R}(\sigma) > 0$ or $\mathcal{R}(\sigma) < 0$, we increase or decrease q by a factor of two, respectively, until $\mathcal{R}(\sigma)$ has changed sign. At this point, we have an upper and lower bound for q_c which is improved via a binary search.

This is all done within one DNS run, and an example of this process is seen in Figure 5.3 which shows the times series of $\langle \theta^{\perp 2} \rangle_{\boldsymbol{x}}/2$ over a shearing background flow. The value of q is adjusted once $\langle \theta^{\perp 2} \rangle_{\boldsymbol{x}}/2$ has increased or decreased by a factor of 10^{10}. The red dashed lines show the growth rate, which is estimated via a linear fit at each q. The time series starts at $q = 5\pi$, a value at which the 3D perturbations are very unstable. Subsequently, q is increased to 10π and 20π before an upper bound for q_c is found and the binary search can start. The time series ends at $q = 50.56$, at which point the upper and lower bounds for q_c are 51.05 and 50.56, respectively.

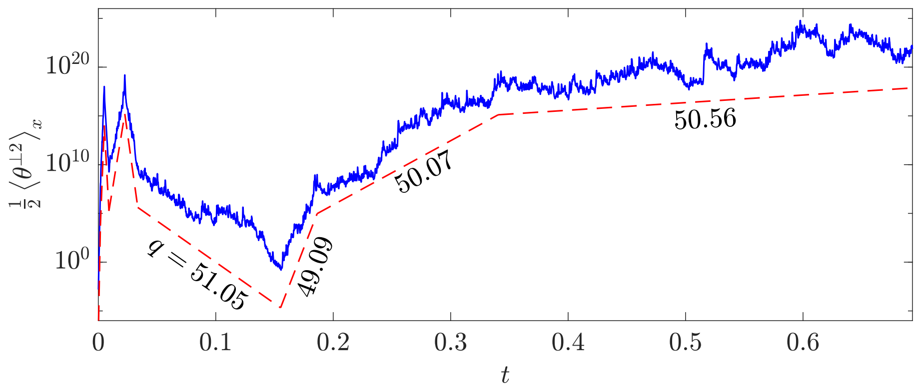

Figure 5.3: Time series of $\langle\theta^{\perp 2}\rangle_{\boldsymbol{x}}/2$ over a shearing background flow as we progressively change q. The red dashed lines show the growth rate, which is estimated via a linear fit at each q.

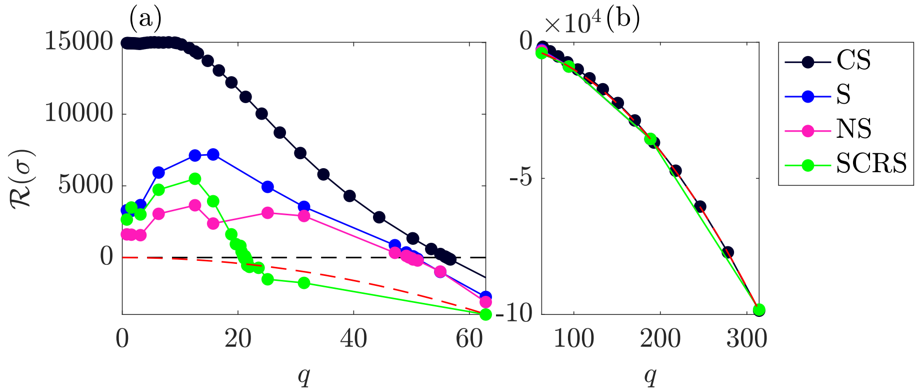

Figure 5.4: The growth rate, $\mathcal{R}(\sigma)$, at different values of q over four different background flows, colour coded in the legend. The red dashed line shows $\mathcal{R}(\sigma) = -q^2$. The approximate values of q_c and $q_{\max}$ are listed in Table 5.1.

In Figure 5.4 we plot the growth rate versus q over the four different background flows described above. The red dashed line shows $\mathcal{R}(\sigma) = -q^2$. The approximate value of q_c, the value of q at which the growth rate peaks ($q_{\max}$), and the associated maximum growth rate ($\mathcal{R}(\sigma_{\max})$) for each background flow are listed in Table 5.1. Interestingly, the q_c values for the shearing and non-shearing states are very close, meaning that that flow becomes two-dimensional at approximately the same value of Γ_z. The value q_c for the SCRS is significantly smaller implying that the SCRS is less likely to be susceptible to 3D perturbations. For $q < q_c$, the growth rate from the shearing state is larger than that from the non-shearing state, indicating that zonal flow has a destabilising effect on the perturbations at these wavenumbers. When $q > 100$, the growth rate for all background flows follows $\sigma \sim -q^2$, as seen in Figure 5.4 (b).

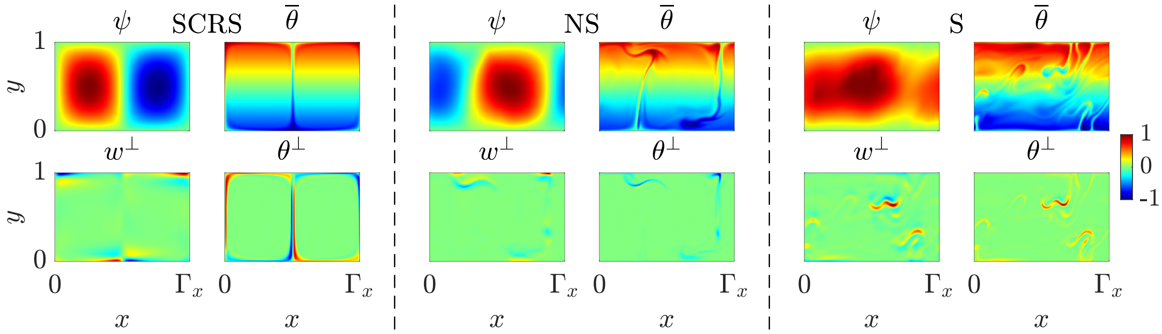

Figure 5.5: Snapshots of ψ, $\overline{\theta}$, $w^{\perp}$, and $\theta^{\perp}$ over the SCRS, non-shearing (NS), and shearing (S) states. Each field is normalised with its maximum absolute value.

In Figure 5.5 we show snapshots of ψ, $\overline{\theta}$, $w^{\perp}$, and $\theta^{\perp}$ for the SCRS, non-shearing and shearing states close to the stability boundary, at $q = 21.3$, 49.58, and 50.56, respectively. The $\perp$ fields are clearly non-zero in regions coinciding with the plumes and boundary layers in the background flow, while remaining close to zero in all other areas.

In the SCRS, we also note that $w^{\perp}$ and $\theta^{\perp}$ contain odd modes only, and in the instance displayed in Figure 5.5, their amplitudes are purely imaginary due to the fixed phases in the SCRS. No such symmetries exist in the non-shearing and shearing states.

Background flow	q_c	$q_{\max}$	$\mathcal{R}(\sigma_{\max})$
CS	56.20	5.5	1.5×10^4
S	51.05	16	7.2×10^3
NS	50.07	13	5.5×10^3
SCRS	21.40	13	3.6×10^3

Table 5.1: The approximate values of q_c, $q_{\max}$, and $\mathcal{R}(\sigma_{\max})$ for each background flow.

5.5.2 Energy Equations

To examine how the $\perp$ fields are forced, we multiply (5.11a), (5.11b), and (5.13) by U, V, and $\theta^\perp$, respectively, and integrate over space, which yields the following energy equations;

$$\partial_t \frac{1}{2}\langle U^2\rangle_{\boldsymbol{x}} = \Pr\langle U(\nabla^2 - q^2)U\rangle_{\boldsymbol{x}} + \langle \psi_{xy}U^2\rangle_{\boldsymbol{x}} + \langle \psi_{yy}VU\rangle_{\boldsymbol{x}} + \langle \nabla^2\psi F_y U\rangle_{\boldsymbol{x}}, \quad (5.16a)$$

$$\partial_t \frac{1}{2}\langle V^2\rangle_{\boldsymbol{x}} = \Pr\langle V(\nabla^2 - q^2)V\rangle_{\boldsymbol{x}} + \mathrm{Ra}\Pr\langle \theta^\perp V\rangle - \langle \psi_{xx}UV\rangle_{\boldsymbol{x}} - \langle \psi_{xy}V^2\rangle_{\boldsymbol{x}} - \langle \nabla^2\psi F_x V\rangle_{\boldsymbol{x}}, \quad (5.16b)$$

$$\partial_t \frac{1}{2}\langle \theta^{\perp 2}\rangle_{\boldsymbol{x}} = \langle \theta^\perp(\nabla^2 - q^2)\theta^\perp\rangle_{\boldsymbol{x}} + \langle v^\perp\theta^\perp\rangle_{\boldsymbol{x}} - \langle \overline{\theta}_x u^\perp\theta^\perp\rangle_{\boldsymbol{x}} - \langle \overline{\theta}_y v^\perp\theta^\perp\rangle_{\boldsymbol{x}}. \quad (5.16c)$$

Note that the inertial terms, eg $\langle\{\psi, U\}U\rangle_{\boldsymbol{x}}$, disappear when integrated over the spatial domain.

In Figure 5.6 we show time series of the terms on the right-hand side of (5.16) over the SCRS, non-shearing and shearing states at the same values $q = 21.3$, 49.58, and 50.56, respectively, as above. These values are close to, but slightly smaller than q_c in each case, so $\partial_t\langle U^2\rangle_{\boldsymbol{x}}$, $\partial_t\langle V^2\rangle_{\boldsymbol{x}}$, and $\partial_t\langle \theta^{\perp 2}\rangle_{\boldsymbol{x}}$ are small, but positive. Therefore, the terms are normalised with respect to $\langle U^2\rangle_{\boldsymbol{x}}$, $\langle V^2\rangle_{\boldsymbol{x}}$, and $\langle \theta^{\perp 2}\rangle_{\boldsymbol{x}}$ in the top, middle, and bottom row, respectively, to remove the marginal exponential growth.

First, we note that the terms in the energy equations undergo large fluctuations over the turbulent non-shearing and shearing states, while they are constant over the steady SCRS after a short transient. In both the non-shearing and shearing states is clear that $\theta^\perp$ is predominantly being forced by the $-\langle \overline{\theta}_y v^\perp\theta^\perp\rangle_{\boldsymbol{x}}$ term, which in turn forces V via the $\mathrm{Ra}\Pr\langle \theta^\perp V\rangle$ term, which finally forces U via the $\langle \psi_{yy}VU\rangle_{\boldsymbol{x}}$ term. The fact that the $-\langle \overline{\theta}_y v^\perp\theta^\perp\rangle_{\boldsymbol{x}}$ term initiates this cascade explains why in Figure 5.5 the $\perp$ fields mimic the thermal plumes and boundary layers observed in $\overline{\theta}$. In each field, energy is being dissipated predominantly via the dissipative terms in red.

The balances look very different over the SCRS. Note first that the $-\langle \overline{\theta}_y v^\perp\theta^\perp\rangle_{\boldsymbol{x}}$ term has now become dissipative while $\theta^\perp$ is instead forced by the $-\langle \overline{\theta}_x u^\perp\theta^\perp\rangle_{\boldsymbol{x}}$ term. The $\mathrm{Ra}\Pr\langle \theta^\perp V\rangle$ term still forces V, but V is also being forced by the background flow directly via the $-\langle \psi_{xy}V^2\rangle_{\boldsymbol{x}}$ term. The $\langle \psi_{yy}VU\rangle_{\boldsymbol{x}}$ term still forces U, but just like for V, U is also being forced directly by the background flow via the $\langle \psi_{xy}U^2\rangle_{\boldsymbol{x}}$ term.

These substantial differences in the mechanisms driving the $\perp$ fields could be the reason for the similar values of q_c over the non-shearing and shearing states, while q_c is significantly smaller over the SCRS.

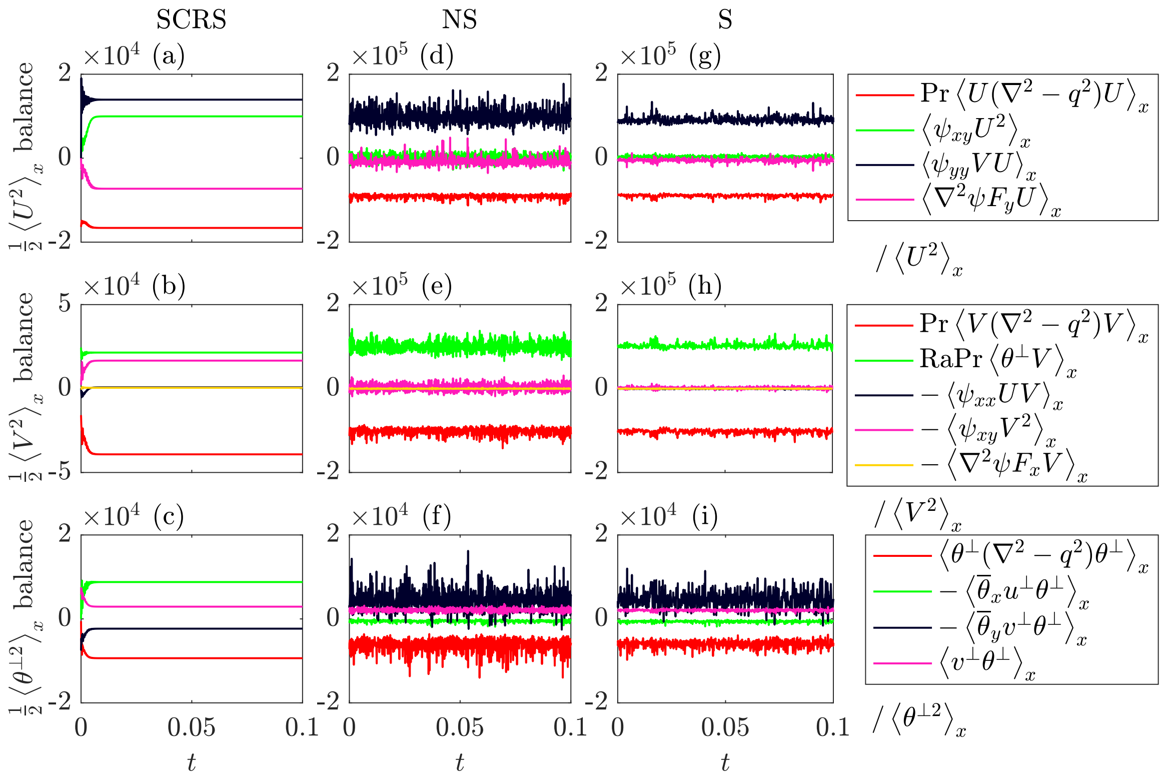

Figure 5.6: Terms on the right-hand side of equations (5.16a), (5.16b), and (5.16c), displayed on the top, middle, and bottom rows respectively. Each column represents a different background flow: the first column corresponds to the SCRS, the second to the non-shearing state, and the third to the shearing state. The transverse wavenumber q is set to 21.3, 49.58, and 50.56 for each of these states, respectively, so that the 3D perturbations are marginally unstable. Each term has been normalised to remove the marginal exponential growth.

In the following sections, we carry out three further experiments. In each, we modify the background flows in some way prior to inputting them into the system (5.11) and (5.13). Our objective is to examine how these modifications influence q_c and the growth rate.

5.5.3 Effects of Kinetic Energy

To study the effects of the time-averaged kinetic energy, $\langle E^u\rangle_t$, in the background flow, we perform an experiment in which we modify ψ according to the transformation below:

$$\psi \mapsto \sqrt{E}\psi, \tag{5.17}$$

which increases the kinetic energy by a factor of E. The background flow is evolved like usual according to (5.3) and the transformation (5.18) is applied only prior to it

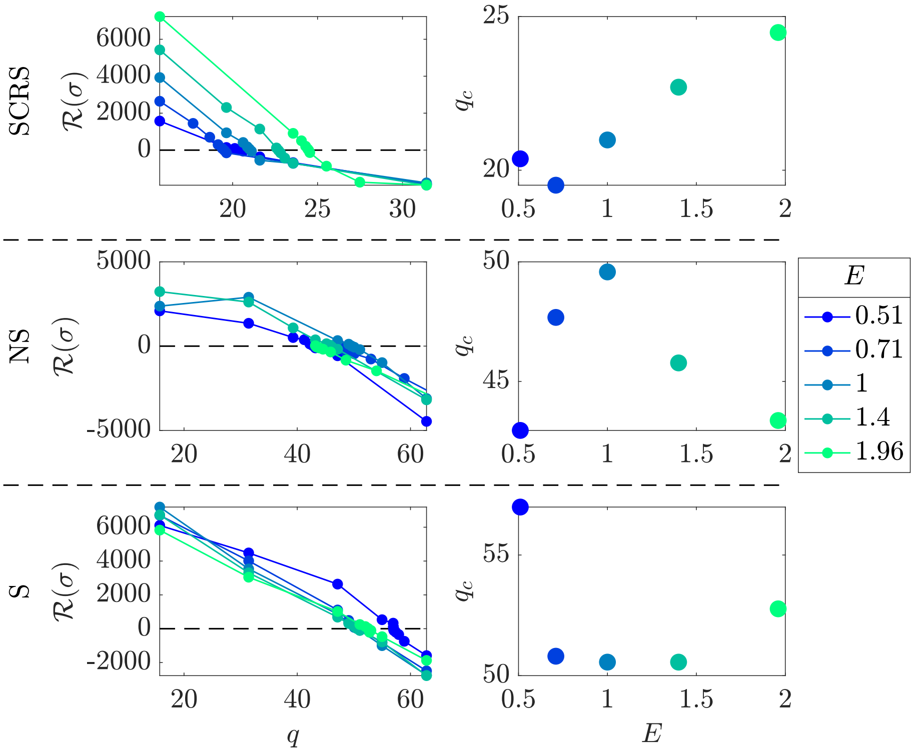

Figure 5.7: The first column shows the growth rate, $\mathcal{R}(\sigma)$, at different values of q over the SCRS, non-shearing and shearing state following the transformation (5.17). The second column shows q_c versus E for each background flow.

being fed to the system (5.11) and (5.13), while $\overline{\theta}$ is unchanged.

There are significant differences between the time-averaged kinetic energies in the SCRS, non-shearing, and shearing states, which are 9.15×10^7, 5.88×10^7, and 4.17×10^7, respectively. However, values of the time-averaged potential energy are approximately the same. This is because while the plume structures are different, the amplitude of the even zonal modes which carry the majority of potential energy, $\widehat{\theta}_{0,k_y}$, are approximately the same in each state. These zonal modes ensure that the temperature is approximately 1/2 in the bulk, except at thermal plumes. For this reason, we study the effect of varying the kinetic rather than potential energy.

In Figure 5.7 we show the growth rate, $\mathcal{R}(\sigma)$, versus q while varying E. The E values 0.51, 0.71, 1.4, and 1.96 are chosen because the time-averaged kinetic energy in the non-shearing state is approximately 1.4 times that in the shearing state and $1.96 = 1.4^2$, $0.71 \approx (1.4)^{-1}$, $0.51 \approx (1.4)^{-2}$. For the SCRS, in the top row, we see that the growth rate increases monotonically with E at $q = 5\pi \approx 15.7$, and so does q_c for $E > 0.71$. However, all q_c are within a 15% range of q_c at $E = 1$.

For the non-shearing state, in the middle row, we observe that q_c is at a maximum value at $E = 1$ and decreases monotonically as we increase or decrease E from 1. All q_c are within a 13% range of q_c at $E = 1$.

For the shearing state, in the bottom row, we observe that q_c is at a minimum value at $E = 1$ and increases monotonically as we increase or decrease E from 1. All q_c are within a 13% range of q_c at $E = 1$.

In summary, we can not say anything universal about the effects of kinetic energy in the background flow as the dependence on E varies depending on the background flow. However, the changes in q_c are small in relation to the large change in the kinetic energy seen in this section.

5.5.4 Effects of Zonal Flow

The distinct characteristic that differentiates the shearing state from the SCRS and non-shearing state is its prominent zonal flow, captured by the $\widehat{\psi}_{0,1}$ mode. To understand how the zonal flow impacts the growth rate and q_c, we perform an experiment in which we modify ψ according to the transformation below:

$$\widehat{\psi}_{k_x,k_y} \mapsto \begin{cases} f\widehat{\psi}_{k_x,k_y} & \text{if } k_x = 0 \text{ and } k_y = 1, \\ \sqrt{1 + (1-f^2)\frac{\langle E^u_{0,1}\rangle_t}{\langle E^u\rangle_t - \langle E^u_{0,1}\rangle_t}}\,\widehat{\psi}_{k_x,k_y} & \text{otherwise.} \end{cases} \tag{5.18}$$

Here, $\langle E^u_{0,1}\rangle_t$ is the kinetic energy contained solely in the $\widehat{\psi}_{0,1}$ mode, as defined below:

$$\langle E^u_{0,1}\rangle_t = \frac{\pi^2}{4}\langle \widehat{\psi}^2_{0,1}(t)\rangle_t. \tag{5.19}$$

Because we want to isolate the influence of the zonal flow, the transformation (5.18) ensures that the time-averaged kinetic energy in the background flow is conserved. Just like in the kinetic energy experiment, the background flow is evolved like usual according to (5.3) and the transformation (5.18) is applied only prior to it being fed to the system (5.11) and (5.13).

Figures 5.8 (a) and (b) show time series of the kinetic energy and $\widehat{\psi}_{0,1}$ in a shearing state at two values of f following the transformation (5.18). The time-averaged kinetic energy is the same in both cases, but the instantaneous kinetic energy exhibits significantly larger fluctuations when $f = 0.2$ as opposed to when $f = 1$. This is because energy has been transferred from the $\widehat{\psi}_{0,1}$ mode to other modes which fluctuate more. This energy transfer is clearly evident in Figures 5.8 (c) and (d), which show instantaneous realisations of ψ after applying the transformation when $f = 0.2$ and $f = 1$, respectively. When $f = 1$, the $\hat{\psi}_{0,1}$ mode dominates, as anticipated

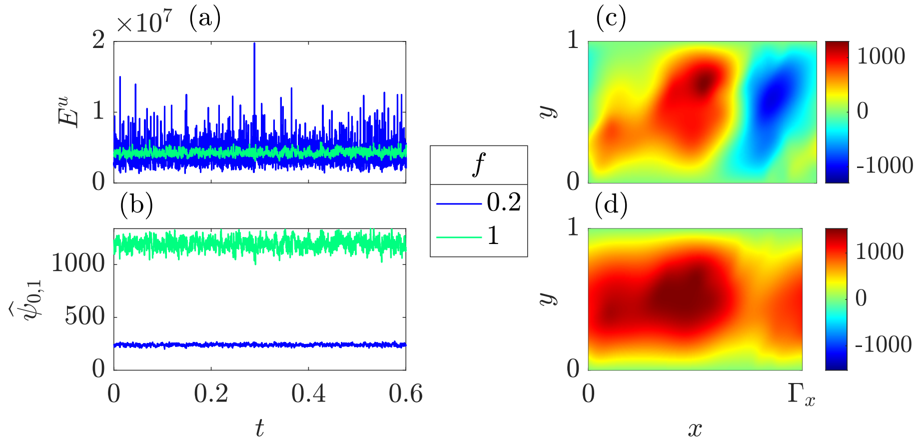

Figure 5.8: Time series of the kinetic energy (a) and $\widehat{\psi}_{0,1}$ mode (b) in a shearing state at two values of f following the transformation (5.18). Instantaneous realisations of ψ after applying the transformation (5.18) are shown for $f = 0.2$ and $f = 1$ in (c) and (d), respectively.

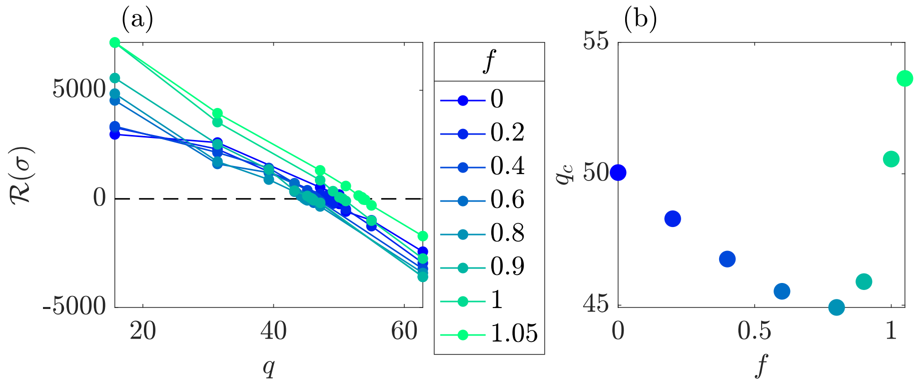

Figure 5.9: The growth rate, $\mathcal{R}(\sigma)$, at different values of q over shearing background flows with different f values (5.18) as colour coded in the legend (a) and q_c versus f (b).

in a shearing state. However, when $f = 0.2$, the flow resembles a non-shearing state, as indicated by the two counter-rotating convection rolls.

In Figure 5.9 (a) we show the growth rate, $\mathcal{R}(\sigma)$, at different q values over shearing background flows with different f values. For $q < 20$, we note a monotonic increase in the growth rate with f, reinforcing our theory that zonal flow has a destabilising effect on the 3D perturbations at small wavenumbers. In Figure 5.9 (b) we show q_c versus f. Interestingly, despite the significant changes in the background flow with varying f, as evident from Figures 5.8 (c) and (d), q_c remains largely unchanged. In fact, all values are within a 13% range of q_c at $f = 1$.

5.5.5 Effects of Time Dependence

As highlighted in Figure 5.4, q_c is significantly smaller in the SCRS than in the shearing and non-shearing state. A key difference between the states is that the SCRS is time-independent, while the shearing and non-shearing states are not. To investigate the effects of time dependence, we conduct an experiment where the SCRS is subject to the following transformation at each time step:

$$\widehat{\psi}_{k_x,k_y} \mapsto e^{i2\pi\phi^{\psi}_{k_x,k_y}}\widehat{\psi}_{k_x,k_y}, \quad \widehat{\psi}_{-k_x,k_y} \mapsto e^{-i2\pi\phi^{\psi}_{k_x,k_y}}\widehat{\psi}_{-k_x,k_y} \quad \text{when } k_x > 0, \tag{5.20a}$$
$$\widehat{\theta}_{k_x,k_y} \mapsto e^{i2\pi\phi^{\theta}_{k_x,k_y}}\widehat{\theta}_{k_x,k_y}, \quad \widehat{\theta}_{-k_x,k_y} \mapsto e^{-i2\pi\phi^{\theta}_{k_x,k_y}}\widehat{\theta}_{-k_x,k_y} \quad \text{when } k_x > 0, \tag{5.20b}$$

where $\phi^{\psi}_{k_x,k_y}$ and $\phi^{\theta}_{k_x,k_y}$ are drawn uniformly from $[0,1]$. We do not transform the zonal modes ($k_x = 0$) since they are necessarily real-valued. The transformation ensures that the kinetic and potential energy in the fields is conserved, while inducing some random time dependence. Figure 5.10 shows the SCRS before and after the transformation. In this instance, the counter-rotating convection rolls in ψ have been shifted by approximately $\Gamma_x/4$ to the right with a slight distortion, while the thermal plumes in θ have been completely distorted.

In Figure 5.11 we show the growth rate, $\mathcal{R}(\sigma)$, versus q over the original SCRS and the time-dependent SCRS (rSCRS), with the transformation (5.20) applied at each time step. We note that q_c is virtually unchanged, but that the absolute value of the growth rate is much larger over the SCRS than over the rSCRS. This observation indicates that time coherence of the background flow enhances the response to 3D perambulations, whether positive or negative.

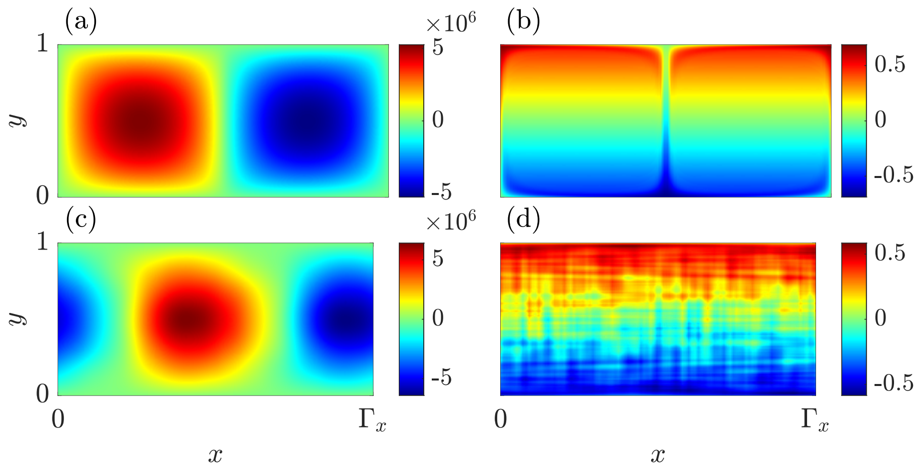

Figure 5.10: The SCRS at $(\mathrm{Ra}, \mathrm{Pr}, \Gamma_x) = (10^7, 30, 2)$ before (a,b) and after (c,d) the transformation (5.20). The streamfunction ψ is shown in (a) and (d), and temperature perturbation $\overline{\theta}$ in (b) and (d).

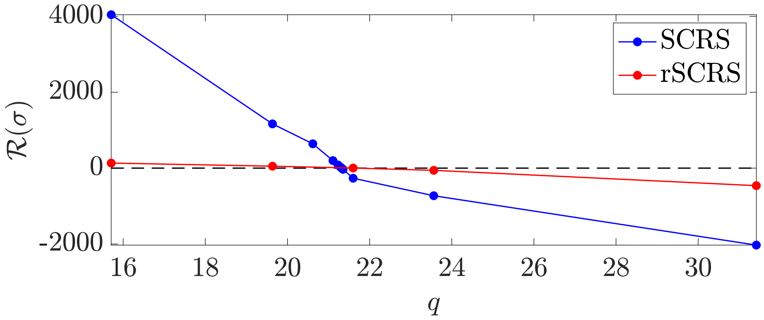

Figure 5.11: The growth rate, $\mathcal{R}(\sigma)$, at different values of q over the SCRS and the rSCRS, in which the transformation (5.20) is applied at every time step (rSCRS).

5.6 Conclusions

In this chapter, we have generalised our analysis from the previously studied 2D flow to a Q2D flow by introducing of a new spatial direction, z, with free-slip boundary conditions. We fix the parameters $(\mathrm{Ra}, \mathrm{Pr}, \Gamma_x) = (10^7, 30, 2)$ and study how 3D perturbations grow over different 2D background flows. Since the perturbations are infinitesimal, we introduce no additional nonlinearities. As has been done in previous studies [8, 126], we can therefore consider individual modes in z and vary Γ_z to examine how different wavenumbers, q, evolve. Such a severe Galerkin truncation in z significantly decreases the dimensionality of our system versus fully 3D simulations allowing us to systematically consider a wide range of wavenumbers while remaining within feasible computational constraints.

We focus on the SCRS, shearing, and non-shearing states as the 2D background flow. Our study reveals that the critical wavenumbers, q_c, at which 3D perturbations become unstable are 51.05, 50.07, and 21.4 for the shearing, non-sharing states, and SCRS, respectively, corresponding to critical values 0.062, 0.063, and 0.15 for the aspect ratio $\Gamma_z = L_z/L_y = \pi/q$.

In studying how the 3D perturbations are forced we observe that they are predominately influenced by the thermal plumes and boundary layers in the background flow. However, the driving mechanisms differ considerably between the shearing and non-shearing state versus the SCRS. We hypothesise that this difference may explain the similar q_c values for the shearing and non-shearing states and the substantially smaller q_c value for the SCRS, albeit this claim is conjectural and requires further investigation.

For small wavenumbers, $q < 20$, the growth rate of the 3D perturbations over the shearing states is notably higher than over the non-shearing state. It appears that zonal flow has a destabilising effect at these wavenumbers, a hypothesis corroborated by the experiment discussed in §5.5.4, which revealed a monotonically increasing relationship between the growth rate and the zonal flow strength. However, a more in-depth analysis is required to delineate the precise mechanism underpinning this observation.

Additional experiments involved systematically varying the kinetic energy in the background flow and inducing random time dependence in the SCRS. The impact on q_c in these tests was moderate, an observation particularly noteworthy given the substantial variations in the background flow.

This study clearly illustrates that the domain needs to be very narrow in z to render the flow truly 2D. Future directions to extend this research include investigating the dependence on the Rayleigh and Prandtl numbers and, in general, understanding what characteristics of the background flow promote or suppress 3D disturbances. Finally, the free-slip conditions imposed in the z-direction could be generalised to more general periodic boundary conditions, which would permit a net zonal flow to occur in the z-direction.

Chapter 6

Spectra Without Boundaries

6.1 Synopsis

In this chapter, we study 2D RB convection in a periodic box. The flow is forced by a constant average vertical temperature gradient, which is an idealised approach to study RB convection far from walls, thereby avoiding the complexities of boundary layers. Prior research in this set-up has primarily focused on Rayleigh number effects with $\mathrm{Pr} = 1$ [10, 14, 28, 29, 38, 106, 154, 162], while there has been limited exploration of Prandtl number effects [29]. In this work, we present global variables and spectral analysis across five orders of magnitude for the Prandtl number ($10^{-3} \leq \mathrm{Pr} \leq 10^{2}$), and four orders of magnitude for the Rayleigh number ($6.2 \times 10^{7} \leq \mathrm{Ra} \leq 6.2 \times 10^{11}$), along with the extreme $\mathrm{Pr} \to 0$ and $\mathrm{Pr} \to \infty$ limits.

A literature review in §6.2 lays the foundation for the work presented in this chapter, and in §6.3, we lay out the problem formulation and define global variables and spectral quantities which will be studied. In §6.4 we study the extreme Prandtl number limits. Our findings indicate that the dynamics is dominated by large-scale runaway solutions, even when including a large-scale dissipation term in the momentum equation.

For finite Prandtl numbers, discussed in §6.5, we find that the Nusselt number adheres to the "ultimate" scaling $\mathrm{Nu} \propto \mathrm{Pr}^{1/2}\mathrm{Ra}^{1/2}$. The kinetic and potential energies both scale like $\mathrm{Ra}\,\mathrm{Pr}$, only the former being consistent with Grossmann-Lohse theory (GL theory) [70, 71, 73, 74]. The viscous dissipation scales like $\mathrm{Pr}^2\mathrm{Ra}^{5/4}$, while the thermal dissipation scales like $(\mathrm{Ra}\,\mathrm{Pr})^{3/2}$. The latter observation is consistent with GL theory [70, 71, 73, 74], while the former follows from the observation that enstrophy scales like $\mathrm{Pr}\,\mathrm{Ra}^{5/4}$. Analysing the energy spectra, we observe an inverse cascade of kinetic energy and a forward cascade of potential energy, yielding kinetic and potential energy spectra that are near, but not consistent with, Bolgiano-Obukhov phenomenology [12, 122].

Finally, we draw our conclusions in §6.6.

6.2 Literature Review

RB convection in a periodic domain, otherwise known as homogeneous thermal convection, is a reasonable way to explore unstably stratified turbulence, particularly far from walls. This aligns with the bulk-region dynamics observed within an RB convective cell [10, 14, 28, 29, 38, 106, 154, 162]. There are two ways to drive the flow: imposing a constant average vertical temperature gradient across the layer [10, 14, 28, 29, 106] or explicitly forcing the temperature field [154, 162].

Homogeneous thermal convection has shown evidence of the "ultimate" scaling of the Nusselt number, $\mathrm{Nu} \propto \sqrt{\mathrm{Ra}\,\mathrm{Pr}}$ [14, 29, 106]. However, previous studies are limited to results where the Prandtl number is unity, primarily due to computational convenience.[1] It has been established that structure functions [10, 162] and spectra [162] are generally in accord with the Bolgiano-Obukhov (BO) scaling when $\mathrm{Pr} = 1$. It is worth noting, though, that Toh et al. [162] did not study the widely considered constant average vertical temperature gradient case, whereas Biskamp et al. [10] overlooked the spectra, a critical aspect of BO scaling.

Calzavarini et al. [28] highlighted the existence of a family of exact, single-scale, exponentially growing, separable solutions of the fully nonlinear system, which can dominate the flow dynamics. Large-scale dissipation terms are often included to suppress this unphysical behaviour and to reach a statistically steady turbulent state [10, 154, 162].

6.3 Problem Formulation

6.3.1 Governing Equations

We consider the 2D Boussinesq equations of thermal convection (2.10) in a periodic square cell of height L in which the driving force is a constant average vertical temperature gradient. Thus the temperature field takes the form $T(x, y, t) =$

[1] Although results are presented for five different Prandtl numbers (1/10, 1/3, 1, 3, 4) in the work by Calzavarini et al. [29], the ultimate scaling is only demonstrated for $\mathrm{Pr} = 1$.

$\Delta T\,(1 - y/L) + \theta(x, y, t)$, where the temperature perturbation, θ, satisfies periodic boundary conditions. The governing equations are written dimensionally as

$$\partial_t \nabla^2 \psi + \{\psi, \nabla^2 \psi\} = \alpha g \partial_x \theta + (-1)^{n+1} \nu \nabla^{2n+2} \psi + \mu \psi, \tag{6.1a}$$

$$\partial_t \theta + \{\psi, \theta\} = \frac{\Delta T}{L} \partial_x \psi + (-1)^{n+1} \kappa \nabla^{2n} \theta. \tag{6.1b}$$

A large-scale dissipation term, $\mu\psi$, has been included in (6.1a) to reach statistically steady states rather than runaway solutions with unbounded energies, which are otherwise prominent in this set-up [28]. This term can be viewed as mimicking the effect of friction when there are boundaries in the z-direction.

We non-dimensionalise, choosing units L for length, L^{2n}/κ for time (thus κ/L^{2n-1} for velocity), and ΔT for temperature, yielding the dimensionless equations

$$\nabla^2 \psi_t + \{\psi, \nabla^2 \psi\} = \mathrm{Ra}\,\mathrm{Pr}\theta_x + (-1)^{n+1} \mathrm{Pr} \nabla^{2(n+1)} \psi + \mathrm{Rh}\sqrt{\mathrm{Ra}\,\mathrm{Pr}}\psi, \tag{6.2a}$$

$$\theta_t + \{\psi, \theta\} = \psi_x + (-1)^{n+1} \nabla^{2n} \theta, \tag{6.2b}$$

where

$$\mathrm{Ra} = \frac{\alpha \Delta T g L^{4n-1}}{\nu\kappa}, \quad \mathrm{Pr} = \frac{\nu}{\kappa}, \quad \mathrm{Rh} = \mu \sqrt{\frac{L^5}{g \alpha \Delta T}}, \tag{6.3}$$

are the Rayleigh, Prandtl and friction Reynolds number, respectively. However, we note that a different scaling must be used in the zero Prandtl number limit; see §6.4.

We also generalise the system (2.10) by including the exponent n. In this chapter, we consider two values, $n = 1$ (normal viscosity) and $n = 4$ (hyperviscosity). The hyperviscous case, albeit not physically realisable, gives a wider inertial range to analyse how the spectra scale, as diffusive and viscous terms kick in abruptly at much smaller scales compared to the normal viscosity case.

The governing equations (6.2) are solved using DNS analogous to that outlined in C.1. The stream function is decomposed into basis functions with Fourier modes in both x- and y-directions, viz.

$$\psi(\mathbf{x}, t) = \sum_{k_x, k_y = -N/2}^{N/2} \widehat{\psi}_{\boldsymbol{k}}(t) e^{i2\pi \boldsymbol{k}\cdot\boldsymbol{x}}, \tag{6.4}$$

where $\widehat{\psi}_{\boldsymbol{k}}$ is the amplitude of the $\boldsymbol{k} = (k_x, k_y)$ mode, and N denotes the number of aliased modes in the x- and y-directions; θ is decomposed in the same way.

In our simulations with normal viscosity and finite Prandtl number, we vary the Rayleigh and Prandtl numbers in the ranges $6.2 \times 10^7 \leq \mathrm{Ra} \leq 6.2 \times 10^{11}$ and

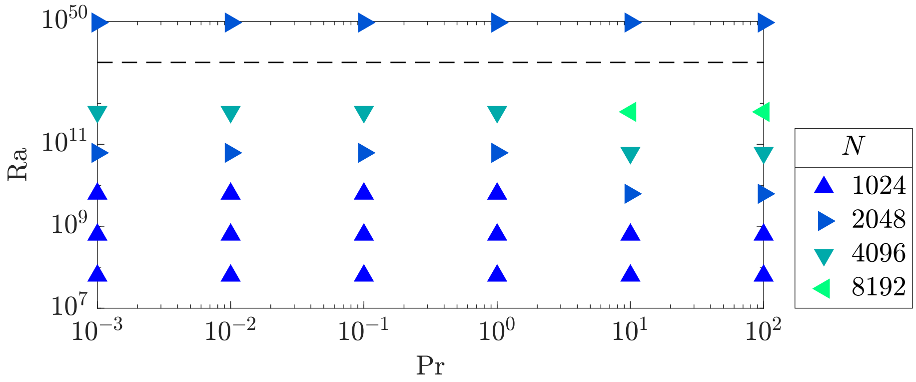

Figure 6.1: Parameter values simulated in the $(\mathrm{Ra}, \mathrm{Pr})$-plane with the resolution, N, used in each case colour-coded in the legend. The black dashed line separates runs with normal viscosity (below line) from those with hyperviscosity (above line).

$10^{-3} \leq \mathrm{Pr} \leq 10^2$. To model very large Rayleigh number dynamics, we set $\mathrm{Ra} = 9.4 \times 10^{49}$ in our hyperviscous simulations. Figure 6.1 shows the parameter values simulated in the $(\mathrm{Ra}, \mathrm{Pr})$-plane as well as the resolution, N, used in each case. In both the normal and hyperviscous simulations, we fix $\mathrm{Rh} = (2\pi)^{5/2} \simeq 100$ to suppress runaway solutions, which are the subject of the next subsection.

6.3.2 Runaway Solutions

Because the system is no longer bounded in the y-direction, the equations (6.2) admit *exact* unidirectional solutions of the form

$$\psi = Ae^{i2\pi k_x x + \sigma t} + c.c., \quad \theta = Be^{i2\pi k_x x + \sigma t} + c.c., \tag{6.5}$$

in which the non-linear terms in (6.2) are identically zero. The exponential growth rate, σ, satisfies the relation

$$\left(\sigma + \mathrm{Pr}(2\pi k_x)^{2n} + \frac{\mathrm{Rh}\sqrt{\mathrm{Ra}\,\mathrm{Pr}}}{(2\pi k_x)^2}\right)\left(\sigma + (2\pi k_x)^{2n}\right) = \mathrm{Ra}\,\mathrm{Pr}. \tag{6.6}$$

It may be shown that the roots, σ, of (6.6) are always real and at least one of them is negative. The mode with wavenumber k_x is suppressed if

$$\mathrm{Rh} > \sqrt{\frac{\mathrm{Pr}}{\mathrm{Ra}} \frac{(\mathrm{Ra} - (2\pi k_x)^{4n})}{(2\pi k_x)^{2(n-1)}}}. \tag{6.7}$$

It is clear that the most dangerous mode is with $k_x = 1$, and all other modes (including modes with $k_y \neq 0$) are stable when this one is. When the inequality (6.7) is not satisfied, solutions of the form (6.5) can grow without bound. However, in Appendix E we show that, with $\mathrm{Rh} = (2\pi)^{5/2}$ and finite Prandtl number, we reliably obtain statistically steady states not dominated by the runaway solutions (6.5), even though the inequality (6.7) is generally not satisfied.

6.3.3 Spectra and Fluxes

The dimensionless energy spectra of the velocity field $\widehat{E}^u(k,t)$ and the temperature field $\widehat{E}^\theta(k,t)$, referred to as the kinetic energy and potential energy spectra, are defined as

$$\widehat{E}^u(k,t) = \frac{1}{2} \sum_{\boldsymbol{k} \in C(k)} k^2 \left| \widehat{\psi}_{\boldsymbol{k}}(t) \right|^2, \tag{6.8a}$$

$$\widehat{E}^\theta(k,t) = \frac{\mathrm{Ra}\,\mathrm{Pr}}{2} \sum_{\boldsymbol{k} \in C(k)} \left| \widehat{\theta}_{\boldsymbol{k}}(t) \right|^2, \tag{6.8b}$$

where the sum is performed over the Fourier modes with wavenumber

$$k = 2\pi|\boldsymbol{k}| = 2\pi\sqrt{k_x^2 + k_y^2} \tag{6.9}$$

in the shell $C(k) = \{\boldsymbol{k} : 2\pi|\boldsymbol{k}| \in [k-\pi, k+\pi)\}$. Using the Fourier transform, we can derive the evolution equations of kinetic and potential energy spectra from equations (6.2), in the forms:

$$\partial_t \widehat{E}^u(k,t) = -\partial_k \Pi_u(k,t) - D_\nu(k,t) - D_\mu(k,t) + F_B(k,t), \tag{6.10a}$$

$$\partial_t \widehat{E}^\theta(k,t) = -\partial_k \Pi_\theta(k,t) - D_\kappa(k,t) + F_B(k,t). \tag{6.10b}$$

Here Π_u and Π_θ are the kinetic and potential energy fluxes, D_ν, D_μ and D_κ are the small-scale, large-scale and thermal dissipation terms, and F_B is the buoyancy term which transfers between kinetic and thermal energies.

The energy flux is a measure of the nonlinear cascades in turbulence [2]. The energy flux for a circle of radius k in the 2D wavenumber space is the total energy transferred from the modes within the circle to the modes outside the circle. Consequently, we define the flux of kinetic energy $\Pi_u(k,t)$ and potential energy $\Pi_\theta(k,t)$ as

$$\Pi_u(k,t) = \sum_{k' \le k} T_u(k',t), \tag{6.11a}$$

$$\Pi_\theta(k,t) = \sum_{k' \le k} T_\theta(k',t), \tag{6.11b}$$

where $T_u(k,t)$ and $T_\theta(k,t)$ are the non-linear kinetic and potential energy transfer across $C(k)$, given by

$$T_u(k,t) = -\sum_{k' \in C(k)} \widehat{\psi}^*_{\boldsymbol{k}'}(t)\widehat{\{\psi, \nabla^2\psi\}}_{\boldsymbol{k}'}(t), \tag{6.12a}$$

$$T_\theta(k,t) = \mathrm{Ra}\,\mathrm{Pr}\sum_{k' \in C(k)} \widehat{\theta}^*_{\boldsymbol{k}'}(t)\widehat{\{\psi, \theta\}}_{\boldsymbol{k}'}(t). \tag{6.12b}$$

Here we have introduced the notation $\widehat{\{\psi, \nabla^2\psi\}}_{\boldsymbol{k}}$ for the $\boldsymbol{k}$th Fourier mode of the Poisson bracket expanded as in equation (6.4), and similarly for $\widehat{\{\psi, \theta\}}_{\boldsymbol{k}}$. Similarly, we define the small-scale viscous dissipation term $D_\nu(k,t)$, the large-scale friction term $D_\mu(k,t)$, the thermal dissipation term $D_\kappa(k,t)$ as

$$D_\nu(k,t) = 2\mathrm{Pr}k^{2n}\widehat{E}^u(k,t), \tag{6.13a}$$

$$D_\mu(k,t) = 2\mathrm{Rh}k^{-2}\widehat{E}^u(k,t), \tag{6.13b}$$

$$D_\kappa(k,t) = 2\mathrm{Ra}\,\mathrm{Pr}k^{2n}\widehat{E}^\theta(k,t), \tag{6.13c}$$

and the bouyancy term as

$$F_B(k,t) = \mathrm{Ra}\,\mathrm{Pr}\sum_{k' \in C(k)} i2\pi k'_x\widehat{\psi}_{k'}(t)\widehat{\theta}^*_{k'}(t). \tag{6.14}$$

6.3.4 Kolmogorov and Bolgiano-Obukhov Phenomenology

The two main semi-analytic theories for how kinetic and potential energy spectra scale in turbulent flows are the so-called Kolmogorov (K41) [93, 94, 95] and Bolgiano-Obukhov (BO) [12, 122] phenomenologies. K41 and BO scalings can be derived in different ways. Here they are derived using the conservation equations (6.10) for kinetic and potential spectra $\widehat{E}^u(k,t)$ and $\widehat{E}^\theta(k,t)$, in spectral space in a statistically steady state in which $\partial_t\widehat{E}^u = \partial_t\widehat{E}^\theta = 0$. Throughout this subsection, we let $n = 1$ and neglect large-scale friction.

In K41 scaling, one assumes that:

1. The energy transfer F_B is active at large length scales, which are of the order of the system size.

2. The effective Reynolds number is large so that energy is dissipated at small length scales.

3. The kinetic energy supplied by F_B cascades to intermediate scales (inertial range) and then to small scales (dissipation range), where it is dissipated.

4. The flow is statistically homogeneous and isotropic at the intermediate and small scales.

With these assumptions, we have that $F_B(k) \approx 0$ and $D_\nu(k) \approx 0$ in the inertial range, and therefore, in the absence of the large-scale dissipation term D_μ, we have

$$\frac{d}{dk}\Pi_u(k) \approx 0 \quad \Rightarrow \quad \Pi_u(k) \approx \text{const}, \tag{6.15}$$

by (6.10a). We can then identify Π_u with the total dissipation ϵ_ν, given in dimensional variables by

$$\epsilon_\nu = \int_0^\infty D_\nu \, dk = 2\nu \int_0^\infty k^2 \widehat{E}^u(k) \, dk, \tag{6.16}$$

since all the kinetic energy which has been supplied at large scales and subsequently transferred to small scales needs to be dissipated. Now, using dimensional analysis, one can derive the one-dimensional kinetic energy spectrum as

$$\widehat{E}^u = K_{\mathrm{Ko}} \Pi_u^{2/3} k^{-5/3}, \tag{6.17}$$

where K_{Ko} is Kolmogorov's constant.

For BO scaling, again one assumes that the effective Reynolds number is large, and that the flow is statistically homogeneous and isotropic at the intermediate and small scales. However, in contrast to K41 scaling; now one assumes that:

1. The flow is moderately buoyant and stably stratified, so in the case of RB convection $F_B \approx \alpha g \theta(k) u(k)$, where $u(k)$ and $\theta(k)$ denote velocity and temperature fluctuations at radial wavenumber k, respectively.

2. In a statistically steady state, inertia balances buoyancy, so $k u^2(k) \approx \alpha g \theta(k)$ in the inertial range.

3. The potential energy flux, $\Pi_\theta(k) \approx (\alpha g L/\Delta T)\theta(k)^2 u(k) k$, is approximately constant and equal to the total potential energy dissipation ϵ_κ.

With these assumptions, one deduces that

$$u(k) \approx \left(\frac{\alpha g \Delta T \epsilon_\kappa}{L}\right)^{1/5} k^{-3/5}, \quad \theta(k) \approx \left(\frac{\Delta T \epsilon_\kappa}{L}\right)^{2/5} (\alpha g)^{-3/5} k^{-1/5}, \tag{6.18}$$

and hence the kinetic energy spectrum $\widehat{E}^u(k) \approx u^2(k)/k$, potential energy spectrum $\widehat{E}^\theta(k) \approx (\alpha g L/\Delta T)\theta^2(k)/k$, and kinetic energy flux $\Pi_u(k) \approx u^3(k)k$ take the forms

$$\widehat{E}^u(k) = c_1 \left(\frac{\alpha g \Delta T \epsilon_\kappa}{L}\right)^{2/5} k^{-11/5}, \tag{6.19a}$$

$$\widehat{E}^\theta(k) = c_2 \left(\frac{L}{\alpha g \Delta T}\right)^{1/5} \epsilon_\kappa^{4/5} k^{-7/5}, \tag{6.19b}$$

$$\Pi_u(k) = c_3 \left(\frac{\alpha g \Delta T \epsilon_\kappa}{L}\right)^{3/5} k^{-4/5}, \tag{6.19c}$$

where c_i are constants. For a more detailed derivation of these scalings, the reader is referred to the papers [12, 93, 94, 95, 122] or the more recent books by Verma [170, 171].

Despite originally being proposed for stably stratified flows, BO scaling have been reported for 3D [30, 89, 107, 117] and 2D RB convection [116, 162, 186]. K41 scaling has been observed in 3D RBC [14, 169, 170], but can be ruled out in 2D due to the inverse cascade of kinetic energy [2, 162].

6.3.5 Time-Averaged Quantities

Time-averaged quantities are computed by time averaging over 1000 realisations within the statistically stationary regime, sufficiently separated in time (at least 5000 numerical time steps) to ensure statistically independent realisations.

Returning to the dimensionless equations (6.2) and (6.10), we recall that the Nusselt number is given by

$$\mathrm{Nu} = 1 + \langle \psi_x \theta \rangle_{\boldsymbol{x},t}, \tag{6.20}$$

where $\langle . \rangle_{\boldsymbol{x},t}$ denotes the average of a quantity over space and time as in (2.14). Either by multiplying (6.2a) and (6.2b) by ψ and θ, respectively, and averaging over $\boldsymbol{x}$ and t, or by summing (6.10) over k, we can derive exact relations for the kinetic and potential energy balances in the statistically stationary regime, namely

$$\epsilon_\theta = \epsilon_u = \epsilon_\kappa = \epsilon_\mu + \epsilon_\nu = \mathrm{Ra}\,\mathrm{Pr}\,(\mathrm{Nu} - 1)\,, \tag{6.21}$$

where we define

$$\epsilon_u = -\mathrm{Ra}\,\mathrm{Pr}\langle\psi\theta_x\rangle_{\boldsymbol{x},t} = \sum_k \langle F_B(k,t)\rangle_t = \text{injection rate of kinetic energy,} \tag{6.22a}$$

$$\epsilon_\nu = (-1)^{n+1}\mathrm{Pr}\langle\psi\nabla^{2(n+1)}\psi\rangle_{\boldsymbol{x},t} = \sum_k \langle D_\nu(k,t)\rangle_t = \text{viscous dissipation rate,} \tag{6.22b}$$

$$\epsilon_\mu = \mathrm{Rh}\sqrt{\mathrm{Ra}\,\mathrm{Pr}}\langle\psi^2\rangle_{\boldsymbol{x},t} = \sum_k \langle D_\mu(k,t)\rangle_t = \text{large scale dissipation rate,} \tag{6.22c}$$

$$\epsilon_\theta = \mathrm{Ra}\,\mathrm{Pr}\langle\psi_x\theta\rangle_{\boldsymbol{x},t} = \sum_k \langle F_B(k,t)\rangle_t = \text{injection rate of potential energy,} \tag{6.22d}$$

$$\epsilon_\kappa = (-1)^n\mathrm{Ra}\,\mathrm{Pr}\langle\theta\nabla^{2n}\theta\rangle_{\boldsymbol{x},t} = \sum_k \langle D_\kappa(k,t)\rangle_t = \text{thermal dissipation rate.} \tag{6.22e}$$

In §6.5 we will use these quantities as diagnostics of the flow in the turbulent regime, but first we briefly discuss the limiting cases where $\mathrm{Pr} \to 0$ and $\mathrm{Pr} \to \infty$.

6.4 Zero and Infinite Prandtl Number

In the $\mathrm{Pr} \to \infty$ limit, to maintain the effects of the large-scale dissipation, we ensure that $\mathrm{Rh}\sqrt{\mathrm{Ra}/\mathrm{Pr}}$ is finite. The system (6.2) thus reduces to

$$\mathrm{Ra}\theta_x = \left[(-1)^n\nabla^{2(n+1)} - \mathrm{Rh}\sqrt{\frac{\mathrm{Ra}}{\mathrm{Pr}}}\right]\psi, \tag{6.23a}$$

$$\theta_t + \{\psi,\theta\} = \psi_x + (-1)^{n+1}\nabla^{2n}\theta. \tag{6.23b}$$

Upon linearising about the conductive state ($\psi = \theta = 0$), we derive the dispersion relation

$$\sigma = \frac{\mathrm{Ra}(2\pi k_x)^2}{k^{2(n+1)} + \mathrm{Rh}\sqrt{\frac{\mathrm{Ra}}{\mathrm{Pr}}}} - k^{2n}. \tag{6.24}$$

The growth rate, σ, is therefore largest when $k_y = 0$, so a mode with no y dependence, i.e.

$$\theta = Be^{ik_x x + \sigma t} + c.c., \tag{6.25}$$

will grow at the onset of convection. Note, as in §6.3.2, that (6.25) is an *exact* solution to (6.23) and unbounded solutions with $\sigma(k_x) > 0$ are possible if

$$\mathrm{Ra} > (2\pi)^{4n} + \mathrm{Rh}\sqrt{\frac{\mathrm{Ra}}{\mathrm{Pr}}}(2\pi)^{2(n-1)}, \tag{6.26}$$

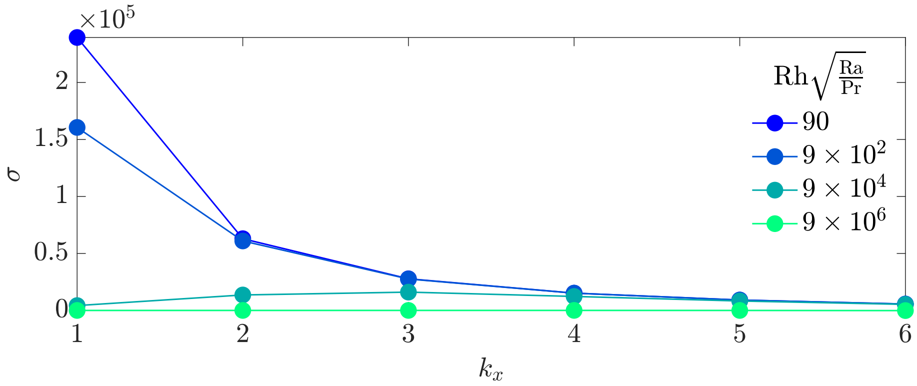

Figure 6.2: Growth rate, σ, given by (6.24) versus k_x in the $\mathrm{Pr} \to \infty$ limit at $\mathrm{Ra} = 10^7$, $n = 1$, $k_y = 0$ and four different values of $\mathrm{Rh}\sqrt{\mathrm{Ra}/\mathrm{Pr}}$, as colour coded in the legend.

which is equivalent to (6.7) with $k_x = 1$. It is not necessarily the $\widehat{\psi}_{1,0}$ mode that is the most unstable. In Figure 6.2 we plot the growth rate, σ, versus k_x in the $\mathrm{Pr} \to \infty$ limit at $k_y = 0$, $\mathrm{Ra} = 10^7$, $n = 1$, and four different values of $\mathrm{Rh}\sqrt{\mathrm{Ra}/\mathrm{Pr}}$. The growth rate peaks at $k_x = 1$, $k_x = 1$, $k_x = 3$, and $k_x = 4$ as we increase $\mathrm{Rh}\sqrt{\mathrm{Ra}/\mathrm{Pr}}$. In general, the maximum growth rate occurs when

$$k_x \approx \frac{1}{2\pi}\left[\frac{\mathrm{Ra}}{2}\left(\sqrt{8B+1} - 2B - 1\right)\right]^{1/4}, \tag{6.27}$$

where $B = \mathrm{Rh}/\sqrt{\mathrm{Ra}\,\mathrm{Pr}} < 1$. However, when the $(1, 0)$ mode is stable, then all other modes are as well.

In the complementary limit of zero Prandtl number, we have to rescale the variables according to

$$\{\psi, \theta, t\} \mapsto \{\mathrm{Pr}\,\psi, \mathrm{Pr}\,\theta, t/\mathrm{Pr}\} \tag{6.28}$$

before letting $\mathrm{Pr} \to 0$, which removes the time derivative and advective term from the heat transport equation (6.2b). As in the $\mathrm{Pr} \to \infty$ case, we maintain the effects of the large-scale dissipation by ensuring that $\mathrm{Rh}\sqrt{\mathrm{Ra}/\mathrm{Pr}}$ is finite. This process reduces the system (6.2) to

$$\nabla^2\psi_t + \{\psi, \nabla^2\psi\} = \mathrm{Ra}\theta_x + (-1)^{n+1}\nabla^{2(n+1)}\psi + \mathrm{Rh}\sqrt{\frac{\mathrm{Ra}}{\mathrm{Pr}}}\psi, \tag{6.29a}$$

$$\psi_x = (-1)^n\nabla^{2n}\theta. \tag{6.29b}$$

Again we linearise about the conductive state and find exact exponential solutions to (6.29), of the form

$$\psi = Ae^{i2\pi \boldsymbol{k}\cdot\boldsymbol{x} + \sigma t} + c.c., \tag{6.30}$$

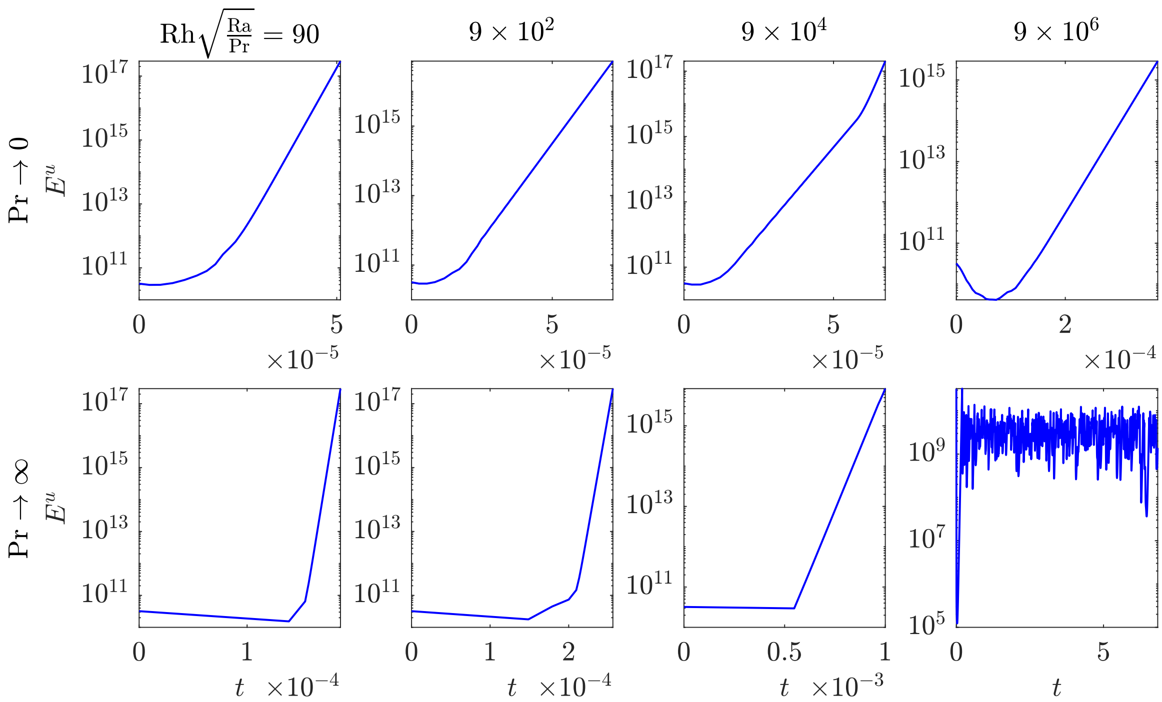

Figure 6.3: Time series of the kinetic energy, E^u, in the $\mathrm{Pr} \to 0$ and $\mathrm{Pr} \to \infty$ limits at $\mathrm{Ra} = 10^7$, $n = 1$, and four different values of $\mathrm{Ra}\sqrt{\mathrm{Ra}/\mathrm{Pr}}$. The time series are initiated with random initial conditions and a resolution $N = 256$ is used.

with growth rate

$$\sigma = \mathrm{Ra}\frac{(2\pi k_x)^2}{k^{2(n+1)}} - k^{2n} - \mathrm{Rh}\sqrt{\frac{\mathrm{Ra}}{\mathrm{Pr}}}k^{-2}. \tag{6.31}$$

Again, unbounded solutions with $\sigma(k_x) > 0$ are possible. However, in this case one can prove that the $\widehat{\psi}_{1,0}$ mode is always the most unstable; see §E.3 in Appendix E.

In Figure 6.3 we plot time series of the kinetic energy in the flow, E^u, in both the $\mathrm{Pr} \to 0$ and $\mathrm{Pr} \to \infty$ limits at $\mathrm{Ra} = 10^7$, $n = 1$, and four different values of $\mathrm{Ra}\sqrt{\mathrm{Ra}/\mathrm{Pr}}$. It is only in the $\mathrm{Pr} \to \infty$, $\mathrm{Rh}\sqrt{\mathrm{Ra}/\mathrm{Pr}} = 9 \times 10^6$ case where the flow converges to a statistically steady state. This value of $\mathrm{Rh}\sqrt{\mathrm{Ra}/\mathrm{Pr}}$ is only 10% smaller than the maximum value given by (6.7) at which all convection is suppressed. For all other parameter values attempted, a runaway solution takes over the dynamics and the energy grows without bound.

At present, we are not able to reliably obtain statistically steady states in the extreme Prandtl numbers limits, unless the large-scale dissipation is made very strong. Instead, we turn to finite Prandtl number.

6.5 Finite Prandtl Number

6.5.1 Global Variables

In this section, we perform DNS on the full system (6.2) and study how the global variables defined in (6.22) depend on Ra and Pr when $n = 1$ and Rh fixed at $(2\pi)^{5/2}$. In Figure 6.4 we show how the time-averaged kinetic and potential energies and the time-averaged quantities defined in (6.22) vary with Pr while keeping $\mathrm{Ra} = 6.2 \times 10^{11}$ fixed ((a)–(c)), and with Ra while keeping $\mathrm{Pr} = 1$ fixed ((d)–(f)). In Figure 6.4 (a) and (d) we see that $\langle E^u \rangle_t$ and $\langle E^\theta \rangle_t$ are both proportional to Ra Pr. In Figure 6.4 (b) and (e) we observe that $\epsilon_u \approx \epsilon_\mu \propto (\mathrm{Pr}\,\mathrm{Ra})^{3/2}$ in the kinetic energy balance, which suggests that the majority of the kinetic energy injected by buoyancy is dissipated at large scales. This phenomenon is due to an inverse cascade of kinetic energy, which is also highlighted in §6.5.3 by plotting the spectral flux (see Figure 6.8 (c)). The viscous dissipation is subdominant and scales like $\epsilon_\nu \propto \mathrm{Ra}^{5/4}\mathrm{Pr}^2$. Finally, in Figure 6.4 (c) and (f), we observe $\epsilon_\kappa \approx \epsilon_\theta \propto (\mathrm{Pr}\,\mathrm{Ra})^{3/2}$. All of these observations are in accord with the theoretical results in (6.21).

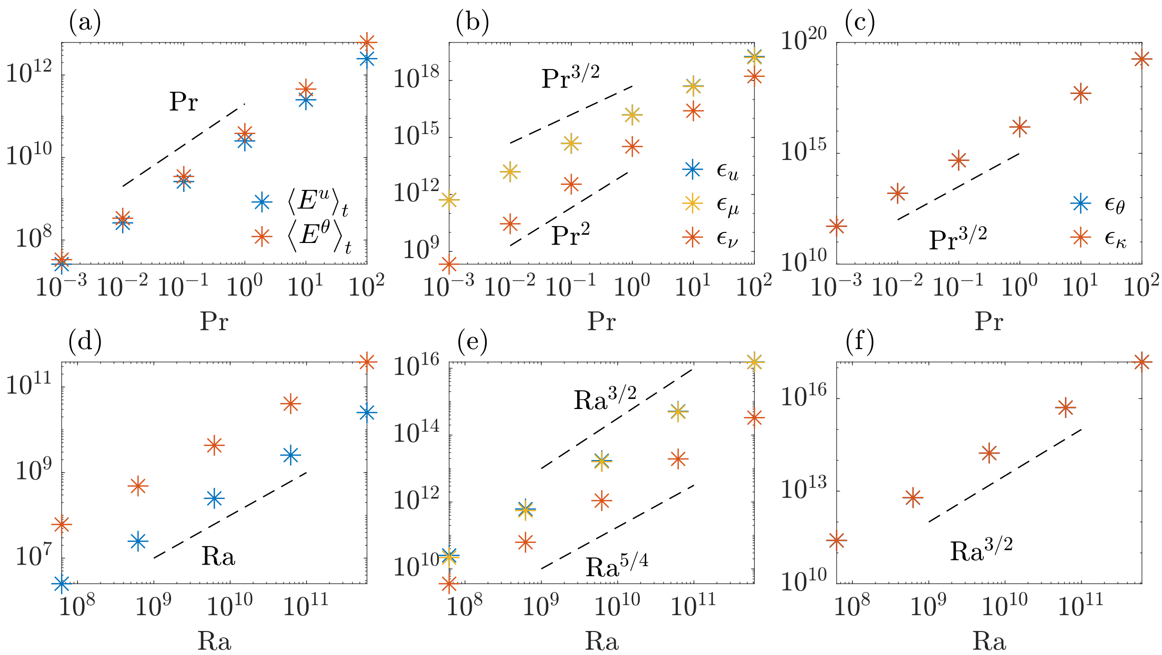

Figure 6.4: Spatiotemporally averaged energies, dissipative and injection rates with normal viscosity as functions of Pr with $\mathrm{Ra} = 6.2 \times 10^{11}$ fixed (see subplots (a) to (c)) and as a function of Ra with $\mathrm{Pr} = 1$ fixed (see subplots (d) to (f)). We fix $n = 1$ and $\mathrm{Rh} = (2\pi)^{5/2}$

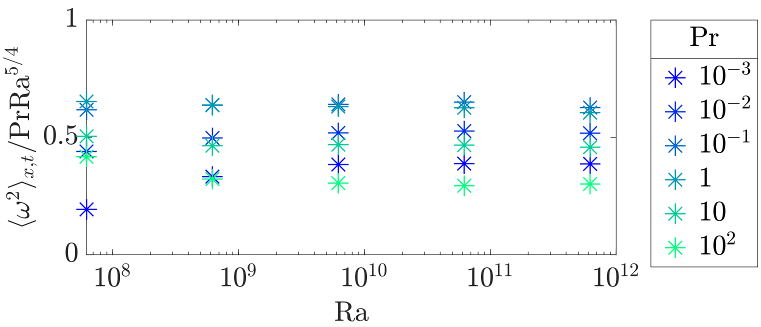

Figure 6.5: Enstrophy $\langle\omega^2\rangle_{\boldsymbol{x},t}$ versus Ra for a range of Prandtl numbers colour coded in the legend.

The theory by Grossmann and Lohse (GL theory) [70, 71, 73, 74] predicts that

$$\langle E^u\rangle_t \propto \mathrm{Ra}\,\mathrm{Pr}, \qquad \langle E^\theta\rangle_t \propto (\mathrm{Ra}\,\mathrm{Pr})^{3/4}, \tag{6.32a}$$

$$\epsilon_\nu \propto \mathrm{Pr}^3\mathrm{Re}^3, \qquad \epsilon_\kappa \approx \mathrm{Ra}\,\mathrm{Pr}\left(c_1\sqrt{\mathrm{RePr}} + c_2\mathrm{RePr}\right), \tag{6.32b}$$

in the core of RB convection, where c_i are constants and Re is the Reynolds number, defined as

$$\mathrm{Re} = \frac{\sqrt{2\langle E^u\rangle_t}}{\mathrm{Pr}}. \tag{6.33}$$

Our results for $\langle E^u\rangle_t$ shown in Figure 6.4 are consistent with the predictions by GL theory, but the results for $\langle E^\theta\rangle_t$ are not. However, they are consistent with the numerical results of Calzavarini et al. [29], who also reported $\langle E^\theta\rangle_t \propto \mathrm{Ra}\,\mathrm{Pr}$. Since $\langle E^u\rangle_t \propto \mathrm{Ra}\,\mathrm{Pr}$, this implies $\mathrm{Ra} \propto \mathrm{PrRe}^2$ by (6.33). So $\epsilon_\nu \propto \mathrm{Ra}^{5/4}\mathrm{Pr}^2$ is consistent with $\epsilon_\nu \propto \mathrm{Pr}^{13/4}\mathrm{Re}^{5/2}$, while $\epsilon_\kappa \propto (\mathrm{Ra}\,\mathrm{Pr})^{3/2}$ is consistent with $\epsilon_\kappa \propto \mathrm{Pr}^2\mathrm{Ra}\,\mathrm{Re}$. The observed scaling for ϵ_κ is therefore in agreement with GL theory, but the scaling for ϵ_ν is not. In fact, GL theory predicts that $\epsilon_\nu \propto \mathrm{Pr}^3\mathrm{Re}^{5/2}$ if energy dissipation is dominated by the boundary layers, only differing by a factor of $\mathrm{Pr}^{1/4}$ from our observations.

The observed scaling for ϵ_ν results from the corresponding scaling for the enstrophy of the flow, defined as

$$\langle\omega^2\rangle_{\boldsymbol{x},t} = \langle|\nabla^{n+1}\psi|^2\rangle_{\boldsymbol{x},t} = (-1)^{n+1}\langle\psi\nabla^{2(n+1)}\psi\rangle_{\boldsymbol{x},t} = \frac{\epsilon_\nu}{\mathrm{Pr}}. \tag{6.34}$$

As can be seen in Figure 6.5, we observe that the enstrophy scales like $\mathrm{Pr}\,\mathrm{Ra}^{5/4}$.

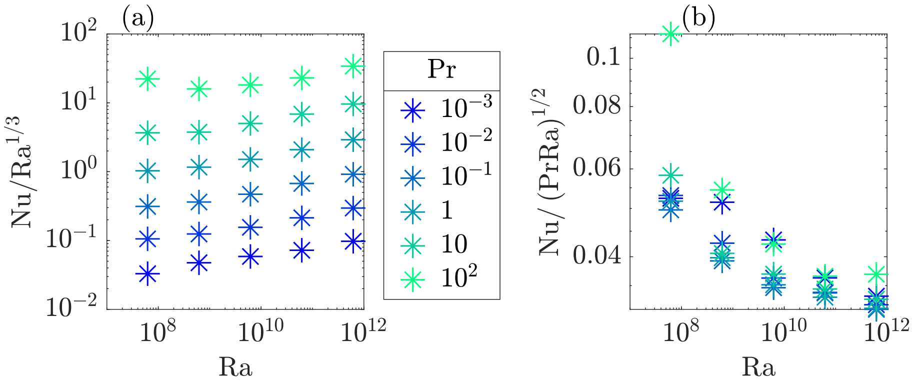

Figure 6.6: The time-averaged Nusselt number compensated with the "classical" and the "ultimate" scaling in (a) and (b), respectively. The Prandtl numbers are colour-coded in the legend.

6.5.2 Ultimate Scaling

The "ultimate" Nusselt number scaling follows directly from the observation that ϵ_u and ϵ_θ scale like $(\mathrm{Ra}\,\mathrm{Pr})^{3/2}$ and the exact relations (6.21). We have that

$$\mathrm{Nu} - 1 = \frac{\epsilon_u}{\mathrm{Ra}\,\mathrm{Pr}} \propto (\mathrm{Ra}\,\mathrm{Pr})^{1/2}, \tag{6.35}$$

and the 1 on the left-hand side is negligible at large $\mathrm{Ra}\,\mathrm{Pr}$.

In Figure 6.6 (a,b), we plot the Nusselt number compensated by the "classical" scaling, $\mathrm{Nu} \propto \mathrm{Pr}^0\mathrm{Ra}^{1/3}$ and the "ultimate" scaling, $\mathrm{Nu} \propto \sqrt{\mathrm{Ra}\,\mathrm{Pr}}$, versus Ra with a range of values of Pr. As Ra increases, the Nusselt number appears to approach the ultimate rather than the classical scaling. This observation is in line with expectations as we have effectively removed the impact of boundary layers through the application of periodic boundary conditions on the computational domain. However, the seminal work of Spiegel and Kraichnan [97, 150] and GL theory [70, 71, 73, 74] both postulate the ultimate regime only for $\mathrm{Pr} \leq 1$ [38]. Figure 6.6 provides clear evidence of progress towards the ultimate regime, even for values of Pr as high as 10^2.

6.5.3 Spectra

In this section, we examine the time-averaged kinetic and potential energy spectra and spectral fluxes. To eliminate finite Rayleigh number effects and to have large enough scale separation, we focus on hyperviscous simulations (with $n = 4$ in equations (6.2)) at $\mathrm{Ra} = 9.4 \times 10^{49}$. Results with normal viscosity ($n = 1$ in equations (6.2)) at $\mathrm{Ra} = 6.2 \times 10^{11}$ are also presented.

As explained in §6.3.4, BO scaling [12, 122] posits that the ratio of the kinetic to the potential energy spectra should scale like $\widehat{E}^u/\widehat{E}^\theta \propto k^{-4/5}$ in the inertial range, since $\widehat{E}^u \propto k^{-11/5}$ and $\widehat{E}^\theta \propto k^{-7/5}$. In Figure 6.7 we plot $\langle\widehat{E}^u\rangle_t/\langle\widehat{E}^\theta\rangle_t$ compensated by $k^{4/5}$ for the hyperviscous simulations and in the inset for the runs with normal viscosity for different Prandtl numbers. The data collapse over a wide range of wavenumbers, but we can not identify a range where the predicted BO scaling is followed. Instead, we observe a $k^{-0.3}$ power-law in the inertial range for all Prandtl numbers considered, suggesting that BO scaling is not supported by our simulations. As anticipated, the $k^{-0.3}$ power-law holds true within a smaller wavenumber range for the normal viscosity simulations. Figure 6.7 also shows that for $\mathrm{Pr} \ll 1$ the kinetic energy is much larger than the potential energy at large wavenumber. This behaviour is expected as the small scales are dominated by thermal diffusivity when $\mathrm{Pr} \ll 1$. Therefore, the dissipation rate of potential energy is much larger than the dissipation rate of kinetic energy. The opposite is true for $\mathrm{Pr} \gg 1$.

In Figure 6.8 (a,b) we plot the kinetic and potential energy spectra multiplied by k^α, where α is the exponent that best compensates for the power-laws that the spectra exhibit, for $\mathrm{Pr} \in [10^{-3}, 10^2]$ as colour-coded in the legends. The hyperviscous runs are in the main plots, and normal viscosity runs in the insets. The kinetic energy spectra broadly follow a $k^{-2.3}$ power-law, while the potential energy spectra follow a $k^{-1.2}$ power-law. This behaviour is close, but not identical, to that predicted by BO theory (6.19a), where the exponents should be -2.2 and -1.4, respectively. It is also in contrast to 3D RBC with periodic boundary conditions where the kinetic and potential energies exhibit $k^{-5/3}$ spectra [14, 29, 106], similar to that in passive scalar turbulence [178] and in agreement with K41 scaling (6.17).

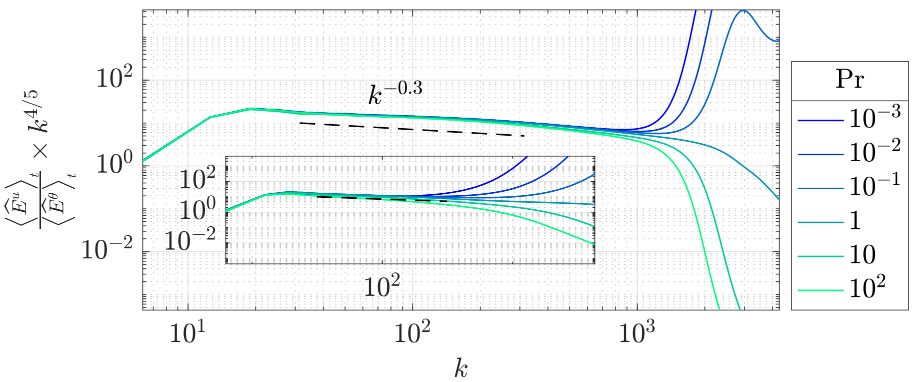

Figure 6.7: The ratio of the kinetic and potential energy spectra $\langle\widehat{E}^u\rangle_t/\langle\widehat{E}^\theta\rangle$ compensated by $k^{4/5}$ for the hyperviscous simulations with $\mathrm{Ra} = 9.4 \times 10^{49}$, $\mathrm{Rh} = (2\pi)^{5/2}$, and for different Prandtl numbers as colour-coded in the legend. The inset shows the same ratio but for runs with normal viscosity at $\mathrm{Ra} = 6.2 \times 10^{11}$. A grid is provided to guide the eye in determining how well the scaling is followed.

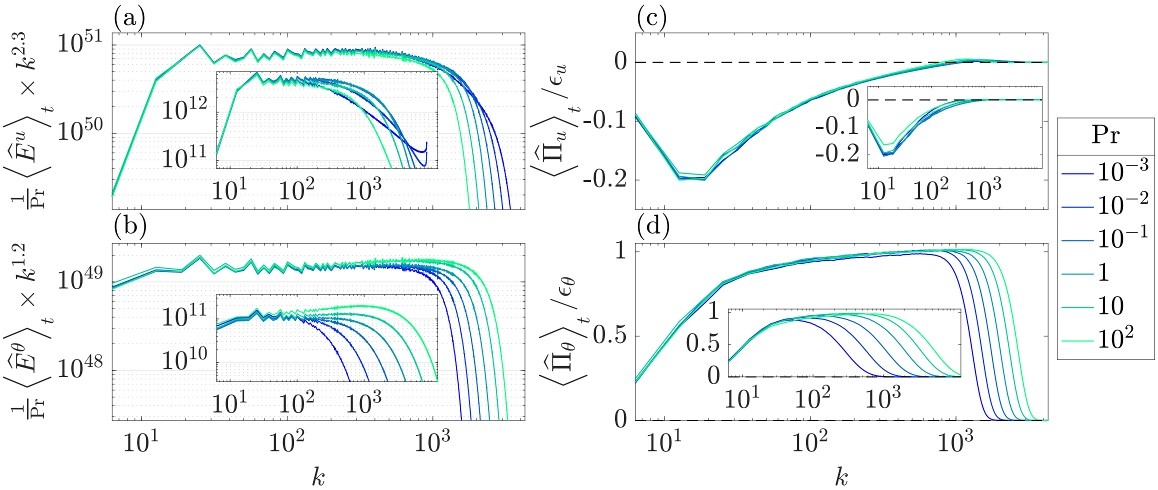

Figure 6.8: (a,b) The time-averaged spectra compensated by best fit exponents of 2.3 and 1.2, respectively, and (c,d) spectral fluxes for the runs with hyperviscosity and Ra $= 9.4 \times 10^{49}$. A grid is provided to guide the eye in determining how well the scalings are followed for each Prandtl number as colour-coded in the legend. The fluxes have been divided by the time-averaged dissipation rates. The insets shows the same quantities but for runs with normal viscosity at Ra $= 6.2 \times 10^{11}$.

To better comprehend the nature of the turbulent cascades, in Figure 6.8 (c,d), we present the kinetic and potential energy fluxes, each normalised by their respective time-averaged energy injection rates due to buoyancy. The positive potential energy flux suggests a strong direct cascade, while there is a weak inverse cascade of kinetic energy, which is typical for 2D flows [2]. For Pr $= 1$ these cascades are in qualitative agreement with [186]. The kinetic energy flux peaks at low wavenumbers, while the potential energy flux peaks at high wavenumbers. The inverse cascade of kinetic energy is not affected by the Prandtl number, and supports the observation in §6.5.1 that the kinetic energy is predominantly dissipated at large scales. However, the direct cascade of potential energy shifts to higher wavenumbers as Pr increases, along with the peak of $\langle \Pi_\theta \rangle_t$. In the inertial range of wavenumber, we note that $\partial_k \langle \Pi_u \rangle_t > 0$ and $\partial_k \langle \Pi_\theta \rangle_t > 0$. This means that energy is being extracted from these scales and transferred to large and small scales in the kinetic and potential energies, respectively.

In Figure 6.9, we present the time-averaged spectra of the terms in the kinetic and potential energy balances (6.10) for runs with hyperviscosity and Pr $= 10^{-2}$ ((a), (d)), Pr $= 1$ ((b), (e)), and Pr $= 10^2$ ((c), (f)). All terms other than the inertial terms, $\partial_k \langle \Pi_u \rangle_t$ and $\partial_k \langle \Pi_\theta \rangle_t$, are positive at all wavenumbers, and the red dots indicate when $\partial_k \langle \Pi_u \rangle_t$ and $\partial_k \langle \Pi_\theta \rangle_t$ are negative. In the kinetic energy balance, we identify three distinct wavenumber ranges, labelled I to III in the plot. In region I, the large-scale

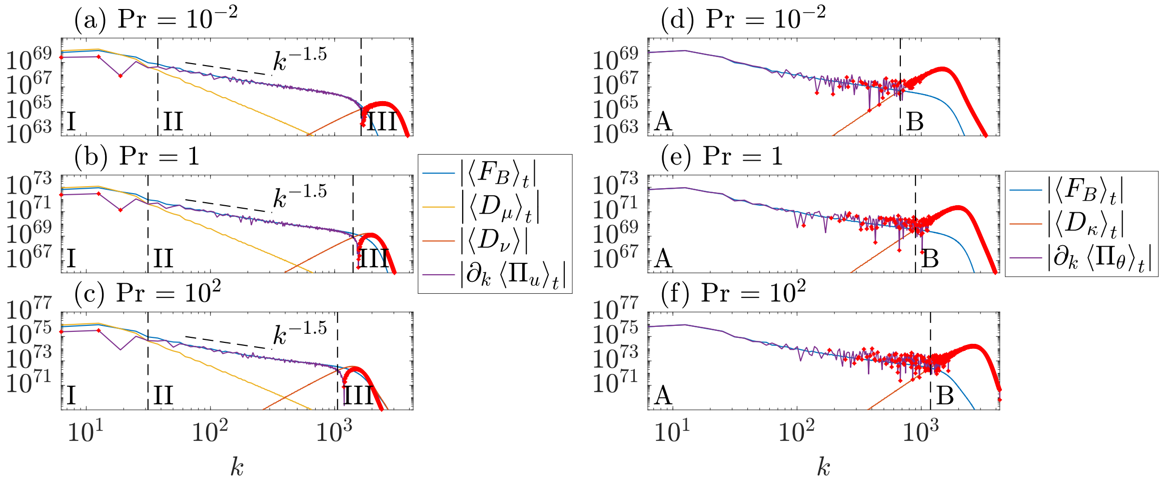

Figure 6.9: (a)–(c) Time-averaged spectra of the terms in the kinetic energy and (d)–(f) potential energy balances (6.10) for the runs with hyperviscosity, Ra $= 9.4 \times 10^{49}$, Rh $= (2\pi)^{5/2}$, and Pr $= 10^{-2}$ (a), (d), Pr $= 1$ (b), (e), and Pr $= 10^2$ (c), (f). The terms displayed in the legend are defined in (6.11), (6.14) and (6.13). In (a)–(c) and (d)–(f), we observe three and two distinct dominant balances, respectively, annotated I–III and A–B. The red dots indicate where the inertial terms become negative.

friction is balanced by buoyancy. In region II, the inertial term balances buoyancy, i.e.

$$\partial_k \langle \Pi_u \rangle_t \approx \langle F_B \rangle_t > 0, \tag{6.36}$$

explaining the k dependence of the kinetic energy flux we see in Figure 6.8 (c) in the inertial range of wavenumbers. Note that region II is largest for small Prandtl numbers, which is further accentuated in the runs with normal viscosity, as presented in Figure E.3 of Appendix E. In region III, the balance between terms depends on the Prandtl number. For Pr $= 10^{-2}$, buoyancy decays rapidly and so small-scale viscous dissipation is balanced by the inertial term, which is negative in this range of wavenumbers. As Pr increases, buoyancy becomes increasingly important at small scales, so for Pr $= 10^2$, the balance is between small-scale viscous dissipation and buoyancy rather than the inertial term, which tails off. This behaviour is shown more clearly with normal viscosity in Figure E.3 (c) of Appendix E, where the small-scale dissipation range is much larger.

In the potential energy balance, we identify two distinct wavenumber ranges, labelled A and B in Figure 6.9 (d)–(f). In these plots we observe the inertial term to be balanced by buoyancy in region A and by small-scale thermal dissipation in region B. At the high end of region A in Figure 6.9 (d)–(f), we observe that $\partial_k \langle \Pi_\theta \rangle_t$ becomes negative for some wavenumbers. This is because $\partial_k \Pi_\theta(k)$ exhibits significant fluctuations between positive and negative values over these wavenumbers. However, for the majority of the wavenumbers in region A we find that

$$\partial_k \langle \Pi_\theta \rangle_t \approx \langle F_B \rangle_t > 0. \tag{6.37}$$

This relation explains the k dependence of the potential energy flux we observe in Figure 6.8 (d) and demonstrates that the BO phenomenology, which assumes that the potential energy flux is constant, does not hold for any of the Pr numbers we studied.

Note that in the region where II and A overlap, we have $\partial_k \langle \Pi_u \rangle_t \approx \partial_k \langle \Pi_\theta \rangle_t \approx \langle F_B \rangle_t$, so $\langle \Pi_u \rangle_t - \langle \Pi_\theta \rangle_t$ is approximately constant.

6.6 Conclusions

In this chapter, we study the effects of varying Rayleigh and Prandtl numbers on the dynamics of 2D RB convection without boundaries, i.e. with periodic boundary conditions. The flow is forced by a constant average vertical temperature gradient.

First, we focus on the limits of $\mathrm{Pr} \to 0$ and $\mathrm{Pr} \to \infty$. Our findings indicate that, unless large-scale dissipation is made very strong, almost suppressing all convection, large-scale runaway solutions dominate the dynamics. Such runaway solutions at extreme Prandtl numbers have long been known, even with boundaries [81], and they have recently been studied more generally at low Rayleigh numbers [28]. Instead, we turn to finite Prandtl numbers.

In all parameter values simulated, the inequality (6.7) is violated, implying that the system admits exact single-mode solutions that grow exponentially without bound. Nevertheless, with finite Prandtl numbers, we found that non-linear interactions between modes continue to allow the system to find a statistically steady state. In general, whether or not the solution blows up must depend on the initial conditions, in a way that is not currently understood.

Examining the Prandtl and Rayleigh number dependence of the terms in the kinetic and potential energy balance, we find that $\langle E^u \rangle_t$ and $\langle E^\theta \rangle_t$ both scale with $\mathrm{Ra}\,\mathrm{Pr}$. The scaling for the kinetic energy is consistent with GL theory, but the potential energy scaling is not as GL theory predicts $\langle E^\theta \rangle_t \propto (\mathrm{Ra}\,\mathrm{Pr})^{3/4}$. However, both our observations are in agreement with the numerical results presented by Calzavarini et al. [29]. We also observe that $\epsilon_u = \epsilon_\mu$, which indicates that most of the kinetic energy injected by buoyancy is dissipated at large scales, consistent with an inverse cascade of kinetic energy.

For the small-scale dissipation, we observe $\epsilon_\nu \propto \mathrm{Pr}^2\mathrm{Ra}^{5/4} \propto \mathrm{Pr}^{13/4}\mathrm{Re}^{5/2}$ and $\epsilon_\kappa \propto (\mathrm{Ra}\,\mathrm{Pr})^{3/2} \propto \mathrm{RaRePr}^2$. The latter is consistent with GL theory [70, 71, 73, 74], while the former is in closer agreement with GL theory at the boundary layers versus the bulk. The scaling for ϵ_ν follows from the observation that enstrophy scales like $\langle\omega^2\rangle_{\boldsymbol{x},t} \propto \mathrm{Pr}\,\mathrm{Ra}^{5/4}$. The Nusselt number adheres to the ultimate scaling $\mathrm{Nu} \propto \mathrm{Pr}^{1/2}\mathrm{Ra}^{1/2}$, even at large Prandtl numbers, which was not predicted by Spiegel and Kraichnan in their seminal papers [38, 97, 150] or by GL theory.

Looking at the kinetic and potential energy spectral fluxes, we find an inverse cascade of kinetic energy and a direct cascade of potential energy in contrast to 3D RBC [170], where both the kinetic and potential energy cascade toward small scales. The inverse cascade is independent of the Prandtl number, while the peak of the potential energy flux moves to higher wavenumbers as the Prandtl number increases. The kinetic and potential energy fluxes are not constant in the inertial range because the spectrum of the buoyancy forcing term, $\langle F_B\rangle_t \propto k^{-1.5}$, is balanced by the inertial terms, which are predominantly positive in this range of wavenumbers. These two balances imply a positive slope in k for the fluxes.

The kinetic energy spectra scale as $\widehat{E}^u \propto k^{-2.3}$, which is close to the $k^{-11/5}$ predicted by BO phenomenology. However, the potential energy spectra scale as $\widehat{E}^\theta(k) \propto k^{-1.2}$, deviating from the $k^{-7/5}$ predicted by the BO scaling arguments. The deviation from the BO phenomenology is more apparent when we test the scaling $\widehat{E}^u/\widehat{E}^\theta \propto k^{-4/5}$, which our spectra do not support. Instead, our spectra align more with $\widehat{E}^u/\widehat{E}^\theta k^{-4/5} \propto k^{-0.3}$.

For the hyperviscous simulations, which have large scale separation, the power-laws in the inertial range of the kinetic and potential energy spectra appear independent of the Prandtl number. We only observe dependence on Pr at the dissipative range of wavenumbers, where viscosity and thermal diffusivity dominate dynamics. In normal viscosity simulations' spectra, Prandtl number effects are more significant due to a lack of scale separation. Consequently, the inertial range is impacted, leading to variance in the exponent when a power-law range can be discerned.

This study clearly demonstrates the necessity for large scale separation to draw clearer conclusions on the spectral dynamics and the power-law exponents of 2D RB convection. This requirement poses significant challenges for similar studies in three dimensions. Developing a phenomenology where buoyancy operates as a broadband spectral forcing is necessary to interpret current observations. Conducting numerical simulations at parameter values outside the range we explored, specifically $\mathrm{Pr} < 10^{-3}$, $\mathrm{Pr} > 10^2$ and $\mathrm{Ra} > 10^{12}$, poses significant challenges, yet would be highly beneficial to corroborate the hyperviscous simulations we performed and provide a more comprehensive view of the asymptotic regime of buoyancy-driven turbulent convection.

Chapter 7

Epilogue

In this final chapter, we first summarise briefly the main results which we have obtained. We then suggest some possible extensions and open questions, which could be considered in future work.

7.1 Summary of Results

In this thesis, we have studied 2D RB convection at a wide range of Prandtl numbers. For numerical and analytical convenience, we considered both fully periodic domains and horizontally periodic domains with free-slip top and bottom boundaries. We predominantly solved the governing equations using DNS, and used a wide range of analytical techniques to analyse the solutions.

In chapter 3, we studied the stability of the SCRS in the Prandtl-Rayleigh number plane. Our study primarily focused on the width-to-height aspect ratio $\Gamma = 2$, but we also considered the effects of varying Γ, particularly in the limiting cases where the Prandtl number is either very small or very large. We partitioned our modes into so-called "even" and "odd" modes. We showed that the SCRS consists of even modes only and no zonal modes with horizontal wavenumber zero. The zonal modes can only emerge once the SCRS has becomes unstable to odd modes.

In particular, we found that the stability boundary in the $(\mathrm{Pr}, \mathrm{Ra})$-plane at $\Gamma = 2$ has many corners and cusps corresponding to points where qualitative changes occur to the most unstable eigenfunction and that there exist three regions where the SCRS loses and subsequently regains stability as the Rayleigh number increases.

We noted that the excitation of odd modes is necessary, but not sufficient, for net zonal flow to exist. The resulting solution can either have a net, instantaneous or no zonal flow depending on the qualitative features of the most unstable eigenfunction.

For example, we observed that zonal modes are completely removed from the unstable eigenfunction at a very large, but finite, Prandtl number.

In the complementary small Prandtl number limit, we observed that the SCRS becomes unstable almost immediately as a new steady state, consisting of both even, and odd modes, and a net zonal flow, emerges in a pitchfork bifurcation. We observed a power-law $\delta\mathrm{Ra} \propto \mathrm{Pr}^2$ along the stability boundary. To explain this, we conducted a weakly non-linear analysis that yielded a two-dimensional model.

We showed that there is excellent agreement between the weakly non-linear model and the full system for the critical Rayleigh number of the initial pitchfork bifurcation, but there is some disparity in the location of a subsequent Hopf bifurcation. However, this difference is significantly reduced once first-order corrections are included in the model. Just like in the DNS, the model reveals bursting behaviour at Rayleigh numbers beyond the Hopf bifurcation. To our knowledge, our model is the first to be derived from the Boussinesq equations that display bursting without *ad hoc* closure assumptions.

As we vary Γ, we observed that the $\delta\mathrm{Ra} \propto \mathrm{Pr}^2$ power-law along the stability boundary disappears abruptly as Γ increases through the value 2.37, meaning that for large aspect ratios, the SCRS is stable until $\mathrm{Ra} \approx 5 \times 10^4$, even for very small Prandtl numbers.

In chapter 4, we studied the dynamics beyond the critical Rayleigh number at which the SCRS has become unstable.

We focused on the $\mathrm{Pr} = 30$, $\Gamma = 2$ case and observed a sequence of bifurcations, highlighted in the PDF of the largest scale mode, $\widehat{\psi}_{0,1}$, leading to reversals of a very strong zonal flow, with an intermediate state with no net zonal flow. A similar set of bifurcations were observed when $15 \leq \mathrm{Pr} \leq 100$.

Zonal flow reversals were also found when $\mathrm{Pr} = 30$ and $\Gamma = 1$. A comprehensive statistical analysis revealed that the waiting time between successive reversals is exponentially distributed and that its mean grows exponentially with the Rayleigh number.

Chapter 5 generalised our analysis from the previously studied two-dimensional flow to a quasi-two-dimensional flow by introducing a new spatial direction, z. We fixed the parameters $(\mathrm{Ra}, \mathrm{Pr}, \Gamma_x) = (10^7, 30, 2)$, and explored how narrow the domain must be in this direction to render the flow truly two-dimensional.

We focused on three different 2D background flows, namely: the SCRS, shearing, and non-shearing states. Our study revealed that the shearing and non-shearing states are much more susceptible to 3D perturbations than the SCRS. Either way, the domain needs to be very narrow in z to render the flow truly 2D.

In studying how the 3D perturbations are forced we observed that they are predominately driven by the thermal plumes and boundary layers in the background flow.

We also studied the effect of varying the strength of the zonal flow, kinetic energy in the background flow, and inducing random time dependence in the SCRS. In each study, the impact on the critical wavenumber in z, q_c, at which 3D perturbations grow was moderate, an observation particularly noteworthy given the substantial variations in the background flow. However, we did observe that a strong zonal flow can have destabilising effects at small wavenumbers.

In chapter 6, we studied RB convection with periodic boundary conditions to emulate the dynamics far from walls.

In the extreme Prandtl number limits, our findings indicated that, unless large-scale dissipation is made very strong, almost suppressing all convection, large-scale runaway solutions dominate the dynamics.

For finite Prandtl numbers, the governing equations also admits exact single-mode solutions that grow exponentially without bound. Nevertheless, we found that nonlinear interactions between modes continue to allow the system to find a statistically steady state.

Looking at the kinetic and potential energy spectral fluxes, we found an inverse cascade of kinetic energy and a direct cascade of potential energy. The inverse cascade was found to be independent of the Prandtl number, while the peak of the potential energy flux moved to higher wavenumbers as the Prandtl number increased. In addition, the kinetic and potential energy fluxes are not constant in the inertial range as they balance the broadband buoyancy forcing term.

We found that the kinetic and potential energy spectra are close, but not fully consistent when the scalings predicted by BO phenomenology. Time-averaged energies and spatiotemporally averaged terms in the energy equations are in partial agreement with GL theory, while the Nusselt number follows the ultimate scaling.

7.2 Future Work

While this thesis has provided useful insight, in particular in the development of zonal flows in 2D RB convection for a large range of Prandtl numbers, several questions re-main unanswered. In this final section, we itemise potential areas of further research, building on the results from each chapter.

Chapter 3: Onset of Zonal Modes

- In §3.5.7, we showed that SCRS is stable until $\mathrm{Ra} \approx 5 \times 10^4$ when $\Gamma = 2.37$ and $\mathrm{Pr} = 10^{-6}$. This observation poses the question of whether there exists a steady state close to $\mathrm{Ra} = \mathrm{Ra}_c$ when $\Gamma \geq 2.37$ even when the Prandtl number is formally set equal to zero.

- In §3.5.6, we showed that there is some disparity between the weakly non-linear model derived in §3.5.3 and the full system in the critical Rayleigh number at which a hopf bifurcation occurs, following two initial pitchfork bifurcations. The analysis in §B.2, where we include $\mathcal{O}(\epsilon^2)$ corrections in the weakly non-linear model, goes some way to correct this disparity. Yet, there is still work to be done here, in particular at small aspect ratios.

- While we have conducted a thorough investigation of the stability of the SCRS in $(\mathrm{Pr}, \mathrm{Ra})$-plane when $\Gamma = 2$, a natural extension of this work would consider general values of Γ. In particular, when $\Gamma \geq 2^{4/3}\sqrt{1 + 2^{2/3}}$ the SCRS consists of both odd and even modes as Ra increases past Ra_c, and it is no longer clear that the odd/even mode decomposition which proves so convenient in our set-up is still able to give some insight.

Chapter 4: Zonal Flow Reversals

- In §4.4, we noted that shearing convection appears to be the inevitable outcome for large enough Rayleigh numbers when $15 \leq \mathrm{Pr} \leq 100$. It would be interesting to explore if this holds for larger Prandtl numbers. In particular, since a key result in chapter 3 was that zonal modes disappear in the most unstable eigenfunction to the SCRS at $\mathrm{Pr} = 7 \times 10^5$.

- While the shearing mechanism provides a high-level explanation of how zonal flow is sustained, a physical mechanism to explain zonal flow reversals is still an open question. The truncated Euler equations could be one way to theoretically understand these dynamics further like in [40, 144], and we made an attempt to construct a simple stochastic process to emulate the $\widehat{\psi}_{0,1}$. We note that the dynamics of $\widehat{\psi}_{0,1}$ partially decouples from the temperature equation since buoyancy only does work on the vertical flow. One can therefore consider the ODE

$$\widehat{\psi}_{0,1}(t)_t = \eta(t) - \mathrm{Pr}\pi^2\widehat{\psi}_{0,1}(t), \quad \eta(t) = \frac{2}{\pi^2\Gamma}\langle\{\psi, \nabla^2\psi\}, \sin(\pi y)\rangle, \tag{7.1}$$

where $\langle\cdot\rangle$ is the inner product (A.2). Note that (7.1) is exact and derived from the governing equations (2.10). One can think of (7.1) as a stochastic differential equation by considering η as a stochastic noise term, whose structure should be guided by the $\langle\{\psi, \nabla^2\psi\}, \sin(\pi y)\rangle$ term from DNS. However, using this method, we were unable to produce results worth reporting in this thesis. It is however worth noting that the mechanism driving zonal flow reversals must differ markedly from the one that has been used to explain reversals of the LSC in RB convection in a box geometry with no-slip walls, where the boundary layers [153] and vortex reconnection [35] play a crucial role for reversals. With free-slip walls, it has been suggested that the nonlinearity in the temperature equation plays a vital role in the reversals of the LSC [168]. This is unlikely the case for zonal flow reversals due to the partial decoupling from the temperature equation.

- We study the emergence of zonal flow in 2D as an idealisation of zonal flows in planetary atmospheres, tokamaks, and annular cylindrical convection experiments. However, these systems are of course better modelled in a fully 3D domain, and many relevant physical effects have been emitted. Most notably, the effects of a magnetic field and rotation. For instance, in planetary atmospheres, rotation can create zonal jets without convective forces and gives the zonal flow a preferred direction [39]. No such symmetry breaking was observed in our study.

- More generally, if one were to consider a 3D flow, there is a conundrum in that although 2D and 3D DNS often compare well, or even exactly, when comparing certain quantities, such as the Nusselt number, other quantities may differ markedly.

Chapter 5: Quasi-Two-Dimensional Rayleigh-Bénard Convection

- We hypothesise that the difference in the driving mechanism of 3D perturbations over shearing and non-shearing background flows versus the SCRS may explain the similar q_c values for the shearing and non-shearing states and the substantially smaller q_c value for the SCRS, albeit this claim is conjectural and requires further investigation. The SCRS contain several symmetries (see §3.3) that the non-shearing and sharing states do not. This observation could be the starting point in such an investigation.

- In this study, we fixed the parameters $(\mathrm{Ra}, \mathrm{Pr}, \Gamma_x) = (10^7, 30, 2)$. A further study could look at the effects of varying one or a combination of these. One could also generalise the boundary conditions in z by instead considering periodic boundary conditions, allowing for a net zonal flow to develop in the z-direction.

- We only considered infinitesimal 3D perturbations, introducing no additional nonlinearities into the governing equations. One could consider the case when the 3D disturbances are non longer infinitesimal and couple to the 2D background flow.

Chapter 6: Spectra Without Boundaries

- For all the simulations in conducted this chapter, the governing equations admits exact single-mode solutions that grow exponentially without bound. A reliable way to suppress these, in particular at the extreme Prandtl numbers, remains elusive at present. In general, whether or not the solution blows up most depend on the initial conditions.

- Conducting numerical simulations in 3D or at parameter values outside the range we explored, specifically $\mathrm{Pr} < 10^{-3}$, $\mathrm{Pr} > 10^2$ and $\mathrm{Ra} > 10^{12}$, poses significant challenges, yet would be highly beneficial to corroborate the result we report in this chapter.

- Finally, while we noted that the Nusselt number adheres to the ultimate scaling in our simulations, this observation is in line with expectations as we have effectively removed the impact of boundary layers through the application of periodic boundary conditions. The transition to the ultimate regime with physically realisable boundary conditions indeed remains a highly contentious topic within the research community.

Appendix A

Computation of SCRS and its Stability

A.1 Newton Method

We wish to find a solution $(\psi^E,\, \theta^E)$ of the steady "even" problem (3.6). We expand both ψ^E and θ^E as in (2.13), i.e. in modes of the form

$$\phi_{k_x,k_y}(x,y) = \mathrm{e}^{2\pi i k_x x/\Gamma}\sin(\pi k_y y), \qquad k_x + k_y \in 2\mathbb{Z}, \tag{A.1}$$

and define the inner product

$$\langle \phi_{k_{x1},k_{y1}}, \phi_{k_{x2},k_{y2}} \rangle = \int_0^1 \int_0^\Gamma \phi_{k_{x1},k_{y1}} \phi^*_{k_{x2},k_{y2}}\, dxdy = \frac{\Gamma}{2} \delta_{k_{x1},k_{x2}} \delta_{k_{y1},k_{y2}}. \tag{A.2}$$

Note that the reflection symmetry (3.7) of the SCRS implies that the modes of ψ^E and θ^E are purely imaginary and real, respectively, which reduces the number of unknowns.

Acting with this inner product on equations (3.6) we find, for each (k_x, k_y),

$$\frac{1}{2} \sum_{\substack{k_{x1}+k_{x1}=k_x \\ |k_{y1}\pm k_{y2}|=k_y}} \widehat{\psi}_{k_{x1},k_{y1}} \widehat{\psi}_{k_{x2},k_{y2}} k^2_{k_{x2},k_{y2}} G(k_{x1}, k_{x2}, k_{y1}, k_{y2}) \\ + k_x \mathrm{RaPr} \widehat{\theta}_{k_x,k_y} - i\mathrm{Pr} k^4_{k_x,k_y} \widehat{\psi}_{k_x,k_y} = \widehat{f}_{k_x,k_y} = 0, \tag{A.3a}$$

$$\frac{i}{2} \sum_{\substack{k_{x1}+k_{x1}=k_x \\ |k_{y1}\pm k_{y2}|=k_y}} \widehat{\psi}_{k_{x1},k_{y1}} \widehat{\theta}_{k_{x2},k_{y2}} G(k_{x1}, k_{x2}, k_{y1}, k_{y2}) \\ - ik_x \widehat{\psi}_{k_x,k_y} + k^2_{k_x,k_y} \widehat{\theta}_{k_x,k_y} = \widehat{g}_{k_x,k_y} = 0, \tag{A.3b}$$

N	Ra
64	$(8\pi^4, 3\times 10^3]$
152	$(3\times 10^3, 6\times 10^5]$
256	$(6\times 10^5, 4\times 10^6]$
400	$(4\times 10^6, 10^8]$

Table A.1: Resolution ($N = N_x = N_y$) used in all computations in the DNS, Newton's method to find the SCRS, and the linear stability analysis, for Ra $\in (8\pi^4, 10^8]$ and $\Gamma = 2$.

where we have introduced the functions

$$k_{k_x,k_y} = \sqrt{\left(\frac{2\pi}{\Gamma}k_x\right)^2 + (\pi k_y)^2}, \tag{A.4a}$$

$$G(k_{x_1}, k_{y_1}, k_{x_2}, k_{y_2}, k_y) = \frac{2\pi^2}{\Gamma}\big(k_{x_1}k_{y_2}h(k_{y_2}, k_{y_1}, k_y) - k_{y_1}k_{x_2}h(k_{y_1}, k_{y_2}, k_y)\big), \tag{A.4b}$$

$$h(x,y,z) = \begin{cases} -1 & \text{if } x = y + z, \\ 1 & \text{otherwise.} \end{cases} \tag{A.4c}$$

The quadratic system of algebraic equations (A.3) is solved using Newton's method, namely

$$v_{n+1} = v_n - J^{-1}(v_n)F(v_n), \tag{A.5}$$

where v_n is a vector of the ψ and θ modes at iteration n, $F(v_n)$ and $J(v_n)$ are the left-hand side of (A.3) and its Jacobian evaluated at v_n, respectively, i.e.

$$v_n = \begin{pmatrix} \mathcal{I}(\widehat{\psi}_{1,1}) \\ \mathcal{I}(\widehat{\psi}_{3,1}) \\ \vdots \\ \mathcal{R}(\widehat{\theta}_{1,1}) \\ \vdots \end{pmatrix}, \; F(v_n) = \begin{pmatrix} \widehat{f}_{1,1} \\ \widehat{f}_{3,1} \\ \vdots \\ \widehat{g}_{1,1} \\ \vdots \end{pmatrix}, \; J(v_n) = \begin{pmatrix} \frac{\partial \widehat{f}_{1,1}}{\partial \mathcal{I}(\widehat{\psi}_{1,1})} & \frac{\partial \widehat{f}_{1,1}}{\partial \mathcal{I}(\widehat{\psi}_{3,1})} & \cdots & \frac{\partial \widehat{f}_{1,1}}{\partial \mathcal{R}(\widehat{\theta}_{1,1})} & \cdots \\ \frac{\partial \widehat{f}_{3,1}}{\partial \mathcal{I}(\widehat{\psi}_{1,1})} & \ddots & & & \\ \vdots & & & & \\ \frac{\partial \widehat{g}_{1,1}}{\partial \mathcal{I}(\widehat{\psi}_{1,1})} & & & & \\ \vdots & & & & \end{pmatrix}. \tag{A.6}$$

For all computations of the SCRS with $\Gamma = 2$, which constitute the majority of computation in this study, we use an equal number N of Fourier modes in both x and y. So that our results are consistent with those from the DNS, we employ the two-thirds dealiasing rule, meaning that the largest retained wavenumbers in x and y are $N/3$ and $2N/3$, respectively. The values of N used for different values of Ra are listed in Table A.1.

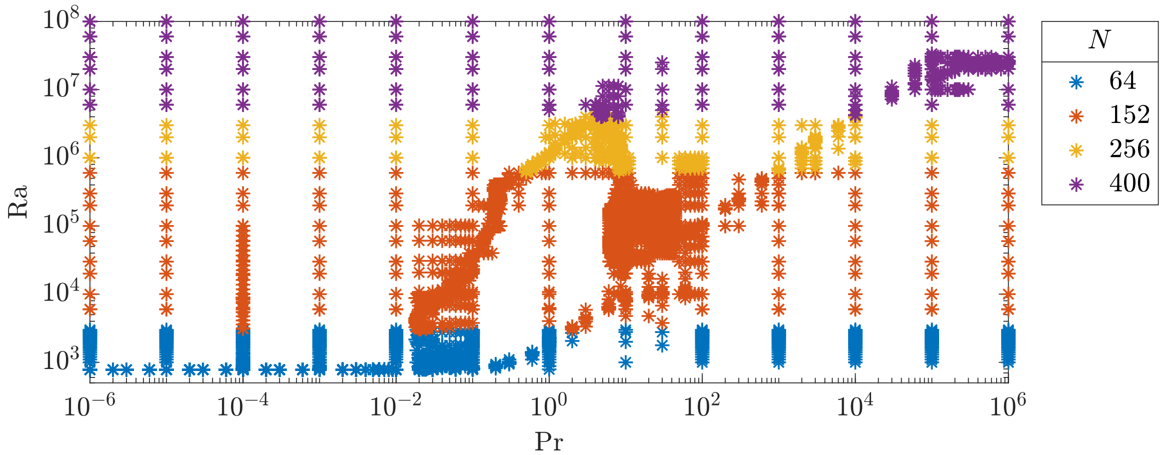

Figure A.1: All SCRS instances calculated with $\Gamma = 2$ in the $(\mathrm{Pr}, \mathrm{Ra})$-plane. Resolutions ($N = N_x = N_y$) are in line with Table A.1 and are colour coded in the legend.

For $\mathrm{Ra} = \mathrm{Ra}_c + r\epsilon^2$, $\epsilon \ll 1$, the SCRS can be found analytically to $\mathcal{O}(\epsilon^2)$ with the weakly non-linear analysis outlined in §3.5.3, which is used as the initial guess v_0 close to the onset. We then use continuation to gradually vary both Ra and Pr whilst increasing N with Ra. All instances computed with $\Gamma = 2$ are shown in Figure A.1.

To validate our computations of the SCRS, in Tables A.2–A.4 we list the Nusselt number (Nu) of the SCRS for parameter values in the range

$$(\mathrm{Pr}, \mathrm{Ra}) \in [10^{-6}, 10^6] \times (8\pi^4, 10^8]. \tag{A.7}$$

We recall from §2.2 that the Nusselt number is defined as the ratio of total mean heat flux in the vertical direction to the flux from conduction alone. It can evaluated using

$$\mathrm{Nu} = 1 + \langle \psi_x^E \theta^E \rangle, \tag{A.8}$$

where ψ^E and θ^E are (dimensionless) SCRS solutions to the steady "even" problem (3.6) and $\langle \cdot \rangle$ indicates an average over space. Table A.5 lists the Nusselt number from the results presented in [182] with $\mathrm{Ra} \in [10^8, 10^3]$ and $\mathrm{Pr} \in [10^{-2}, 10^2]$. There is excellent agreement with the corresponding results presented in Table A.3.

Ra	N	Nu			
		$\mathrm{Pr} = 10^{-6}$	$\mathrm{Pr} = 10^{-5}$	$\mathrm{Pr} = 10^{-4}$	$\mathrm{Pr} = 10^{-3}$
10^3	64	1.46633	1.46633	1.46633	1.46633
2×10^3	64	2.54127	2.54127	2.54127	2.54124
3×10^3	64	3.11158	3.11158	3.11158	3.11153
6×10^3	152	4.15903	4.15903	4.15902	4.15895
10^4	152	5.08008	5.08008	5.08007	5.07999
2×10^4	152	6.61094	6.61094	6.61093	6.61084
3×10^4	152	7.68231	7.68231	7.68230	7.68220
6×10^4	152	9.88104	9.88104	9.88103	9.88093
10^5	152	11.8579	11.8579	11.8579	11.8578
2×10^5	152	15.1387	15.1387	15.1386	15.1385
3×10^5	152	17.4397	17.4397	17.4397	17.4396
6×10^5	152	22.1706	22.1706	22.1706	22.1705
10^6	256	26.4286	26.4286	26.4286	26.4285
2×10^6	256	33.4971	33.4971	33.4971	33.4970
3×10^6	256	38.4560	38.4560	38.4560	38.4559
6×10^6	400	48.6515	48.6515	48.6515	48.6514
10^7	400	57.8266	57.8266	57.8265	57.8264
2×10^7	400	73.0618	73.0618	73.0617	73.0616
3×10^7	400	83.7543	83.7543	83.7543	83.7542
6×10^7	400	105.699	105.699	105.699	105.699
10^8	400	125.102	125.102	125.102	125.102

Table A.2: The value of the Nusselt number (Nu) for the SCRS with $\mathrm{Ra} \in [10^3, 10^8]$, $\mathrm{Pr} \in [10^{-6}, 10^{-3}]$ and $\Gamma = 2$. The resolutions ($N_x = N_y = N$) are also given.

Ra	N	Nu				
		$\mathrm{Pr} = 10^{-2}$	$\mathrm{Pr} = 10^{-1}$	$\mathrm{Pr} = 1$	$\mathrm{Pr} = 10$	$\mathrm{Pr} = 10^{2}$
10^3	64	1.46630	1.46614	1.46687	1.46716	1.46718
2×10^3	64	2.54093	2.53805	2.53065	2.53948	2.54099
3×10^3	64	3.11103	3.10613	3.08042	3.09180	3.09613
6×10^3	152	4.15820	4.15066	4.08758	4.05554	4.06805
10^4	152	5.07914	5.07051	4.98831	4.86435	4.88129
2×10^4	152	6.60992	6.60055	6.50471	6.18817	6.19053
3×10^4	152	7.68126	7.67164	7.57095	7.12370	7.09066
6×10^4	152	9.87995	9.87001	9.76305	9.10021	8.91216
10^5	152	11.8568	11.8467	11.7360	10.9457	10.5267
2×10^5	152	15.1375	15.1271	15.0121	14.0979	13.1717
3×10^5	152	17.4386	17.4280	17.3108	16.3403	15.0125
6×10^5	152	22.1694	22.1584	22.0380	20.9875	18.8001
10^6	256	26.4275	26.4165	26.2929	25.1935	22.2598
2×10^6	256	33.4959	33.4849	33.3580	32.2031	28.2230
3×10^6	256	38.4548	38.4437	38.3150	37.1323	32.6025
6×10^6	400	48.6503	48.6388	48.5076	47.2839	42.0018
10^7	400	57.8253	57.8138	57.6805	56.4309	50.7119
2×10^7	400	73.0605	73.0491	72.9134	71.6332	65.4185
3×10^7	400	83.7531	83.7419	83.6060	82.3098	75.8429
6×10^7	400	105.698	105.688	105.560	104.250	97.3668
10^8	400	125.101	125.093	124.983	123.711	116.541

Table A.3: The value of the Nusselt number (Nu) for the SCRS with $\mathrm{Ra} \in [10^3, 10^8]$, $\mathrm{Pr} \in [10^{-2}, 10^2]$ and $\Gamma = 2$. The resolutions ($N_x = N_y = N$) are also given.

Ra	N	Nu $\mathrm{Pr} = 10^3$	$\mathrm{Pr} = 10^4$	$\mathrm{Pr} = 10^5$	$\mathrm{Pr} = 10^6$
10^3	64	1.46719	1.46719	1.46719	1.46719
2×10^3	64	2.54114	2.54116	2.54116	2.54116
3×10^3	64	3.09659	3.09664	3.09664	3.09664
6×10^3	152	4.06959	4.06975	4.06976	4.06977
10^4	152	4.88409	4.88438	4.88441	4.88441
2×10^4	152	6.19538	6.19591	6.19596	6.19597
3×10^4	152	7.09670	7.09740	7.09748	7.09748
6×10^4	152	8.91937	8.92044	8.92055	8.92056
10^5	152	10.5325	10.5339	10.5341	10.5341
2×10^5	152	13.1660	13.1680	13.1683	13.1683
3×10^5	152	14.9872	14.9898	14.9901	14.9901
6×10^5	152	18.6827	18.6863	18.6868	18.6869
10^6	256	21.9674	21.9716	21.9724	21.9725
2×10^6	256	27.3643	27.3671	27.3685	27.3687
3×10^6	256	31.1230	31.1211	31.1231	31.1233
6×10^6	400	38.8158	38.7834	38.7868	38.7873
10^7	400	45.7362	45.6338	45.6387	45.6393
2×10^7	400	57.3332	56.9488	56.9556	56.9567
3×10^7	400	65.6360	64.8617	64.8686	64.8702
6×10^7	400	83.3475	81.0633	81.0635	81.0664
10^8	400	99.9470	95.4377	95.4182	95.4226

Table A.4: The value of the Nusselt number (Nu) for the SCRS with $\mathrm{Ra} \in [10^3, 10^8]$, $\mathrm{Pr} \in [10^3, 10^6]$ and $\Gamma = 2$. The resolutions ($N_x = N_y = N$) are also given.

Ra	$N_x \times N_y$	Nu $\mathrm{Pr} = 10^{-2}$	$\mathrm{Pr} = 10^{-1}$	$\mathrm{Pr} = 1$	$\mathrm{Pr} = 10$	$\mathrm{Pr} = 10^2$
10^3	128×65	1.46630	1.46614	1.46687	1.46716	1.46718
10^4	128×65	5.07914	5.07051	4.98831	4.86435	4.88129
10^5	128×65	11.8568	11.8467	11.7360	10.9457	10.5267
10^6	256×97	26.4274	26.4164	26.2929	25.1935	22.2598
10^7	512×129	57.8250	57.8132	57.6802	56.4307	50.7115
10^8	512×129	125.484	125.472	125.330	123.991	116.909

Table A.5: These results are taken from [182] and show the value of the Nusselt number (Nu) for the SCRS with $\mathrm{Ra} \in [10^3, 10^8]$, $\mathrm{Pr} \in [10^{-2}, 10^2]$ and $\Gamma = 2$. The resolution of Fourier modes (N_x) and Chebyshev collocation points (N_y) is also given. There is excellent agreement with the results we calculated in Table A.3.

A.2 Stability Analysis

Here, we provide further details of the linear stability analysis discussed in §3.4. For given Ra and Pr, we construct a steady solution (ψ^E, θ^E) to the even system (3.6) as described in §A.1. Odd perturbations to this steady state satisfy the "odd" part of the Boussinesq equations, namely the linear, time-autonomous system of PDEs (3.4). We make the ansatz (3.8) and act on (3.4) with the inner product (A.2) to obtain an eigenvalue problem for the odd growth rate σ^o, namely

$$\frac{i}{2} \sum_{\substack{k_{x_o}+k_{x_E}=k_x \\ |k_{y_o}\pm k_{y_E}|=k_y}} \widehat{\psi}^o_{k_{x_o},k_{y_o}} \widehat{\psi}^E_{k_{x_E},k_{y_E}} G(k_{x_E}, k_{y_E}, k_{x_o}, k_{y_o}, k_y) \left[k^2_{k_{x_o},k_{y_o}} - k^2_{k_{x_E},k_{y_E}}\right] \\ - ik_x \mathrm{RaPr} \widehat{\theta}^o_{k_x,k_y} - \mathrm{Pr} k^4_{k_x,k_y} \widehat{\psi}^o_{k_x,k_y} = \sigma^o k^2_{k_x,k_y} \widehat{\psi}^o_{k_x,k_y}, \quad \text{(A.9a)}$$

$$\frac{i}{2} \sum_{\substack{k_{x_o}+k_{x_E}=k_x \\ |k_{y_o}\pm k_{y_E}|=k_y}} \left[\widehat{\theta}^o_{k_{x_o},k_{y_o}} \widehat{\psi}^E_{k_{x_E},k_{y_E}} - \widehat{\psi}^o_{k_{x_o},k_{y_o}} \widehat{\theta}^E_{k_{x_E},k_{y_E}}\right] G(k_{x_E}, k_{y_E}, k_{x_o}, k_{y_o}, k_y) \\ + ik_x \widehat{\psi}^o_{k_x,k_y} - k^2_{k_x,k_y} \widehat{\theta}^o_{k_x,k_y} = \sigma^o \widehat{\theta}^o_{k_x,k_y}. \quad \text{(A.9b)}$$

where k^2, G and h are as in (A.4).

Similarly, for even perturbations, we let $\psi = \psi^E + \delta\psi^e e^{\sigma^e t}$ and $\theta = \theta^E + \delta\theta^e e^{\sigma^e t}$, and linearise (3.5) with respect to δ to obtain the same system as in (A.9), but with $o \mapsto e$.

To check that our stability analysis is giving the correct results, we compare them with those obtained from the DNS. In the DNS, we initiate the fields at the SCRS with a small perturbation of odd modes. We then determine the growth rate $(\mathcal{R}(\sigma))$ of the odd modes by tracking $\widehat{\psi}_{0,1}$. The frequency $(f = \mathcal{I}(\sigma)/2\pi)$ is found by computing the FFT of the time series. In Table A.6, we see that there is excellent agreement between DNS and stability analysis for Rayleigh numbers close to the stability boundary where the SCRS becomes unstable to odd perturbations and $\mathrm{Pr} \in \{10^{-2}, 10^{-1}, 1, 10\}$.

To further illustrate this point, in Figure A.2, we plot the time series of $\widehat{\psi}_{0,1}$ from the DNS (red full) alongside the growth rate predicted by the linear stability analysis (black dashed). In Figure A.3, we plot the FFT of $\widehat{\psi}_{0,1}$ from the DNS (red full) with the predicted frequency from the linear stability analysis (black dashed). In Figure A.4, we show an extension of the times series presented in Figure 3.7 to clearly illustrate the exponential growth and decay of $\widehat{\psi}_{0,1}$ close to the point q_3. In all cases, we observe that the stability analysis provides excellent predictions of the linear growth rate of small perturbations to the SCRS. We can therefore be confident that both the stability analysis and DNS are working well.

Pr	Ra	$\mathcal{R}(\sigma_{\mathrm{DNS}})$	f_{DNS}	$\mathcal{R}(\sigma_{\mathrm{SA}})$	f_{SA}
10^{-2}	7.85×10^2	-1.21×10^{-3}	-	-1.21×10^{-3}	-
	7.86×10^2	1.62×10^{-3}	-	1.62×10^{-3}	-
10^{-1}	3.7×10^4	-1.10×10^{-2}	-	-1.10×10^{-2}	-
	3.8×10^4	2.43×10^{-3}	-	2.43×10^{-3}	-
1	1.1×10^6	-1.19	8.18	-1.23	8.17
	1.2×10^6	1.42	8.39	1.37	8.33
10	3.2×10^4	-3.41×10^{-1}	24.5	-3.37×10^{-1}	24.5
	3.3×10^4	4.95×10^{-1}	24.9	4.99×10^{-1}	24.9

Table A.6: The growth rate ($\mathcal{R}(\sigma)$) and frequency (f) of an odd perturbation added to the SCRS as calculated from the DNS and the linear stability analysis. Both σ and f are non-dimensionalised with respect to the thermal diffusive time-scale (d^2/κ).

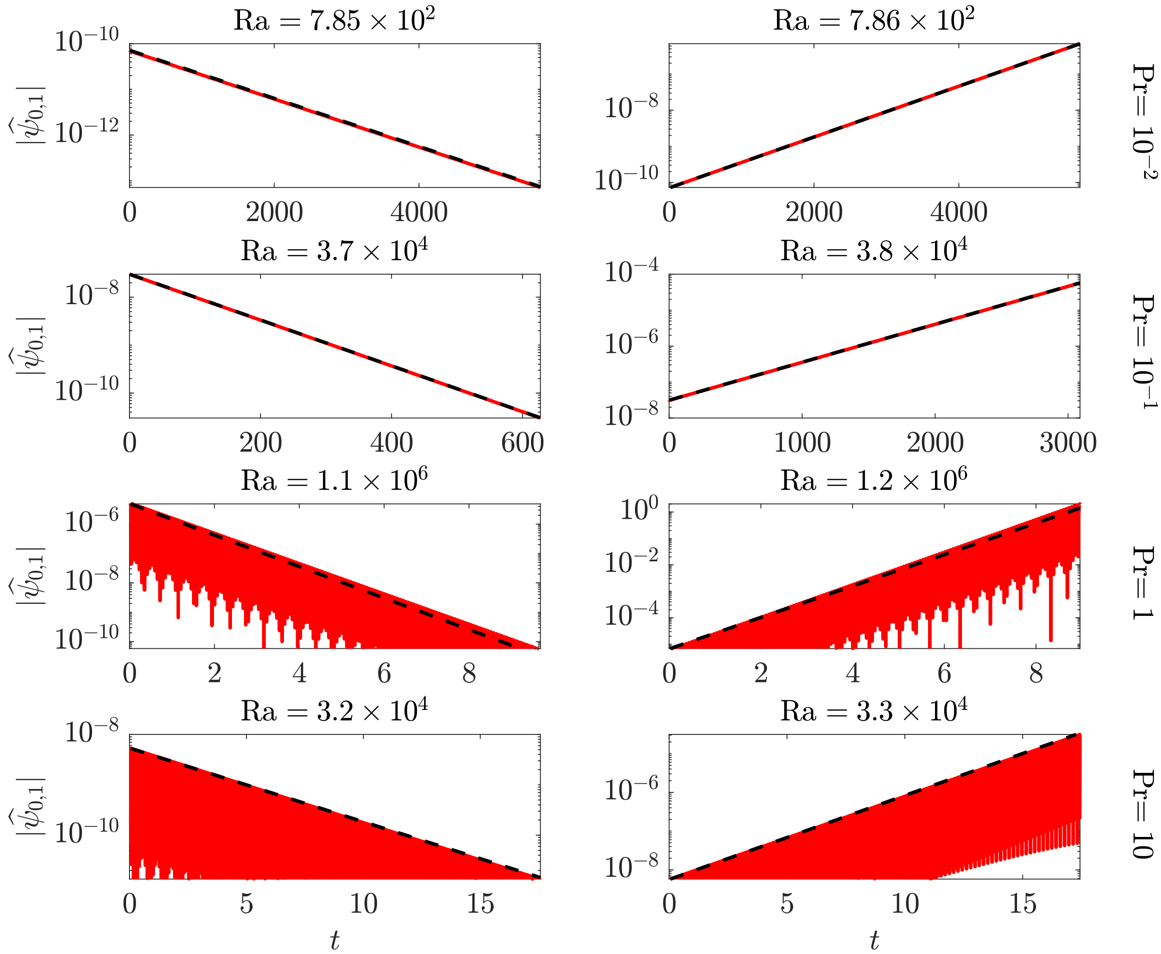

Figure A.2: Time series of $\widehat{\psi}_{0,1}$ from DNS (red full) compared with the predicted growth rate from the linear stability analysis (black dashed).

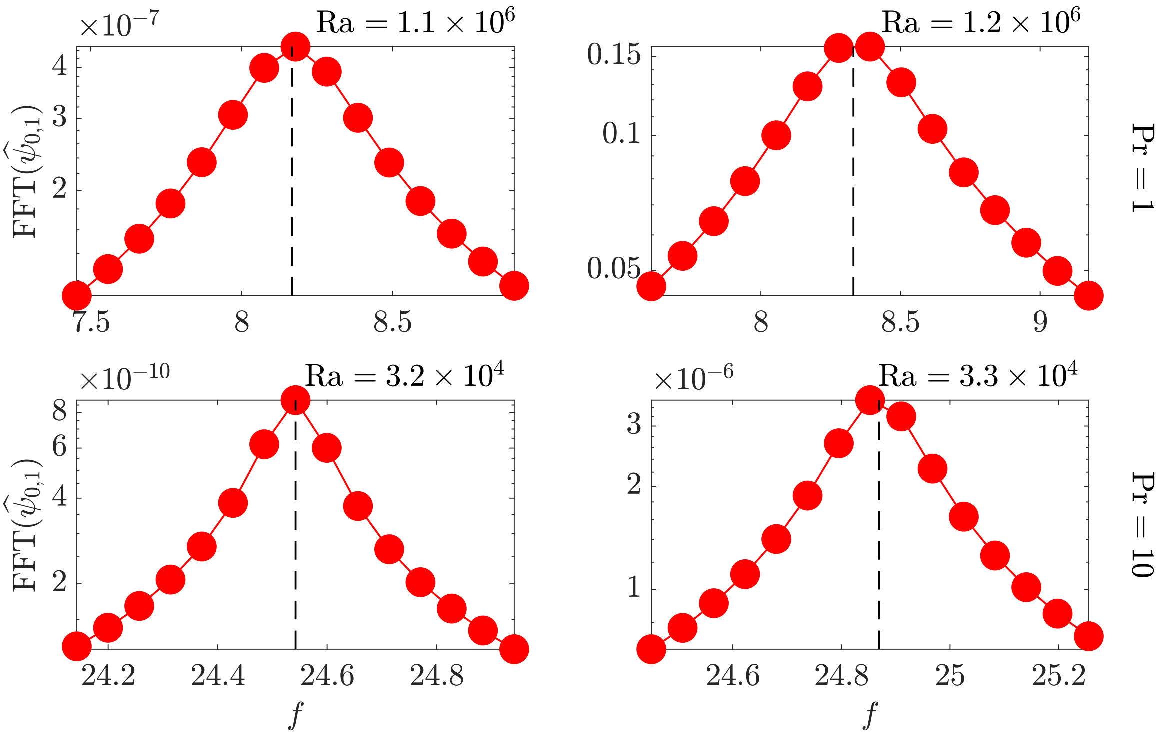

Figure A.3: The FFT of $\widehat{\psi}_{0,1}$ from the DNS (red full) with the predicted frequency from the linear stability analysis (black dashed).

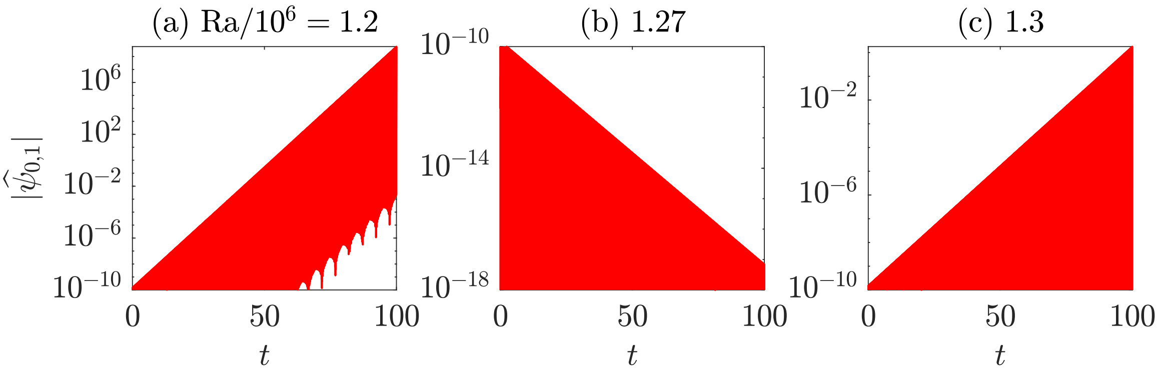

Figure A.4: An extension of the time series presented in Figure 3.7. We fix Pr = 8.57.

Appendix B

Weakly Non-Linear Analysis

B.1 Leading-Order Analysis

In this appendix, we provide some details on the construction of the eigenvalue problem (3.33) and the derivation of the amplitude equation (3.36) for the odd modes.

First, substitution of the decomposition (3.32) into the first-order odd equation (3.31) results in the linear system

$$\frac{\mathrm{d}\widehat{\psi}_{k_x,k_y}}{\mathrm{d}\tau_O} = A(\tau_E) \sum_{(n,m)\in S} \frac{\pi\Gamma}{2}\left(k_{n,m}^2 - \frac{k_{1,1}^4}{k_{n,m}^2}\right)\big(nh(n,k_x,1) - mh(m,k_y,1)\big)\widehat{\psi}_{n,m} + \frac{\Gamma}{2}\left(\frac{4\pi^2\mathrm{Ra}_c k_x^2}{\Gamma^2 k_{k_x,k_y}^4} - k_{k_x,k_y}^2\right)\widehat{\psi}_{k_x,k_y}, \quad \text{(B.1)}$$

where S denotes the set

$$S = \big\{(k_x+1,k_y+1),(k_x-1,k_y+1),(k_x+1,k_y-1),(k_x-1,k_y-1)\big\}, \quad \text{(B.2)}$$

and k_{k_x,k_y}^2 and h are as in (A.4). The first and second terms on the right-hand side of equation (B.1) respectively define the elements of the matrix M and of the diagonal matrix D in equation (3.33), which takes the form

$$\epsilon^2 \frac{\mathrm{d}\boldsymbol{\psi}_1^O}{\mathrm{d}\tau_E} = \big(A(\tau_E)M + D\big)\boldsymbol{\psi}_1^O \quad \text{(B.3)}$$

on the slow time-scale τ_E.

We seek the solution for $\boldsymbol{\psi}_1^O$ as a WKB asymptotic expansion of the form

$$\boldsymbol{\psi}_1^O(\tau_E) \sim \mathrm{e}^{\varphi(\tau_E)/\epsilon^2}\boldsymbol{C}(\tau_E;\epsilon) \sim \mathrm{e}^{\varphi(\tau_E)/\epsilon^2}\sum_{n\in\mathbb{N}}\boldsymbol{C}_n(\tau_E)\epsilon^{2n}, \quad \text{(B.4)}$$

following which (B.3) becomes

$$\left(\dot{\varphi}I - A(\tau_E)M - D\right)\boldsymbol{C} + \epsilon^2\dot{\boldsymbol{C}} = \mathbf{0}. \quad \text{(B.5)}$$

To leading order in ϵ, we find that $\dot{\varphi} = \sigma(A)$ and $\boldsymbol{C}_0 = b(\tau_E)\boldsymbol{v}(A)$, where σ and $\boldsymbol{v}$ satisfy the eigenvalue problem

$$(\sigma I - AM - D)\,\boldsymbol{v} = \boldsymbol{0}. \tag{B.6}$$

For a modal truncation such that our system is of size N, we (in general) have N eigenvalues $\sigma_j(A)$, ordered such that $\mathcal{R}(\sigma_j(A)) \geq \mathcal{R}(\sigma_{j+1}(A))$, and corresponding eigenvectors $\boldsymbol{v}_j(A)$, assumed to be normalised such that $\|\boldsymbol{v}_j(A)\|_{l^2} = 1$. The general leading order solution for $\boldsymbol{\psi}_1^O$ is then

$$\boldsymbol{\psi}_1^O(\tau_E) \sim \sum_{j=1}^{N} b_j(\tau_E)\mathrm{e}^{\varphi_j(\tau_E)/\epsilon^2}\boldsymbol{v}_j\big(A(\tau_E)\big), \tag{B.7}$$

with $\dot{\varphi}_j(\tau_E) = \sigma_j(A(\tau_E))$.

Since $\mathcal{R}(\sigma_j) \geq \mathcal{R}(\sigma_{j+1})$, the solution (B.7) is dominated by the first term in the sum. In fact, we find that the dominant eigenvalue σ_1 is real and that $\mathcal{R}(\sigma_2) < 0$, meaning that all terms except the first are exponentially small after a short transient. We thus have

$$\boldsymbol{\psi}_1^O(\tau_E) \sim B(\tau_E)\boldsymbol{v}_1\big(A(\tau_E)\big), \tag{B.8}$$

where the leading-order amplitude is given by $B(\tau_E) = b_1(\tau_E)e^{\varphi_1(\tau_E)/\epsilon^2}$. Taking derivatives with respect to τ_E leaves us with

$$\epsilon^2\dot{B}(\tau_E) \sim \sigma_1\big(A(\tau_E)\big)B + O(\epsilon^2), \tag{B.9}$$

which is equivalent to equation (3.36).

B.2 First-Order Corrections

In the above analysis, the evolution equation for the prefactor b_1 has not been included, as it does not affect the leading-order evolution of B. However, we will now show that it does affect the value of $r = \delta Ra Pr^{-2}$ at which the mixed steady state loses stability. The evolution equation for b_1 is derived from the solvability condition for $\boldsymbol{C}_1$, where at $\mathcal{O}(\epsilon^2)$, we have

$$(\sigma_1 I - AM - D)\boldsymbol{C}_1 = -\dot{\boldsymbol{C}}_0. \tag{B.10}$$

Since $\sigma_1 I - AM - D$ is singular, the corresponding adjoint problem,

$$(\sigma_1 I - AM^* - D)\boldsymbol{y}_1 = \boldsymbol{0}, \tag{B.11}$$

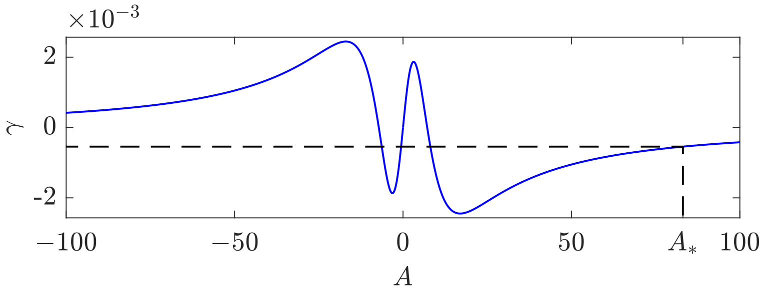

Figure B.1: The function $\gamma(A)$ as it appears in (B.15) with $\Gamma = 2$. The value of A in the mixed steady state is $A_* = 83.1$ and $\gamma(A_*) = -5.43 \times 10^{-4}$.

admits non-trivial solutions. The solvability condition for (B.10) is then

$$\langle \boldsymbol{y}_1, \dot{\boldsymbol{C}}_0 \rangle = \dot{b}_1 \langle \boldsymbol{y}_1, \boldsymbol{v}_1 \rangle + b_1 \dot{A} \langle \boldsymbol{y}_1, \boldsymbol{v}_1' \rangle = 0, \tag{B.12}$$

where $\dot{} = d/d\tau_E$ and $' = d/dA$. Now we calculate $\boldsymbol{v}_1'$ numerically and hence the $\mathcal{O}(\epsilon^2)$ correction to (B.9)

$$\epsilon^2 \dot{B} = \left(\sigma_1 + \epsilon^2 \frac{\dot{b}_1}{b_1} \right) B = \left(\sigma_1(A) - \epsilon^2 \gamma(A) \dot{A} \right) B, \tag{B.13}$$

where we set

$$\gamma(A) = \frac{\langle \boldsymbol{y}, \boldsymbol{v}_1' \rangle}{\langle \boldsymbol{y}, \boldsymbol{v}_1 \rangle}. \tag{B.14}$$

In summary, our system now looks like

$$\dot{A} = rA - A^3 - B^2 \lambda(A), \tag{B.15a}$$
$$\epsilon^2 \dot{B} = (\sigma_1(A) - \epsilon^2 \gamma(A) \dot{A}) B, \tag{B.15b}$$

where in addition to the scaling (3.39), we have set $\gamma = \widehat{\gamma}/a$ and dropped the hats. In Figure B.1, we plot the function γ as it appears in (B.15). Note that the addition of γ does not change the steady-state values of A and B, but it does change the value of r at which the mixed steady state

$$A = A_*, \quad \sigma_1(A_*) = 0, \tag{B.16a}$$
$$B = B_* = \sqrt{(rA_* - A_*^3)/\lambda(A_*)} \tag{B.16b}$$

loses stability. To illustrate this effect, we perturb about the steady-state with

$$A = A_* + \alpha, \quad B = B_* + \beta. \tag{B.17}$$

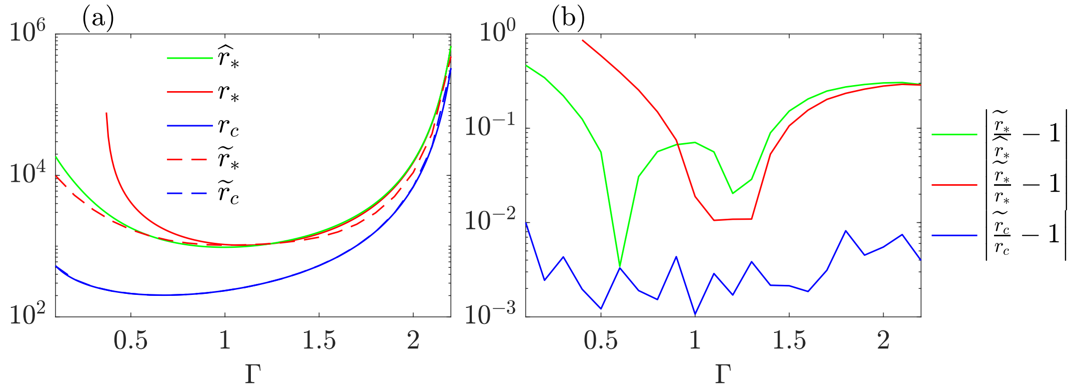

Figure B.2: (a) r_c and r_*, from the the weakly non-linear model in §3.5.3, $\widetilde{r}_c$ and $\widetilde{r}_*$, from the full system (2.10) with $\mathrm{Pr} = 10^{-3}$, and $\widehat{r}_*$ from the revised weakly non-linear model (B.15) versus aspect ratio Γ. (b) error plot of quantities in (a).

Linearising with respect to α and β yields the system

$$\begin{pmatrix} \dot{\alpha} \\ \dot{\beta} \end{pmatrix} = \begin{pmatrix} r - 3A_*^2 - B_*^2\lambda'(A_*) & -2B_*\lambda(A_*) \\ \sigma'(A_*)B_*\epsilon^{-2} + \gamma(A_*)B_*(B_*^2\lambda'(A_*) + 3A_*^2 - r) & 2\gamma(A_*)B_*^2\lambda(A_*) \end{pmatrix} \begin{pmatrix} \alpha \\ \beta \end{pmatrix}. \tag{B.18}$$

The mixed steady state loses stability when the trace of the matrix in (B.18) equals zero, which occurs at

$$r = \widehat{r}_* = A_*^2 + \frac{2A_*^2\lambda(A_*)}{2A_*\lambda(A_*)\gamma(A_*) + \lambda(A_*) - A_*\lambda'(A_*)}. \tag{B.19}$$

In the weakly non-linear model presented in §3.5.3 we obtained the stability threshold with $\gamma(A_*)$ set to zero in (B.19).

Figure B.2 is an updated version of Figure 3.15. In Figure B.2 (a) we plot r_c and r_* from the system presented in §3.5.3, $\widetilde{r}_c$ and $\widetilde{r}_*$, from the full system (2.10), and we have added $\widehat{r}_*$ from (B.19). The error ratios are shown in Figure B.2 (b). First, we note that the r at which the SCRS loses stability to the mixed steady state in the §3.5.3 system, r_c, is unchanged due to the correction presented here. However, r_* and $\widehat{r}_*$ do differ. Most notably, $\widehat{r}_*$ does not disappear at small aspect ratios, a significant improvement from the leading-order model which disappeared at $\Gamma = 0.37$. For larger Γ, the model continues to estimate $\widetilde{r}_*$ well.

To summarise, even though the evolution of b_1 does not affect the leading-order evolution of B, it does affect the r at which the mixed steady state loses stability, and provides a better match with the full system, in particular for small Γ.

Appendix C

Direct Numerical Simulations

C.1 Parallelisation and Numerical Recipe

The objective of this section is to present an overview of the Direct Numerical Simulations (DNS) code, which forms the basis for many of the results detailed in this thesis. This DNS is an adaptation of the MPI scheme for scalable parallel pseudospectral computations for fluid turbulence by Gómez et al. [67] written in Fortran and run on multiple CPUs. It integrates the 2D Boussinesq equations using the pseudospectral method [123] where both the streamfunction, ψ, and perturbation from the steady state temperature, θ, are expanded in the Fourier-sine basis (2.13). Pseudospectral methods provide a very useful tool to study the problem because of their computational efficiency and high-order numerical convergence. The governing equations are evolved in spectral space, while non-linear terms are calculated in physical space and then transformed to spectral space using a fast Fourier transform (FFT) [56] with computational complexity $N \log(N)$, where N is the linear resolution.

Both ψ and θ can be thought of as rectangular arrays of $N_x \times N_y$ real numbers, where N_x and N_y are the spatial resolutions on x and y, respectively. The parallelisation is done by giving each processor a so-called "slab" of size $N_x \times M$, where $M = N_y/N_{MPI}$ and N_{MPI} is the number of processors, as visualised in Figure C.1. However, pseudospectral methods require global spectral transforms, i.e. one that considers the entire data set at once when performing the transformation. This is achieved by first doing a 1D FFT in x, transforming the $N_x \times M$ array into one of size $(N_x/2+1) \times M$. The array size has now decreased: only half of the complex modes are needed since the physical flow fields are real. To do the FFT in y, an all-to-all communication is performed, so that the data can be partitioned into slabs of size $P \times N_y$, where $P = (N_x/2+1)/N_{MPI}$. Each processor now holds P complex modes in the Fourier-sine expansion of ψ and θ.

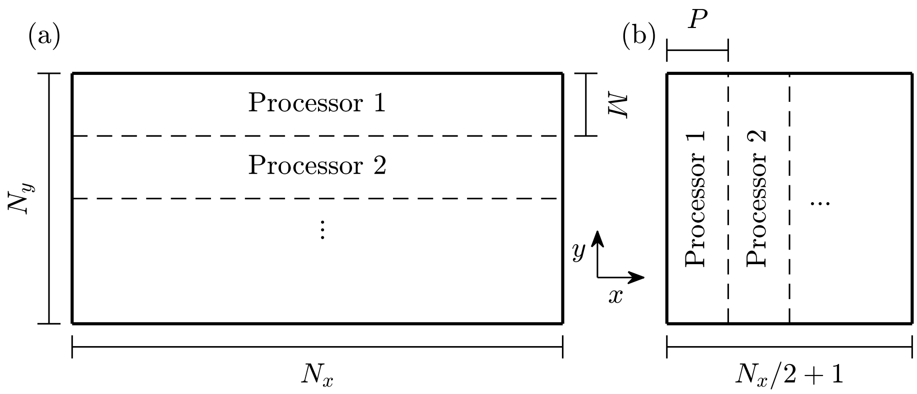

Figure C.1: (a) Shows the slab decomposition before the FFT in x. Each processor works on a slab of size $N_x \times M$, where $M = N_y/N_{MPI}$. The FFT yields partially transformed data of size $(N_x/2+1) \times M$, in each processor. To do the FFT in y, an all-to-all communication is done and the data is transformed into the slab decomposition in (b). Each processor works on a slab of size $P \times N_y$, where $P = (N_x/2+1)/N_{MPI}$.

The code solves the governing equations in their dimensional form. A third-order Runge-Kutta scheme [31] is used for time advancement. The aliasing errors are removed with the two-thirds dealiasing rule [16] which implies that the maximum wave numbers are $k_x^{\max} = \lfloor N_x/3 \rfloor$ and $k_y^{\max} = \lfloor 2N_y/3 \rfloor$, where $\lfloor \cdot \rfloor$ denotes the floor function. We integrate convective terms in (2.10) explicitly and diffusive terms implicitly, yielding the following time advancement for ψ and θ from time p to $p+1$:

$$
\begin{aligned}
f(dt, \psi^p, y_i, z_i) &= \frac{\psi^p + dt k^{-2}(\{y_i, \nabla^2 y_i\} - gaik_x z_i)}{1 + dt\nu k^2}, \\
g(dt, \theta^p, y_i, z_i) &= \frac{\theta^p + dt(-\{y_i, z_i\} + \frac{\Delta T}{L_y} ik_x y_i)}{1 + dt\kappa k^2}, \\
y_1 = \psi^p, &\qquad z_1 = \theta^p, \\
y_2 = f(dt/3, \psi^p, y_1, z_1), &\qquad z_2 = g(dt/3, \theta^p, y_1, z_1), \\
y_3 = f(dt/2, \psi^p, y_2, z_2), &\qquad z_3 = g(dt/2, \theta^p, y_2, z_2), \\
\psi^{p+1} = f(dt, \psi^p, y_3, z_3), &\qquad \theta^{p+1} = g(dt, \theta^p, y_3, z_3),
\end{aligned}
\tag{C.1}
$$

where $k^2 = k_x^2 + k_y^2$. The CFL condition is imposed ensuring that the timestep dt is smaller than both the convective and diffusive time scales, i.e.

$$
dt \leq \min\Bigg(\underbrace{\frac{\sigma_i dx}{\sqrt{\boldsymbol{u}_{\max}^2} w'_m}}_{\text{convective}}, \underbrace{\frac{\sigma_r dx^2}{\max(\nu, \kappa) w''_m}}_{\text{diffusive}} \Bigg),
\tag{C.2}
$$

where

$$
dx = \min\left(\frac{L_x}{k_x^{\max}}, \frac{L_y}{k_y^{\max}} \right)
\tag{C.3}
$$

is the smallest length scale in the system, and σ, w_m are constants that ensure the stability of the numerical scheme, taken from the literature [103].

In the following section, the DNS is verified by comparison with the results presented by Goluskin et al. [63].

C.2 Time Series Validation

In Figure C.2 we plot the Nusselt number and the horizontal and vertical kinetic energies from our simulations with the DNS described in §C.1. We consider the Rayleigh numbers $\mathrm{Ra} = 2 \times 10^6$ and $\mathrm{Ra} = 2 \times 10^8$, and Prandtl numbers $\mathrm{Pr} = 1$ and $\mathrm{Pr} = 10$. These parameter values have been chosen to compare with Figures 7 and 11 in the paper by Goluskin et al. [63]. Indeed, there is great qualitative agreement between our results and theirs. To compare our results quantitatively, in Table C.1,

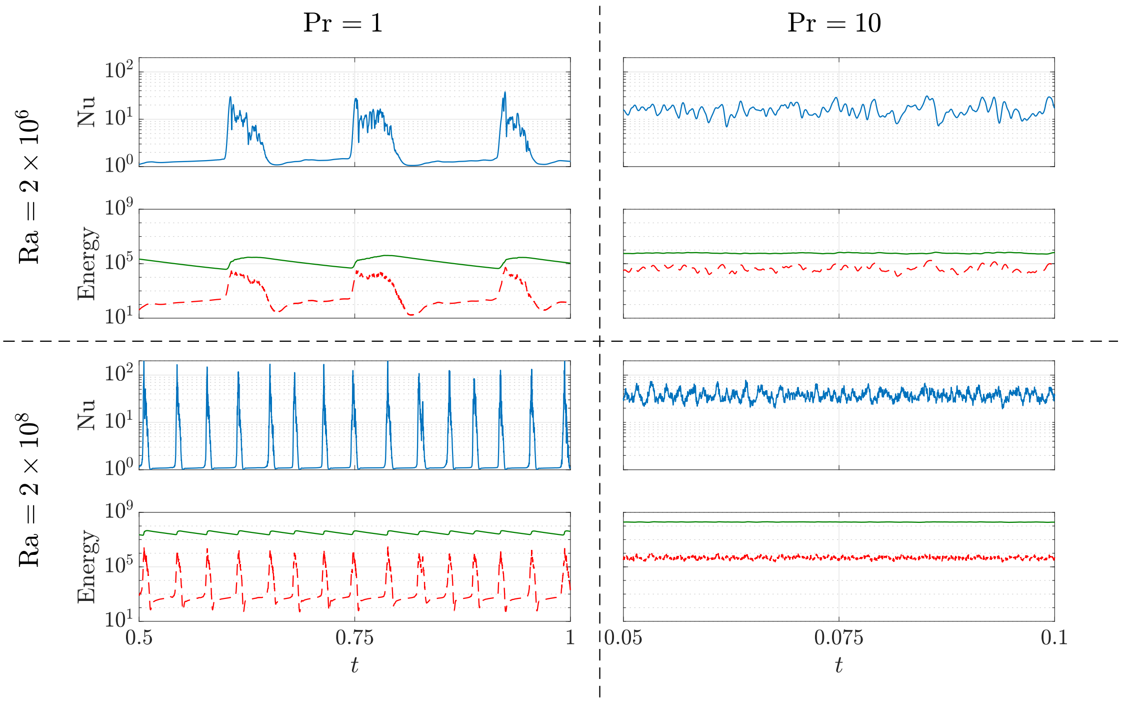

Figure C.2: Time series of the Nusselt number (rows 1 and 3) and the horizontal and vertical kinetic energies, E_x^u and E_y^u (rows 2 and 4). In green we plot E_x^u whilst E_y^u is dashed and plotted in red. For all plots, we have that $E_x^u > E_y^u$. All quantities are calculated as per equations (2.19) and (2.15) and have been normalised with respect to the length scale L_y and the time scale L_y^2/κ, in line with Goluskin et al. [63]. The first column has $\mathrm{Pr} = 1$ and the second $\mathrm{Pr} = 10$. The Rayleigh number is 2×10^6 in the first two rows and 2×10^8 in the bottom two. The aspect ratio has been fixed to $\Gamma = 2$.

Pr	Ra	τ	TBB	Nu	TBB	Nu
1	10^6	74.37	0.155	3.74	0.144	3.69
1	10^7	24.21	0.120	3.59	0.132	3.67
1	10^8	1.39	0.0470	4.85	0.0486	4.73
10	2×10^6	0.57	-	15.66	-	15.83
10	2×10^7	0.55	-	25.58	-	25.59
10	2×10^8	0.37	-	38.27	-	38.38

Table C.1: To the left of the double line are our results, normalised with respect to the length scale L_y and the time scale L_y^2/κ, in line with Goluskin et al. [63]. Tau (τ) is the dimensionless integration time after transients and TBB is the dimensionless time between successive bursts when Pr = 1. To the right of the double line are results presented in Goluskin et al [63], Tables 1 and 3.

we list the time-averaged Nusselt number, for both Pr = 1 and Pr = 10, and TBB (time between bursts) when Pr = 1. The largest discrepancy in TBB is 9% and only 2% in the Nusselt number. This should be considered good agreement since bursts are rare (only 50 were simulated in the run by Goluskin et al. [63] at $(\mathrm{Ra}, \mathrm{Pr}) = (10^8, 1)$) and time averages by Goluskin et al. [63] were deemed converged when the Nusselt number and kinetic energy over the whole time series differed by less than 2% versus their values over half the time series.

C.3 Resolutions

The resolutions used for each run are listed in Table C.2. To illustrate that these are sufficient, in Figure C.3 we plot the time-averaged potential energy spectra, $\langle \widehat{E}^\theta \rangle_t$, as defined in (2.15), compensated with k^2 with the parameters $\mathrm{Ra} = 2 \times 10^8$, Pr = 10 and $\Gamma = 2$, i.e. the largest Rayleigh number considered, with different resolutions $N_x \times N_y$. We examine the potential rather than the kinetic energy because $\mathrm{Pr} \geq 1$, i.e. $\nu \geq \kappa$, for all results in chapter 4, meaning that viscous dissipation is more prominent than thermal diffusion. Therefore, the smallest scales are in θ rather than ψ.

Ra	$N_x \times N_y$
$[10^4, 10^6)$	128×128
$[10^6, 10^7)$	256×256
$[10^7, 2.5 \times 10^7)$	512×256
$[2.5 \times 10^7, 2 \times 10^8]$	512×512

Table C.2: The resolution $N_x \times N_y$ used for each Rayleigh number in chapter 4.

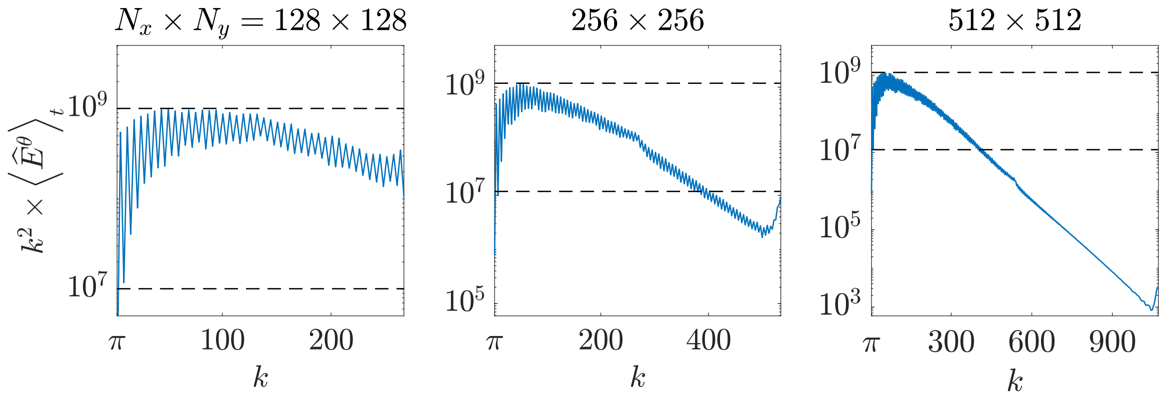

Figure C.3: Time averaged potential energy spectrum, $\langle \widehat{E}^{\theta} \rangle_t$, compensated with k^2, with $\mathrm{Ra} = 2 \times 10^8$, $\mathrm{Pr} = 10$ and $\Gamma = 2$ for different resolutions $N_x \times N_y$. The dashed lines are two orders of magnitudes apart.

For sufficient resolution, we require that the peak of the compensated spectra is two orders of magnitude larger than the spectra at the maximum wavenumber, ensuring that the length scale where the most dissipation occurs is well resolved. With this requirement in mind, we conclude that a resolution with $N_x \times N_y = 128 \times 128$ does not resolve θ, 256×256 is marginally resolved and 512×512, which is what we use in practice (see Table C.2), is very well resolved.

C.4 Initial Conditions and Convergence

One can only start collecting statistics for global variables of spectra once the flow is fully developed and has attained a statistically stationary state [1, 105]. To accomplish this, we start by using random initial conditions, viz,

$$\nabla^2 \widehat{\psi}_{k_x,k_y}(0) = e^{i\pi\phi^{\psi}_{k_x,k_y}}, \tag{C.4a}$$

$$\widehat{\theta}_{k_x,k_y}(0) = e^{i\pi\phi^{\theta}_{k_x,k_y}}, \tag{C.4b}$$

where both $\phi^{\psi}_{k_x,k_y}$ and $\phi^{\theta}_{k_x,k_y}$ are drawn uniformly from $[0,2]$ when $k_x > 0$, or from a fair Bernoulli distribution ($p = 0.5$) when $k_x = 0$. Then we use initial conditions generated from a previous run that has already reached a statistically stationary state. Transients are very short, albeit shorter in the latter case. A typical time series with random initial conditions and parameter values $\mathrm{Ra} = 3.6 \times 10^6$, $\mathrm{Pr} = 30$, and $\Gamma = 2$ is shown in Figure C.4. A statistically stationary state has been reached after approximately 50 eddy turnover times. To accumulate reliable statistics, each run was integrated to at least 10^4 eddy turnover times, not including transients.

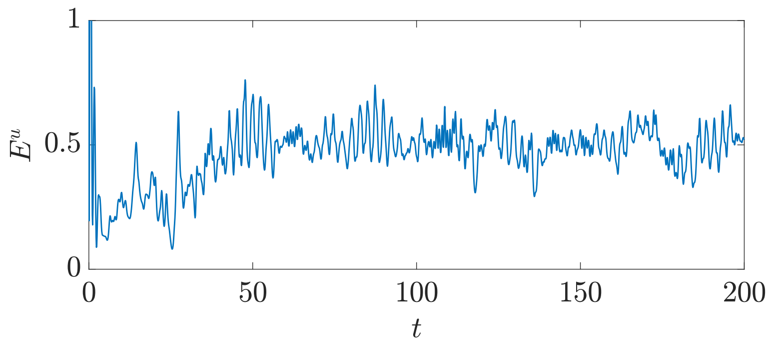

Figure C.4: Time series of the kinetic energy normalised with respect to the rms velocity, u_{rms}, and eddy turnover time, L_y/u_{rms}. The parameters are $\mathrm{Ra} = 3.6 \times 10^6$, $\mathrm{Pr} = 30$, and $\Gamma = 2$. The initial conditions are random, and prescribed according to (C.4). A statistically stationary state has been reached at $t \approx 50$.

Appendix D

Additional Results to Q2D Rayleigh-Bénard Convection

D.1 Eigenvalue Problem

In this section, we derive the eigenvalue problem for the growth rate, σ, of U, V, and $\theta^{\perp}$ over a steady background flow, to validate the DNS used to solve (5.11) and (5.13) in chapter 5. We use a Fourier-sine basis for the expansion of V and $\theta^{\perp}$, while U is expanded using a Fourier-cosine basis. So there are two families of modes, the "s" basis and the "c" basis

$$\phi^{s}_{k_x,k_y}(x,y) = e^{2\pi i k_x/\Gamma_x}\sin(\pi k_y y), \quad k_x \in \mathbb{Z},\ k_y \in \mathbb{Z}_{>0}, \tag{D.1a}$$

$$\phi^{c}_{k_x,k_y}(x,y) = e^{2\pi i k_x/\Gamma_x}\cos(\pi k_y y), \quad k_x \in \mathbb{Z},\ k_y \in \mathbb{Z}_{\geq 0}, \tag{D.1b}$$

and we define the inner product

$$\langle \phi^{s/c}_{k_{x_1},k_{y_1}}, \phi^{s/c}_{k_{x_2},k_{y_2}} \rangle = \int_0^1 \int_0^{\Gamma} \phi^{s/c}_{k_{x_1},k_{y_1}} \phi^{s/c*}_{k_{x_2},k_{y_2}}\, dx dy. \tag{D.2}$$

We act with this inner product on (5.11) and (5.13) to obtain an eigenvalue problem for σ, namely

$$\frac{2}{\Gamma_x}\langle \{\widetilde{U},\psi\} + \psi_{xy}\widetilde{U} + \psi_{yy}\widetilde{V} + \nabla^2\psi\widetilde{F}_y, \phi^{c}_{k_x,k_y}\rangle \\ - \mathrm{Pr}\left(k^2_{k_x,k_y} + q^2\right)\widehat{U}_{k_x,k_y} = \sigma\widehat{U}_{k_x,k_y} \tag{D.3a}$$

$$\frac{2}{\Gamma_x}\langle \{\widetilde{V},\psi\} + \mathrm{PrRa}\widetilde{\theta}^{\perp} - \psi_{xx}\widetilde{U} - \psi_{xy}\widetilde{V} - \nabla^2\psi\widetilde{F}_x, \phi^{s}_{k_x,k_y}\rangle \\ - \mathrm{Pr}\left(k^2_{k_x,k_y} + q^2\right)\widehat{V}_{k_x,k_y} = \sigma\widehat{V}_{k_x,k_y} \tag{D.3b}$$

$$\frac{2}{\Gamma_x}\langle\{\widetilde{\theta}^{\perp},\psi\} - \overline{\theta}_x\left(\widetilde{U}+\widetilde{F}_x\right) - \left(\overline{\theta}_y - 1\right)\left(\widetilde{V}+\widetilde{F}_y\right), \phi^s_{k_x,k_y}\rangle$$
$$- \Pr\left(k^2_{k_x,k_y}+q^2\right)\widehat{\theta}^{\perp}_{k_x,k_y} = \sigma\widehat{\theta}^{\perp}_{k_x,k_y}, \quad \text{(D.3c)}$$

where $\widetilde{U}$, $\widetilde{V}$, and $\widetilde{\theta}^{\perp}$ are defined as in (5.15),

$$\widetilde{F} = \frac{\widetilde{U}_x + \widetilde{V}_y}{q^2 - \nabla^2}, \quad \text{(D.4a)}$$

$$k^2_{k_x,k_y} = \left(\frac{2\pi}{\Gamma_x}k_x\right)^2 + (\pi k_y)^2, \quad \text{(D.4b)}$$

and

$$\langle fg, \phi^c_{k_x,k_y}\rangle = \frac{1}{2}\begin{cases} \displaystyle\sum_{\substack{k_{x_1}+k_{x_2}=k_x \\ |k_{y_1}\pm k_{y_2}|=k_y}} \widehat{f}_{k_{x_1},k_{y_1}}\widehat{g}_{k_{x_2},k_{y_2}} & \text{if } f \text{ and } g \text{ are in } c \text{ basis.} \\ \displaystyle\sum_{\substack{k_{x_1}+k_{x_2}=k_x \\ |k_{y_1}\pm k_{y_2}|=k_y}} h_c(k_y,k_{y_1},k_{y_2})\widehat{f}_{k_{x_1},k_{y_1}}\widehat{g}_{k_{x_2},k_{y_2}} & \text{if } f \text{ and } g \text{ are in } s \text{ basis.} \end{cases} \quad \text{(D.5a)}$$

$$\langle fg, \phi^s_{k_x,k_y}\rangle = \frac{1}{2}\sum_{\substack{k_{x_1}+k_{x_2}=k_x \\ |k_{y_1}\pm k_{y_2}|=k_y}} h_s(k_y,k_{y_1},k_{y_2})\widehat{f}_{k_{x_1},k_{y_1}}\widehat{g}_{k_{x_2},k_{y_2}} \quad f, g \text{ are in } s \text{ and } c \text{ bases, respectively.} \quad \text{(D.5b)}$$

$$h_c(k_y,k_{y_1},k_{y_2}) = \begin{cases} -1 & \text{if } k_y = k_{y_1}+k_{y_2}, \\ 1 & \text{otherwise.} \end{cases} \quad \text{(D.5c)}$$

$$h_s(k_y,k_{y_1},k_{y_2}) = \begin{cases} -1 & \text{if } k_y = k_{y_2}-k_{y_1}, \\ 1 & \text{otherwise.} \end{cases} \quad \text{(D.5d)}$$

D.2 Growth Rate in the $q \to \infty$ Limit

In §5.5.1, we noted that $\sigma \sim -\min(\Pr, 1)q^2 = -q^2 < 0$ to leading order as $q \to \infty$, where σ is the linear growth rate of the 3D perturbations and q the wavenumber in z. In this section, we provide a more detailed derivation of this fact.

We seek a solution to the system (5.11)–(5.13) of the form

$$\begin{pmatrix} U \\ V \\ \theta^{\perp} \\ F \end{pmatrix} = \begin{pmatrix} \widetilde{U} \\ q^2\widetilde{V} \\ q^4\widetilde{\theta}^{\perp} \\ \widetilde{F} \end{pmatrix} e^{-q^2 t}, \quad \text{(D.6)}$$

and expend the $\widetilde{\cdot}$ variables in powers of q^2, i.e. $\widetilde{U} = \widetilde{U}_0 + q^2\widetilde{U}_1 + \dots$. Then, to leading order as $q \to \infty$,

$$(\mathrm{Pr}-1)\widetilde{U}_0 = \partial_{yy}\psi\widetilde{V}_0, \tag{D.7a}$$

$$(\mathrm{Pr}-1)\widetilde{V}_0 = \mathrm{PrRa}\widetilde{\theta}_0^{\perp} \tag{D.7b}$$

$$\widetilde{F}_0 = \partial_{yy}\widetilde{V}_0, \tag{D.7c}$$

and $\widetilde{\theta}_0^{\perp}$ satisfies

$$\partial_t\widetilde{\theta}_0^{\perp} + \{\psi, \widetilde{\theta}_0^{\perp}\} = \nabla^2\widetilde{\theta}_0^{\perp}, \tag{D.8}$$

subject to periodic boundary conditions in x and $\widetilde{\theta}_0^{\perp} = 0$ at $y = 0, 1$. So, $\widetilde{\theta}_0^{\perp}$ is governed by the 2D convection-diffusion equation, whose solution must decay to 0 as $t \to \infty$. Suppose $\widetilde{\theta}_0^{\perp}(x, y, t) \sim e^{-\sigma_1 t}$ as $t \to \infty$, then we have

$$\sigma \sim -q^2 - \sigma_1, \tag{D.9}$$

as $q \to \infty$.

We can get a bound on σ_1. Let

$$E_1 = \int_0^1 \int_0^{\Gamma_x} \frac{1}{2}\widetilde{\theta}_0^{\perp 2}\, dxdy, \tag{D.10}$$

then

$$\frac{dE_1}{dt} = -\int_0^1 \int_0^{\Gamma_x} |\widetilde{\theta}_0^{\perp}|^2\, dxdy \leq -2\pi^2 E_1, \tag{D.11}$$

by the Poincaré inequality. This gives $\sigma_1 \leq -\pi^2$, with equality when $\psi = 0$.

Appendix E

Additional Results to Spectra Without Boundaries

E.1 DNS Resolution and Convergence

The spatial resolutions used for each run are listed in Figure 6.1. To illustrate that these are sufficient, in Figure E.1 (a) we plot the time-averaged potential energy spectrum (6.8b) compensated with k^2. We plot the $\mathrm{Pr} = 10^2$ and $\mathrm{Pr} = 10$ cases in green and blue, respectively, while keeping $\mathrm{Ra} = 6.2 \times 10^{11}$ fixed with normal viscosity. Both cases, representing the most computationally demanding runs in section chapter 6, employ a resolution of $N = 8192$. We choose to examine the runs with $\mathrm{Pr} > 1$ and the potential rather than the kinetic energy spectrum since the kinetic energy undergoes an inverse cascade while the potential energy experiences a forward cascade. Thus, smaller scales are more prominent in the potential energy spectrum, posing a higher resolution challenge.

In determining the adequacy of the DNS resolution, we conclude that a run is well resolved if the tail of the compensated spectrum is at least two orders of magnitude smaller than its peak, ensuring that the length scale where the most dissipation occurs is well resolved. With this requirement in mind, it is clear that the scenario with $\mathrm{Pr} = 10$ meets this high resolution standard, while the run with $\mathrm{Pr} = 10^2$ might be considered marginally unresolved. However, all other runs in section chapter 6 satisfy this stringent resolution requirement.

An alternative way to determine resolution requirements is to ensure that the DNS resolves the Batchelor length scale, η_B [6]. This is the smallest length scale in the flow, assuming that the velocity field does not adhere to Kolmogorov scaling, there are no boundary layers present, and the Prandtl number is greater than 1 [141]. The dimensionless Batchelor length scale is

$$\eta_B = \left(\frac{\mathrm{Pr}}{\epsilon_\nu} \right)^{1/4}, \tag{E.1}$$

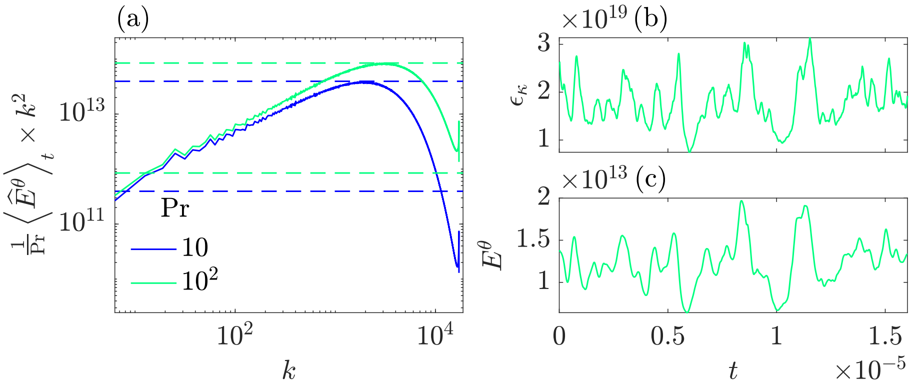

Figure E.1: (a) Compensated potential energy spectra for $\mathrm{Pr} = 10^2$ and $\mathrm{Pr} = 10$ in green and blue, respectively, while keeping $\mathrm{Ra} = 6.2 \times 10^{11}$ fixed. The dashed lines are two orders of magnitude below the spectra peaks. (b) Time series of the thermal dissipation rate and (c) the potential energy from the $\mathrm{Pr} = 10^2$ run.

where ϵ_ν is the viscous dissipation rate, as defined in (6.22). We consider the Batchelor length scale resolved as long as the condition $k_{max}\eta_B > 1$ is met, where $k_{max} = \lfloor N/3 \rfloor L$ is the largest dimensionless wavenumber in the DNS. In the case of our simulation with $\mathrm{Pr} = 10^2$ and $\mathrm{Ra} = 6.2 \times 10^{11}$, we observe that

$$k_{max}\eta_B \approx 1.52 > 1, \tag{E.2}$$

Based on this result, we conclude that the Batchelor length scale is resolved.

In terms of convergence in time, one can only start collecting statistics for global variables of spectra once the flow is fully developed and has attained a statistically stationary state [1, 105]. To minimise transients in our most computationally challenging runs, we initiate our simulations at a resolution of $N = 1024$, subsequently doubling it once a statistically steady state is attained. This process continues until the target resolution is achieved. Figures E.1 (b) and (c) display an example of this progression, showing the time series of thermal dissipation rate and potential energy respectively. The parameters here are $\mathrm{Ra} = 6.2 \times 10^{11}$ and $\mathrm{Pr} = 10^2$, with a resolution of $N = 8192$. The initial conditions are taken from the end of a simulation with identical parameter values but at a resolution of $N = 4096$. Evidently, the transient is very short, indicating that data can be collected close to $t = 0$.

E.2 Choosing the Value for Rh

In chapter 6, a large-scale dissipation term has been included in the momentum equation (6.2a). The dimensionless number, Rh, determines the strength of the large-scale dissipation and it is chosen such that the kinetic energy spectrum peaks at $k = 2$,

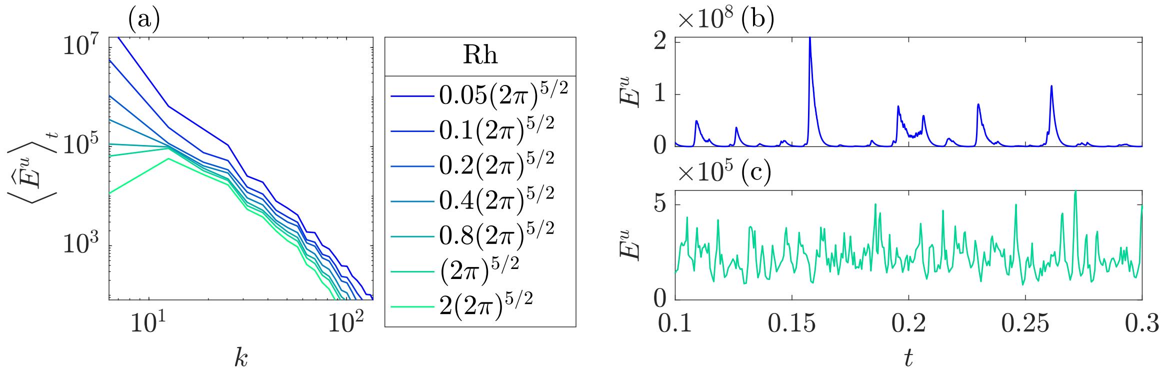

Figure E.2: (a) Kinetic energy spectra for runs with $\mathrm{Ra} = 5.1 \times 10^6$ and $\mathrm{Pr} = 1$, while varying Rh, as colour coded in the legend. (b) and (c) Kinetic energy time series for runs with $\mathrm{Rh} = 0.05(2\pi)^{5/2}$ and $(2\pi)^{5/2}$, respectively. In each run, a $N = 256$ resolution was used.

meaning that the dynamics is not dominated by large-scale runaway solutions (6.5) with $k_x = 1$.

In Figure E.2 (a) we plot the kinetic energy spectra for runs with $\mathrm{Ra} = 5.1 \times 10^6$ and $\mathrm{Pr} = 1$, while varying Rh, as colour coded in the legend. We observe that the smallest value of Rh which yields a kinetic energy spectrum peak at $k = 2$ is $\mathrm{Rh} = (2\pi)^{5/2}$. Consequently, this is the Rh value chosen for our study in chapter 6. To further demonstrate how Rh variations impact flow dynamics, we present the kinetic energy time series for $\mathrm{Rh} = 0.05(2\pi)^{5/2}$ and $(2\pi)^{5/2}$ in Figure E.2 (b) and (c), respectively. When $\mathrm{Rh} = 0.05(2\pi)^{5/2}$, the flow is dominated by the $\widehat{\psi}_{1,0}$ mode, displaying a pattern of intermittent exponential growth and decay, as seen in [28]. In contrast, when $\mathrm{Rh} = (2\pi)^{5/2}$, the large-scale friction effectively suppresses the $\widehat{\psi}_{1,0}$ mode, and it no longer dominates the flow dynamics.

E.3 A Proof in the $\mathrm{Pr} \to 0$ Limit

In §6.4, we derived the growth rate

$$\sigma(k_x, k_y) = \mathrm{Ra}\frac{(2\pi k_x)^2}{k^{2(n+1)}} - k^{2n} - Ck^{-2}. \tag{E.3}$$

of the $\widehat{\psi}_{k_x,k_y}$ mode in the $\mathrm{Pr} \to 0$ limit where $k = 2\pi\sqrt{k_x^2 + k_y^2}$ and $C = \mathrm{Rh}\sqrt{\mathrm{Ra}/\mathrm{Pr}}$. Here we provide a short proof that the $\widehat{\psi}_{1,0}$ mode is always the most unstable in that, if there exists at least one mode with a positive growth rate, then $\sigma(0, 1)$ is the largest.

First note that

$$\sigma + \frac{(k/2\pi)^2}{2(n+1)k_y}\frac{\partial\sigma}{\partial k_y} = -\left[\frac{nC + (2n+1)k^{2(n+1)}}{(n+1)k^2}\right] < 0. \tag{E.4}$$

So, although it is possible for σ to have local extrema with $k_y > 0$, they can only occur when $\sigma < 0$: local maxima with $\sigma > 0$ can only occur with $k_y = 0$, in which case

$$\sigma = \frac{\mathrm{Ra}}{(2\pi k_x)^{2n}} - (2\pi k_x)^{2n} - \frac{C}{(2\pi k_x)^2}. \tag{E.5}$$

Then we have

$$\sigma + \frac{k_x}{2^n}\frac{\partial\sigma}{\partial k_x} = -\frac{2}{(2\pi k_x)^{2n}} - \frac{(n-1)C}{n(2\pi k_x)^2} < 0. \tag{E.6}$$

So, again, although there can be local extrema in $\sigma(k_x)$, they can only occur when $\sigma < 0$; i.e. when $\sigma > 0$, it is a decreasing function of k_x. It follows that, if *any* mode is unstable, the most unstable mode is $\widehat{\psi}_{1,0}$.

It also follows that the system is unstable precisely when $\sigma(1,0) > 0$, i.e. when $\mathrm{Ra} > (2\pi)^{4n} + C(2\pi)^{2(n-1)}$, which is exactly the same criterion as (6.7).

E.4 Additional Plots

In Figure 6.9, we presented the time-averaged spectra of the terms in the kinetic and potential energy balances for runs with hyperviscosity. In Figure E.3, we present the complementary plot with normal viscosity and $\mathrm{Pr} = 10^{-2}$ (Figure E.3 (a), (d)), $\mathrm{Pr} = 1$ (Figure E.3 (b), (e)), and $\mathrm{Pr} = 10^2$ (Figure E.3 (c), (f)).

In the kinetic energy balance, we identify the same three wavenumber regimes, labelled I to III, as in Figure 6.9. In region I, the large-scale friction is balanced by buoyancy, while in region II, the inertial term balances buoyancy. In region III, the balance depends on the Prandtl number. For $\mathrm{Pr} = 10^{-2}$ and 1 the small-scale dissipation balances the inertial term, while for $\mathrm{Pr} = 10^2$, the balance is between the small-scale dissipation and buoyancy.

In the potential energy balance, there are two distinct wavenumber ranges, labelled A and B. The inertial term balances buoyancy in region A and the small-scale dissipation in region B.

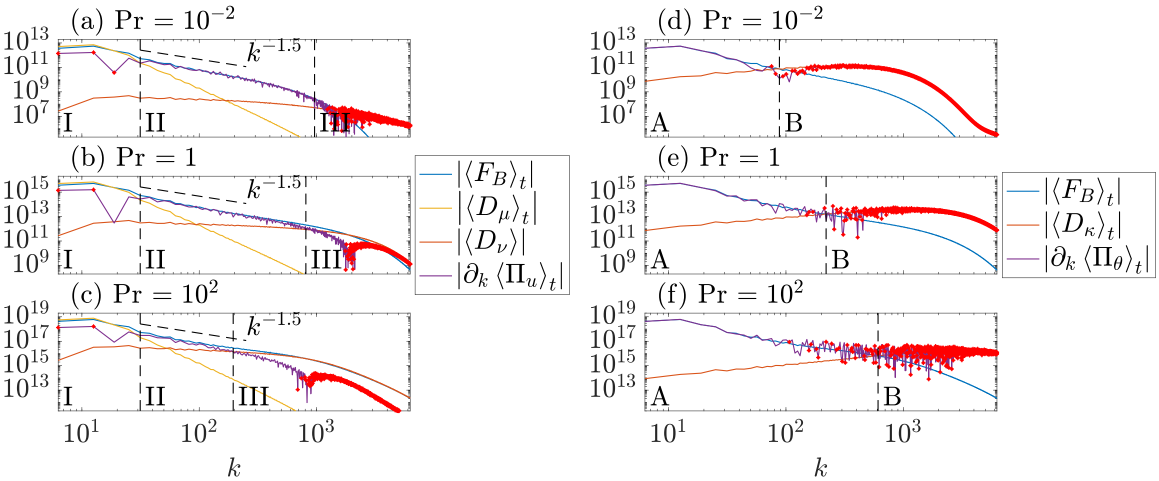

Figure E.3: (a)–(c) Time-averaged spectra of the terms in the kinetic energy and (d)–(f) potential energy balances (6.10) for the runs with normal viscosity, $\mathrm{Ra} = 6.2 \times 10^{11}$, $\mathrm{Rh} = (2\pi)^{5/2}$, and $\mathrm{Pr} = 10^{-2}$ (a), (d), $\mathrm{Pr} = 1$ (b), (e), and $\mathrm{Pr} = 10^{2}$ (c), (f). The terms displayed in the legend are defined in (6.11), (6.14) and (6.13). In (a)–(c) and (d)–(f), we observe three and two distinct dominant balances, respectively, annotated I–III and A–B. The red dots indicate where the inertial terms become negative.

Bibliography

[1] G. Ahlers, E. Bodenschatz, R. Hartmann, et al. "Aspect ratio dependence of heat transfer in a cylindrical Rayleigh-Bénard cell (supplementary material)". In: *Physical Review Letters* 128 (2022), p. 084501 (cit. on pp. 134, 140).

[2] A. Alexakis and L. Biferale. "Cascades and transitions in turbulent flows". In: *Physics Reports* 767-769 (2018), pp. 1–101 (cit. on pp. 94, 97, 105).

[3] T. Aoyagi, M. Yagi, and S.-I. Itoh. "Comparison analysis of Lorenz model and five components model". In: *Journal of the Physical Society of Japan* 66.9 (1997), pp. 2689–2701 (cit. on p. 15).

[4] M. Avila, D. Barkley, and B. Hof. "Transition to turbulence in pipe flow". In: *Annual Review of Fluid Mechanics* 55 (2023), pp. 575–602 (cit. on p. 13).

[5] G. K. Batchelor. "Considerations of Convective Instability From the Viewpoint of Physics. Discussion". In: 1. Bologna, Italy: Supplemento del Nuovo Cimento XXII, Nicola Zanichelli, 1960, pp. 385–402 (cit. on p. 11).

[6] G. K. Batchelor. "Small-scale variation of convected quantities like temperature in turbulent lluid part 1. General discussion and the case of small conductivity". In: *Journal of Fluid Mechanics* 5.1 (1959), pp. 113–133 (cit. on p. 139).

[7] H. Bénard. "Les tourbillons cellulaires dans une nappe liquide". In: *Revue Générale des Sciences Pures et Appliquées* 11 (1900), pp. 1261–1271 (cit. on p. 12).

[8] S. J. Benavides and A. Alexakis. "Critical transitions in thin layer turbulence". In: *Journal of Fluid Mechanics* 822 (2017), pp. 364–385 (cit. on pp. 74, 88).

[9] M. Berning and K. H. Spatschek. "Bifurcations and transport barriers in the resistive-g paradigm". In: *Physical Review E* 62 (2000), pp. 1162–1174 (cit. on p. 15).

[10] D. Biskamp, K. Hallatschek, and E. Schwarz. "Scaling laws in two-dimensional turbulent convection". In: *Physical Review E* 63 (2001), p. 045302 (cit. on pp. 3, 90, 91).

[11] E. Bodenschatz, W. Pesch, and G. Ahlers. "Recent developments in Rayleigh-Bénard convection". In: *Annual Review of Fluid Mechanics* 32.1 (2000), pp. 709–778 (cit. on p. 4).

[12] R. Bolgiano Jr. “Turbulent spectra in a stably stratified atmosphere”. In: *Journal of Geophysical Research (1896-1977)* 64.12 (1959), pp. 2226–2229 (cit. on pp. 91, 95, 97, 103).

[13] E. W. Bolton and F. H. Busse. “Stability of convection rolls in a layer with stress-free boundaries”. In: *Journal of Fluid Mechanics* 150 (1985), pp. 487–498 (cit. on p. 22).

[14] V. Borue and S. A. Orszag. “Turbulent convection driven by a constant temperature gradient”. In: *Journal of Scientific computing* 12 (1997), pp. 305–351 (cit. on pp. 3, 12, 90, 91, 97, 104).

[15] N. Boullé, V. Dallas, and P. E. Farrell. “Bifurcation analysis of two-dimensional Rayleigh-Bénard convection using deflation”. In: *Physical Review E* 105 (2022), p. 055106 (cit. on p. 13).

[16] J. Boyd. *Chebyshev and Fourier Spectral Methods*. Dover Publication, 2000 (cit. on pp. 37, 131).

[17] A. D. Brent, V. R. Voller, and K. J. Reid. “Enthalpy-porosity technique for modeling convection-diffusion phase change: application to the melting of a pure metal”. In: *Numerical Heat Transfer* 13.3 (1988), pp. 297–318 (cit. on p. 2).

[18] B. Brown, M. Browning, A. Brun, et al. “Rapidly rotating suns and active nests of convection”. In: *The Astrophysical Journal* 689 (2008), p. 1354 (cit. on pp. 19, 72).

[19] E. Brown and G. Ahlers. “Large-scale circulation model for turbulent Rayleigh-Bénard convection”. In: *Physical Review Letters* 98 (2007), p. 134501 (cit. on p. 60).

[20] N. H. Brummell and J. E. Hart. “High Rayleigh number β-convection”. In: *Geophysical & Astrophysical Fluid Dynamics* 68.1-4 (1993), pp. 85–114 (cit. on p. 19).

[21] F. H. Busse. “On the stability of two-dimensional convection in a layer heated from below”. In: *Journal of Mathematics and Physics* 46.1-4 (1967), pp. 140–150 (cit. on p. 22).

[22] F. H. Busse and E. W. Bolton. “Instabilities of convection rolls with stress-free boundaries near threshold”. In: *Journal of Fluid Mechanics* 146 (1984), pp. 115–125 (cit. on p. 22).

[23] F. Busse. “A simple model of convection in the Jovian atmosphere”. In: *Icarus* 29.2 (1976), pp. 255–260 (cit. on p. 15).

[24] F. Busse. “Generation of mean flows by thermal convection”. In: *Physica D: Nonlinear Phenomena* 9.3 (1983), pp. 287–299 (cit. on pp. 16, 22).

[25] F. Busse, G. Hartung, M. Jaletzky, et al. “Experiments on thermal convection in rotating systems motivated by planetary problems”. In: *Dynamics of Atmospheres and Oceans* 27.1-4 (1998), pp. 161–174 (cit. on p. 1).

[26] M. Buzzicotti, H. Aluie, L. Biferale, et al. "Energy transfer in turbulence under rotation". In: *Physical Review Fluids* 3.3 (2018), p. 034802 (cit. on p. 74).

[27] O. Cadot, A. Evrard, and L. Pastur. "Imperfect supercritical bifurcation in a three-dimensional turbulent wake". In: *Physical Review E* 91 (2015), p. 063005 (cit. on p. 59).

[28] E. Calzavarini, C. R. Doering, J. D. Gibbon, et al. "Exponentially growing solutions in homogeneous Rayleigh-Bénard convection". In: *Physical Review E* 73 (2006), p. 035301 (cit. on pp. 3, 90–92, 107, 141).

[29] E. Calzavarini, D. Lohse, F. Toschi, et al. "Rayleigh and Prandtl number scaling in the bulk of Rayleigh–Bénard turbulence". In: *Physics of Fluids* 17.5 (2005), p. 055107 (cit. on pp. 3, 12, 90, 91, 102, 104, 107).

[30] E. Calzavarini, F. Toschi, and R. Tripiccione. "Evidences of Bolgiano-Obhukhov scaling in three-dimensional Rayleigh-Bénard convection". In: *Physical Review E* 66 (2002), p. 016304 (cit. on p. 97).

[31] C. Canuto, M. Y. Hussaini, A. Quarteroni, et al. *Spectral methods in fluid dynamics*. Springer Science & Business Media, 2012 (cit. on p. 131).

[32] B. Castaing, G. Gunaratne, F. Heslot, et al. "Scaling of hard thermal turbulence in Rayleigh-Bénard convection". In: *Journal of Fluid Mechanics* 204.-1 (1989), p. 1 (cit. on p. 12).

[33] A. Celani, S. Musacchio, and D. Vincenzi. "Turbulence in more than two and less than three dimensions". In: *Physical Review Letters* 104.18 (2010), p. 184506 (cit. on p. 74).

[34] M. Chandra and M. K. Verma. "Dynamics and symmetries of flow reversals in turbulent convection". In: *Physical Review E* 83 (2011), p. 067303 (cit. on pp. 24, 59).

[35] M. Chandra and M. K. Verma. "Flow reversals in turbulent convection via vortex reconnections". In: *Physical Review Letters* 110 (2013), p. 114503 (cit. on pp. 59, 60, 72, 114).

[36] S. Chandrasekhar. *Hydrodynamic and Hydromagnetic Stability*. Oxford University Press, 1961 (cit. on p. 5).

[37] X. Chavanne, F. Chillà, B. Chabaud, et al. "Turbulent Rayleigh–Bénard convection in gaseous and liquid He". In: *Physics of Fluids* 13.5 (2001), pp. 1300–1320 (cit. on p. 11).

[38] F. Chillà and J. Schumacher. "New perspectives in turbulent Rayleigh-Bénard convection". In: *The European Physical Journal E* 35.7 (2012) (cit. on pp. 3, 11, 90, 91, 103, 108).

[39] J. Y.-K. Cho and L. M. Polvani. "The emergence of jets and vortices in freely evolving, shallow-water turbulence on a sphere". In: *Physics of Fluids* 8.6 (1996), pp. 1531–1552 (cit. on p. 114).

[40] V. Dallas, K. Seshasayanan, and S. Fauve. “Transitions between turbulent states in a two-dimensional shear flow”. In: *Physical Review Fluids* 5 (2020), p. 084610 (cit. on pp. 59, 72, 113).

[41] G. F. Davies and M. A. Richards. “Mantle convection”. In: *The Journal of Geology* 100.2 (1992), pp. 151–206 (cit. on p. 1).

[42] G. Decristoforo, A. Theodorsen, and O. E. Garcia. “Intermittent fluctuations due to Lorentzian pulses in turbulent thermal convection”. In: *Physics of Fluids* 32.8 (2020), p. 085102 (cit. on p. 19).

[43] T. DeVries, M. Holzer, and F. Primeau. “Recent increase in oceanic carbon uptake driven by weaker upper-ocean overturning”. In: *Nature* 542.7640 (2017), pp. 215–218 (cit. on p. 1).

[44] P. H. Diamond, S.-I. Itoh, K. Itoh, et al. “Zonal flows in plasma—a review”. In: *Plasma Physics and Controlled Fusion* 47.5 (2005), R35–R161 (cit. on pp. 19, 20).

[45] C. R. Doering, S. Toppaladoddi, and J. S. Wettlaufer. “Absence of evidence for the ultimate regime in two-dimensional Rayleigh-Bénard convection”. In: *Physical Review Letters* 123 (2019), p. 259401 (cit. on p. 12).

[46] C. R. Doering. “Turning up the heat in turbulent thermal convection”. In: *Proceedings of the National Academy of Sciences* 117.18 (2020), pp. 9671–9673 (cit. on p. 10).

[47] T. E. Dowling and A. P. Ingersoll. “Jupiter’s great red Spot as a shallow water system”. In: *Journal of Atmospheric Sciences* 46.21 (1989), pp. 3256–3278 (cit. on p. 15).

[48] R. E. Ecke. “From 2D to 3D in fluid turbulence: unexpected critical transitions”. In: *Journal of Fluid Mechanics* 828 (2017), pp. 1–4 (cit. on p. 74).

[49] K. A. Emanuel et al. *Atmospheric convection.* Oxford University Press on Demand, 1994 (cit. on p. 1).

[50] S. Fauve, J. Herault, G. Michel, et al. “Instabilities on a turbulent background”. In: *J. Stat. Mech.: Theory and Experiment* 2017.6 (2017), p. 064001 (cit. on p. 59).

[51] S. Fauve, C. Laroche, A. Libchaber, et al. “Chaotic phases and magnetic order in a convective fluid”. In: *Physical Review Letters* 52 (1984), pp. 1774–1777 (cit. on p. 23).

[52] J. M. Finn, J. F. Drake, and P. N. Guzdar. “Instability of fluid vortices and generation of sheared flow”. In: *Physics of Fluids B: Plasma Physics* 4.9 (1992), pp. 2758–2768 (cit. on p. 17).

[53] A. C. Fowler. *Mathematical Models in the Applied Sciences.* Cambridge University Press, 1997 (cit. on pp. 32, 36).

[54] A. C. Fowler, P. D. Howell, and T. S. Khaleque. “Convection of a fluid with strongly temperature and pressure dependent viscosity”. In: *Geophysical & Astrophysical Fluid Dynamics* 110.2 (2016), pp. 130–165 (cit. on p. 1).

[55] D. Freedman and P. Diaconis. "On the histogram as a density estimator: L 2 theory". In: *Zeitschrift für Wahrscheinlichkeitstheorie und verwandte Gebiete* 57.4 (1981), pp. 453–476 (cit. on p. 70).

[56] M. Frigo and S. G. Johnson. "The Design and Implementation of FFTW3". In: *Proceedings of the IEEE* 93.2 (2005), pp. 216–231 (cit. on p. 130).

[57] A. Fujisawa. "A review of zonal flow experiments". In: *Nuclear Fusion* 49 (2008), p. 013001 (cit. on pp. 2, 15).

[58] B. Gallet. "Exact two-dimensionalization of rapidly rotating large-Reynolds-number flows". In: *Journal of Fluid Mechanics* 783 (2015), pp. 412–447 (cit. on p. 74).

[59] O. E. Garcia, N. H. Bian, J.-V. Paulsen, et al. "Confinement and bursty transport in a flux-driven convection model with sheared flows". In: *Plasma Physics and Controlled Fusion* 45.6 (2003), pp. 919–932 (cit. on p. 19).

[60] O. E. Garcia, V. Naulin, A. Nielsen, et al. "Turbulence simulations of blob formation and radial propagation in toroidally magnetized plasmas". In: *Physica Scripta* 2006 (2006), p. 89 (cit. on pp. 19, 20).

[61] T. Gastine and J. Wicht. "Effects of compressibility on driving zonal flow in gas giants". In: *Icarus* 219.1 (2012), pp. 428–442 (cit. on p. 15).

[62] A. V. Getling. *Rayleigh-Bénard Convection: Structures and Dynamics*. World Scientific Publishing Co., 1998 (cit. on p. 4).

[63] D. Goluskin, H. Johnston, G. R. Flierl, et al. "Convectively driven shear and decreased heat flux". In: *Journal of Fluid Mechanics* 759 (2014), p. 360 (cit. on pp. 2, 13, 16–18, 21, 40, 57, 61, 65, 132, 133).

[64] D. Goluskin. *Internally heated convection and Rayleigh-Bénard convection*. Springer, 2016 (cit. on p. 4).

[65] D. Goluskin. "Zonal flow driven by convection and convection driven by internal heating". PhD thesis. Columbia University, 2013 (cit. on pp. 15, 16, 20).

[66] D. Goluskin and C. R. Doering. "Bounds for convection between rough boundaries". In: *Journal of Fluid Mechanics* 804 (2016), pp. 370–386 (cit. on p. 12).

[67] D. O. Gómez, P. D. Mininni, and P. Dmitruk. "Parallel simulations in turbulent MHD". In: *Physica Scripta* 2005.T116 (2005), p. 123 (cit. on p. 130).

[68] H. Gramberg, P. Howell, and J. Ockendon. "Convection by a horizontal thermal gradient". In: *Journal of Fluid Mechanics* 586 (2007), pp. 41–57 (cit. on p. 2).

[69] D. D. Gray and A. Giorgini. "The validity of the boussinesq approximation for liquids and gases". In: *International Journal of Heat and Mass Transfer* 19.5 (1976), pp. 545–551 (cit. on p. 7).

[70] S. Grossmann and D. Lohse. “Scaling in thermal convection: a unifying theory”. In: *Journal of Fluid Mechanics* 407 (2000), pp. 27–56 (cit. on pp. 90, 102, 103, 108).

[71] S. Grossmann and D. Lohse. “Fluctuations in turbulent Rayleigh–Bénard convection: The role of plumes”. In: *Physics of Fluids* 16.12 (2004), pp. 4462–4472 (cit. on pp. 90, 102, 103, 108).

[72] S. Grossmann and D. Lohse. “Multiple scaling in the ultimate regime of thermal convection”. In: *Physics of Fluids* 23.4 (2011), p. 045108 (cit. on p. 11).

[73] S. Grossmann and D. Lohse. “Prandtl and Rayleigh number dependence of the Reynolds number in turbulent thermal convection”. In: *Physical Review E* 66 (2002), p. 016305 (cit. on pp. 90, 102, 103, 108).

[74] S. Grossmann and D. Lohse. “Thermal convection for large Prandtl numbers”. In: *Physical Review Letters* 86 (2001), pp. 3316–3319 (cit. on pp. 90, 102, 103, 108).

[75] G. Hadley. “VI. Concerning the cause of the general trade-winds”. In: *Philosophical Transactions of the Royal Society of London* 39.437 (1735), pp. 58–62 (cit. on p. 1).

[76] E. Halley. “An historical account of the trade winds, and monsoons, observable in the seas between and near the Tropicks, with an attempt to assign the physical cause of the said winds”. In: *Philosophical Transactions of the Royal Society of London* 16.183 (1686), pp. 153–168 (cit. on p. 1).

[77] J. von Hardenberg, D. Goluskin, A. Provenzale, et al. “Generation of large-scale winds in horizontally anisotropic convection”. In: *Physical Review Letters* 115 (2015), p. 134501 (cit. on pp. 2, 20).

[78] M. Heimpel and J. Aurnou. “Convective bursts and the coupling of Saturn’s equatorial storms and interior rotation”. In: *The Astrophysical Journal* 746 (2012), p. 51 (cit. on p. 19).

[79] M. Heimpel, J. Aurnou, and J. Wicht. “Simulation of equatorial and high-latitude jets on Jupiter in a deep convection model”. In: *Nature* 438 (2005), pp. 193–6 (cit. on p. 15).

[80] K. B. Hermiz, P. N. Guzdar, and J. M. Finn. “Improved low-order model for shear flow driven by Rayleigh-Bénard convection”. In: *Physical Review E* 51 (1995), pp. 325–331 (cit. on p. 15).

[81] J. R. Herring. “Convection at zero Prandtl number”. In: *Woods Hole Oceanogr. Inst. Tech. Rep.* 70.1 (1970), pp. 115–118 (cit. on pp. 23, 51, 107).

[82] W. Horton, G. Hu, and G. Laval. “Turbulent transport in mixed states of convective cells and sheared flows”. In: *Physics of Plasmas* 3.8 (1996), pp. 2912–2923 (cit. on p. 15).

[83] J. Houghton. *The Physics of Atmospheres*. Cambridge University Press, 2002 (cit. on p. 74).

[84] L. N. Howard and R. Krishnamurti. "Large-scale flow in turbulent convection: a mathematical model". In: *Journal of Fluid Mechanics* 170 (1986), pp. 385–410 (cit. on pp. 15, 16).

[85] S. Huisman, R. Van der Veen, C. Sun, et al. "Multiple states in highly turbulent Taylor-Couette flow". In: *Nature communications* 5 (2014), p. 3820 (cit. on p. 17).

[86] A. p. Ingersoll and J. N. Cuzzi. "Dynamics of Jupiter's cloud bands". In: *Journal of the Atmospheric Sciences* 26.5 (1969), pp. 981–985 (cit. on p. 15).

[87] K. P. Iyer, J. D. Scheel, J. Schumacher, et al. "Classical 1/3 scaling of convection holds up to Ra= 1015". In: *Proceedings of the National Academy of Sciences* 117.14 (2020), pp. 7594–7598 (cit. on p. 11).

[88] C. A. Jones and K. M. Kuzanyan. "Compressible convection in the deep atmospheres of giant planets". In: *Icarus* 204.1 (2009), pp. 227–238 (cit. on p. 15).

[89] M. Kaczorowski and K.-Q. Xia. "Turbulent flow in the bulk of Rayleigh–Bénard convection: small-scale properties in a cubic cell". In: *Journal of Fluid Mechanics* 722 (2013), pp. 596–617 (cit. on p. 97).

[90] Y. Kaspi, E. Galanti, W. B. Hubbard, et al. "Jupiter's atmospheric jet streams extend thousands of kilometres deep". In: *Nature* 555 (2018), p. 223 (cit. on p. 19).

[91] T. S. Khaleque, A. C. Fowler, P. D. Howell, et al. "Numerical studies of thermal convection with temperature- and pressure-dependent viscosity at extreme viscosity contrasts". In: *Physics of Fluids* 27.7 (2015), p. 076603 (cit. on p. 1).

[92] E. Knobloch. "Onset of zero Prandtl number convection". In: *Journal de Physique II* 2.5 (1992), pp. 995–999 (cit. on p. 23).

[93] A. N. Kolmogorov. "Dissipation of Energy in the Locally Isotropic Turbulence". In: *Proceedings: Mathematical and Physical Sciences* 434.1890 (1991), pp. 15–17. (Visited on 06/20/2023) (cit. on pp. 95, 97).

[94] A. N. Kolmogorov. "On degeneration (decay) of isotropic turbulence in incompressible viscous liquid". In: *Doklady Akademii Nauk* 31 (1941), p. 538 (cit. on pp. 95, 97).

[95] A. Kolmogorov. "The local structure of turbulence in incompressible viscous fluid for very large Reynolds' numbers". In: *Comptes Rendus (Doklady) de l'Académie des Sciences de l'URSS, Nouvelle Série* 30 (1941), pp. 301–05 (cit. on pp. 95, 97).

[96] D. Kong, K. Zhang, and G. Schubert. "Origin of Jupiter's cloud-level zonal winds remains a puzzle even after Juno". In: *Proceedings of the National Academy of Sciences* 115 (2018), p. 201805927 (cit. on pp. 15, 19).

[97] R. H. Kraichnan. "Turbulent thermal convection at arbitrary Prandtl number". In: *Physics of Fluids* 5.11 (1962), p. 1374 (cit. on pp. 11, 103, 108).

[98] R. Krishnamurti and L. N. Howard. "Large-scale flow generation in turbulent convection". In: *Proceedings of the National Academy of Sciences U.S.A.* 78 (1981), p. 1981 (cit. on pp. 19, 20).

[99] K. Kumar, S. Fauve, and O. Thual. "Critical self-tuning: the example of zero Prandtl number convection". In: *Journal de Physique II* 6 (1996), pp. 945–951 (cit. on p. 23).

[100] R. Labbé, J.-F. Pinton, and S. Fauve. "Study of the von Kármán flow between coaxial corotating disks". In: *Physics of Fluids* 8.4 (1996), pp. 914–922 (cit. on p. 58).

[101] A. S. Landsberg and E. Knobloch. "Direction-reversing traveling waves". In: *Physics Letters A* 159.1 (1991), pp. 17–20 (cit. on p. 22).

[102] J.-N. Leboeuf, L. A. Charlton, and B. A. Carreras. "Shear flow effects on the nonlinear evolution of thermal instabilities". In: *Physics of Fluids B* 5.8 (1993), pp. 2959–2966 (cit. on p. 19).

[103] S. K. Lele. "Compact finite difference schemes with spectral-like resolution". In: *Journal of Computational Physics* 103 (1997), pp. 16–42 (cit. on p. 132).

[104] X.-M. Li, J.-D. He, Y. Tian, et al. "Effects of Prandtl number in quasi-two-dimensional Rayleigh–Bénard convection". In: *Journal of Fluid Mechanics* 915 (2021), A60 (cit. on p. 74).

[105] E. Lindborg. *Comment on evidence of a transition to the ultimate regime of heat transfer*. 2023 (cit. on pp. 12, 134, 140).

[106] D. Lohse and F. Toschi. "Ultimate state of thermal convection". In: *Physical Review Letters* 90 (2003), p. 034502 (cit. on pp. 3, 12, 90, 91, 104).

[107] D. Lohse and K.-Q. Xia. "Small-scale properties of turbulent Rayleigh-Bénard convection". In: *Annual Review of Fluid Mechanics* 42.1 (2010), pp. 335–364 (cit. on p. 97).

[108] P. Maity, A. Bittracher, P. Koltai, et al. *Collective variables between large-scale states in turbulent convection*. 2023 (cit. on p. 60).

[109] P. Maity, P. Koltai, and J. Schumacher. "Large-scale flow in a cubic Rayleigh-Bénard cell: long-term turbulence statistics and Markovianity of macrostate transitions". In: *Philosophical Transactions of the Royal Society A: Mathematical, Physical and Engineering Sciences* 380.2225 (2022) (cit. on p. 60).

[110] M. A. Malkov, P. H. Diamond, and M. N. Rosenbluth. "On the nature of bursting in transport and turbulence in drift wave–zonal flow systems". In: *Physics of Plasmas* 8.12 (2001), pp. 5073–5076 (cit. on p. 19).

[111] W. V. R. Malkus. "The heat transport and spectrum of thermal turbulence". In: *Proceedings of the Royal Society of London. Series A. Mathematical and Physical Sciences* 225.1161 (1954), pp. 196–212 (cit. on p. 10).

[112] W. V. R. Malkus and G. Veronis. "Finite amplitude cellular convection". In: *Journal of Fluid Mechanics* 4.3 (1958), pp. 225–260 (cit. on p. 22).

[113] J. Marshall and F. Schott. “Open-ocean convection: Observations, theory, and models”. In: *Reviews of Geophysics* 37.1 (1999), pp. 1–64 (cit. on p. 1).

[114] J. M. Massaguer, E. A. Spiegel, and J.-P. Zahn. “Convection-induced shears for general planforms”. In: *Physics of Fluids A* 4 (1992), p. 1333 (cit. on p. 20).

[115] J. Maurer and A. Libchaber. “Rayleigh-Bénard experiment in liquid helium; frequency locking and the onset of turbulence”. In: *Journal de Physique Lettres* 40.16 (1979), pp. 419–423 (cit. on p. 23).

[116] A. Mazzino. “Two-dimensional turbulent convection”. In: *Physics of Fluids* 29.11 (2017), p. 111102 (cit. on p. 97).

[117] P. K. Mishra and M. K. Verma. “Energy spectra and fluxes for Rayleigh-Bénard convection”. In: *Physical Review E* 81 (2010), p. 056316 (cit. on p. 97).

[118] S. Musacchio and G. Boffetta. “Split energy cascade in turbulent thin fluid layers”. In: *Physics of Fluids* 29.11 (2017) (cit. on p. 74).

[119] R. Ni, S.-D. Huang, and K.-Q. Xia. “Reversals of the large-scale circulation in quasi-2D Rayleigh–Bénard convection”. In: *Journal of Fluid Mechanics* 778 (2015), R5 (cit. on pp. 60, 72).

[120] J. J. Niemela, L. Skrbek, K. R. Sreenivasan, et al. “Turbulent convection at very high Rayleigh numbers”. In: *Nature* 404.6780 (2000), pp. 837–840 (cit. on pp. 11, 12).

[121] L. Novi, J. von Hardenberg, D. W. Hughes, et al. “Rapidly rotating Rayleigh-Bénard convection with a tilted axis”. In: *Physical Review E* 99 (2019), p. 053116 (cit. on p. 20).

[122] A. M. Obukhov. “On influence of buoyancy forces on the structure of temperature field in a turbulent flow”. In: *Doklady Akademii Nauk* 125 (1959), pp. 1246–48 (cit. on pp. 91, 95, 97, 103).

[123] S. A. Orszag and D. Gottlieb. *Numerical analysis of spectral methods: theory and application*. SIAM, 1977 (cit. on p. 130).

[124] P. Pal, P. Wahi, S. Paul, et al. “Bifurcation and chaos in zero-Prandtl-number convection”. In: *Europhysics Letters* 87.5 (2009), p. 54003 (cit. on pp. 23, 32).

[125] A. Pandey, M. K. Verma, and M. Barma. “Reversals in infinite-Prandtl-number Rayleigh-Bénard convection”. In: *Physical Review E* 98 (2018), p. 023109 (cit. on pp. 60, 72).

[126] J. Parker, C. Howland, C. Caulfield, et al. “Optimal perturbation growth on a breaking internal gravity wave”. In: *Journal of Fluid Mechanics* 925 (2021), A16 (cit. on pp. 74, 88).

[127] S. Paul, M. K. Verma, P. Wahi, et al. “Bifurcation analysis of the flow patterns in two-dimensional Rayleigh-Bénard convection”. In: *International Journal of Bifurcation and Chaos* 22.05 (2012), p. 1230018 (cit. on pp. 15, 22, 28).

[128] S. Paul, P. Pal, P. Wahi, et al. “Dynamics of zero-Prandtl number convection near onset”. In: *Chaos (Woodbury, N.Y.)* 21 (2011), p. 023118 (cit. on p. 23).

[129] A. Persson. “Hadley’s Principle: Part 1 – A brainchild with many fathers”. In: *Weather* 63.11 (2008), pp. 335–338 (cit. on p. 1).

[130] E. Poel, R. Stevens, K. Sugiyama, et al. “Flow states in two-dimensional Rayleigh-Bénard convection as a function of aspect-ratio and Rayleigh number”. In: *Physics of Fluids* 24 (2012), p. 085104 (cit. on p. 17).

[131] E. P. van der Poel, R. Ostilla-Mónico, R. Verzicco, et al. “Effect of velocity boundary conditions on the heat transfer and flow topology in two-dimensional Rayleigh-Bénard convection”. In: *Physical Review E* 90 (2014), p. 013017 (cit. on pp. 2, 17, 20).

[132] C. Priestley. “Convection from a large horizontal surface”. In: *Australian Journal of Physics* 7.1 (1954), p. 176 (cit. on p. 10).

[133] M. R. E. Proctor and N. O. Weiss. “Symmetries of time-dependent magnetoconvection”. In: *Geophysical & Astrophysical Fluid Dynamics* 70.1-4 (1993), pp. 137–160 (cit. on p. 22).

[134] L. Rayleigh. “On convection currents in a horizontal layer of fluid, when the higher temperature is on the under side”. In: *Philosophical Magazine* 32 (1916), pp. 529–546 (cit. on pp. 12, 21, 24, 79).

[135] P.-E. Roche, B. Castaing, B. Chabaud, et al. “Observation of the $\frac{1}{2}$ power law in Rayleigh-Bénard convection”. In: *Physical Review E* 63 (2001), p. 045303 (cit. on p. 11).

[136] A. M. Rucklidge and P. C. Matthews. “Analysis of the shearing instability in nonlinear convection and magnetoconvection”. In: *Nonlinearity* 9 (1996), pp. 311–351 (cit. on pp. 2, 15, 16, 19, 22, 55).

[137] M. J. Schmeits and H. A. Dijkstra. “Bimodal behavior of the Kuroshio and the Gulf Stream”. In: *Journal of Physical Oceanography* 31.12 (2001), pp. 3435–3456 (cit. on p. 59).

[138] G. Schubert, D. L. Turcotte, and P. Olson. *Mantle convection in the Earth and planets*. Cambridge University Press, 2001 (cit. on p. 1).

[139] M. Shats, D. Byrne, and H. Xia. “Turbulence decay rate as a measure of flow dimensionality”. In: *Physical Review Letters* 105 (2010), p. 264501 (cit. on p. 74).

[140] O. Shishkina. “Momentum and heat transport scalings in laminar vertical convection”. In: *Physical Review E* 93 (2016), p. 051102 (cit. on p. 4).

[141] O. Shishkina, R. J. A. M. Stevens, S. Grossmann, et al. “Boundary layer structure in turbulent thermal convection and its consequences for the required numerical resolution”. In: *New Journal of Physics* 12.7 (2010), p. 075022 (cit. on pp. 11, 139).

[142] A. Showman. “Numerical simulations of forced shallow-water turbulence: effects of moist convection on the large-scale circulation of Jupiter and Saturn”. In: *Journal of Atmospheric Sciences* 64 (2007), pp. 3132– (cit. on p. 15).

[143] B. I. Shraiman and E. D. Siggia. “Heat transport in high-Rayleigh-number convection”. In: *Physical Review A* 42.6 (1990), pp. 3650–3653 (cit. on p. 12).

[144] V. Shukla, S. Fauve, and M.-E. Brachet. “Statistical theory of reversals in two-dimensional confined turbulent flows”. In: *Physical Review E* 94 (2016) (cit. on pp. 72, 113).

[145] E. D. Siggia. “High Rayleigh number convection”. In: *Annual Review of Fluid Mechanics* 26.1 (1994), pp. 137–168 (cit. on pp. 4, 12).

[146] J. Sommeria. “Experimental study of the two-dimensional inverse energy cascade in a square box”. In: *Journal of Fluid Mechanics* 170 (1986), pp. 139–168 (cit. on p. 74).

[147] J. Sommeria and R. Moreau. “Why, how, and when, MHD turbulence becomes two-dimensional”. In: *Journal of Fluid Mechanics* 118 (1982), pp. 507–518 (cit. on p. 74).

[148] E. A. Spiegel. “Convection in stars I. Basic Boussinesq convection”. In: *Annual Review of Astronomy and Astrophysics* 9.1 (1971), pp. 323–352 (cit. on p. 1).

[149] E. A. Spiegel and G. Veronis. “On the Boussinesq Approximation for a Compressible Fluid”. In: *The Astrophysical Journal* 131 (1960), p. 442 (cit. on p. 7).

[150] E. A. Spiegel. “A generalization of the mixing-length theory of turbulent convection.” In: *The Astrophysical Journal* 138 (1963), pp. 216–225 (cit. on pp. 11, 103, 108).

[151] R. J. A. M. Stevens, J.-Q. Zhong, H. J. H. Clercx, et al. “Transitions between turbulent states in rotating Rayleigh-Bénard convection”. In: *Physical Review Letters* 103 (2009), p. 024503 (cit. on p. 58).

[152] R. J. Stevens, R. Verzicco, and D. Lohse. “Radial boundary layer structure and Nusselt number in Rayleigh–Bénard convection”. In: *Journal of Fluid Mechanics* 643 (2010), pp. 495–507 (cit. on p. 11).

[153] K. Sugiyama, R. Ni, R. J. A. M. Stevens, et al. “Flow reversals in thermally driven turbulence”. In: *Physical Review Letters* 105 (2010), p. 034503 (cit. on pp. 59, 72, 114).

[154] E. Suzuki and S. Toh. “Entropy cascade and temporal intermittency in a shell model for convective turbulence”. In: *Physical Review E* 51 (1995), pp. 5628–5635 (cit. on pp. 3, 90, 91).

[155] P. Tabeling, B. Perrin, and S. Fauve. “Instability of a linear array of forced vortices”. In: *Europhysics Letters* 3.4 (1987), p. 459 (cit. on p. 74).

[156] R. J. Teed, C. A. Jones, and R. Hollerbach. “On the necessary conditions for bursts of convection within the rapidly rotating cylindrical annulus”. In: *Physics of Fluids* 24.6 (2012), p. 066604 (cit. on p. 19).

[157] P. Terry. “Suppression of turbulence and transport by sheared flow”. In: *Reviews of Modern Physics* 72.1 (2000), p. 109 (cit. on p. 19).

[158] C. Textor, H. Graf, M. Herzog, et al. “Volcanic particle aggregation in explosive eruption columns. Part I: Parameterization of the microphysics of hydrometeors and ash”. In: *Journal of Volcanology and Geothermal Research* 150.4 (2006), pp. 359–377 (cit. on p. 2).

[159] R. Thompson. “Venus's general circulation is a merry-go-round”. In: *Journal of the Atmospheric Sciences* 27 (1970), p. 1107 (cit. on pp. 15, 16).

[160] S. Thomson and M. Mcintyre. “Jupiter's unearthly jets: a new turbulent model exhibiting statistical steadiness without large-scale dissipation”. In: *Journal of the Atmospheric Sciences* 73 (2016) (cit. on p. 15).

[161] O. Thual. “Zero-Prandtl-number convection”. In: *Journal of Fluid Mechanics* 240 (1992), pp. 229–258 (cit. on pp. 23, 32, 51).

[162] S. Toh and E. Suzuki. “Entropy cascade and energy inverse transfer in two-dimensional convective turbulence”. In: *Physical Review Letters* 73 (1994), pp. 1501–1504 (cit. on pp. 3, 90, 91, 97).

[163] S. Toppaladoddi, S. Succi, and J. S. Wettlaufer. “Roughness as a route to the ultimate regime of thermal convection”. In: *Physical Review Letters* 118.7 (2017) (cit. on p. 12).

[164] S. Toppaladoddi, A. J. Wells, C. R. Doering, et al. “Thermal convection over fractal surfaces”. In: *Journal of Fluid Mechanics* 907 (2021), A12 (cit. on p. 12).

[165] S. Toppaladoddi and J. S. Wettlaufer. “Penetrative convection at high Rayleigh numbers”. In: *Physical Review Fluids* 3.4 (2018), p. 043501 (cit. on p. 4).

[166] A. de la Torre and J. Burguete. “Slow dynamics in a turbulent von Kármán swirling flow”. In: *Physical Review Letters* 99 (2007), p. 054101 (cit. on p. 58).

[167] P. Urban, V. Musilová, and L. Skrbek. “Efficiency of heat transfer in turbulent Rayleigh-Bénard convection”. In: *Physical Review Letters* 107 (2011), p. 014302 (cit. on p. 11).

[168] M. K. Verma, S. C. Ambhire, and A. Pandey. “Flow reversals in turbulent convection with free-slip walls”. In: *Physics of Fluids* 27 (2015), p. 047102 (cit. on pp. 24, 59, 60, 72, 114).

[169] M. Verma, A. Kumar, and A. Pandey. “Phenomenology of buoyancy-driven turbulence: Recent results”. In: *New Journal of Physics* 19 (2017) (cit. on p. 97).

[170] M. K. Verma. *Physics of Buoyant Flows*. World Scientific Publishing Co., 2018 (cit. on pp. 12, 97, 108).

[171] M. K. Verma. *Energy Transfers in Fluid Flows*. Cambridge University Press, 2019 (cit. on p. 97).

[172] G. Veronis. “The Analogy Between Rotating and Stratified Fluids”. In: *Annual Review of Fluid Mechanics* 2.1 (1970), pp. 37–66 (cit. on p. 19).

[173] F. Wagner. "A quarter-century of H-mode studies". In: *Plasma Physics and Controlled Fusion* 49.12B (2007), B1 (cit. on p. 20).

[174] B. Wang, Q. Wang, Z.-H. Wan, et al. "The influence of aspect ratio on flow states in the buoyancy-driven turbulence with free slip boundaries". In: *International Journal of Heat and Mass Transfer* 178 (2021), p. 121639 (cit. on pp. 2, 74).

[175] Q. Wang, K. L. Chong, R. J. A. M. Stevens, et al. "From zonal flow to convection rolls in Rayleigh–Bénard convection with free-slip plates". In: *Journal of Fluid Mechanics* 905 (2020), A21 (cit. on pp. 2, 13, 16, 17, 20, 57).

[176] Q. Wang, Z. Wan, R. Yan, et al. "Multiple states and heat transfer in two-dimensional tilted convection with large aspect ratios". In: *Physical Review Fluids* 3 (2018), p. 113503 (cit. on p. 17).

[177] Y. Wang, P.-Y. Lai, H. Song, et al. "Mechanism of large-scale flow reversals in turbulent thermal convection". In: *Science Advances* 4.11 (2018) (cit. on p. 59).

[178] Z. Warhaft. "Passive scalars in turbulent flows". In: *Annual Review of Fluid Mechanics* 32.1 (2000), pp. 203–240 (cit. on p. 104).

[179] E. Warneford and P. Dellar. "Thermal shallow water models of geostrophic turbulence in Jovian atmospheres". In: *Physics of Fluids* 26 (2014), p. 016603 (cit. on p. 15).

[180] E. R. Weeks, Y. Tian, J. S. Urbach, et al. "Transitions between blocked and zonal flows in a rotating annulus with topography". In: *Science* 278.5343 (1997), pp. 1598–1601 (cit. on p. 59).

[181] A. J. Wells, J. S. Wettlaufer, and S. A. Orszag. "Nonlinear mushy-layer convection with chimneys: stability and optimal solute fluxes". In: *Journal of Fluid Mechanics* 716 (2013), pp. 203–227 (cit. on p. 1).

[182] B. Wen, D. Goluskin, M. LeDuc, et al. "Steady Rayleigh–Bénard convection between stress-free boundaries". In: *Journal of Fluid Mechanics* 905 (2020), R4 (cit. on pp. 118, 121).

[183] J. Wettlaufer, M. G. Worster, and H. E. Huppert. "Natural convection during solidification of an alloy from above with application to the evolution of sea ice". In: *Journal of Fluid Mechanics* 344 (1997), pp. 291–316 (cit. on p. 1).

[184] P. Winchester, V. Dallas, and P. D. Howell. "Zonal flow reversals in two-dimensional Rayleigh-Bénard convection". In: *Physical Review Fluids* 6 (2021), p. 033502 (cit. on p. 3).

[185] P. Winchester, P. D. Howell, and V. Dallas. "The onset of zonal modes in two-dimensional Rayleigh–Bénard convection". In: *Journal of Fluid Mechanics* 939 (2022), A8 (cit. on pp. 3, 30, 52, 53).

[186] J.-H. Xie and S.-D. Huang. "Bolgiano–Obukhov scaling in two-dimensional isotropic convection". In: *Journal of Fluid Mechanics* 942 (2022), A19 (cit. on pp. 97, 105).

[187] Y.-C. Xie, G.-Y. Ding, and K.-Q. Xia. “Flow topology transition via global bifurcation in thermally driven turbulence”. In: *Physical Review Letters* 120 (2018) (cit. on p. 17).

[188] X. Zhang, D. P. M. van Gils, et al. “Boundary zonal flow in rotating turbulent Rayleigh-Bénard convection”. In: *Physical Review Letters* 124 (2020), p. 084505 (cit. on pp. 2, 15).

[189] X. Zhu, V. Mathai, R. J. A. M. Stevens, et al. “Transition to the Ultimate Regime in Two-Dimensional Rayleigh-Bénard Convection”. In: *Physical Review Letters* 120 (2018), p. 144502 (cit. on p. 12).

[190] X. Zhu, R. J. A. M. Stevens, O. Shishkina, et al. “Scaling enabled by multiscale wall roughness in Rayleigh–Bénard turbulence”. In: *Journal of Fluid Mechanics* 869 (2019) (cit. on p. 12).

[191] X. Zhu, R. J. A. M. Stevens, R. Verzicco, et al. “Roughness-facilitated local 1/2 scaling does not imply the onset of the ultimate regime of thermal convection”. In: *Physical Review Letters* 119 (2017), p. 154501 (cit. on p. 12).